Fire in bored tunnels

Structural behaviour, during fire conditions, of bored tunnels made with a concrete segmental lining

B.B.G. Lottman

TU Delft

ABAQUS

Main report

Author:
B.B.G. Lottman
Study number: 1228471

Delft University of Technology
Faculty of Civil Engineering and Geosciences
Master Structural Engineering
Concrete Structures
Stevinweg 1, Delft, Netherlands

Master thesis committee:

Prof. dr. ir. J.C. Walraven	Delft University of Technology
Dr. ir. C.B.M. Blom	Delft University of Technology / Gemeentewerken Rotterdam
Dr. ir. P.C.J.. Hoogenboom	Delft University of Technology
Dr. ir. E.A.B. Koenders	Delft University of Technology
Ir. V. Bouwman	ABAQUS Benelux B.V.
Ir. T. van Overbeek	TNO Built Environment and Geosciences
Ir. L.J.M. Houben	Delft University of Technology

July 2007

Preface

The presented master thesis is written to obtain the degree of master in Civil Engineering with the specialisation structural engineering at the Technical University the Delft in the Netherlands. This master thesis is conducted in cooperation with Delft University of Technology, faculty of Civil Engineering, section Buildings and Civil Constructions and the company ABAQUS Benelux B.V.. In this master thesis the aim is to develop a better understanding about the structural behaviour of bored tunnel, made with a concrete segmental lining, during fire conditions. The master thesis mainly deals with spalling of concrete and consists out of describing the main process which leads to spalling and presenting a analytical and numerical model which predict the process and the occurrence of spalling in concrete.

The master thesis committee consists of the following members:

Prof. dr. ir. J.C. Walraven	Delft University of Technology
Dr. ir. C.B.M. Blom	Delft University of Technology / Gemeentewerken Rotterdam
Dr. ir. P.C.J.. Hoogenboom	Delft University of Technology
Dr. ir. E.A.B. Koenders	Delft University of Technology
Ir. V. Bouwman	ABAQUS Benelux B.V.
Ir. T. van Overbeek	TNO Built Environment and Geosciences
Ir. L.J.M. Houben	Delft University of Technology

Furthermore, I would like to take this opportunity to thank some persons. First of all I would like to thank Prof. J.C. Walraven who gave me the opportunity to graduate at the section of Buildings and Civil Constructions at the faculty of Civil Engineering. Furthermore, I would like to thank the members of my committee for their advice and guidance throughout this master thesis. I especially would like to thank C.B.M. Blom for his guidance in my master thesis and in discussing my opportunities after graduating. Furthermore, I would like to thank E.A.B. Koenders for the opportunity to participate in the promotion project “Explosive Spalling of concrete”. I would also like to thank the company ABAQUS Benelux B.V. for helping me to develop the numerical model for spalling and to obtain a better understanding in finite elements programs. I especially would like to thank V. Bouwman, G. Kloosterman and T. Verbruggen.

Delft, July 2007
B.B.G. Lottman

Summary

In recent years there have been a number of serious fires in tunnels throughout Europe. The most well-known are the Mont Blanc tunnel fire and the Channel tunnel fire. In most of these tunnel fires there were injured people and sometimes even human casualties. Furthermore, there was damage to the tunnel and sometimes even significant damage which jeopardized the structural integrity of the tunnel. Finally, there was always economical damage due to repair costs for tunnel reconstruction, loss of income for the tunnel authority and hinder for the traffic, resulting in longer waiting periods or extra miles to by-pass to a different tunnel. This short description indicates why fire in tunnels can have a serious impact on human life and why research is needed to develop a better understanding of the behaviour of concrete structures during exposure to a fire.

The presented master thesis is written in light of these developments and the main goal is therefore to obtain more knowledge about the structural behaviour of tunnels during a fire. To obtain this main goal, two separate goals are stated which are to obtain a general overview of concrete exposed to a fire and especially the process which leads to spalling of concrete which also includes the main theories and factors influencing this process. Furthermore, the goal is also to derive a analytical and numerical model which are relative simple and therefore the main theories and factors influencing the process of spalling can be identified and examined. The derived numerical can then be used in a case study of the “Groene Hart” tunnel.

The main theory of the process which causes spalling of concrete is the penetration of the heat from the fire into the cross section of concrete and the subsequent evaporation of water from the pores of the concrete. Due to the phase change the development of water vapour coincides with an increase in pore pressure, which induces the flow of water vapour. In time the water vapour increasingly flows into the cross section and condensates into water which causes the gradual development of a fully saturated layer called a moisture clog. This layer impedes further water vapour transport and on the front of this layer the pore pressure can build up and could lead to spalling of the layer in front of the fully saturated layer.

The main factor of the material which influences the occurrence of spalling is the permeability of the concrete. When the permeability of the concrete decreases, the pore structure is badly interconnected and therefore the possibility of spalling increases. The factors of the material which contribute to the occurrence of spalling are the porosity, the initial degree of saturation and the tensile strength of the concrete. When the porosity decreases and/or the initial degree of saturation increases, the amount of empty space which the water vapour can fill reduces and therefore the possibility of spalling increases. The tensile strength of the concrete determines the capability of the concrete to withstand the development of pore pressures and therefore when the tensile strength of the concrete reduces, the possibility of spalling increases.

The main factor of the fire which influences the occurrence of spalling is the heating rate of the concrete. The heating rate determines the progress of the evaporation front and the development of the pore pressures. The possibility of spalling increases when the heating rate of the concrete increases. The factor of the fire which contributes to

the occurrence of spalling is the number of sides of the construction which are exposed to the fire. A construction which is exposed to a fire at two or more sides is heated up with a greater speed and therefore the possibility of spalling increases.

The factors of the construction which contribute to the occurrence of spalling are the loading of construction and reinforcement. Compressive stresses, especially on the heated surface, tend to close the cracks which are formed by the degradation process of the concrete and therefore the permeability is locally reduced increasing the possibility of spalling. Furthermore, compressive Eigen stresses cause cracks parallel to the heated surface which reduce the tensile strength in the direction perpendicular to heated surface. Tensile stresses in the cross section decrease the capability of the concrete to withstand tensile stresses due to pore pressure build up and therefore the possibility of spalling increases. Concrete with dense reinforcement in a construction tends to impede further water vapour transport and exhibit locals tensile stress peaks which increases the possibility of spalling.

The described process which leads to the occurrence of spalling is then used to derive an analytical model which consists of four parts. The first part is the determination of the temperature distribution followed by the temperature stresses which is the second part. The third part determines the evaporation of water and the flow of water vapour. From this the degree of saturation throughout the cross section can be determined. The last part determines if a saturated layer has been formed and the development of the pore pressure at the front of this saturated layer. In the analytical model, the cross section of the concrete surface is subdivided into elements with an arbitrary length of 4mm. In every time increment the temperature distribution is determined by using the Fourier differential equation. From the temperature distribution, the progress of the 100 ^{o}C front can be calculated. This distribution is used to determine the start of the evaporation process in every element. The evaporation process is modelled by using the amount of evaporable water present in each element and the latent heat of vaporization needed to evaporate this amount of water. This leads to an estimate about the amount of water which is evaporated in the current time increment. By using the saturated vapour pressure an estimate can be made about the pressure in the pores of the concrete at the location of evaporation and, by using the atmospheric pressure, an estimate can be made for the pressure in the interior of the concrete as well. This leads to a pressure difference, which is used to determine the flow speed of water vapour into the interior of the concrete, while using Darcy's law. Together with the amount of water evaporated in the current time increment, an estimate is made about the amount of water vapour which flows through the concrete. This process continues until the evaporation process reaches an element in which all the pores are filled with water, which represents a saturated element. To determine if a saturated layer has been formed, a check is made whether the speed of the 100 ^{o}C front is higher than the flow speed of the water vapour. Is this case, the water vapour cannot condensate back to water and thus a saturated layer is starting to be formed. Whenever the water is evaporated from this saturated layer, it is assumed to flow towards the surface of the concrete and, associating with an expansion of the water vapour due to the increase in temperature. Hence, the restrained expansion and hindered flow of the water vapour, is taken into account by using the equation by Kodres. From this equation, which takes the pressure difference and the temperature difference into account, a mass flux can be determined. This equation is used to determine the build up of pore pressure at the front of the saturated layer. This model shows a saturated layer after around 5

minutes at a depth of 16 mm and a thickness of 12 mm. The pore pressures are developed high enough to cause spalling and therefore this model estimates spalling with a depth of 16 mm.

Furthermore, a numerical model is developed in conjunction with ABAQUS Benelux BV by using ABAQUS/Standard. The finite element model consists of two main modules. The first part is the Heat transfer model. The second part is the model which determines the pore pressure development and the flow of water vapour through the concrete. The first part of the numerical model is based upon an uncoupled heat transfer calculation. This means that the temperature is the only degree of freedom. The obtained temperature distribution is used as input in the second part of the numerical model. The second part of the numerical model is based upon a coupled Pore fluid/Stress model. The flow of the wetting liquid is modelled by using Darcy's law. However, the soil model is only capable of modelling the flow of wetting liquid with a single phase. In case of the process which causes spalling, a two phase flow is present. The behaviour of the wetting liquid is therefore adapted. The wetting liquid behaves like water at temperatures below 100 ^{o}C. In the temperature interval of 100 ^{o}C –150 ^{o}C the water in the pores of the concrete is evaporated and the wetting liquid has to behave like a mixture of water and water vapour. With further increasing temperatures, the wetting liquid behaves like water vapour. In the numerical model the behaviour of the wetting liquid, whenever the evaporation process takes place, is modelled by introducing a temperature dependent expansion coefficient for the wetting liquid and a temperature dependent bulk modulus. This expansion coefficient determines the pore pressure build up in the wetting liquid which normally arises from the evaporation of water into water vapour. The bulk modulus takes into account the change in compressibility when the water is evaporated into water vapour. The numerical model estimates spalling after around 4,5 minutes with a depth of 29 mm. As a part of the numerical model a FORTRAN based subroutine is implemented which checks whether the estimated tensile stresses, resulting from the pore pressure development, exceed the prevailing limit tensile stress of the concrete. In that case the calculation is aborted and the subroutine estimates the depth of spalling. The calculation is restarted using the pressure and stress distribution throughout the cross section at the end of the previous calculation and the modified geometry, taking the spalled of layer into account.

The developed numerical model is used in a case study of the "Groene Hart" tunnel. The tunnel is first modelled with a Heat transfer analysis to determine the heat penetration into the lining. The fire inside the tunnel is modelled as a fire box which heats up according to the HSL-Zuid fire curve and submits, through radiation and conductance, heat to the surface of the lining. Furthermore, the reaction from the tunnel is subdivided into two models. The first model is a spring supported ring which is subjected to the soil loading and the results from the Heat transfer model. This model determines the stress distribution in the lining due to the heat penetration and the soil loading. The second model is the Pore fluid/Stress model and consists of a simply supported ring which is only subjected to the results from the Heat transfer model. This model determines the pore pressure distribution, which is then prescribed on the Soil loading model to obtain the complete resulting stress distribution. The stress distribution in the lining should be checked against the biaxial strength of the concrete and by taking into account the temperature dependence of the tensile strength of the concrete.

Table of Contents

1. Introduction 1

2. Fire in tunnels 2

2.1. General 2

2.2. Tunnel fires in recent years 2

3. Goal of this master thesis 6

4. Behaviour of concrete during fire 7

4.1. Chemical dehydration and decomposition process 7

4.2. Mechanical properties of concrete under fire 9

4.2.1. Compressive strength 9
4.2.2. Tensile strength 11
4.2.3. Modulus of Elasticity 11
4.2.4. Stress-Strain relationship 12
4.2.5. Transient thermal creep 13

4.3. Time dependent behaviour of concrete during fire 16

4.3.1. Creep 16
4.3.2. Relaxation 16
4.3.3. Shrinkage 17

4.4. Thermal properties of concrete during fire 17

4.4.1. Density 17
4.4.2. Heat capacity 17
4.4.3. Thermal conductivity 18
4.4.4. Thermal diffusitivity 19
4.4.5. Thermal expansion 19

4.5. Permeability and porosity of concrete at elevated temperatures 20

4.5.1. Permeability and porosity at elevated temperatures 21

4.6. Spalling of concrete 23

4.6.1. Different types of spalling behaviour 23
4.6.2. The process which leads to spalling 23
4.6.3. Different types of gas flow 27
4.6.4. Factors influencing spalling 28
4.6.5. Spalling of High Performance Concrete 29
4.6.6. Structural protection against spalling 31

5. Analytical model 33

5.1. General outline and goal of the presented model 33

5.2. The different parts of the analytical model 33

5.3. First part: temperature distribution 33

5.3.1. Theory 33
5.3.2. Numerical solution 34
5.3.3. Assumptions 35
5.3.4. Material properties used in the analytical model 36
5.3.5. Results and analysis 36

5.4. Second part: internal stresses due to the temperature distribution 38

5.4.1. Theory 38
5.4.2. Numerical solution 40
5.4.3. Assumptions 41
5.4.4. Material properties used in the analytical model 41
5.4.5. Results and analysis 42

5.5. Third part: prediction of water vapour transport 45
5.5.1. Theory 45
5.5.2. General idea 49
5.5.3. Assumptions 52
5.5.4. Numerical solution for flow to the next element 53
5.5.5. Numerical solution for the flow to multiple elements 56
5.5.6. Material properties used in the analytical model 56
5.5.7. Numerical example for the calculation of the transport of water vapour 58
5.5.8. Results and analysis 60

5.6. Fourth part: check saturated layer and build up of pore pressure 64
5.6.1. Theory 64
5.6.2. Saturated layer and build up of pore pressure: general idea 69
5.6.3. Assumptions 72
5.6.4. Numerical solution 73
5.6.5. Material properties used in the analytical model 75
5.6.6. Results and analysis 75

6. Numerical model 84

6.1. General outline and goal of the presented model 84

6.2. The different parts of the numerical model 84

6.3. First part: Heat transfer model 84
6.3.1. Theory 84
6.3.2. Numerical implementation 87
6.3.3. Assumptions 89
6.3.4. Material properties used in the numerical model 89
6.3.5. Results and analysis 89

6.4. Second part: Pore fluid/Stress model 91
6.4.1. General idea 91
6.4.2. Theory 96
6.4.3. Numerical implementation until spalling occurs 104
6.4.4. Numerical implementation to resume the calculation 111
6.4.5. Assumptions 113
6.4.6. Material properties used in the numerical model 114
6.4.7. Results and analysis 116

7. Comparison and validation of the analytical and the numerical model 129

7.1. General 129

7.2. Comparison 129

7.3. Validation 133
7.3.1. Theoretical validation 133
7.3.2. Experimental validation 134

8. Case study: HSL-Zuid 'Groene Hart' tunnel 138

8.1. General 138

8.2. The Heat transfer model 139

8.3. The Pore fluid/Stress model 140

8.4. Results and analysis 145

8.5. Remarks 152

9. Conclusions and recommendations 154

9.1. Conclusions 154
9.1.1. General conclusions 154
9.1.2. Conclusions about the analytical and numerical model 155

9.2. Recommendations 157

Appendices

Appendix A : HSL –Zuid fire curve I

Appendix B : Material properties used in the analytical model III

Appendix C : Material properties used in the numerical model VIII

Appendix D : User subroutine used in ABAQUS for the 1D model XI

Appendix E : References XIX

1. Introduction

In the last 10 years there have been fires in a numerous of tunnels for instance in the Channel tunnel (1996), Mont Blanc tunnel (1999) or more recent the Viamala tunnel (2006). In all of these fires there were humans injured and most of the time also human casualties. Besides the human impact, the tunnel itself suffered serious structural damage and had to be repaired. This results in direct cost for repair of the tunnel, but also in indirect cost because of the tunnel not being operational during repair. Together these costs form the economical impact. To reduce the direct repair costs, increasingly more money is spend on fire resistant measures of the tunnel, such as fire resistant sprayed concrete. The fire resistant cladding is seen as an investment to reduce the damage to the structure of the tunnel in case of fire. The indirect costs can also be quite considerable, because of the loss of income for the tunnel authority, but also the extra costs for the user, due to extra miles to be covered to a different tunnel and possibly extra waiting periods. In light of these developments the European Commission has set up different projects in which the current safety of tunnels is reviewed and the guidelines are improved [29]. The goal is to insure that in the future people have enough time to safe themselves and that there is a minimum of damage to the structure of the tunnel. This master thesis is written in light of these developments and aims to predict the behaviour of bored tunnels made with concrete segmental lining during fire conditions.

This report contains the master thesis about the structural behaviour of bored tunnels, made with a concrete segmental lining, under fire conditions. The master thesis mainly deals with spalling of concrete and consists out of describing the main process which leads to spalling and presenting a analytical and numerical model which predict the process and the occurrence of spalling in concrete.

This report consists of four parts. The first part discusses briefly the major tunnel fires of recent years and the main goal of this master thesis. The second part deals with the behaviour of concrete at increasing temperatures and incorporates an overview about the general material properties, the process which causes spalling and the main theories and factors influencing this process. The third part is the largest part of this master thesis and discusses the development, behaviour and results of the analytical and numerical model which predict the process and the occurrence of spalling. Finally, in the fourth part the conclusions and recommendations are presented.

2. Fire in tunnels

2.1. General

Tunnel fires can have a significant impact on the safety of the tunnel. During fire conditions the tunnel is subjected to extreme high temperatures. This heating of the structure will have a direct and indirect thermal impact, i.e. loss of strength and stiffness of the concrete and the reinforcement as well as the internal stresses resulting of the heating and the strain and deformations occurring during and after the fire [10]. Another import topic is spalling. Spalling is potentially the most damaging for the structure of the tunnel. This phenomenon can result, in case of explosive spalling, in damage to the structure and in case of extensive damage ultimately cause collapse of the structure. In case of bored tunnels the chances of spalling are further enlarged by the use of high strength concrete with low permeability and the fact that the structure is permanently under pressure by the soil. However, in case of bored tunnels a relative large amount of damage can be allowed, because the reinforcement steel is mainly present for the construction phase. During the service life of the tunnel the reinforcement steel plays a less vital part in the load bearing capacity and therefore a reduction in strength of the reinforcement steel does not automatically lead to collapse [41]. However, a tunnel which is extensive damaged due to explosive spalling maybe difficult to repair.

Besides the above mentioned short term effects of the fire there are also long term effects such as the loss of load bearing capacity and durability. During the fire conditions the concrete and reinforcement lose their strength and stiffness and after the fire these are only partly restored. This means that the load bearing capacity is reduced. For the durability it is important that during the fire conditions micro cracks are formed and these make the concrete accessible to for instance chloride and may result in corrosion of the reinforcement. For both aspects it holds that if the damage is too extensive, the damaged concrete and reinforcement have to be removed and replaced by new concrete and reinforcement.

2.2. Tunnel fires in recent years

In the last 10 years there have been numerous of tunnels which suffered tunnel fires. In all of these fires humans were injured and in most of the cases there were human casualties. Besides the human impact, the structure of the tunnel itself suffered serious damage. All of the hereafter mentioned tunnels were closed for a longer period of time due to repair.

The Channel tunnel fire, November 18, 1996

The Channel tunnel consists of 3 separate tubes buried 40 meters under the ground of the Sea. This rail road tunnel connects France to England. On November 18, 1996 there was a fire in a lorry aboard the train. The fire spread fast to the rear of the train. According to the official accident report [8] the temperatures rose to 1000 ^{o}C. All the passengers were evacuated safely. The tunnel was extensive damaged over a length of 2 kilometres. In some segments the thickness of the lining, which used to be 40 centimetres, was reduced to as little as 2 centimetres (figure 2.1). The thickness of the lining, on average, was reduced to 17 centimetres.

Fig 2.1 damage to tunnel lining Channel tunnel

The only reason why the tunnel did not collapse and filled with water, was the fact that the ground conditions were favourable at the given location. That particular section was surrounded in rock. The total repair costs were 200 million pound.

Mont Blanc tunnel fire, March 24, 1999

The Mont Blanc tunnel consists of 1 tube with traffic in 2 directions and connects Italy with France by way of a tunnel with a length of 11,6 kilometres. On March 24, 1999 a truck loaded with 9 tons of margarine and 12 tons of flour drove into the tunnel in the directions of Italy. On board of the truck there already was a small fire. A few kilometres into the tunnel the fire was noticed and the truck stopped. Within minutes the tunnel was, as a witness said, like an oven. The temperature increased to 1000 ^{o}C and the smoke was toxic. Besides these already devastating circumstances there was also made a crucial mistake. The Italian operator seeing people fleeing on foot judged it was preferable to introduce oxygen to give those people a chance instead of switching the ventilation to maximum extraction. This added oxygen helped the flames to spread much more rapidly and created a blow of toxic smoke towards the French side. The fire lasted for 50 hours and there were 41 human casualties. The tunnel itself was seriously damaged over a length of 900 meters (figure 2.2). In some segments the underlying rock could be seen trough holes in the concrete walls. The tunnel was closed for repairs until December 2001.

Kaprun tunnel fire, November 11, 2000

This tunnel is different from the rest of the tunnel mentioned in this section. The tunnel near Kaprun, in Austria, has a length of 3,2 kilometres and goes up a mountain to an alpine resort. It is used for transporting people. On November 11, 2000 a fire started in the train caused by a disfunctioning radiator. There were 155 human casualties. The reason for this very high number is the fact that the doors would not open (figure 2.3).

Fig 2.2 damage to Mont Blanc tunnel

Fig 2.3 damage to Kaprun tunnel

Gotthard tunnel fire, October 24, 2001

The Gotthard tunnel consists also of 1 tube with traffic in 2 directions. This tunnel with a length of 16,9 kilometres connects Italy with Switzerland. The tunnel fire started with the collision of 2 trucks. The fire resulted in temperatures of 1000 ^{o}C. Most of the 11 human casualties died of suffocation. Due to the fire part of the roof of the tunnel collapsed (figure 2.4). The tunnel was closed for repairs for 2 months.

Fig 2.4 fire and subsequent damage to Gotthard tunnel

Frejus tunnel fire, June 4, 2005

This tunnel, with a length of 12,9 kilometres, has the same layout as the Gotthard and Mont Blanc tunnel. Together with the Mont Blanc tunnel this tunnel connects Italy to France. On June 4, 2005 a lorry carrying tires caught fire. The subsequent fire caused 2 human casualties. The tunnel was serious damaged and closed for repairs.

Viamala tunnel fire, September 16, 2006

This tunnel fire is the latest one in a long series of tunnel fires. The Viamala tunnel, in Switzerland, is a relatively short tunnel, with a length of 742 meters. On September 16, 2006 an accident between a bus and a car caused a tunnel fire that resulted in 6 human casualties. The tunnel suffered structural damage and was to be closed for repair (figure 2.5).

Fig 2.5 damage to Viamala tunnel

3. Goal of this master thesis

Main goal

In the previous chapter it is indicated that the tunnel fires, which occurred throughout Europe in recent years, all had serious social, structural and economical consequences and therefore has lead to the development of various projects which all have the main goal of improving the safety in tunnels during a fire. One way of improving the safety in tunnels is a better understanding about the structural behaviour of tunnels during a fire. The main goal of this master thesis is therefore to obtain more knowledge about the structural behaviour of tunnels during a fire. In this master thesis the emphasis is on bored tunnels made with a concrete segmental lining due to the large number of these tunnels being present and build in the Netherlands and throughout Europe. To obtain this main goal, two separate goals are stated.

First goal

The first goal of this master thesis is to obtain a general overview of concrete exposed to a fire and in particular the phenomenon which is now as spalling of concrete. This incorporates a general overview of the important material factors of concrete and the effect the increasing temperature has on these properties. Furthermore, the phenomenon of spalling is to be further examined to incorporate a description of the process which causes spalling to occur and the main theories and factors influencing this process.

Second goal

The second goal is to derive a analytical and numerical model which are relatively simple and therefore the main theories and factors influencing the process of spalling can be identified and examined. From this it can be concluded which information is already present and in which fields further information needs to be gathered. Furthermore the analytical and the numerical model need to give a good impression of the behaviour of concrete during exposure to a fire and especially the process of spalling.

The developed numerical model can then be used to do a case study of the “Groene Hart” tunnel in the HSL-Zuid, which is the new high speed railway link in the Netherlands. This case study is to incorporate the simulation of a railway fire insight the tunnel and the effect the fire has on the concrete of the lining and especially the occurrence of spalling.

4. Behaviour of concrete during fire

4.1. Chemical dehydration and decomposition process

Concrete is usually described as a two-component material, consisting of hydrated cement paste and aggregate. The properties of concrete are determined by the properties of its components and the interface between them. The cement, for instance portland cement, cures by the hydration of its components on addition of water. The hereby formed product is called cement paste. The principal component of the cement paste is an impure, quasi amorphous calcium silicate hydrate called CSH-gel [23]. The CSH-gel is roughly 70 percent of the weight of the fully hydrated cement paste and is formed out of the C3S and C2S of the cement. Another major component is calcium hydroxide, Ca(OH)2, called CH (portlandite). CH is present in fairly well developed crystals embedded in de CSH-gel and is 20 percent of the weight. The paste also contains a number of other hydrates. All these components together are, in practise, referred to as 'the gel'.

The hydrated cement can be schematized as a gel matrix and a system of capillary pores. The capillary pores are the residue of the originally water-filled and air filled spaces that have not become invaded by the gel [23]. The gel is a porous material, in which the gel pores are narrow, interconnected spaces in the CSH-gel. These spaces are most of the time filled with evaporable water, which is being held there by van der Waals forces. The capillary pores are larger and usually not fully interconnected. To which extent the capillary pores are filled with water depends on the ambient atmosphere. The water is being held in the there by capillary forces. The water in the gel pores and the capillary pores is called evaporable water. Besides evaporable water there is also non-evaporable water.

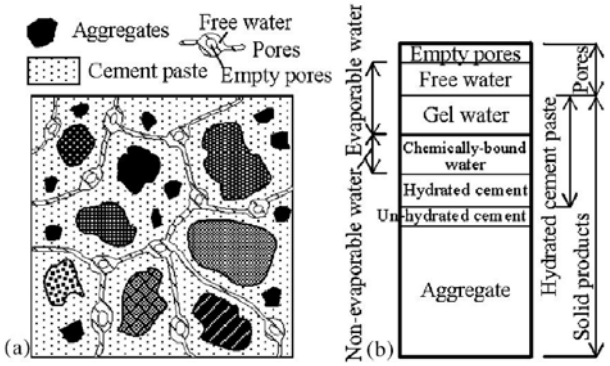

Fig 4.1 (a) Schematic description of the concrete structure and (b) the volumetric proportions of the concrete components [26]

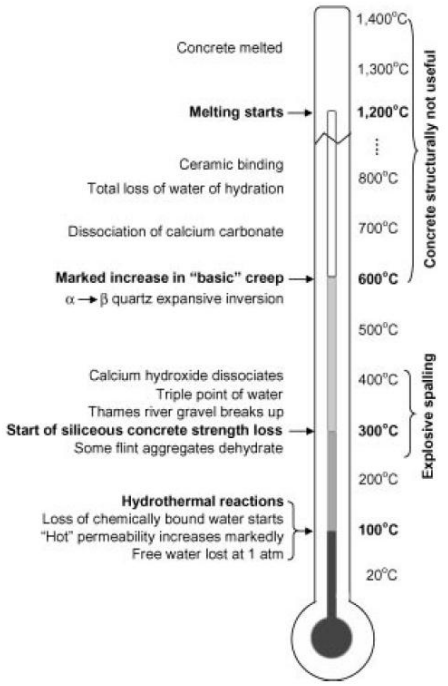

Fig 4.2 chemical dehydration and decomposition processes in the concrete at elevated temperatures [28]

This is water that is chemically bounded in the cement paste. This water only becomes available when, at elevated temperatures, the degradation of the cement paste takes place. In figure 4.1 the basis of the material concrete is schematically depicted.

Upon heating the temperature will rise and a degradation process in the concrete will start. This means that there occurs a progressive detoriation in the structure of the concrete [23,42]. The temperature increases further and at a temperature of 100 ^{o}C the cement paste will first lose the evaporable water held by the capillary forces in the capillary pores. After the capillary water is evaporated, the water held by the van der Waals forces in de gel pores in evaporated. As the temperature becomes higher than 100 ^{o}C, the evaporation will proceed at a faster rate. This is because the water is being expelled as a result of above-atmospheric vapour pressure. By the time the temperature reaches 120 ^{o}C, there will only be non-evaporable water present. As the temperature rises further the decomposition of the gel has already begun. This process begins with the dehydration of the CSH-gel. The maximum dehydration rate occurs at a temperature of 180 ^{o}C. This process continues until at a temperature of 300 ^{o}C. In the temperature interval of 450-550 ^{o}C there is a rapid decomposition of the CH. During this decomposition, CH (Ca(OH)2) is decomposed into clay (CaO) and water (H2O) is released. This water, which used to be chemically bounded and non-evaporable, now becomes evaporable. At a temperature of 570 ^{o}C the α-β inversion of quartz takes place. This process is reversible. At a temperature of 600 ^{o}C until 700 ^{o}C the decomposition of the CSH-gel into β-C2S occurs. Again this decomposition process produces water. In some aggregates, in the temperature range of 120-600 ^{o}C, there is also the release of water. In concrete with limestone aggregates, at a temperature interval of 600-900 ^{o}C, there is an additional loss in weight. This is due to the decarbonation reaction, in other words the decomposition of the calcium carbonate. At temperatures in excess of 900 ^{o}C, there is no further weight loss. At a temperature of 1150-1200 ^{o}C the concrete melts. In some cases this can lead to bloating of the aggregate. The weight loss at increasing temperature is depicted in figure 4.3, which shows that weight loss can reach up to 6 – 14 percent of its initial weight. The dehydration and decomposition processes of the concrete are depicted in figure 4.2. The temperatures which are depicted are the temperatures of the material concrete and not the fire. However, the temperatures indicated for explosive spalling are the temperatures on the surface of the concrete.

The described degradation process gradually decrease the amount of cement paste, which means that the connection between the aggregate particles reduces and therefore the concrete loses strength. However, the decrease of cement paste increases the amount of pores which increases the permeability of the concrete. Furthermore, the difference in thermal expansion between the aggregate and the cement paste causes internal cracking which also reduces the connection between the cement paste and the aggregate.

After the fire, the temperature of the concrete gradually decreases. During this cooling process, absorption of water vapour from the atmosphere takes place, which induces the reaction of CaO to form CH. CSH-gel is not recovered during cooling. CH formed when cooling is less crystalline than the original CH and its temperature of thermal decomposition is lower [7].

4.2. Mechanical properties of concrete under fire

4.2.1. Compressive strength

The compressive strength of concrete during heating is frequently investigated. The reason is that the value of the compressive strength gives a good indication about the overall quality of the concrete. According to different authors [42,6,11] is the compressive strength of ordinary concrete until a temperature of roughly 200 ^{o}C unchanged. At temperatures higher than 200 ^{o}C there is a significant reduction in the compressive strength. At a temperature of 600 ^{o}C, on average, only 30% of the original compressive strength remains. At temperatures of 800-1000 ^{o}C no compressive strength remains. In figure 4.4 the compressive strength at increasing temperature according to different experiments is shown.

The authors Poon, Azhar, Anson and Wong [37] have done research into the compressive strength, of normal- and high strength concrete, at elevated temperatures. These concrete mixes also contained fillers. The fillers used in this research are: pulverized fly ash (PFA) and silica fume (SF). PFA and SF are fillers which are used in concrete to increases strength and durability. In the temperature range of 20-200 ^{o}C concrete with PFA as filler showed an increase in strength. The maximum strength gain, around 22 percent, is in high strength concrete with PFA [37]. This strength gain is due to the formation of tobermorite, which is the product of lime and PFA at high pressure and temperature and is stronger than the CSH-gel. In the temperature range of 200-400 ^{o}C most high strength concretes maintain their compressive strength, while normal strength concrete undergo a strength decrease of 20-30 percent [37]. In the temperature range of 400-600 ^{o}C a severe loss in strength occurs, both for normal and high strength concrete, however the strength loss is the greatest in case of high strength concrete.

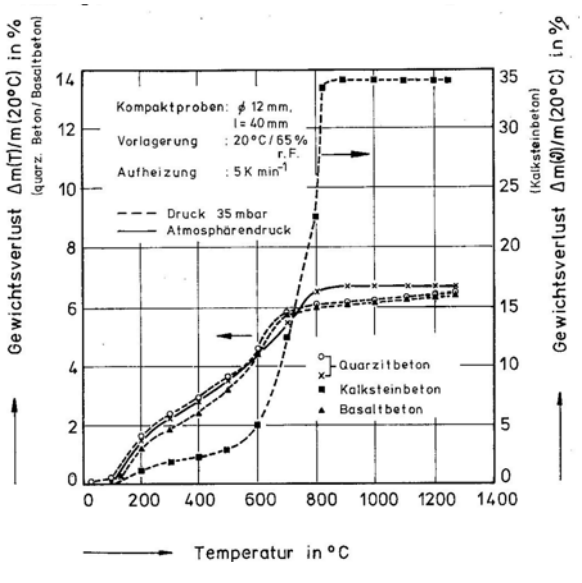

Fig 4.3 weight loss of normal weight concrete as function of increasing temperature made with Portland cement [42]

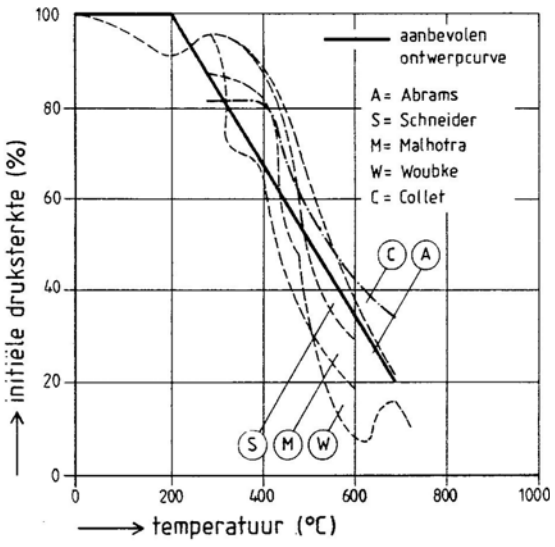

Fig 4.4 compressive strength of concrete as function of increasing temperature [6]

The residual compressive strength of concrete with silica fume (SF) as filler is less than ordinary concrete with portland cement. The maximum relative residual strength is obtained for high strength concrete with 30 percent PFA [37]. The better performance of PFA in this temperature range is due to the reduced amount of CH, which otherwise results in strength loss and disintegration. At a temperature of 800 ^{o}C all concretes, normal and high strength, show severe deterioration due to the decomposition of the CSH-gel. The relative residual compressive strength is in case of high strength concrete higher than in case of normal strength concrete [37].

The behaviour of concrete during fire is mainly influenced by the following factors [42,11,20]:

1. *Aggregate/cement ratio:* This factor has a significant effect on the strength of concrete. In concrete mixes with a high cement contend the compressive strength declines more with increasing temperature than with concrete mixes with a low cement contend.
2. *Type of aggregate:* Type of aggregate is one of the main factors influencing the compressive strength of concrete at increasing temperature. In case of concrete with light weight and calcareous (limestone) aggregates is the compressive strength reduction and higher temperatures less than concrete with siliceous (normal sand and gravel) aggregates.
3. *Sustained stress during heating:* This factor affects the shape of the compressive strength-temperature relation. The reduction of the compressive strength is in case of loaded concrete less than in case of unloaded concrete. The difference of thermal expansion between the aggregate and the cement paste causes tensile stresses. The external compressive stress is usually enough to compensate these tensile stresses and therefore the compressive strength, in case of loaded concrete, reduces less. The stress level ($\alpha = f_{c,t}/f_{c,20}$) itself has little effect on the ultimate strength as long as $\alpha > 0{,}20$, but becomes important if $\alpha < 0{,}20$. In figure 4.5 the influence of the load level, on the compressive strength during heating, is depicted.

Factors that do not influence the compressive strength of concrete during fire are:

1. Compressive strength at room temperature
2. Largest grain size of the aggregate
3. Type of cement used
4. Rate of heating
5. Height of the water/cement ratio

Cyclic temperature exposure: this leads to a continuous decrease in compressive strength. The main strength loss occurs after the first temperature cycle.

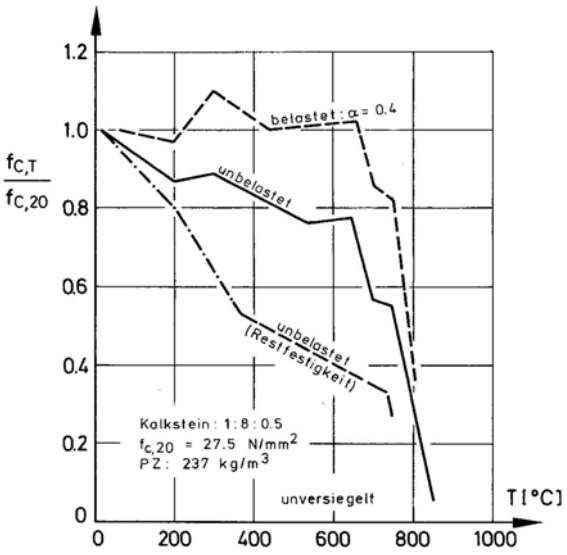

Fig 4.5 influence of the loading on the compressive strength during heating [42]

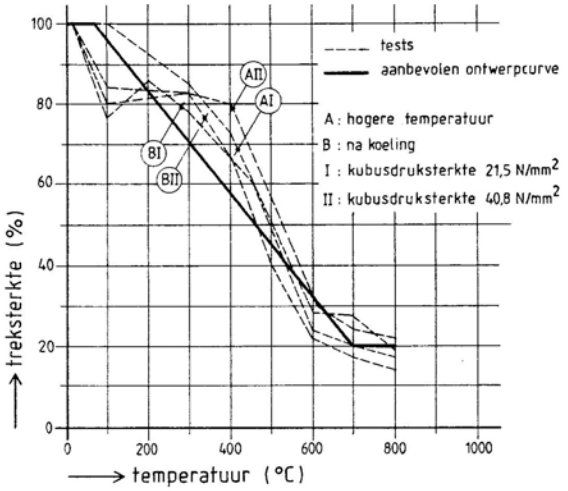

Fig 4.6 tensile strength of concrete at elevated temperatures [6]

4.2.2. Tensile strength

The temperature influence on the tensile strength of concrete is less investigated than the compressive strength. According to van Breugel [6] reduces the tensile strength also with increasing temperature, however the reduction already takes place at a temperature of 50 ^{o}C. At this temperature there is a decrease of tensile strength with increasing temperature and at a temperature of 800 ^{o}C the tensile strength is only 20 percent of the initial tensile strength. In figure 4.6 the tensile strength at increasing temperature according to different experiments are depicted.

The main factors influencing the tensile strength at increasing temperature are [42,11]:

1. *Cement contents:* The mix proportion affects the tensile strength at increasing temperatures. The reduction of tensile strength at increasing temperatures is less with concrete mixes that have a low cement content than with concretes with a high cement content.
2. *Type of aggregate:* The type of aggregate has a significant influence on the tensile strength at increasing temperature. The decrease in tensile strength at increasing temperatures in case of concrete with calcareous aggregates is more than in case of concrete with siliceous aggregates.

Factors such as the water/cement ratio and rate of heating have little influence on the tensile strength at elevated temperatures. The relative decrease in concrete strength with increasing temperature is greater for tensile strength than for compressive strength [42].

4.2.3. Modulus of Elasticity

A limited number of publications consider the elastic properties of concrete at increasing temperatures. Besides the limited number of investigations there is also a difference in test method used. The test procedures also have an influence on the determinations of the modulus of elasticity (Young's modulus). Most of the

experiments conducted are with constant temperature, but also experiments with increasing temperature have been reported [11].

From these test it follows that the modulus of elasticity decreases with increasing temperature. The decrease of Young's modulus starts at a temperature of 50 ^{o}C. In figure 4.7 and figure 4.8 the modulus of Elasticity at increasing temperature is depicted.

The main factors influencing the modulus of elasticity at increasing temperature are [42,11]:

1. *Type of aggregate:* This factor has the strongest influence on the modulus of elasticity at increasing temperature. In case of light weight concrete and concrete with calcareous aggregates is the reduction in modulus of elasticity less than in case of concrete with siliceous aggregates.
2. *Sustained stress during heating:* This affects the elasticity-temperature relation. The reduction of the modulus of elasticity in case of loaded concrete is less than in case of unloaded concrete. The stress level ($\alpha = \sigma_b'/f_b'$) itself has little influence as long as $\alpha = 0{,}1 - 0{,}3$.

Factors that do not influence the modulus of elasticity of concrete during fire are:

1. Compressive strength at room temperature
2. Height of the water/cement ratio
3. Type of cement used
4. Duration of temperature

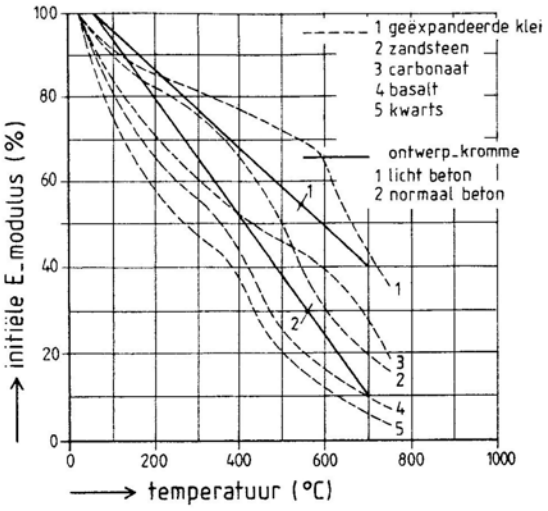

Fig 4.7 modulus of elasticity at elevated temperatures [6]

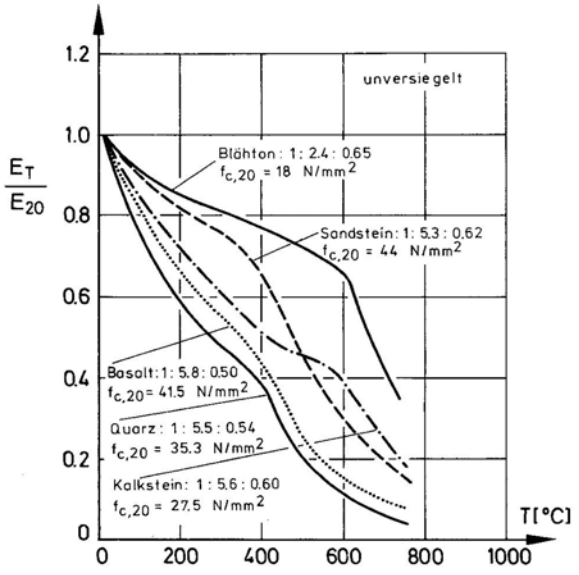

Fig 4.8 influence of the type of aggregate and the original strength of the concrete on the modulus of elasticity [42]

4.2.4. Stress-Strain relationship

The behaviour of concrete during increasing temperature can be displayed with a stress-strain diagram. According to CUR 149 [11] is the stress-strain curve dependent on the loading of the concrete during increasing temperature.

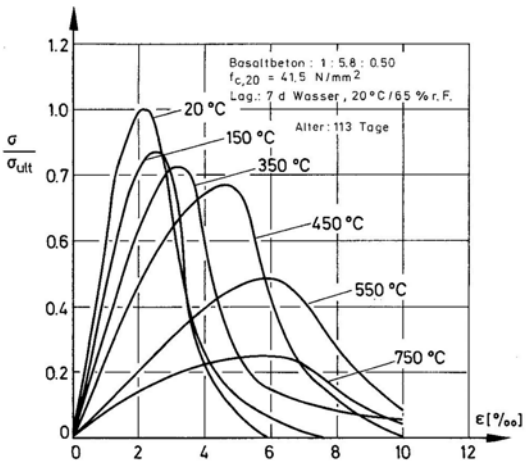

Fig 4.9 stress-strain relationship of normal concrete in a strain rate controlled test [42]

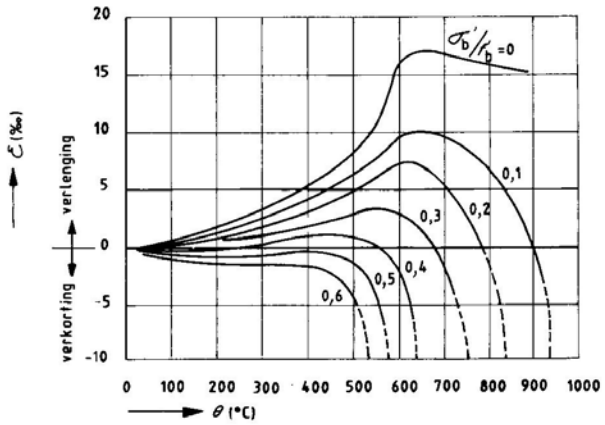

Fig 4.10 strain development at constant compressive stress and increasing temperature [11]

From figure 4.9 it can be seen that with increasing temperature the stress-strain behaviour changes. At a temperature of 350 ^{o}C the ultimate stress is 30 percent lower and the strain 1,5 times larger than at a temperature of 20 ^{o}C. At increasing temperature this behaviour continues. At a temperature 750 ^{o}C the ultimate stress is only 25 percent of the stress at a temperature of 20 ^{o}C.

In figure 4.10 is the stress-strain relationship, besides temperature, also dependent on the loading of the concrete. Upon loading of the concrete the stress-strain relationship changes shape with increasing temperature. At a higher load level of for instance 0,5, at a temperature of 550 ^{o}C, the stress-strain diagram shows a sharp drop. Generally it is valid that concrete which sustained loading during heating indicate an increase of compressive strength and modulus of elasticity compared to concrete which is not loaded during heating [42]. This behaviour is independent of the concrete being tested and is also shown in figure 4.11.

According to Schneider [42] the following factors influence the stress-strain behaviour of concrete during fire:

1. *Type of aggregate:* This factor is the main factor affecting the shape of the stress-strain curve. Concrete made with siliceous or basaltic aggregates generally have a steeper decrease of the initial slope than light weight aggregates. Light weight aggregates show no change in the shape of the stress-strain curve for temperature up to 300 ^{o}C. The ultimate strain is nearly independent of the type of aggregate.
2. *Aggregate/cement ratio:* This ratio has an effect on the modulus of elasticity and therefore determines the initial slope of the curve.

Factors such as compressive strength at room temperature, water/cement ratio and type of cement have little effect on the stress-strain relationship.

4.2.5. Transient thermal creep

When concrete is heated under constant load, it exhibits strains far different from those related only to the elasticity and thermal expansion of the material, especially

during first time heating. These strains in excess of purely thermo-elastic behaviour are defined as 'transient thermal creep' [24]. Transient thermal creep starts at a temperature of around 50 ^{o}C and the rate of development increases slightly with increase in temperature. This increase becomes more important after a temperature of 200 ^{o}C.

Transitional thermal creep results in relaxation and redistribution of thermal stresses. Furthermore, transitional thermal creep accommodates, to a large extent, the thermal strain incompatibilities between the aggregates and the cement paste. In this way transient thermal creep helps to avoid excessive damage to the concrete, especially at temperature above 100 ^{o}C when the cement paste shrinks and the aggregate expands. During cooling, when transient thermal creep is absent, the tensile thermal and incompatibility stresses can lead to the development of cracking and weaken the material.

Transient thermal creep develops irrecoverably during first time heating of a concrete specimen under load. It usually takes a month to fully develop [30]. On reheating to the same upper temperature limit, transient thermal creep is reduced or disappears, depending upon whether it is allowed to fully develop during the first heat cycle and upon the period at ambient temperature between the first and the second heat cycle. Transient thermal creep reappears if in the second heat cycle the initial temperature limit is exceeded and develops like virgin heating [30]. To give a example of the extent of transient thermal creep, in figure 4.12 in case of normal concrete at a load level of 0,60 the thermal strains are almost completely countered by the stress-induced deformations of the concrete [6]. According to CUR 149 and Van Breugel [6,11] is the thermal strain countered by the transient strain if $\sigma_b'/f_b' = 1/2{,}35 = 0{,}425$.

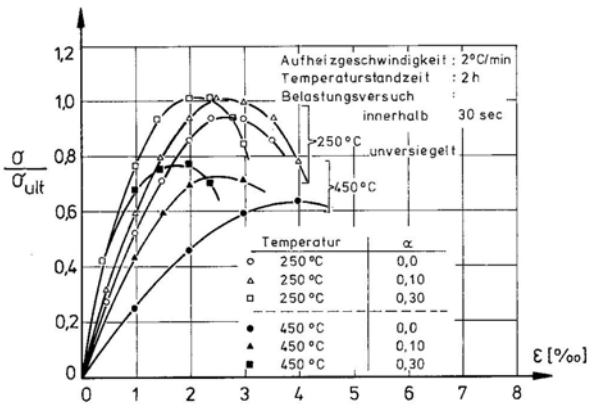

Fig 4.11 stress-strain relationship of loaded normal concrete at increasing temperature [42]

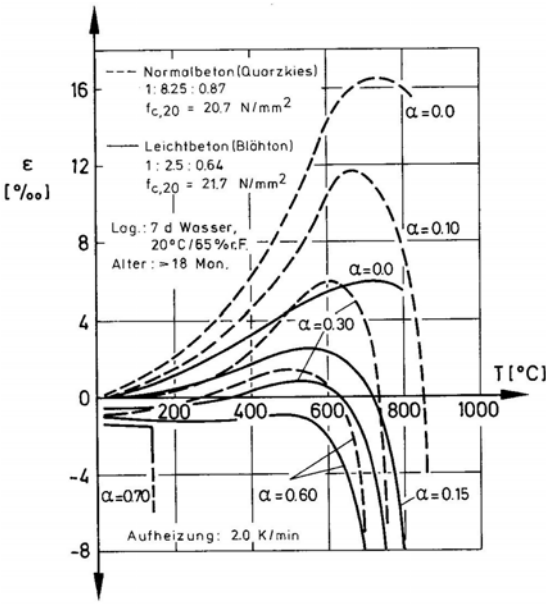

Fig 4.12 total deformation of loaded normal concrete and light weight concrete [42]

There are several theories about transient thermal creep [24,30].

1. Transient thermal creep is related to the thermal incompatibilities between the cement paste and the aggregates, especially above a temperature of 100 ^{o}C. In this case transient thermal creep may be a result of the shrinkage of the cement paste being restricted by the expanded aggregates. This is not the reason for transient thermal creep, because, in one case, adding aggregate reduced transient thermal creep by 70 percent.
2. Thermal stresses causing transient thermal creep is not the case. Even at very slow heating rates and negligible temperature gradients, transient thermal creep appeared.
3. Transient thermal creep is also not caused by increase in elastic strain upon heating. First, elastic strain is recoverable, transient thermal creep is not. Second, elastic strain can sometimes experience little change when concrete is heated under load.
4. Internal moisture migration is not the reason for transient thermal creep. The redistribution of water in the micro pores of cement paste takes place within a few hours, as compared with as period up to a month for transient thermal creep.

The above mentioned theories of transient thermal creep are all not the reason for the phenomenon. It further more shows that the process is difficult to predict and to explain. However transient thermal creep is, according to Hassen and Colina [24], partially affected by physical-chemical transformations that occur in the CSH-gel and the micro cracks generated in concrete during heating. The transient thermal creep is a sort of thermo-chemical damage. In the temperature range of 200-400 ^{o}C the most important part of the dehydration of the CSH-gel takes place. This dehydration leads to the decomposition of the CSH-gel, which is largely responsible for the cement paste strength. At a temperature of 400 ^{o}C also the CH decomposes into clay en water.

Both processes change the porous network. The pore volume increases with temperature and the micro structure is modified. In figure 4.13 the estimated transient thermal creep of high performance concrete is depicted.

The following factors influence the transient thermal creep of concrete [42]:

1. *Type of aggregate:* The harder the aggregate and the lower its thermal expansion the lower the total deformations of normal concretes. Light weight concretes with expanded clay aggregate indicate the lowest total deformations due to transient thermal creep.
2. *Moisture content and movement:* In the temperature range of 20-300 ^{o}C is transient thermal creep influenced by moisture content and movement.
3. *Aggregate/cement ratio:* This factor has great influence on the shape of the strain-temperature curve.

Factors such as compressive strength at room temperature and water/cement ratio do not have an influence on the transient thermal creep of concrete.

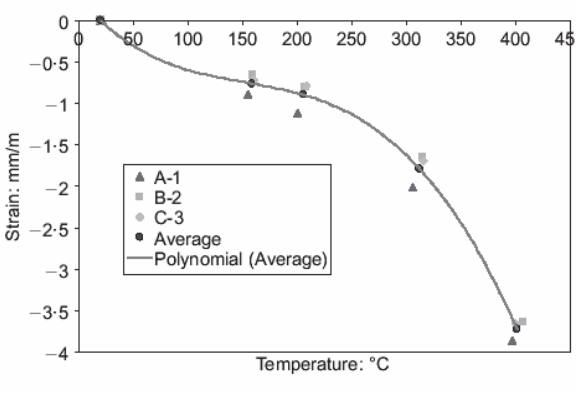

Fig 4.13 estimated transient thermal creep values of high performance concrete [24]

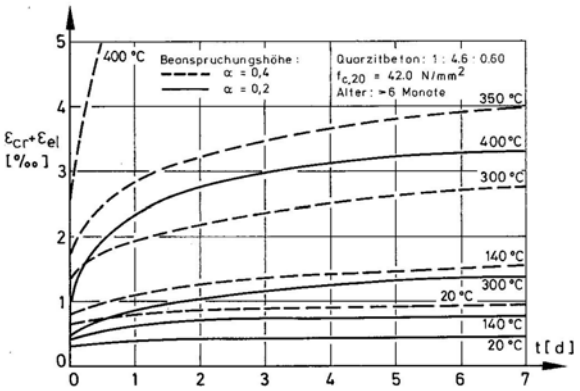

Fig 4.14 influence of the load level on the creep of normal concrete at elevated temperatures [42]

4.3. Time dependent behaviour of concrete during fire

4.3.1. Creep

Creep is defined as an increase of the deformation in time compared to the direct deformation upon loading. There have been many researches into the creep of concrete under elevated temperatures. However these researches where mostly carried out at temperatures below 150 ^{o}C. Only a few researches have been conducted with temperatures higher than 150 ^{o}C.

As with the general behaviour of concrete during increasing temperature is the amount of creep also dependent on the temperature. However according to van Breugel [6] there is a large scatter in the values for the amount of creep. Most of this scatter comes from the difficulty in obtaining the creep value. The test method, amount of moisture movement and duration of the test are determining factors in obtaining the creep value. In figure 4.14 the creep behaviour of concrete at elevated temperature and different load levels is given. At a temperature of 200-300 ^{o}C the creep rate is 3-6 times higher than the creep rate a temperature of 20 ^{o}C. At temperature above 300 ^{o}C a serious increase in creep rate is to be expected [42,11].
The following factors have an influence on the creep behaviour of concrete:

1. *Normal and light weight concretes:* Both types of concrete show similar creep effects. Concrete with quartzite aggregate show higher creep strains than concrete with expanded clay at temperatures over 300 ^{o}C.
2. *Modulus of elasticity:* Concrete with a low modulus of elasticity has a higher amount of creep.

Factors such as the type of concrete and the load level have little influence on the creep behaviour of concrete at elevated temperatures.

4.3.2. Relaxation

Relaxation is defined as a decrease in stress in time with constant high temperature and constant deformation. Relaxation test are difficult to perform and therefore only little information is available.

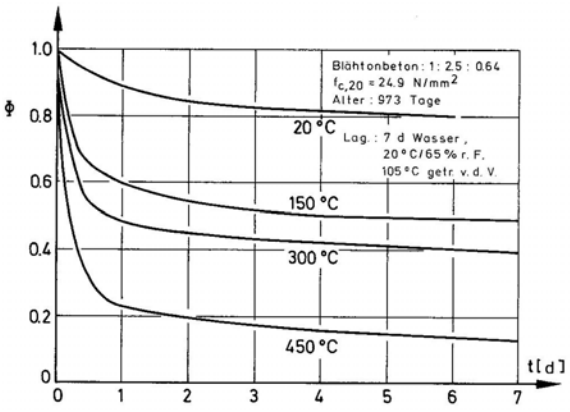

Fig 4.15 relaxation of light weight concrete with expanded clay aggregate at elevated temperatures [42]

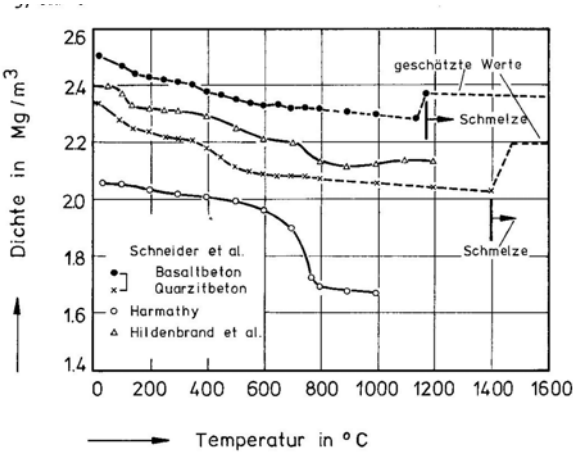

Fig 4.16 density of concrete with siliceous aggregates [42]

The amount of relaxation is closely related to the phenomenon creep at constant temperature and load and the additional deformation due to transient strain at increasing temperature. Therefore the factors determining creep and transient strain also determine relaxation. Figure 4.15 shows that stress relaxation develops quickly at elevated temperatures. The main part of the stress relaxation occurs immediately after loading.

4.3.3. Shrinkage

The shrinkage at elevated temperature is little compared to the other deformations and therefore it can be neglected [42,11].

4.4. Thermal properties of concrete during fire

4.4.1. Density

The density of concrete depends on the density of the aggregates and the moisture content [42]. In the temperature range of 20-150 ^{o}C the evaporable water is dehydrated. This causes a loss in weight and thus a loss in density. With further increasing temperature the density further decreases. At the temperature range of 600-900 ^{o}C, in case of concrete with limestone, the decomposition of the limestone starts. This causes a porous structure in the concrete and also a decrease in density. In concrete with siliceous aggregates the decline in density up to 700 ^{o}C is higher. At higher temperatures the greater thermal expansion of quartzite is responsible for the sharper decline in density. General can be stated that the density of concrete is decreasing with increasing temperature, as is depicted in figure 4.16.

4.4.2. Heat capacity

Heat capacity is the thermal property which is least understood. In general it can be stated that the specific heat capacity increases somewhat at increasing temperature [6]. The specific heat capacity at a temperature of 20 ^{o}C is in general 0,80 kJ/kgK [6]. In figure 4.17 the specific heat capacity at increasing temperature for various concretes with siliceous aggregates is given. The difference in specific heat at 20 ^{o}C is mainly caused by the presence of water. The specific heat capacity is increased by the

presence of water. At higher temperatures the chemical reactions contribute to increasing the specific heat [42].

The following factors influence the specific heat capacity of concrete:

1. *Mix properties:* Concrete mixes with high cement content have a higher latent heat capacity due to dehydration effects.
2. *Water content:* Water content is important at temperatures below 200 ^{o}C. Concrete with high water content have a higher specific heat capacity.
3. *Type of aggregate:* At temperature up to 800 ^{o}C there is no influence, but for temperature above 800 ^{o}C calcareous concrete, due to decarbonization reaction, give a rise in specific heat capacity.

4.4.3. Thermal conductivity

The thermal conductivity of concrete depends on the conductivities of its constituents [42]. In many researches there are found different values for the thermal conductivity. The reason for such variations is the difference in constitution of the different concretes. The thermal conductivity at 20 ^{o}C is in case of normal concrete 2,0 W/mK [6]. At low temperatures and with moist concrete very high values for the thermal conductivity exist. This is because the conductivity of the solid skeleton of the material is the highest and because of the heat transfer between the walls of the pores is relatively good on account of the water in them. At little below a temperature 100 ^{o}C the thermal conductivity decreases, because the water filled pores are partly emptied. The heat transfer condition between the walls of the pores is less. At a temperature of 300-400 ^{o}C there is a further decrease in thermal conductivity, because the conductivity of the solid skeleton becomes lower and, furthermore, the heat transfer in the pores is worsened by drying. However, at temperatures from 300 ^{o}C increased cracking develops as a consequence of incompatibilities between the aggregate and the cement paste.

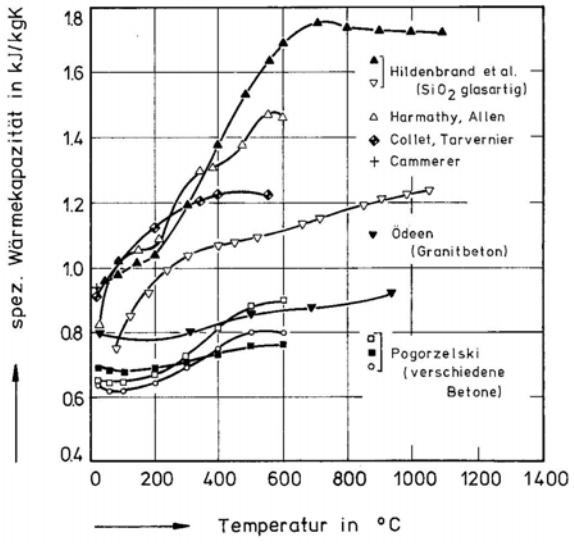

Fig 4.17 specific heat capacity of concrete with siliceous aggregate [42]

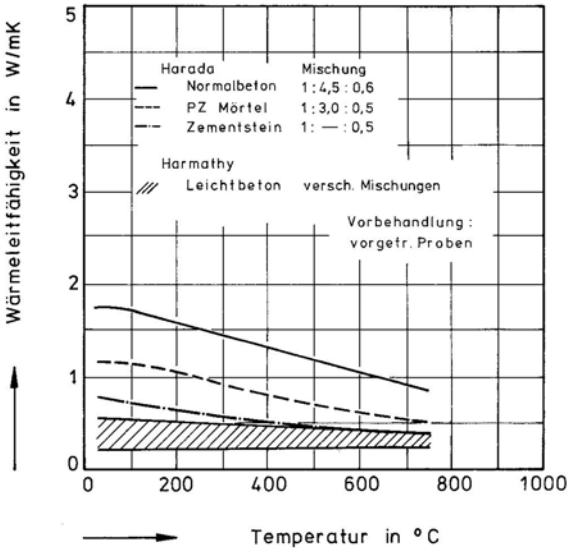

Fig 4.18 thermal conductivity of normal and light weight concrete, mortar and cement stone [42]

As a consequence the heat transfer between the pore walls increases. From temperatures of 600 ^{o}C and up the thermal conductivity further decreases because the conductivity of the solid skeleton decreases. In general it can be stated that the thermal conductivity decreases at increasing temperature, as is depicted in figure 4.18 [42,6].

According to Schneider [42] the following factors influence the thermal conductivity:

1. *Moisture content:* The thermal conductivity of any concrete varies linearly with moisture content. The thermal conductivity increases with increasing water content. The higher the conductivity of a concrete the greater is the loss in conductivity due to the loss of moisture during heating.
2. *Type of aggregate:* An increase of conductivity of the aggregate causes an increase in conductivity of the concrete.
3. *Mix properties:* Cement paste has a lower conductivity than the aggregate, therefore concrete mixes with a low cement contends have a higher conductivity.

4.4.4. Thermal diffusitivity

The thermal diffusitivity of concrete is determined by the thermal properties of its constituents [42]. The type of aggregate, mix proportion and the water content have the same effect on the thermal diffusitivity as was noted for the thermal conductivity. Therefore the thermal diffusivity has the same trend as the thermal conductivity. At a temperature of 20 ^{o}C the thermal diffusitivity is in the range of 0,6*10-6 – 1,1*10-6 m^2/s and declines to 0,35*10-6 m^2/s at a temperature of 1000 ^{o}C [42,6]. In figure 4.19 there is scatter at a temperature below 200 ^{o}C. This is due to the difference in moisture content.

4.4.5. Thermal expansion

There has been a considerable amount of research done into the thermal expansion of concrete [42]. From this research it was learned that thermal strain is a non-linear function of temperature, even at low temperatures. Furthermore, the type of aggregate is the main factor affecting the thermal strain. At low temperatures, below 200 ^{o}C, the moisture content, water/cement ratio and the type of cement are only relevant. At very high temperatures, 600-800 ^{o}C, the concrete shows no further expansion. The thermal expansion decreases if the rate of heating increases.

In figure 4.20 and figure 4.21 the thermal expansion of calcareous and siliceous aggregate concretes is shown. In case of calcareous aggregate concretes the expansion increases until 900 ^{o}C and the expansion decreases to around zero at a temperature of 1000-1300 ^{o}C. This is due to the increasing decarbonation of the limestone. At higher temperatures the porosity of the decarbonated limestone decreases and the thermal expansion follows the same line. The thermal expansion of siliceous aggregate concrete shows the same trend with increasing temperature. However, it is about twice that of calcareous aggregate concrete on account of the higher thermal expansion of quartzite. The transformation that quartz, at a temperature of 570 ^{o}C, undergoes accounts for the steep increase in the thermal expansion. At a temperature of 700 ^{o}C siliceous aggregate concrete also show a contraction.

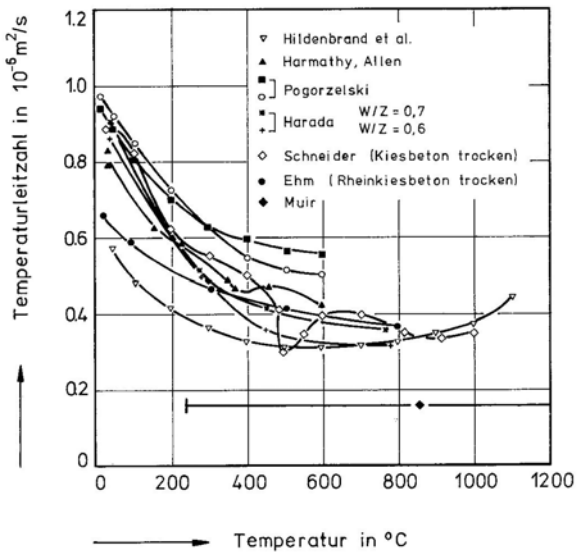

Fig 4.19 thermal diffusivity of siliceous concrete [42]

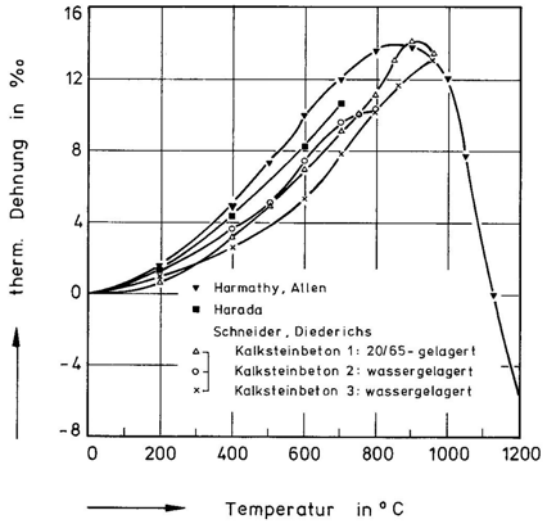

Fig 4.20 thermal expansion of limestone concrete [42]

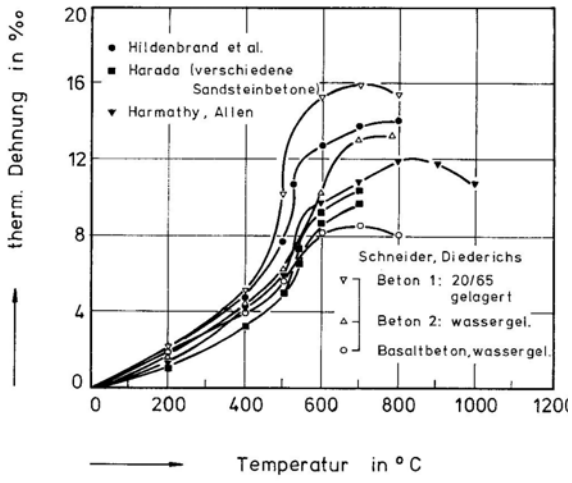

Fig 4.21 thermal expansion of siliceous concrete [42]

This contraction is attributed to the contraction of the cement paste and the decomposition of the CSH phases.

4.5. Permeability and porosity of concrete at elevated temperatures

When concrete is exposed to fire and the temperature of the concrete rises, the internal structure of the concrete and thus the permeability and porosity change. The porosity describes how densely the material is packed. It is the proportion of the non-solid volume (pores and liquid) to the total volume of material [23]. The permeability is defined as the 'ease' with which fluids can pass through its pores [23].

4.5.1. Permeability and porosity at elevated temperatures

In the previous paragraph the physical and chemical processes which change the internal structure of concrete were described. These processes are important for the change in porosity and permeability.

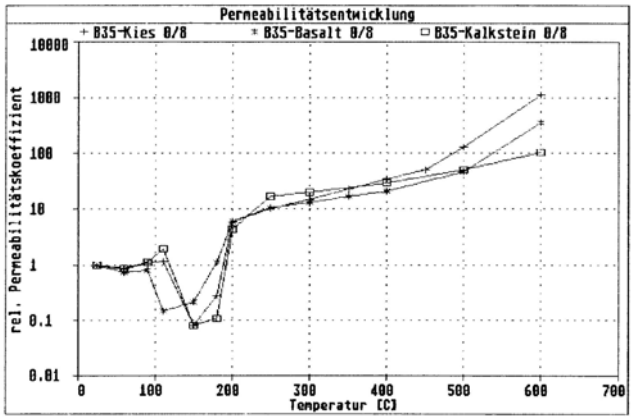

Fig 4.22 influence of aggregate on the permeability of concrete [43]

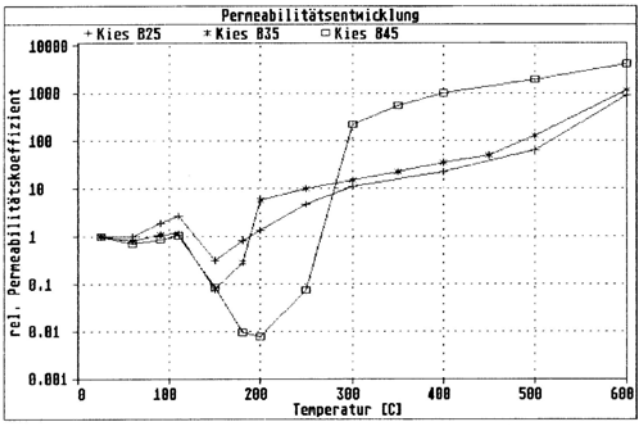

Fig 4.23 influence of compressive strength on the permeability of concrete [43]

In figure 4.22 and figure 4.23 the change in permeability of different concrete mixes with increasing temperature are shown. In both figures the coefficients of the permeability are expressed in the permeability at 20 ^{o}C. The influence of the aggregate on the permeability of the concrete is depicted in figure 4.22. The following can be concluded [43]:

1. *Temperature range 25-110 ^{o}C:* In this temperature range the difference in permeability and also the increase in permeability are caused by the initial pore system.
2. *Temperature range 110-250 ^{o}C:* This temperature range is influenced by the rise of pressure in the pore system caused by the evaporation of water. The dehydration capability of each type of concrete is influenced by its pore system. For all concrete mixes is the evaporation of water stopped at a temperature of 250 ^{o}C.
3. *Temperature range 250-500 ^{o}C:* This temperature range is influenced by the difference in thermal expansion between the aggregate and the cement paste. In the temperature range of 300-100 ^{o}C the cement paste shrinks 3 percent and the aggregate expands 1,5 percent. This difference leads to the development of micro cracks. The more the temperature rises, the more the micro cracks develop into an interconnected system. The system of micro cracks gradually becomes the main transport system.
4. *Temperature above 500 ^{o}C:* The micro cracks have developed in a complete interconnected system and this system is the main transport system.

The influence of the water/cement ratio and the compressive strength on the permeability of the concrete is depicted in figure 4.23. The concrete mixes B25, B35 and B45 have subsequent the following water/cement ratio 0,7 , 0,5 and 0,45. The following can be concluded [43]:

1. *Temperature range 25-110 ^{o}C:* In this temperature range the initial water/cement ratio is important. The lower this water/cement ratio, the lower

the initial permeability is. At increasing temperature the low initial water/cement ratio reduces the water flow and the rise of permeability.
2. *Temperature range 110-250 ^{o}C:* In this temperature range the influence of the initial water/cement ratio is more pronounced. In case of a low water/cement ratio, the permeability reduces more.
3. *Temperature range 250-500 ^{o}C:* This temperature range is mainly influenced by the development of the micro crack system. In case of concrete with high compressive strength, in which the pore pressure is higher, the micro cracks develop at lower temperatures.
4. *Temperature above 500 ^{o}C:* All types of concrete have developed a micro crack system. The water/cement ratio is of less importance at these high temperatures.

The porosity is depicted in figure 4.24. This figure shows the development of the pore radius distribution with increasing temperature. The following can be concluded [43]:

1. *Temperature of 20 ^{o}C:* The concrete is not exposed to elevated temperatures. The pore size distribution maximum is 20 nm.
2. *Temperature of 90 ^{o}C:* In case of heating the concrete up to a temperature of 90 ^{o}C the maximum splits into two new maximums. This is due to the dehydration of the pore system. The second maximum has a value of 37 nm, which is caused by the dehydration process and subsequent enlargement of the capillary pore size. The first maximum is the capillary pores which have not been dehydrated.
3. *Temperature of 250 ^{o}C:* All the capillary pores have been dehydrated and therefore there is one maximum at 30 nm. The maximum at 650 nm is the development of micro cracks.
4. *Temperature of 500 ^{o}C:* The micro cracks are further developed into an interconnected system and therefore the maximum is at 1800 nm.

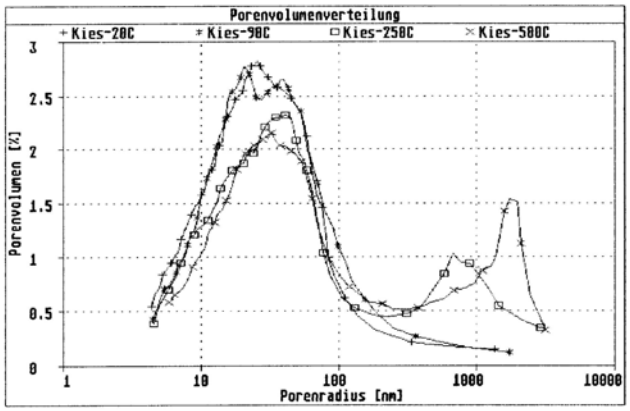

Fig 4.24 pore volume distribution of concrete at different temperatures [43]

4.6. Spalling of concrete

Tunnel fires can have a significant impact on the safety of the tunnel. During fire conditions the tunnel is subjected to extreme high temperatures. This heating of the structure will have a direct and indirect thermal impact.

1. The concrete and reinforcement steel lose their strength and stiffness. This aspect was dealt with in the preceding paragraph.
2. During heating a temperature gradient will occur, which causes internal stresses. Internal stresses will also be generated by the strain and deformations occurring during and after the fire [10].
3. Another important topic is spalling. Spalling is potentially the most damaging for the structure of the tunnel. This phenomenon can lead, in case of explosive spalling, to sever damage to the structure and ultimately cause collapse of the structure. This topic will be dealt with in this paragraph.

4.6.1. Different types of spalling behaviour

According to different authors [42,11,12,44] there are mainly three different kinds of spalling.

1. *Explosive spalling:* Also known as destructive spalling. In this case a few large pieces 'jump off' the surface of the concrete. This kind of spalling usually occurs during the first 10 to 50 minutes of fire exposure and leads to sever damage and possibly collapse of the element.
2. *Local spalling:* This kind of spalling incorporates the local 'jump off' of relative small pieces from particular places of the surface of the concrete. For instance the spalling from the edges of the cross section is considered local spalling.
3. *Sloughing off:* Small layers of concrete 'fall off' the surface of the concrete element. This kind of spalling usually occurs at higher temperatures and propagates through time. This results in gradually decreasing of the cross section.

Fig 4.25 spalling in lining segment with sprayed concrete [25]

Fig 4.26 spalling along the edges of the lining segment [25]

4.6.2. The process which leads to spalling

In the first minute the heat penetrates the cross section of concrete and the evaporable water in the surface layer of the concrete evaporates into water vapour. This water vapour will flow mostly towards the heated surface under influence of a difference in pore pressure. This difference in pore pressure causes a pore pressure gradient to be present and occurs due to the evaporation of water. The evaporation of water into

water vapour and thus the phase change of water, leads to an expansion of the water and thus an increase in pore pressure. On the surface of the concrete this water vapour escapes the cross section, which can be seen as steam coming of the surface. In time, the heated layer progresses further into the cross section and the water vapour increasingly flows into the cooler interior of the concrete. This is caused by the temperature in the heated layer. As the heated layer progresses further into the concrete, the temperature in the heated layer also increases. The water vapour flow, which is caused by the pressure difference, is largely influenced by this rise in temperature. During the flow of the water vapour the temperature of the water vapour increases and accordingly the water vapour wants to expand. This is restrained by the structure of the pores and this restrained expansion leads to friction forces along the walls of the pores which hinder the flow of the water vapour. Furthermore, the surface of the concrete is strongly compressed, due to the temperature stresses, which reduce the amount of micro cracks present in this layer and thus limiting the amount of passages which are available for the water vapour to flow through. In figure 4.27 the process which leads to spalling is schematically depicted. The above described first part of the process is depicted in part a [50].

After some time the most of the water vapour is flowing towards the cooler interior of the concrete. When the conditions are met, that the temperature is below 100 ^{o}C, the water vapour condensates back to water and is reabsorbed into the pores of the concrete.

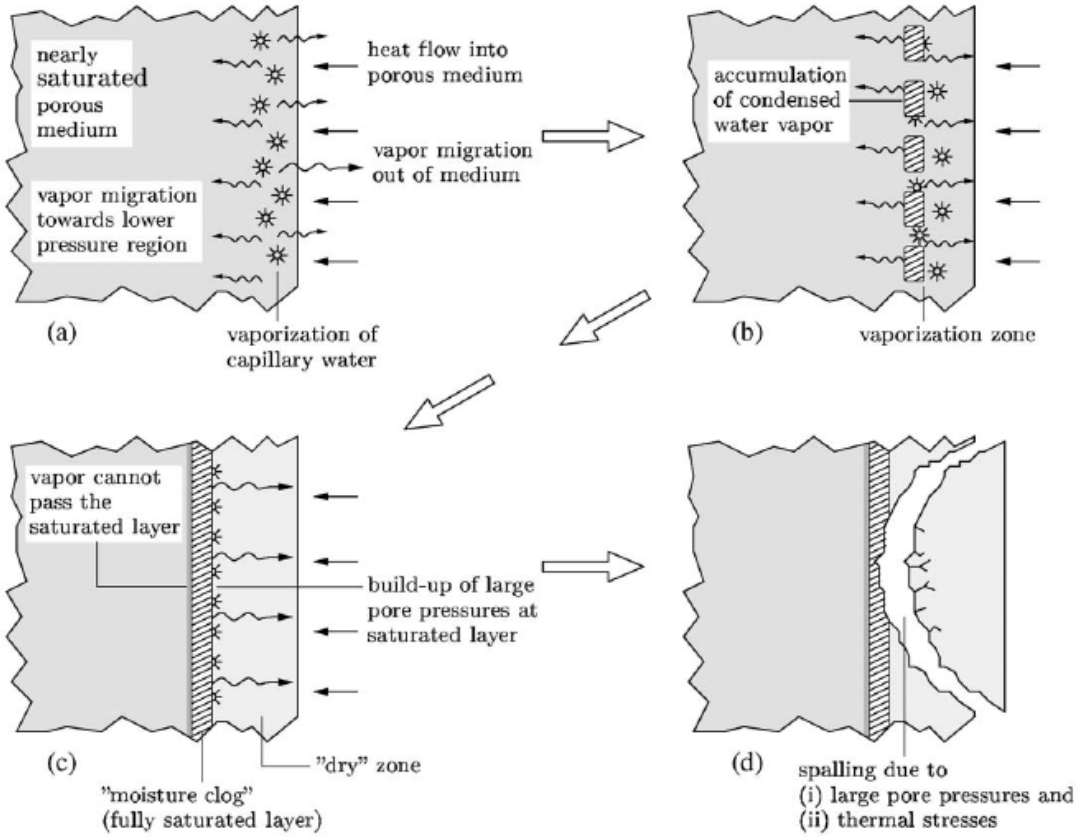

Fig 4.27 schematic representation of the process which leads to spalling [50]

The amount of evaporable water in the pores therefore increases, because besides the reabsorbed water there is also evaporable water present which is present in concrete when it is still in its initial state. This process continues. The thickness of the heated layer gradually grows and behind the front of the heated layer, where the temperature reaches 100 ^{o}C, evaporation of evaporable water takes place and this water vapour flows mostly towards the cooler interior of the concrete. Deeper into the heated layer the decomposition of the cement paste takes place which produces evaporable water which is evaporated and also flows mostly towards the cooler interior of the concrete. At first the speed with which the water vapour flows is much larger than the speed with which the 100 ^{o}C front proceeds through the concrete. Gradually, in front of the 100 ^{o}C front, in the pores of the concrete, an accumulation of water will be formed. When the 100 ^{o}C front further progresses through the concrete it takes increasing more time to fully evaporate this accumulation of water and therefore the progress of the 100 ^{o}C front decreases. Furthermore, the pressure difference becomes increasing insufficient to 'push' the formed water vapour forwards, because the thickness and degree of saturation of this accumulation zone of water increases in time and gradually impedes the flow of the formed water vapour. This means that in front of the 100 ^{o}C front the zone with an accumulation of water grows and the pressure difference slowly becomes insufficient to level off the water vapour and water deeper into the concrete. Furthermore, the accumulation layer of water also causes the pore pressure to develop gradually higher. After some time the layer with an accumulation of water becomes to large and a saturated layer develops, called a moisture clog. In figure 4.27 this part of the process is indicated by part b and c [50].

The transition between the drying zone (dehydrating zone) and the saturated layer is sharply defined [23]. When the 100 ^{o}C front coincides with this interface, evaporation of water from the saturated layer takes place. In the meantime, the temperature in the dehydrated zone increases further and therefore a steep temperature gradient develops across the dehydrated zone, resulting in a high rate of heat flow and intense evaporation of water from the saturated layer [23]. This saturated layer impedes further transport of water and the formed water vapour into the interior of the concrete and therefore the water vapour is forced to flow in the direction of the surface of the concrete. However, in the direction of the surface of the concrete a steep temperature gradient is present which increases in the direction of the surface of the cross section. This means that the temperature increases rapidly from the front of the saturated layer onto the surface of the concrete. This temperature increase influences the flow of water vapour. During the flow of water vapour, which is caused by the pressure difference, the temperature of the water vapour increases and accordingly the water vapour wants to expand. This is restrained by the structure of the pores. This restrained expansion leads to friction forces along the walls of the pores which hinder the flow of the water vapour. The pressure difference is insufficient to 'push' enough water vapour onto the surface of the concrete and therefore, at the front of the saturated layer, a pore pressure starts to develop higher than the previous obtained pore pressures. In figure 4.28 the schematic development of the pore pressure in concrete with heating time is depicted [40]. The concrete cross section is subdivided into different zones. At the front of the cross section the dried zone (dehydrated zone) is present. This zone is followed by the drying zone (dehydrating zone) and the (quasi) saturated layer. In the remainder of the cross section the concrete is still in its initial state. As soon as the saturated layer is formed, the vapour pressure on the front of the saturated layer starts to build up.

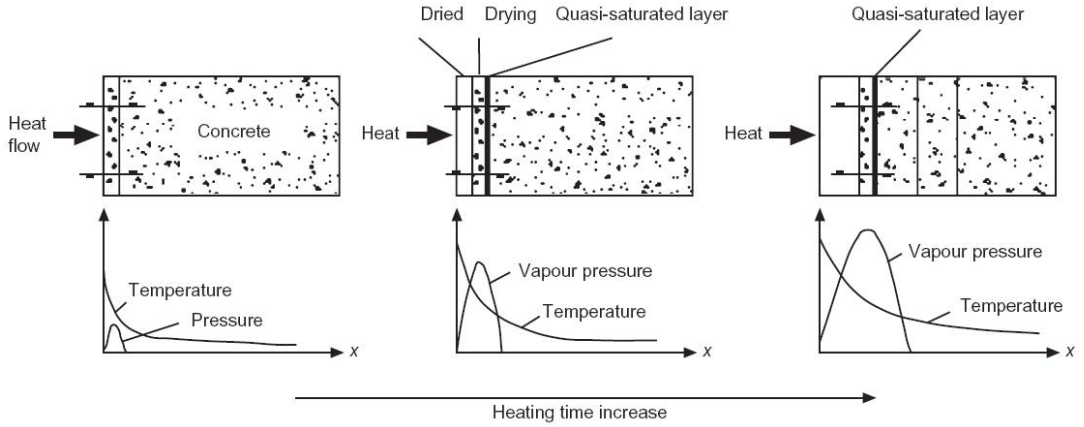

Fig 4.28 schematic representation for the development of vapour pressure in concrete with heating time [40]

The flow of water vapour through the heated layer is through interconnected passages. In the previous paragraph it was mentioned that the elevated temperatures in the surface layer cause a decomposition process in the concrete. This decomposition process leads to an increase in permeability of the concrete. This means that the amount of interconnected pores which can be used a passage for the water vapour also gradually increases from the saturated layer onto the surface of the concrete. Furthermore, it was also mentioned that due to the difference in thermal expansion between the aggregate and the cement paste micro cracks are developed. This further increases the amount of passages which can be used as passage for the water vapour. However, the surface layer of the concrete is strongly compressed which reduces the amount of micro cracks and therefore the amount of passage which can be sued by the water vapour to flow through. The flow of water vapour is dominated by the pressure difference, the temperature difference and the permeability. In case of a pressure difference and the permeability of the concrete is high, than the amount of passages which is available to the water vapour is sufficient to transport enough water vapour away from the saturated layer to ease the build up of pore pressure. The temperature of the water vapour still increases during the flow to the surface and therefore the water vapour still wants to expand, but the number and the size of the passages is sufficient to accommodate the expansion of the water vapour and the flow is therefore only mildly hindered. If the permeability is low and insufficient to transport enough water vapour away from the saturated layer, the pore pressure will continue to build up. The pressure difference is then insufficient to 'push' enough water vapour through the pores onto the surface of the concrete. The rate of evaporation of water increases at elevated temperatures and therefore the amount of water which needs to be transported away from the saturated layer gradually increases. This process of pore pressure build up continues until the pressure difference becomes large enough to 'push' enough water vapour through the pores onto the surface of the concrete to ease the pore pressure build up. This point is the maximum pore pressure which can be generated. After this point the remainder of the saturated layer will evaporate, but the amount of formed water vapour is not enough to increase or maintain the pore pressure. The developed pore pressure will gradually decrease, because the amount of water vapour which can be transported onto the surface of the concrete becomes higher than the amount of water that is being evaporated from the saturated layer.

The build up of pore pressure leads to tensile stresses tangential to the pores of the concrete. These tensile stresses have to be resisted by the tensile strength of the concrete at elevated temperatures. In case the tensile strength of the concrete is sufficient to resist these tensile stresses, then this saturated layer and its pore pressure development does not lead to damage to the concrete. After most of the saturated layer is evaporated, the 100 ^{o}C front propagates further into the cross section of the concrete and the process of the build up of saturated layer continues and a new saturated layer will be developed further into the cross section of the concrete. In case the tensile strength of the concrete is insufficient, then these tensile stresses will generate cracks which propagate in radial direction. These cracks weaken the structure of the concrete and when the crack pattern has sufficiently weakened the concrete, a layer will be pushed out of the cross section of the concrete with a thickness of approximately the dehydrated layer. This effect is called spalling of concrete. After the spalling the process continues, because the part of the cross section which was just behind the spalled of layer now becomes the surface layer. This means that the temperature quickly increases on this 'new' surface and therefore the process of the build up of a saturated layer and possibly spalling starts again. In figure 2.3 this is depicted by part d.

4.6.3. Different types of gas flow

In the previous description of the process which leads to spalling, the flow of water vapour through the concrete is important and determines the build up of a saturated layer and the pore pressure. It was further elaborated that the flow of water vapour was dominated by the pressure difference. However, the transport of water vapour through the pores of the concrete is dominated by four different transport processes, which are depicted in figure 4.29 [22]. Which type of transport process is dominant depends on the pore size and the mean free path length. The mean free path length is the average distance between collisions for a gas molecule. The first transport process is Knudsen diffusion which occurs when the mean free path is relatively long compared to the pore size. The molecules move independently of each other and collide frequently with the pore wall. Knudsen diffusion is dominant for pores with a diameter in the range between 2 and 50 nm. The second is diffusion. There are different sort of diffusion. In case of molecular or Fickian diffusion the transport occurs when the mean free path is relatively short compared to the pore size. Diffusion is caused by a concentration gradient. The third is viscous flow, which is the flow of gases through a channel under the condition that the mean free path is small compared with the diameter of the channel. The flow characteristics are mainly determined by the collisions between gas molecules.

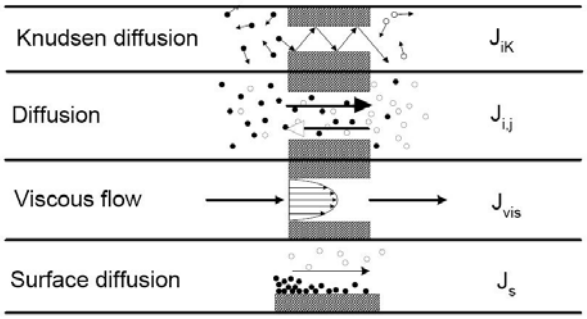

Fig 4.29 the different transport processes [22]

Viscous flow is caused by a pressure gradient. The fourth is surface diffusion in which molecules adsorb on the surface of the pore and hop from one site to another through interactions between the surface and the molecules. Surface diffusion is caused by a gradient of the number density of the hopping molecules.

4.6.4. Factors influencing spalling

The following factors influencing the development of spalling [42,11,12,34,32]:

Material factors

The material factors are mostly determined by the mix proportions, which determine the pore structure of the concrete.

- *Permeability:* The main factor of the material which influences the occurrence of spalling is the permeability of the concrete, which is determined from the size and the interconnection of the pores of the concrete. The permeability is determined by the amount and the size of the pores and the interconnecting channels available for the formed water vapour to flow through. When the permeability of the concrete decreases, the pore structure is badly interconnected and therefore the possibility of spalling increases.
- *Porosity and initial moisture content:* These factors of the material influence to a lesser extent the occurrence of spalling. The porosity of the concrete, which is determined from the size and the amount of the pores of the concrete, together with the initial moisture content, which means the initial degree of saturation, determines the amount of evaporable water present in the pores of the concrete and the empty space available for the water vapour to fill. When the porosity decreases and/or the initial degree of saturation increases, the possibility of spalling increases. In normal concrete the possibility of spalling is minimal if the initial moisture contents is 5 percent or lower [11]. In practice the moisture contents is usually around 5 to 10 percent, depending on the environmental conditions [13].
- *Aggregate:* Light weight, porous aggregates absorb more water and therefore the moisture content increases. This increases the possibility of spalling.
- *Tensile strength:* The tensile strength of the concrete influences to a lesser extent the occurrence of spalling. The tensile strength of the concrete determines the capability of the concrete to withstand the development of pore pressures and therefore when the tensile strength of the concrete reduces, the possibility of spalling increases.

Fire conditions

This category describes the fire loading and exposure of the construction.

- *Heating rate:* The main factor of the fire which influences the occurrence of spalling is the heating rate of the concrete, which is determined from the rate in which the heat from the fire develops and progresses through the cross section. The heating rate determines the progress of the evaporation front and the development of the pore pressures. The possibility of spalling increases when the heating rate of the concrete increases. Furthermore, by increasing the heating rate, the process which leads to spalling occurs at a higher speed and therefore the process develops faster. This leads to explosive spalling to occur more frequently, but the depth of the spalled of layer decreases.
- *Heating exposure:* The factor of the fire which influences to a less extent the occurrence of spalling is the number of sides of the construction which are

exposed to the fire. A construction which is exposed to a fire at two or more sides is heated up with a greater speed and therefore the possibility of spalling increases.

Geometry and structural loading of the cross section

- *Structural loading:* The factor of the construction which influences to a lesser extent the occurrence of spalling is the loading of construction. The loading of the construction causes stresses to be present in the construction. Compressive stresses, especially on the heated surface, tend to close the formed cracks by the degradation process of the concrete and therefore the permeability is locally reduced increasing the possibility of spalling. Tensile stresses in the cross section decrease the capability of the concrete to withstand tensile stresses due to pore pressure build up and increase the possibility of spalling.
- *Reinforcement*: Concrete with dense reinforcement in a construction tends to impede further water vapour transport and therefore the fully saturated layer develops at the position of the reinforcement and the pore pressure builds up together with local tensile stress peaks. Therefore in concrete with dense reinforcement the possibility of spalling increases. However, these zones also have a beneficial influence, because the high amount of moisture consumes a large amount of thermal energy during evaporation and therefore decreases the rise of temperature and thermal stresses in the cross section [9].
- *Thickness of the member:* The thickness of the member influences the possibility of spalling. When the thickness of a member increases, the heating rate of the cross section decreases and therefore the possibility of spalling decreases. In figure 4.30 and figure 4.31 the influence the thickness of the member has on the possibility of spalling is depicted.

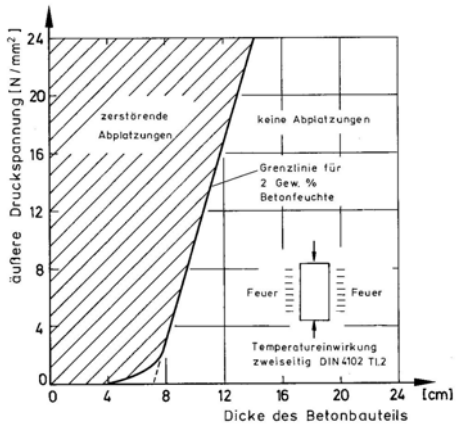

Fig 4.30 influence of the external compressive stress and the member thickness [42]

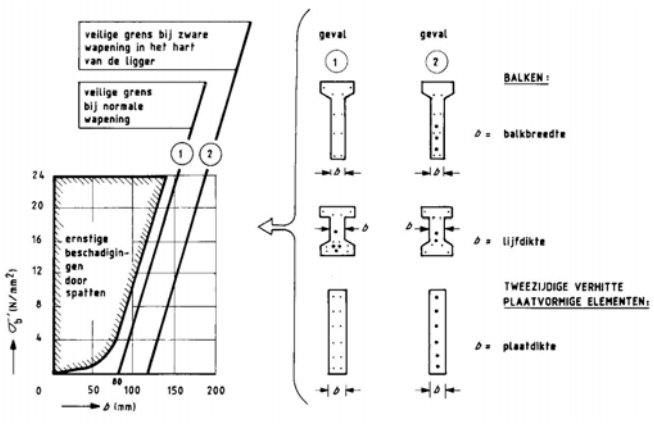

Fig 4.31 influence of the external compressive stress and the member thickness [11]

4.6.5. Spalling of High Performance Concrete

In the last 20 years, concrete has evolved to provide better performance. One of these concrete mixes is high performance concrete (HPC). The main advantage of high performance concrete is the high compressive strength and compactness [27]. The high compactness yields a better durability, but it is also the main parameter responsible for spalling at high temperatures [27,35]. As mentioned is spalling mainly influenced by moisture content and permeability. In case of high performance

concrete the high compactness causes low permeability. This low permeability in high performance concrete causes the water inside the concrete to be come superheated and therefore the pressure in the pores rises [35]. The lower this permeability is, the sooner the moisture clog is generated and the higher the pressure and the pressure gradient [27].

In figure 4.32 and figure 4.33 the difference between normal concrete and high performance concrete is depicted. The height of the pressure peak is in case of M30 (normal concrete, normal strength around 35 MPa) at a temperature of 600 ^{o}C around 18 bars at 30 mm. In case of M100 (high performance concrete, normal strength around 92 MPa) at the same temperature the pressure peak is 37 bars at 50 mm. This difference in height of pressure peak and the fact that the pressure gradient are higher in case of M100 explains for a major part why high performance concrete is more subject to spalling. The difference in permeability can also be seen both figures. In case of M30 the pressure peak rises until 30 mm and than decreases. This is due to the high permeability of the M30. In M100 concrete the pressure peak rises with increasing depth and does not decrease. In case of using high performance concrete the possibility of spalling can be reduced by improving the design of the structural element, modifying the design of the structure itself or adding polypropylene fibers [50].

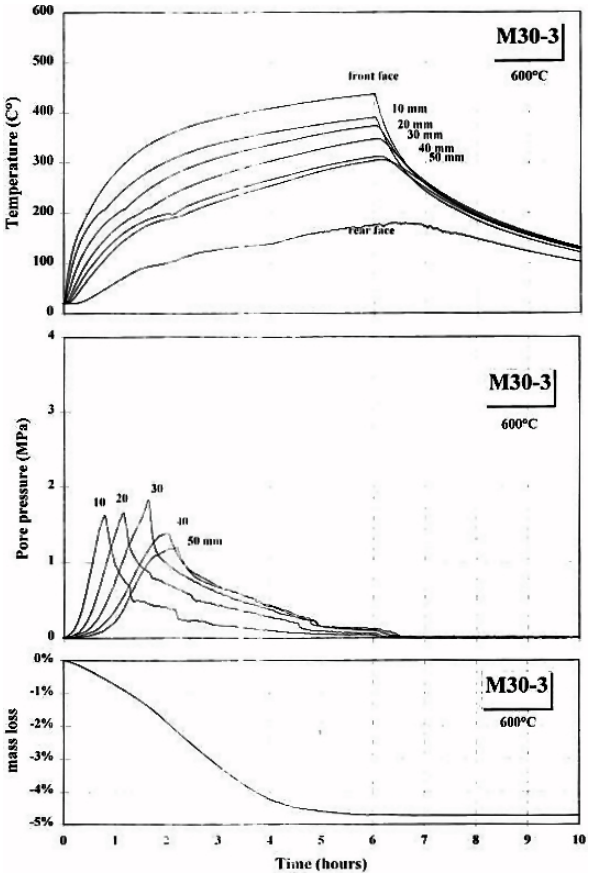

Fig 4.32 temperature, pore pressure and mass loss distribution in heated normal concrete [27]

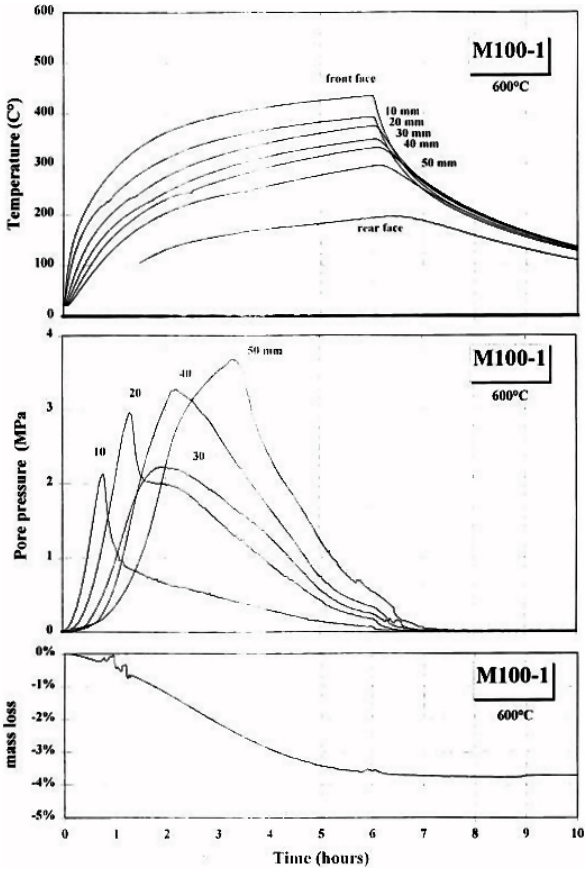

Fig 4.33 temperature, pore pressure and mass loss distribution in heated HPC concrete [27]

With this last option the micro structure of the concrete is changed. The polypropylene fibers, which are organic fibers, increase the permeability for as much as 3 to 4 times the permeability of concrete without fibers, as is depicted in figure 4.34. The reason for this increase in permeability is that the fibers melt at a temperature of 170 ^{o}C and finally evaporated at a temperature of 340 ^{o}C. This melting and subsequent evaporating of the fibers leads to a higher crack density in the concrete. However, the cracks have a smaller crack width [50]. This improved connectivity of the crack network leads to higher permeability. Above a temperature of 200 ^{o}C the permeability decreases in the same way for concrete with or without fibers. At this temperature, the temperature induced damage of the concrete reduces the overall effect of the polypropylene fibers [50].

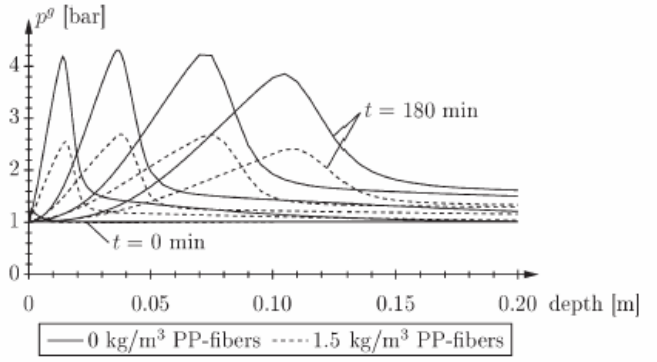

Fig 4.34 influence of polypropylene fibers on the pore pressure distribution [50]

4.6.6. Structural protection against spalling

Different failure modes

In case of fire exposure of a building or structural element there are three different failure modes can occur:

1. The spalling of concrete can cause locally the 'jump off' of the concrete cover on the reinforcement steel and because of this the reinforcement steel becomes exposed to the fire. The reinforcement steel is directly exposed to the heat of the fire and the strength, stiffness and load bearing capacity decreases. This kind of failure usually occurs in static determined structures, because there is little or no possibility for redistribution of forces.
2. The spalling of concrete gradually decreases the cross-section of the structural element. This kind of spalling was named sloughing off. The cross section decreases until the remaining cross section cannot carry the load anymore. This kind of failure usually occurs in thin, possibly compression loaded, cross sections.
3. The spalling of concrete causes holes in partitioning walls. The load bearing function is maintained, but according to the Eurocode II [18] this also qualifies as a failure mode. The fire can use these holes to propagate.

Measures against spalling

The measures against spalling can be subdivided into measures reducing spalling and measures preventing spalling [33,45,19,13].

1. *Measures reducing spalling:* This group consist out of four different types of measures which can be used to reduce spalling:

- *Concrete technological measures:* These measures consist of choosing type of aggregate, concrete mix, fillers and polypropylene fibers.
- *Static measures:* Choosing statically undetermined systems, because these structures have the possibility the redistribute forces, reducing the maximal compression stress.
- *Constructive measures:* Choosing shape and dimensions of the cross section, concrete cover and reinforcement layout.
- *Partial applying heat resistant measures:* Sprayed coatings, sprayed concrete or boards [39].

2. *Measures preventing spalling:* This group mainly consists out off applying heat resistant measures for the entire structural element. The general idea behind applying heat resistant cover is placing the material between the fire and the structure. The material ensures that the temperature on the surface of the concrete stays below 350 ^{o}C and the temperature of the reinforcement steel below 250 ^{o}C during the required fire resistance period [33,18,45,48,41].

5. Analytical model

5.1. General outline and goal of the presented model

In this chapter an analytical model is presented which describes the effects of exposure of the concrete to a fire. In case concrete is subjected to a fire, the surface of the concrete is exposed to the heat of the fire. This will cause the temperature of the surface of the concrete to increase and due to the thermal diffusitivity of concrete the heat will also penetrate into the concrete and cause the temperature inside the concrete to increase. This causes the strength and stiffness of the concrete to decrease. Furthermore, due to evaporation of water from the pores of the concrete the process which leads to the development and occurrence of spalling arises.

The main goal of this chapter is to derive an analytical model which is relatively simple and therefore the main theories and factors influencing the process can be identified and examined. From this it can be concluded which information is already present and in which fields further information needs to be gathered. Furthermore the analytical model needs to give a good impression in the behaviour of concrete during exposure to a fire. Especially the water vapour transport, build up of a saturated layer and the development of the pore pressure should be modelled. Finally, the obtained results from the analytical model can be compared to experimental data to validate if the model behaves correctly.

5.2. The different parts of the analytical model

The analytical model is divided into four main parts. The first part determines the temperature distribution in the cross section. The temperature distribution is used to determine the second part, the internal stresses due to this temperature distribution. The temperature distribution is also used to determine the water vapour transport and development of a saturated layer, which is the third part. The last part is the determination whether a saturated layer exists and the determination of the build up of pore pressure and the resulting tensile stresses.

5.3. First part: temperature distribution

5.3.1. Theory

Due to the heat penetration of the concrete a temperature distribution over the cross section will occur. This temperature distribution will be non-linear and the shape will be that of a quadratic parabola. The temperature distribution over the cross section is dependent on the thickness, the material properties of the concrete and the moisture content. However, most material properties as well as the moisture content are dependent on the temperature. This leads to an interaction between the material properties, the moisture content and the temperature distribution. The material properties and the moisture content determine the increase in temperature in the concrete and this leads, for temperatures of 100 ^{o}C or higher, to a change in the material properties and the moisture content. In general it holds that the heating of the cross section will be faster and the temperature difference, between the surface and the inside, will be larger, if the moisture content of the concrete is lower. Furthermore, it holds that the thicker the cross section, the slower the heating of the cross section will occur.

The temperature distribution is determined with the three dimensional differential equation by Fourier which is depicted in equation 5.1 [6,32].

$$\frac{\partial T}{\partial t} = a_c * \left[\frac{\partial^2 T}{\partial x^2} + \frac{\partial^2 T}{\partial y^2} + \frac{\partial^2 T}{\partial z^2} \right] \tag{5.1}$$

With: a_c = thermal diffusitivity of concrete [m^2/s] => $a_c = \frac{\lambda_c}{\rho_c c_c}$

λ_c = thermal conductivity of concrete [W/mK]

ρ_c = density of concrete [kg/m^3]

c_c= specific heat of concrete [kJ/kgK]

T(x,y,z,t) = temperature of the concrete [K]

x,y,z = coordinates [m]

t = time [min]

In the thermal diffusitivity parameter the material properties influencing the temperature distribution are combined. Each of these material properties is temperature dependent. The moisture content and the influence of this parameter are not included.

Concrete elements which have relative large width and height compared to the thickness can be schematized as a semi-infinite concrete element. In these elements a one dimensional temperature distribution is present. In this special case the differential equation is simplified and becomes the differential equation which is depicted in equation 5.2 [6,32].

$$\frac{\partial T}{\partial t} = a_c * \left[\frac{\partial^2 T}{\partial x^2} \right] \tag{5.2}$$

5.3.2. Numerical solution

From the one dimensional differential equation the temperature distribution can numerically be obtained with the method by Binder-Schmidt [6]. The cross section of the element is therefore, in depth direction, divided into small elements, each with a width of Δx. In figure 5.1 the basis for the numerical solution is depicted.

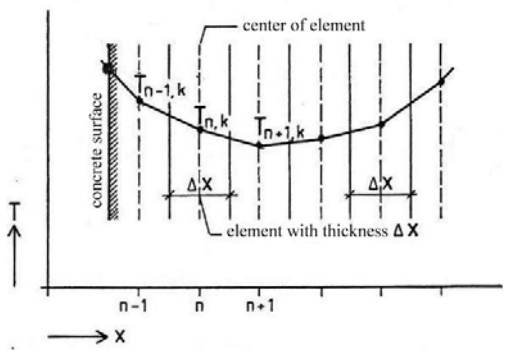

Fig 5.1 basis of the numerical solution by dividing the cross section into elements [6]

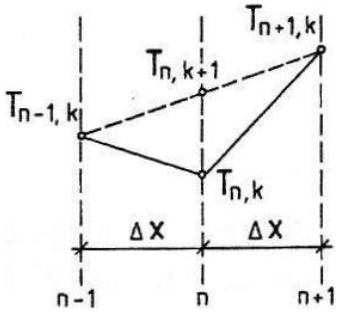

Fig 5.2 graphical representation of equation 5.6 [6]

The temperatures in the middle of these elements are then calculated and the curved temperature distribution is estimated by connecting the temperatures in the middle of the elements with straight lines.

To calculate the temperatures the finite differences of the equation 5.3 are substituted into the differential equation 5.2 and equation 5.4 is obtained [6].

$$\frac{\partial T}{\partial t} => \frac{\Delta T}{\Delta t} = \frac{T_{n,k+1} - T_{n,k}}{\Delta t}$$
$$\frac{\partial^2 T}{\partial x^2} => \frac{\Delta^2 T}{(\Delta x)^2} = \frac{T_{n+1,k} + T_{n-1,k} - 2 * T_{n,k}}{(\Delta x)^2} \quad (5.3)$$

With: n = indication for the middle of element Δx
k = indication for the time step Δt

$$T_{n,k+1} - T_{n,k} = 2 * a_c * \frac{\Delta t}{(\Delta x)^2} * \left(\frac{T_{n+1,k} + T_{n-1,k}}{2} - T_{n,k} \right) \quad (5.4)$$

For this numerical solution to be stable, the equation 5.4 needs to be stable. Therefore equation 5.5 is formulated. In case equation 5.5 is equal to ½, the numerical solution in equation 5.6 is obtained, which is depicted in figure 5.2 [6].

$$a_c * \frac{\Delta t}{(\Delta x)^2} \leq 1/2 => a_c * \frac{\Delta t}{(\Delta x)^2} = 1/2 \quad (5.5)$$

$$T_{n,k+1} = \frac{T_{n+1,k} + T_{n-1,k}}{2} \quad (5.6)$$

The numerical solution, in equation 5.6, is used to determine the temperature distribution over the cross section by implementing this equation in Microsoft Office Excel[tm].

5.3.3. Assumptions

In this part of the analytical model the following assumptions are made:

1. The evaporation of water will consume heat and therefore slow down the rate at which the temperature penetrates the cross section. This effect is neglected in the heat transfer model.
2. The thermal diffusitivity of concrete is constant. This means that the temperature dependence of the material properties is neglected.
3. The boundary condition on the heated surface is prescribed by the temperature of the HSL-Zuid fire curve. (appendix A) This is an assumption, because the surface temperature of the concrete differs from the temperature of the fire curve. This difference occurs because part of the heat of the fire is lost during radiation and convection.
4. The influence of reinforcement on the temperature distribution is not taken into account.

5.3.4. Material properties used in the analytical model

The grade of the concrete used in the numerical simulation is B35 (C28/35). The material properties of this type of concrete, which are used in the analytical model, are depicted in table 5.1. In the last column of this table the indication is given which of the material properties that are used are temperature dependent.

Material property		**Temp. dependent**
Concrete grade	B35 (C28/35)	
Thickness	400 mm	
Width	1000 mm	
Height	1000 mm	
Number of elements	100	
Thermal conductivity of concrete	2,55 W/mK	No
Density of concrete	2400 kg/m^3	No
Specific heat of concrete	0,8 kJ/kgK	No
a_c = thermal diffusitivity of concrete $a_c = \frac{\lambda_c}{\rho_c c_c}$	22,22 mm^2/min	No
Stability criterion: $a_c * \frac{\Delta t}{(\Delta x)^2} \leq 1/2$	$\Delta t = 0{,}36\,\text{min}$, $\Delta x = 4mm$	
Initial temperature	20 ^{o}C	

Table 5.1 material properties used in the analytical model

5.3.5. Results and analysis

The thermal diffusitivity of the concrete and the distribution of the surface temperature determine the rate at which the heat penetrates the cross section of the and thus the temperature distribution throughout the cross section. In figure 5.3 the temperature distribution over the cross section on different moments in time is depicted. The temperature on the surface of the concrete increases with time and after 5 minutes the temperature reaches 1000 ^{o}C. After 60 minutes the temperature on the surface of the concrete starts the decrease until around 170 minutes into the fire the temperature becomes 20 ^{o}C again. This is in accordance with the HSL-Zuid fire curve.

The heat rapidly penetrates the concrete and after 5 minutes the first 40 mm already experiences an increase in temperature ranging from just over 20 ^{o}C until 1000 ^{o}C on the surface of the concrete. This process continues and after 10 and 20 minutes the heated layer has grown to respectively 60 mm and 100 mm. The maximum depth the heated layer reaches after 180 minutes is around 250 mm. After 60 minutes the surface temperature decreases, but the temperature within the concrete only gradually follows this decrease. The peak of the temperature distribution shifts, in time, into the cross section of the concrete. This can be clearly seen if the temperature distribution after 60 minutes is compared to the temperature distribution after 90 and 120 minutes.

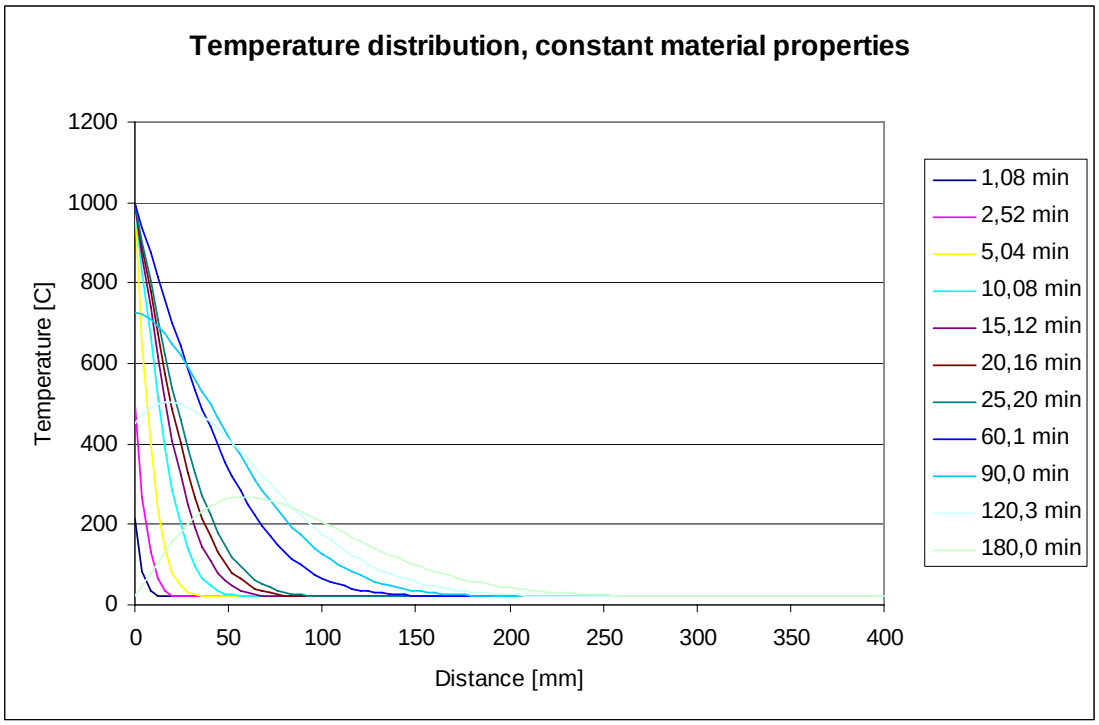

Fig 5.3 temperature distribution in the cross section with constant a_c=22,22 mm^2/min

From the temperature distributions a graph can be obtained which represent the progress of the 100 °C temperature through the concrete. This will also be referred to as the 100 °C front and is depicted in figure 5.4. The 100 °C front reaches 20 mm and 40 mm after respectively 5,5 and 14,5 minutes. The 100 °C front reaches a maximum depth of 148 mm after 180 minutes. From figure 5.4 the speed of the 100 °C front is also calculated and this is depicted in figure 5.5. In the first 10 minutes the speed at which the 100 °C front penetrates the concrete decreases from 5,46 mm/min to 1,98 mm/min. After the 10 minutes the speed of the 100 °C front gradually decreases to 0,34 mm/min.

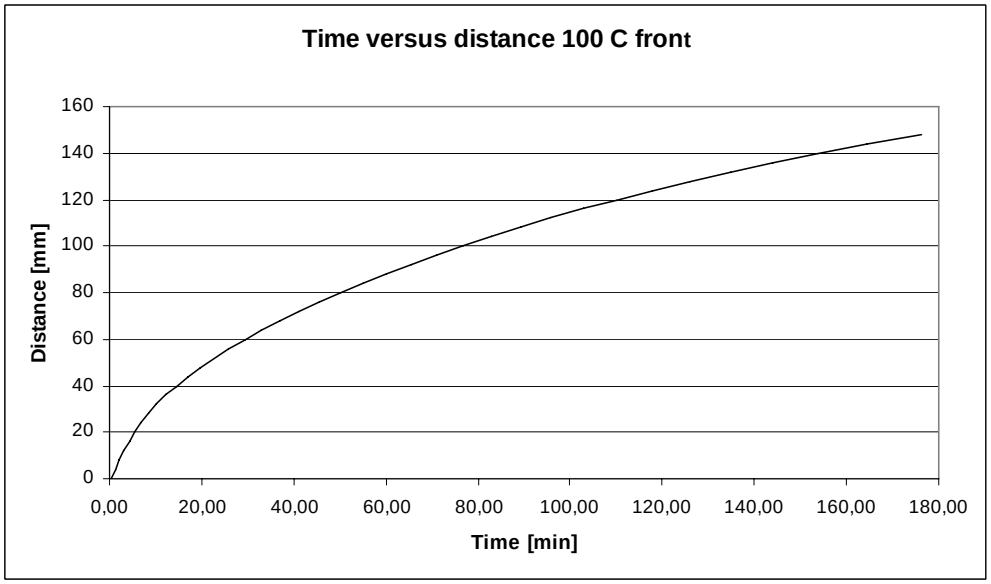

Fig 5.4 development of time versus distance of 100 °C front

The temperature distribution and the speed of the 100 ^{o}C front indicate that in the early stages of the fire the heat rapidly penetrates the concrete and the heated layer rapidly grows. After around 10 minutes the speed at which the heated layer grows gradually reduces over time.

The explanation for this is that the HSL-Zuid fire curve reaches its maximum temperature after 5 minutes and remains at its maximum temperature of 1000 ^{o}C for 55 minutes. This means that the concrete element is rapidly heated up in the first 5 minutes and after that the amount of heat penetrating the concrete gradually becomes constant. Furthermore, only the temperature in the surface layer of the concrete increases, whereas the temperature in the deeper interior of the concrete stays unchanged. This is due to the poor thermal diffusitivity and thus good insulation of concrete compared to other building materials. The theory behind the numerical solution confirms these observations, because this method is affected by the distribution of the surface temperature and the thermal diffusitivity of the concrete. This means that also the heat penetration and the rate of the heat penetration are influenced by these aspects. The thermal diffusitivity depends on the material properties of the concrete of which the thermal conductivity and the specific heat capacity are the most important. In addition, the temperature distribution also shows that the cooling down of the concrete is, just as the heating up of the concrete, influenced by the diffusitivity of the concrete.

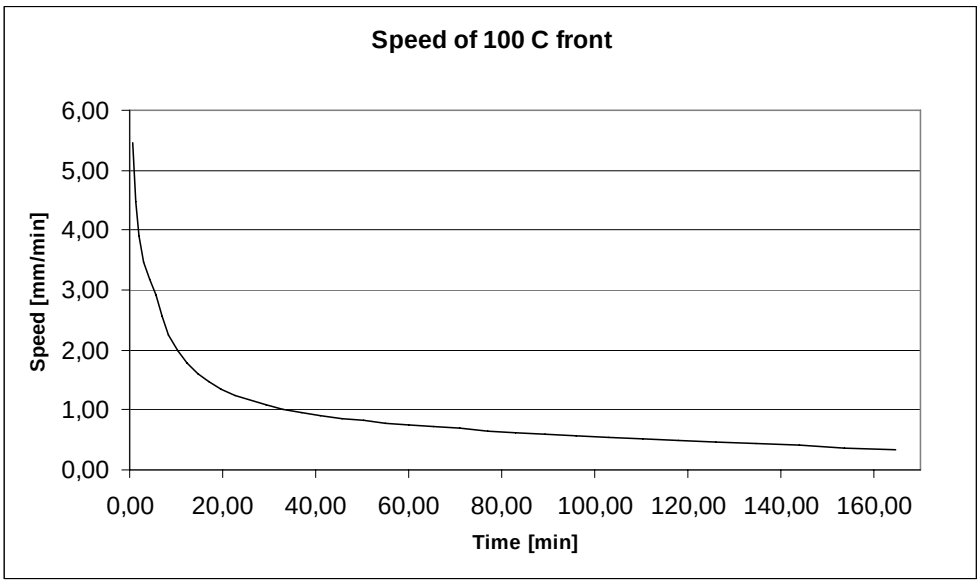

Fig 5.5 speed of 100 ^{o}C front

5.4. Second part: internal stresses due to the temperature distribution

5.4.1. Theory

The temperature distribution over the cross section is non linear and leads to restrained expansion and internal temperature stresses through the cross section. On the heated surface there will be compression stresses and inside the cross section there will be tensile stresses. In case of one side heating these tensile stresses will occur through the cross section including the non-heated opposite surface. These stresses are called Eigen stresses.

To obtain the response of the construction the temperature distribution is divided into three different parts: the average temperature, the temperature difference and the Eigen temperature.

1. The average temperature => this temperature profile is constant over the cross section and is calculated by multiplying the area underneath the temperature distribution with the inverse of the area of the concrete cross section. In case of free deformation this temperature leads to a lengthening or shortening. In case of restrained deformation a normal force is introduced [6].

$$\Delta T_{avg} = \frac{1}{A_c} * \int_{x_1}^{x_2} \Delta T(x) * b * dx \tag{5.7}$$

With A_c = area of the concrete cross section [m^2]
b = width of the cross section [m]
x_1,x_2 = thickness direction of the cross section is the x-axis [m]

2. The temperature difference => this temperature profile is linear over the cross section and is calculated by equation 5.8 [6]. In case of free deformation, this temperature leads to a curvature which can be calculated by equation 5.9 [6].

$$\Delta T_b(x) = \frac{\Delta T_b}{h} * x \tag{5.8}$$

$$\kappa(\Delta T_b) = \frac{\Delta T_b * \alpha_c}{h} \tag{5.9}$$

With $$\Delta T_b = \frac{h}{I_c} * \int_{x_1}^{x_2} \Delta T(x) * b * x * dx \tag{5.10}$$

κ = curvature [1/m]
h = thickness of the cross section [m]
I = moment of inertia around the y-axis [m^3]
α_c = thermal expansion coefficient [1/K]

3. Eigen temperature => this temperature profile satisfies the condition that the Eigen temperatures in the cross section are in equilibrium with each other. The stresses in the cross section, resulting from the Eigen temperature, are called Eigen stresses and are also in equilibrium with each other and therefore there will be no deformation by these stresses. The Eigen temperature is calculated by equation 5.11 [6]. From the Eigen temperature the Eigen stresses can be calculated with equation 5.12 [6].

$$\Delta T_e(x) = \Delta T(x) - \left(\Delta T_{avg} + \Delta T_b(x)\right) \tag{5.11}$$

$$\sigma_c(\Delta T_e(x)) = \alpha_c * \Delta T_e(x) * E_{c,T} \tag{5.12}$$

With E_c = modulus of Elasticity => $E_{c,T} = E_c * \psi(\tau,t) * \alpha_\theta$ [N/m^2]
$\psi(\tau,t)$ = relaxation and creep factor [-]
α_θ = factor which incorporates the reduction of the modulus of Elasticity by the increasing temperature [-]

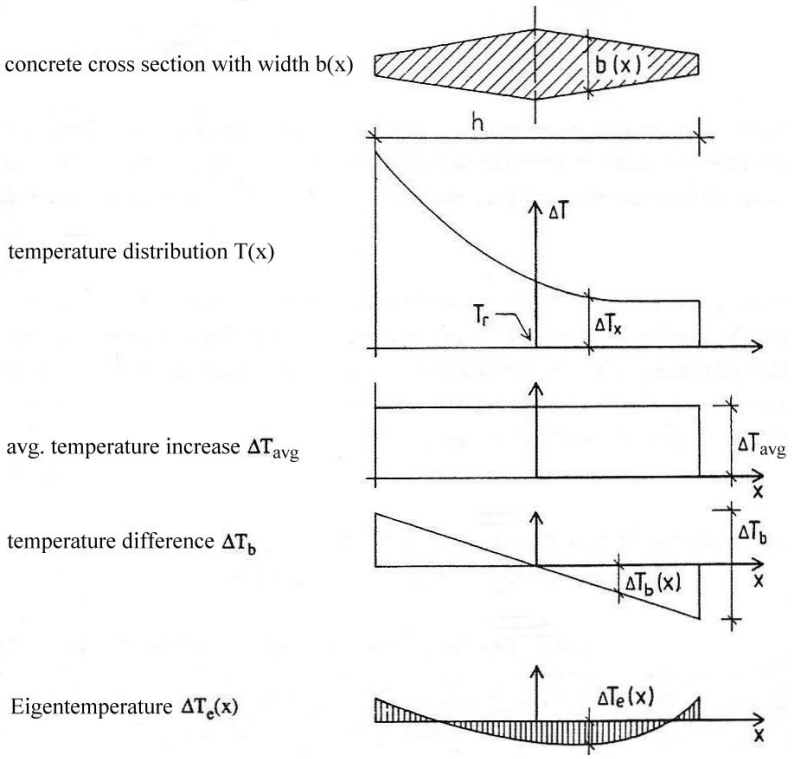

Fig 5.6 temperature distribution over the cross section divided into different temperature distributions [6]

In figure 5.6 the different temperature distributions and the resulting Eigen temperature are depicted.

5.4.2. Numerical solution

The equations 5.7 and 5.10 both contain integrals, which can numerically be calculated. The integral in equation 5.7 calculates the area under the temperature distribution and numerically this can be solved by dividing this area in discrete elements. The width of these elements is equal to the width of the elements used in the temperature distribution calculation. The height of the elements is equal to the calculated temperature. In equation 5.13 the numerical integration is depicted.

$$\Delta T_{avg} = \frac{1}{A_c} * \int_{x_1}^{x_2} \Delta T(x) * b * dx \approx \frac{1}{A_c} * \sum_{n=1}^{n=100} (T_n * \Delta x * width) \qquad (5.13)$$

The integral in equation 5.10 differs from the above described integral by the addition of ‘x’. Numerically this can be solved by calculating ‘x’ as the distance from the centre of the discrete elements to the centre of the cross section. In equation 5.14 this is depicted.

$$\Delta T_b = \frac{h}{I_c} * \int_{x_1}^{x_2} \Delta T(x) * b * x * dx \approx \frac{h}{I_c} * \sum_{n=1}^{n=100} \left(T_n * \Delta x * width * \left| \left(\frac{Thickness}{2} \right) - x_n \right| \right) (5.14)$$

The numerical solution is used to determine the Eigen stress distribution over the cross section by implementing these equations in Microsoft Office Excel[tm].

5.4.3. Assumptions

In this part of the analytical model the following assumptions are made:

1. The modulus of elasticity used in this model is 25 % of the initial modulus of elasticity and is constant throughout the cross section. This is an assumption, because the temperature distribution has a large influence on the modulus of Elasticity [6]. Towards the surface of the cross section the temperature rapidly increases and this causes the modulus of Elasticity to decrease. The reduction of the modulus of Elasticity starts at a temperature of 50 ^{o}C. Deeper into the cross section the temperature is below 50 ^{o}C and the modulus of Elasticity is not reduced. Furthermore, the increasing temperature also has an influence on the creep and relaxation of the concrete, with are both also time dependent. The increasing temperature is incorporated by a reduction factor of 50 % on the initial modulus of Elasticity. Effects such as creep and relaxation are difficult to include because most of the researches into these phenomena have been carried out for temperatures below 150 ^{o}C. In this model creep and relaxation are included by reducing factor of 50 % on the initial modulus of Elasticity. Both effects together reduce the initial modulus of Elasticity for 75 %. The numerical solution is obtained for a constant modulus of Elasticity and therefore the modulus of Elasticity can only be kept constant throughout the cross section. This is a simplification, but in the next paragraph the effect of the temperature on the modulus of Elasticity and the consequences for the stresses is explained.
2. It is assumed that the concrete element can deform freely. This means that due to the average temperature distribution the element will first lengthen and then shorten. The temperature difference will lead to a curvature which leads to stresses in the concrete. Both aspects are in this model not calculated.

5.4.4. Material properties used in the analytical model

The grade of the concrete used in the numerical simulation is B35 (C28/35). The material properties of this type of concrete, which are used in the analytical model, are depicted in table 5.2. In the last column of this table the indication is given which of the material properties that are used are temperature dependent. The material properties indicated by (*) are graphically depicted in the Appendix B.

Material property		**Temp. dependent**
Concrete grade	B35 (C28/35)	
Thickness	400 mm	
Width	1000 mm	
Modulus of Elasticity (E_c) [6]	30.000 N/mm^2 (*)	No
Relaxation and creep factor ($\psi(\tau,t)$) Reduction factor for temperature (α_θ)	0,5 0,5	
Corrected Modulus of Elasticity ($E_{c,T}$)	7500 N/mm^2	No
Thermal expansion coefficient	1,00*10^{-5} 1/K	N
Cross section of concrete (A_c) A_c = width * thickness	400.000 mm^2	
Moment of Inertia (I_c) 1/12 * width * thickness^3	5,33*10^9 mm^3	

Table 5.2 material properties used in the analytical model

5.4.5. Results and analysis

In figure 5.7 and 5.8 the Eigen stress distribution over the cross section on different moments in time are depicted. As mentioned before these stresses are in equilibrium with each other. On the surface of the concrete the compressive Eigen stress develops quickly and after 5 minutes the compressive stress already reaches 50 MPa. After 5 minutes this compressive stress gradually reduces and after 60 minutes the compressive Eigen stress reduced to 35 MPa. This process continues and after 130 minutes the Eigen stress on the surface of the concrete shift from compressive to tensile Eigen stress. At 180 minutes this tensile Eigen stress reaches a value of 13 MPa.

The zone of the cross section which is in compression gradually increases from 28 mm after 15 minutes to 48 mm after 60 minutes. The maximum length of the compression zone, with the surface of the concrete still under compression, is 80 mm after 130 minutes. With the gradually increase of the length of the compression zone the tensile zone of the concrete shifts into the concrete. After 60 minutes the right end of the tensile zone is at 268 mm and after 180 minutes at 288 mm. The peak tensile Eigen stress also shifts further into the concrete. After 5 minutes the peak tensile stress is 6,23 MPa at 36 mm and after 60 minutes the peak tensile stress has increased to 12,18 MPa at 110 mm and this is also the largest tensile Eigen stress.

The Eigen stress distribution changes when the temperature on the surface of the concrete starts to decrease. When the layer with a reduced temperature increases, the Eigen stress distribution gradually changes. On the surface of the concrete, the Eigen stress gradually changes from a compressive stress to a tensile stress. The Eigen stress distribution it self changes from a compressive zone, tensile zone and compressive zone to a tensile zone, compressive zone, tensile zone and a compressive zone.

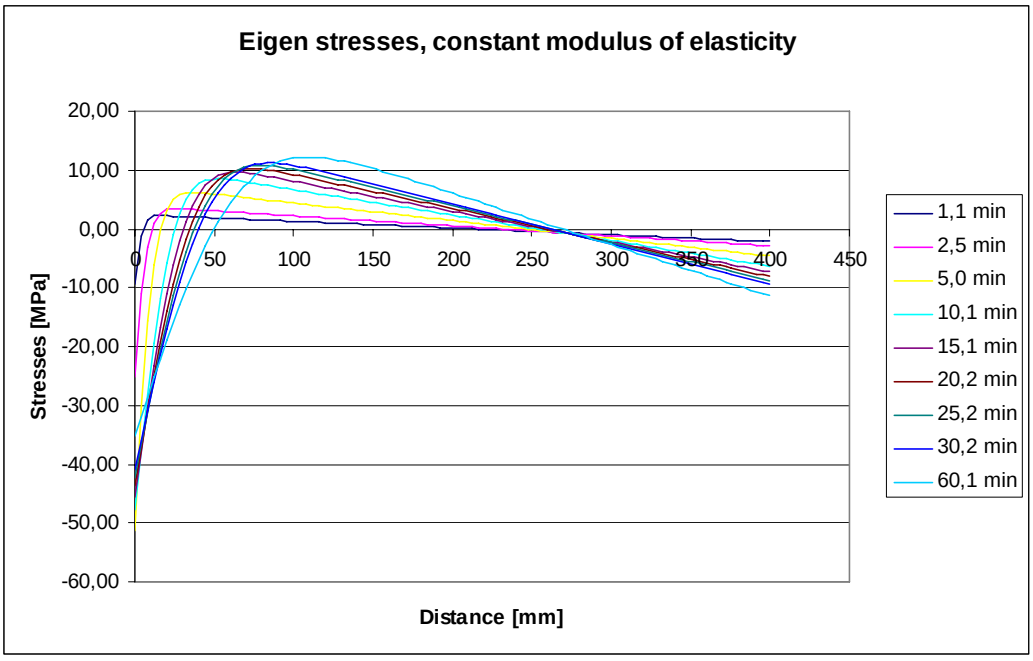

Fig 5.7 Eigen stresses distribution over the cross section with constant $E_{c,T}$ = 7500 kN/m^2 (0 -60 minutes)

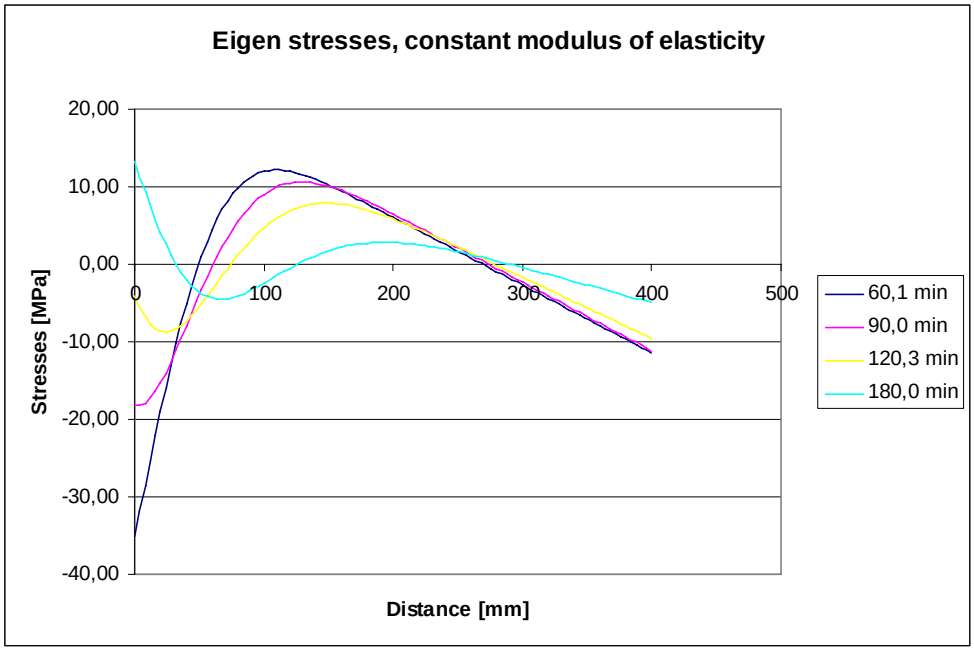

Fig 5.8 Eigen stresses distribution over the cross section with constant $E_{c,T}$ = 7500 kN/m^2 (60 – 180 minutes)

In figure 5.9 and 5.10 the Eigen stress distribution of different point in time are depicted. In general it can be stated that in time the points in the cross section change from either compression to tension or from tension to compression. The points with the largest change in Eigen stress are the points on and close to the surface of the concrete. The surface of the concrete changes from 51 MPa in compression to 14 MPa in tension. Also the points at 50 to 60 mm change from 9,5 MPa in tension to 5 MPa in compression.

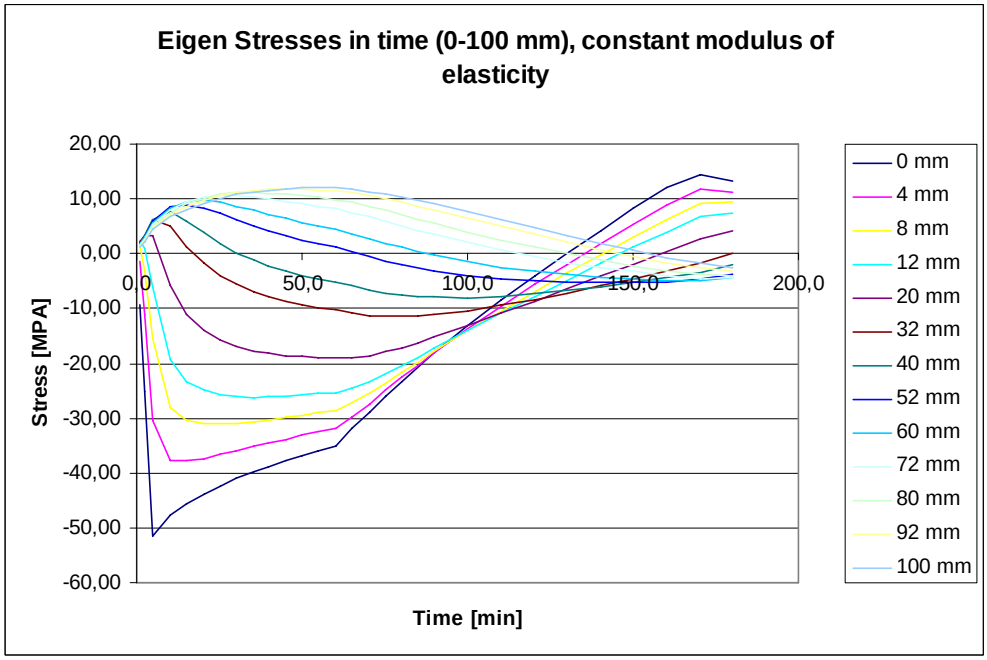

Fig 5.9 Eigen stresses distribution of different point in time with constant $E_{c,T}$ = 7500 kN/m^2 (0 – 100 mm)

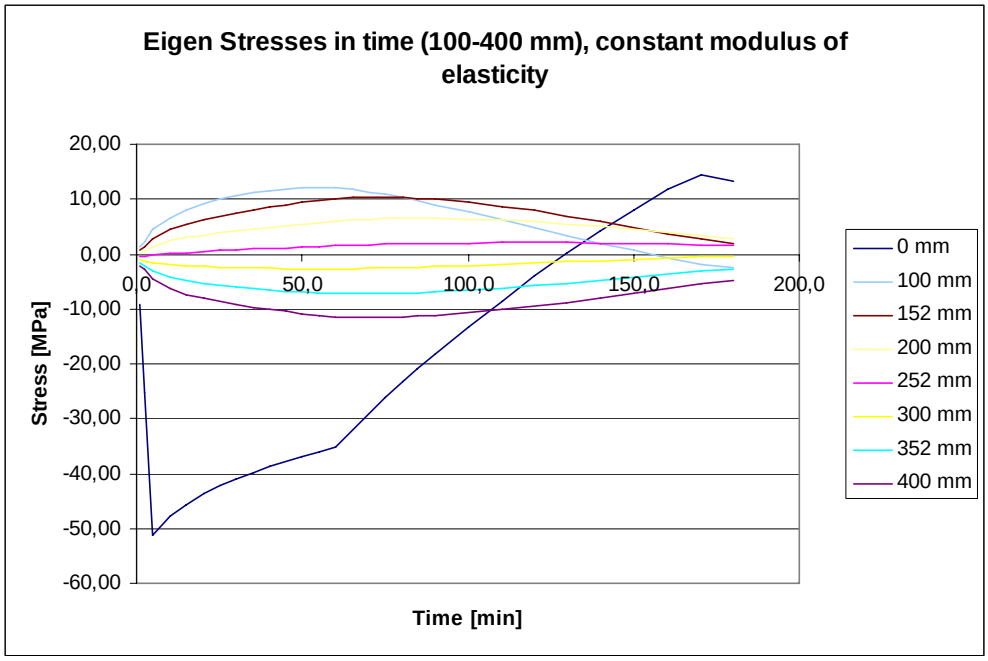

Fig 5.10 Eigen stresses distribution of different point in time with constant $E_{c,T}$ = 7500 kN/m^2 (0 – 100 mm)

In the analytical model the modulus of Elasticity is reduced and kept constant throughout the cross section of concrete. However, this is, as is already explained in the assumptions, not correct. The modulus of Elasticity is largely influenced by the temperature.

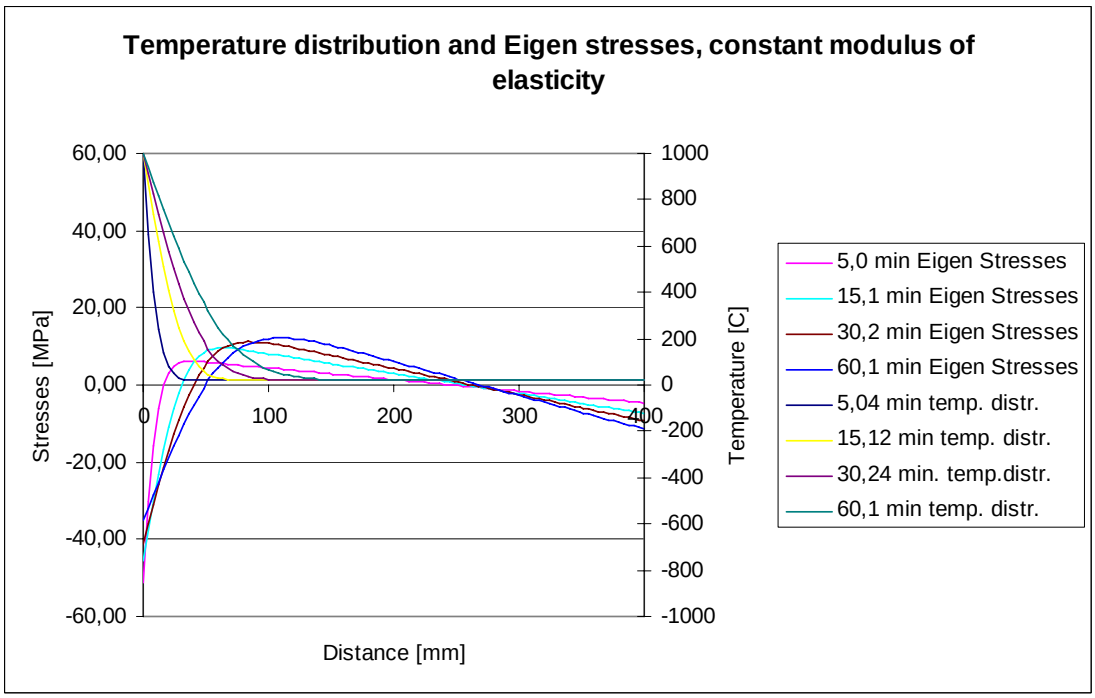

Fig 5.11 Temperature and Eigen stresses distribution over the cross section with constant $E_{c,T}$ = 7500 kN/m^2

In the surface layer of the cross section, a compressive zone is present in which the compressive Eigen stresses are larger than the compressive strength of the concrete. These Eigen stresses occur in the surface layer of the concrete where the temperature becomes much larger than 50 ^{o}C, which is depicted in figure 5.11. At this temperature the modulus of Elasticity starts to decrease and therefore the stresses, including the Eigen stresses, decrease. At temperature of 700 ^{o}C or higher the modulus of Elasticity reduces to 10 percent. This means that the largest compressive stresses in the surface layer of the concrete are in fact much smaller. However, in the tensile zone which follows the compressive zone, tensile Eigen stresses are developed which are larger than the tensile strength of the concrete. These Eigen stresses are developed in a region where the temperature is rapidly reducing and therefore the modulus of Elasticity is only partly reduced or in the deeper parts of this tensile zone, where the largest tensile stress are developed, not reduced. This means that these tensile Eigen stresses can therefore lead to cracking of the concrete.

5.5. Third part: prediction of water vapour transport

5.5.1. Theory

In chapter 4 the process which leads to spalling was described and one of the most important aspects is the transport of water vapour. Furthermore, the four main transport processes where explained. In this part of the analytical model the transport of water vapour through the larger pore sizes is assumed. This means that from the four transport processes depicted in figure 2.5 the viscous flow and diffusion are the most obvious for the modelling of the flow of water vapour. The choice between both transport processes is determined by the available information. In this part of the analytical model the viscous flow is chosen as the transport process. This means that the flow of water vapour is assumed to be viscous and the speed of the flow of water vapour is slow and therefore the flow is characterized as laminar.

Furthermore, the choice for viscous flow implies that not all the available pores sizes are used for the transport of water vapour. The smaller pore sizes are to narrow to be used for viscous flow and therefore the permeability of the concrete needs to be corrected for this. This is done by reducing the permeability by that percentage of pore sizes which is smaller than the mean free path length. The mean free path length is determined by equation 5.15 [I].

$$l = (\sqrt{2} * n * \sigma)^{-1} \tag{5.15}$$

With l = mean free path length [nm]
n = number of particles per unit volume [-]
σ = effective cross sectional area for the collision [m^2]

In equation 5.15 the number of particles and the cross sectional area are unknown. The number of particles can be obtained from the ideal gas law, which is depicted in equation 5.16 [III]. The cross sectional area is determined by assuming figure 5.12. The cross sectional area is calculated as the area needed for two molecules to pass each other without colliding. This is determined by using the diameter of a water vapour molecule, which can be obtained by the Van der Waals Equation of State, equation 5.17 [IV]. The Van der Waals Equation of State is a modification of the ideal gas law.

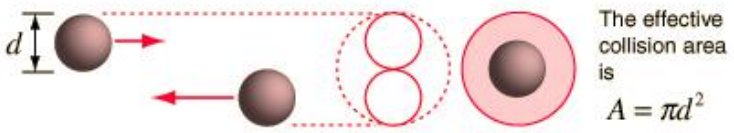

Fig 5.12 determination of effective cross sectional area [II]

The ideal gas law assumes that the molecules are point particles and that the collisions are perfectly elastic. However, the Van der Waals Equation of State takes into account molecular size and interaction forces.

Ideal gas law => $P*V = n*R*T = N*k*T$ (5.16)

Van der Waals Equation of State => $\left[P + a*\left(\frac{n}{V}\right)^2\right]*\left(\frac{V}{n} - b\right) = R*T$ (5.17)

With
P = pressure [Pa]
V = volume [m^3]
T = temperature [K]
n = number of moles [-]
R = universal gas constant = 8,3145 J/mol K
N = number of molecules [-]
k = Boltzmann constant =1,38066*10^{-23} J/K, k = R/N_a
N_a = Avogadro's number = 6,0221*10^{23} mol^{-1}
a => constant which is a correction for the intermolecular forces [-]
b => constant which is a correction for finite molecular size [-]

The constant b can be used as an estimate for the molecular volume. In equation 5.18 the volume of a sphere is used to estimate the radius of a water vapour molecule [IV].

$$V = \frac{b}{N_a} = \frac{4*\pi*r^3}{3} => \frac{30{,}52*10^{-6}}{6.02*10^{23}} = \frac{4*\pi*r^3}{3} => r = 0{,}23nm \quad (5.18)$$

This radius can then be used to estimate the cross sectional area and together with the number of molecules obtained from the ideal gas law the mean free path length can be determined. This is then used to reduce the permeability. In table 5.3 examples of the calculation of the mean free path length is given.

Temperature [K]	**Volume [m^3]**	**Pressure [Pa]**	**Number of molecules [-]**	**Eff. collision area [m^2]**	**Mean free path length [nm]**
293,15	1,00	101325,00	2,50*10^{25}	6,62*10^{-19}	42,7
373,15	1,00	100659,21	1,954*10^{25}	6,62*10^{-19}	54,7
523,15	1,00	4224156,32	5,848*10^{26}	6,62*10^{-19}	1,8

Table 5.3 example of calculation of mean free path length

These mean free path lengths are than used to reduce the permeability obtained by Zeiml [14]. Zeiml describes the permeability with a function which is time dependent. The pore size distribution of figure 4.24 together with the determined mean free path lengths are used to reduce the permeability by that percentage of pore sizes which is smaller than the mean free path length. The formula obtained by Zeiml can be rewritten to incorporate this reduced permeability.

Two aspects determine the viscous flow of water vapour through the concrete. The first is the already mentioned permeability. The second is the pressure difference. The viscous flow of water vapour is caused by a pressure difference. This pressure difference is caused by the evaporation process. Evaporation is a surface phenomenon which is depicted in the left part of figure 5.13 [V]. When heat is added to the water, some molecules have enough kinetic energy to break free of the surface of the water, which means that part of the water is evaporated. The amount of energy needed for this is called latent heat of vaporisation or specific enthalpy of evaporation. This is the amount of heat necessary to transform 1 kilogram of water into water vapour without change of the temperature. In other words the thermal energy needed during change from a liquid state to a vapour state. If the space is closed, which is the case in the pores of the concrete, part of the escaped molecules will return back to the surface of the water. This is depicted in the right part of figure 5.13. Equilibrium is reached when the number of molecules which escapes the surface is equal to the number of molecules returning to it. At this point the vapour is saturated and the pressure at which this happens is called the saturated vapour pressure, which increases when the temperature increases. This saturated vapour pressure determines the pressure in the dehydrating zone where the evaporation process is developing and the pressure difference arises, because in the cooler interior of the concrete the atmospheric pressure is present.

In figure 5.14 the phase diagram of a material is shown. The saturated vapour pressure line is the p_s (T) line. Clapeyron has experimentally established equation 5.19 which describes the slope of this line [49]. This equation is only valid for the transition from liquid to vapour.

$$\frac{dP}{dT} = \frac{r_{1\to 2}}{T(v_2 - v_1)} \tag{5.19}$$

With P = Pressure [Pa]
T = Temperature [K]
$r_{1\to 2}$ = heat needed to change from a liquid state to a vapour state [J/mol]
v_2 / v_1 = specific molar volume of vapour respectively liquid [m^3/mol]

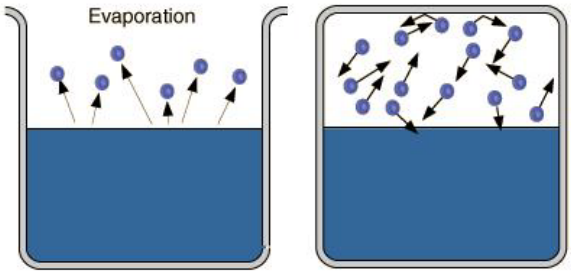

Fig 5.13 schematic representation of the evaporation process [V]

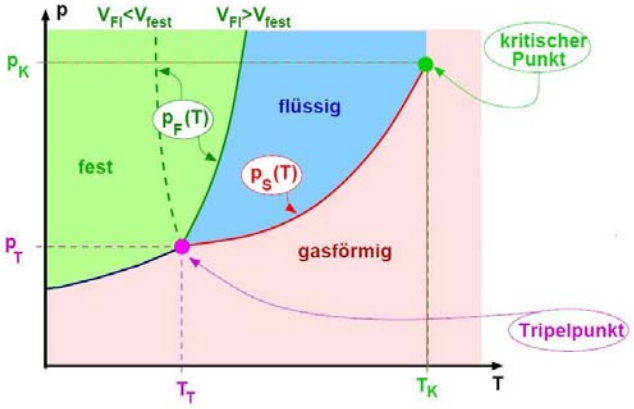

Fig. 5.14 phase diagram of a material [21]

In general is it possible, in the change from a liquid state to a vapour state, to neglect the liquid volume. Furthermore, if an ideal gas is assumed, then equation 5.19 can be transformed, with the aid of equation 5.16, into equation 5.20.

$$v_2 - v_1 \approx v_2 = \frac{R*T}{P}$$
$$\frac{dP}{dT} = \frac{r*P}{R*T^2} \Rightarrow \frac{dP}{p} = \frac{r*dT}{R*T^2} \quad (5.20)$$

With V = volume [m^3]
n = number of moles [-]
R = universal gas constant = 8,3145 J/mol K
N = number of molecules [-]
k = Boltzmann constant =1,38066*10^{-23} J/K

If r is independent from T, than the solution of equation 5.20 is equation 5.21. In this equation A is a variable which is based on the substance and the system parameters.

$$\ln P = A - \frac{B}{T}, B = \frac{r}{R} \quad (5.21)$$

The saturated vapour pressure can also be approximated with equation 5.22 when the temperature is known and this leads to figure 5.15 [VI,VII].

$$P_{sv} = 610{,}78 * \exp\left(\frac{T}{T + 238{,}3} * 17{,}2694\right) \quad (5.22)$$

With P_{sv} = saturated vapour pressure [Pa]
T = temperature [^oC]

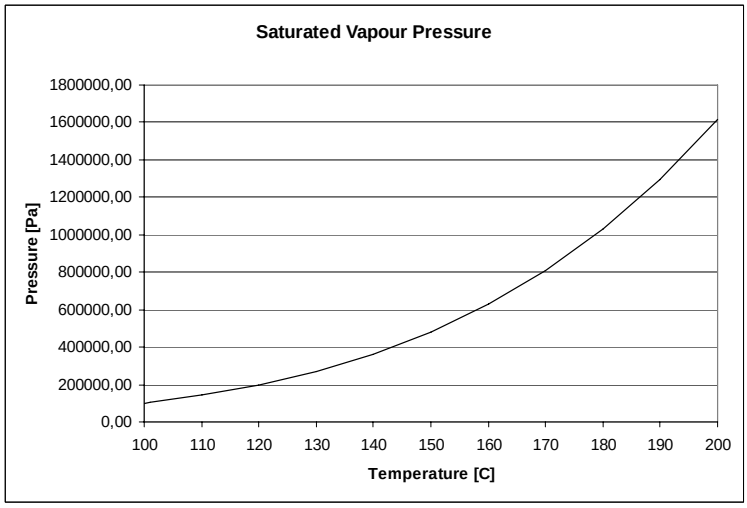

Fig 5.15 estimated saturated vapour pressure curve [VI,VII]

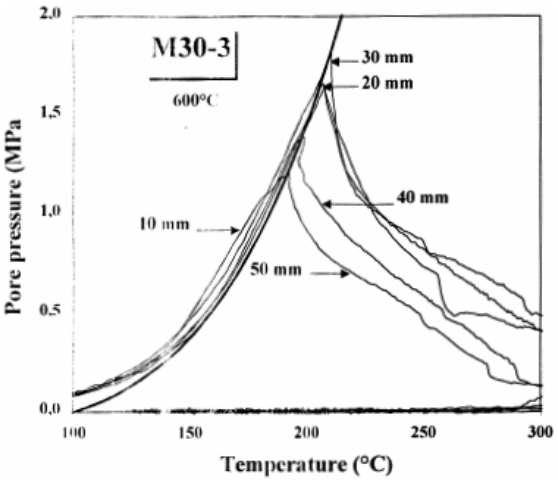

Fig. 5.16 experimental measurement of pressure in the cross section of concrete during heating [27]

5.5.2. General idea

The general idea behind this part of the analytical model is the one dimensional numerical calculation of the evaporation of water, the flow of water vapour and the build up of a saturated layer. These three aspects are in fact three different processes. In figure 5.17 the general idea of the analytical model is depicted.

The cross section of the concrete is divided into elements which are indicated, at the front of an element, with an 'n' placed inside a light blue circle. The three processes are depicted with the respectively the green, white and red circle. Furthermore, the analytical model has 5 different zones. From the surface to the interior of the concrete these zones are: the dry or dehydrated zone, the drying or dehydrating zone, the saturated zone, the accumulation of water zone and the initial state zone. These zones in the cross section of the concrete all have there specific contribution to the above described three processes.

In case a cross section of concrete is subjected to a fire, the surface temperature will increase. Due to the thermal diffusitivity of the concrete, the heat penetrates the concrete and everywhere the temperature reaches 100 ^{o}C water is evaporated into water vapour. This part of the process takes place in the second zone, the drying or dehydrating zone. In case all the water is evaporated out of the pores of the concrete, this part of the concrete than becomes part of the dry or dehydrated zone. The water vapour flows towards the interior of the concrete and when the conditions are met, the water vapour condensates back to water and is reabsorbed into the pores of the concrete. This part of the process takes place in the accumulation of water zone. In case all the pores of the concrete are filled with water, this part of the concrete than becomes part of the saturated zone. The water vapour flow then has to flow past the saturated zone deeper into the interior of the concrete and there, behind the saturated zone, a new accumulation of water zone starts. This means that the thickness of the saturated zone increases from behind.

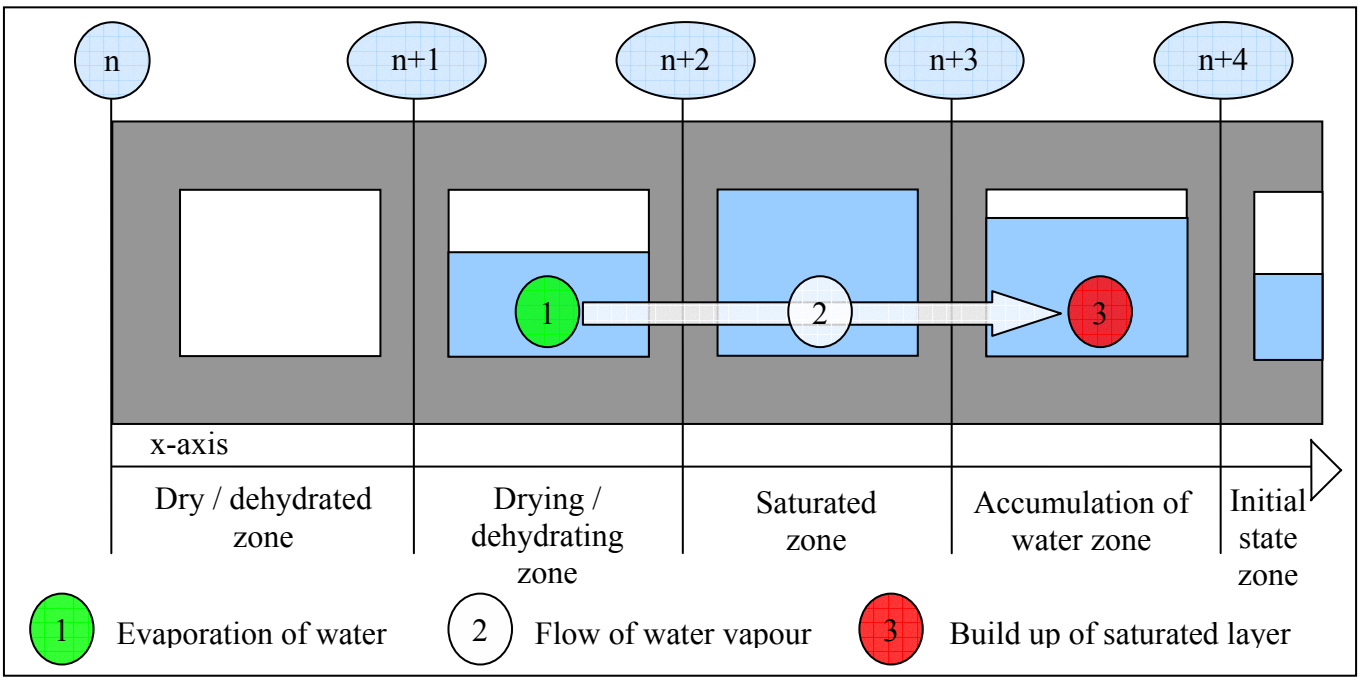

Fig. 5.17 General idea for the calculation of water vapour transport and the build up of a saturated layer

The front of the saturated zone only shifts backwards when the 100 ^{o}C front reaches it and starts to evaporate water. Behind the accumulation of water zone the initial state zone is situated. This zone is still not affected by the water vapour transport.

In figure 5.18 the general idea for this part of the analytical model is transferred to a schematic representation of the basis of a model. The three main processes from figure 5.17 are again indicated as main parts and subdivided into intermediate steps which are given a number to indicate the correct order. Also the input needed in this part of the analytical model is indicated in the top right corner. The input for this part of the analytical model is the result from the temperature distribution calculation. This calculation provides the distribution of the temperature over the cross section at different points and at different time steps. Furthermore, the cross section of the concrete was divided into elements. From every element at every time step the temperature at the middle of the element is known. This result can be used as input in this part of the analytical model. For the calculation of the water vapour transport and the build up of a saturated layer the same number and division of elements is used as for the calculation of the temperature distribution.

The first part is the evaporation of water. This part starts with the check if the temperature at the front of an element reaches a temperature of 100 ^{o}C. (start). To obtain this information, the temperature at the middle of an element is shifted to the left and thus the front of an element. This gives a good enough approximation of the temperature at the front of an element. In case the check is fulfilled and the temperature at the front of an element actually reaches 100 ^{o}C, this part then calculates the heat input from the fire into this concrete element (step 1 and 2). This is done by using the specific heat property of the concrete and the temperature increase at the front of this element during a single time step. Furthermore, the latent heat of vaporisation is used to calculate the amount of heat needed to evaporate all the water in the pores of this concrete element (step 3). These both heat calculations together give an estimate for the time needed to evaporate all the water in the pores of this concrete element (step 4).

The second part deals with the flow of water vapour. The general theory about the process which causes spalling indicates that the water vapour can flow, under influence of a pressure difference, onto the surface and into the cross section. However, the flow of water vapour in this part of the analytical model is assumed to be into the cross section of concrete. This assumption is made for two reasons. First of all, the flow of water vapour is governed by Darcy's law, which is depicted in equation 5.23 [23,43]. Darcy's law holds for the flow of water vapour into the cross section, because it incorporates the flow of a gas due to a pressure difference and the influence of the temperature can be neglected. Furthermore, the speed with which the water vapour flows is relative slow and therefore can be characterized as laminar. The flow of water vapour onto the surface of the cross section is however besides the pressure difference also influenced by the temperature difference which is due to the rapidly increasing temperature towards the surface. The high pressure difference close to the surface of the concrete causes Darcy's law to predict very high flow speeds of water vapour towards this surface which is due to the neglected influence of the increasing temperature. This behaviour therefore causes the saturated layer not to develop in the model. Furthermore, the general described theory of the process which causes spalling also states that in time, due to the progressing 100 ^{o}C front the water

vapour increasingly starts to flow towards the interior of the cross section. With the progressing 100 °C front the pressure gradient towards the surface of the cross section decreases, because the distance to the surface of the cross section increases. Furthermore, the temperature towards the surface of the cross section increases in time and therefore increasingly hinders the flow of water vapour. Therefore the assumption is made that the water vapour flows only into the cross section of concrete. First the speed with which the water vapour flows into the cooler interior of the concrete is calculated (step 5). This is calculated with Darcy's law and the pressure difference is estimated using the saturated vapour pressure at the location of evaporation and the atmospheric pressure at the interior of the concrete. The saturated vapour pressure is used in this part of the analytical model to predict the pore pressure at the location of evaporation. The actual pore pressure is determined by a mixture of water and water vapour. However, due to the confinement of the pores it is assumed that the saturated vapour pressure curve can be used to estimate the pore pressure. In figure 5.16 a graph is depicted which shows experimental measurements of the pressure inside the cross section of concrete during heating. The pressure development follows the saturated vapour pressure curve. Furthermore, flow of water vapour is also determined by the coefficient of permeability of the concrete and the dynamic viscosity of the water vapour.

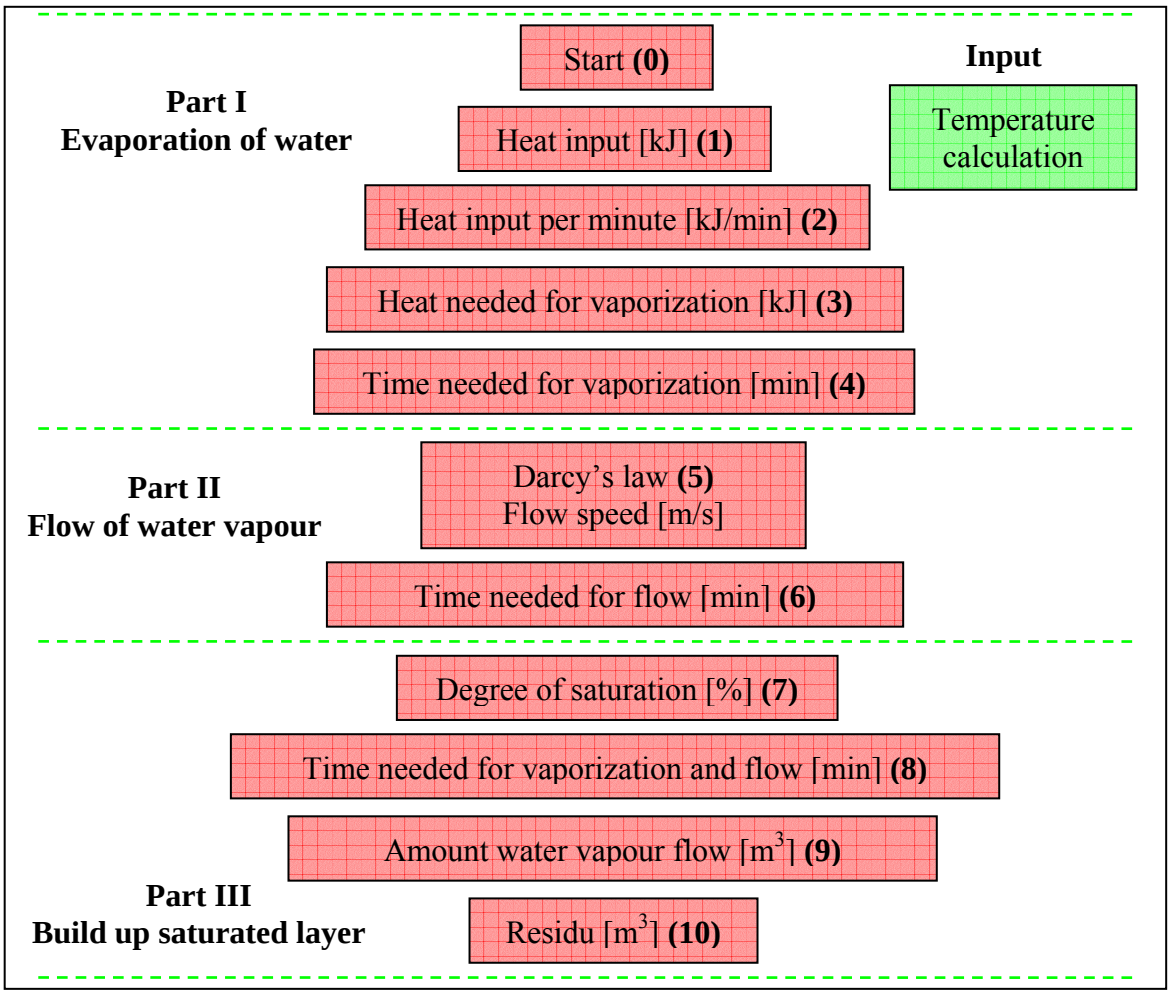

Fig 5.18 Basic parts and intermediate steps for the calculation of the water vapour transport and the build up of a saturated layer

The flow speed of the water vapour is then used to calculate the time that is needed for the water vapour to flow to the destination in the interior of the concrete (step 6).

$$\text{Darcy's law} \Rightarrow v = \frac{\kappa}{\mu}\frac{dP}{dl} \tag{5.23}$$

With
v = flow speed of the fluid [m/s]
κ = coefficient of permeability [m^2]
μ = dynamic viscosity of the fluid [kg/ms]
P = pressure [Pa]
l = length [m]

Finally, the third part deals with the build up of a saturated layer. First this part calculates the level of saturation in the elements behind the evaporating element, which can be obtained from the porosity of the concrete and the initial water content combined with the already transported water vapour to this element (step 7). This is then used to predict the amount of water which can be added to these elements in the next time step. This calculated amount combined with the time needed for the evaporating element to evaporate this amount of water and the time needed for the water vapour to flow to this destination is compared with the available time in this time step (step 8). This then leads to the amount of water vapour which actually flows to the next elements (step 9) and the residue of water vapour in the pores of the evaporating element (step 10).

The saturated layer develops, because an accumulation of water over multiple elements is developing. The general idea is that when an element is fully saturated, then the water vapour has to flow to the next element behind this saturated element. This means that the thickness of the saturated layer increases from behind. The front of the saturated layer only moves backward when the temperature on the front of the first element reaches a temperature 100 ^{o}C.

5.5.3. Assumptions

In this part of the analytical model the following assumptions are made:

1. The evaporation of water from the pores of the concrete starts at a temperature of 100 ^{o}C. Before this temperature is reached the water in the pores of the concrete remains in these pores and does not undergo a phase change.
2. The results from the temperature calculation are used as input in this part of the model. The total amount of heat the fire generates and penetrates the concrete is used for the evaporation of the evaporable water in the pores of the concrete.
3. The water vapour is considered an ideal gas. This means that the water vapour behaves according to the ideal gas law. This means that the saturated vapour pressure curve and the specific enthalpy of evaporation can be used. Furthermore, water is assumed to incompressible.
4. During evaporation of water at elevated temperatures, the pressure inside the pores increases. It is assumed that, due to the confinement of the pores, the pressure can be characterized with the saturated vapour pressure.
5. The evaporable water which is generated during the decomposition process of the concrete is not taken into account. The evaporable water used in this

calculation is the evaporable water which is present in the pores of the concrete under normal conditions.
6. For the calculation of the flow of water vapour Darcy's law is assumed. This means that the flow is assumed to be viscous and slow and the flow is therefore characterized as laminar.
7. For the development of a saturated layer, the flow of the water vapour is assumed to be into the cross section of concrete.
8. The pore structure of the concrete is assumed to homogenous.
9. It is assumed that the contribution of the air, inside the pores of the concrete to the pressure development, can be neglected.
10. In the pores of the concrete only water is present. This means that it is assumed that during one time step the amount of water that is evaporated also flows to the correct destination in the interior of the concrete.
11. The remaining empty pores of the concrete can be fully filled with water to form a saturated state. It is assumed that the space the air inside the pores occupies can be neglected.
12. The thickness of the saturated layer increases from behind. In reality the pressure difference levels the water vapour of and therefore the water in the accumulation of water zone is also levelled off to the interior of the concrete. This means that the complete accumulation layer shifts into the concrete. In this analytical model the assumption is made that the water vapour flows towards the accumulation layer. In case a part of this layer is already saturated, than the water vapour fills the pores behind this saturated part. The front of the saturated layer only shifts backwards when the 100 ^{o}C front reaches it.
13. The influence of reinforcement on the water vapour transport is not taken into account.

5.5.4. Numerical solution for flow to the next element

The above mentioned description is the general idea and this is transformed into a flow chard which gives a schematic representation and a complete overview in detail of the process of the evaporation of water, the transport of water vapour and the build up of a saturated layer in every time step for every element. On this flow yard, which is depicted in figure 5.19, the same intermediate steps as mentioned in figure 5.18 are indicated by red rectangles and given a number, indicating the order in which they are used. The results from the temperature analysis and thus the input for the numerical calculation are indicated by green rectangles. The additional steps are indicated by white rectangles. The material properties used in the model are put in ellipse and given a colour. The colour grey indicates a concrete material property and the colour light blue indicates a property of water or water vapour. The arrows indicate the connection between the different major steps and the additional steps used. Furthermore, in this flow chard only the water vapour flow to the next element is indicated. This has been done to give a general and complete overview of this part of the analytical model, which calculates the water vapour transport and the development of a saturated layer, in one flow chard.

The general idea and the most important parameters which are depicted in figure 5.19 were already elaborated in the paragraph which deals with the description of the general idea. Therefore, only the numerical implementation is elaborated here. The flow chard depicted in figure 5.19 is numerically implemented and calculated by using Microsoft Office Excel^{tm}. The most important part of this numerical

implementation is the division of the cross section into elements and the needed information of each of these elements to implement the flow chard of figure 5.19. Each element is described by six parameters:

1. Number of element => the number of the element indicates the position of the front of the element in the cross section of the concrete and is indicated by $E_{n,k}$. The subscript 'n' stands for the element number and the subscript 'k' stands for the time step.
2. Temperature at the front of the element at each time step => this temperature is obtained from the result of the temperature distribution calculation and is indicated by $T_{n,k}$.
3. The amount of original water => this is the amount of water which is present in the pores of the concrete in its initial state and is the same for every element.
4. The residue of water => this amount is numerically used in different ways. In case the water vapour, from an evaporating element, flows to the next element, then this amount of water is placed in the next element is this parameter. In case an element is evaporating, then the next time step the remaining amount of water is placed in this parameter.
5. Total amount of water => this is the summation of the water that is present in each element at every time step. Normally, this is the summation of the amount of original water and the residue of water. In case an element is evaporating, then the next time step the original amount of water is no longer added to the total amount of water.
6. The amount of pores => this is calculated by using the porosity of the concrete and is used to determine the amount of water that can be added to the pores of the element to become fully saturated.

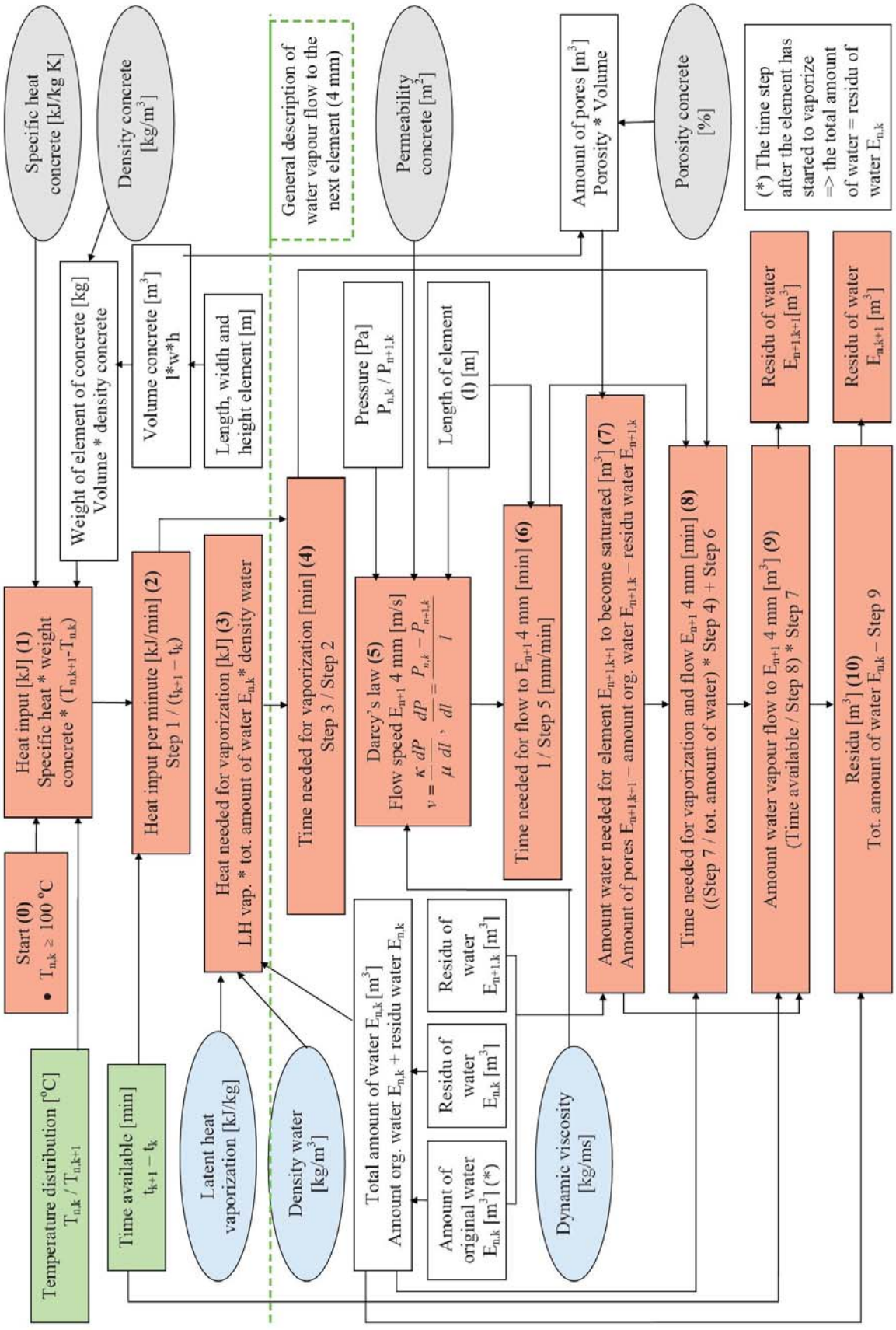

Fig 5.19 Flow chard which describes the third part of the analytical model

5.5.5. Numerical solution for the flow to multiple elements

The previous flow chard (figure 5.19) describes the intermediate steps needed for the general case of water vapour flow to the next element. However, usually multiple elements are evaporating and behind these elements an accumulation of water over multiple elements is developing. The analytical model therefore allows for water vapour to flow not only to the next element, but also the elements situated father away. Furthermore, the analytical model increases the thickness of the saturated layer from behind. In the analytical multiple scenarios are present for flow of water vapour:

- In case an element is evaporating, the water vapour first flows towards the next element into the interior of the concrete and partly fills this.
- In case an element is evaporating and due to the flow of water vapour the next element becomes saturated, than the water vapour also flows to the next element, situated behind this saturated element. This only happens when enough time is present in this particular time step.
- In case the next element is saturated, than the water vapour flows directly to the next element situated behind this saturated element and partly fills this.
- This process continues over as many layers a possible in each time step.
- In case two or more elements are evaporating at the same time, the element which started to evaporate the earliest also fills the element situated the closest, which are not evaporating. This ensures that the dry of dehydrated front follows the elements in a logical order, from the surface towards the interior.

In the flow chard 5.20 the water vapour flow towards the interior of the concrete and to multiple elements is depicted. This flow chard starts at step 4, ‘the time needed for vaporization’. In the previous flow chard, 5.19, this is indicated by the green-dashed line. On this flow chard the same colour and shape indication is used as in the previous flow chard.

5.5.6. Material properties used in the analytical model

The grade of the concrete used in the numerical simulation is B35 (C28/35). The material properties of this type of concrete, which are used in the analytical model, are depicted in table 5.4. In the last column of this table the indication is given which of the material properties that are used are temperature dependent. The material properties indicated by (*) are graphically depicted in the Appendix B.

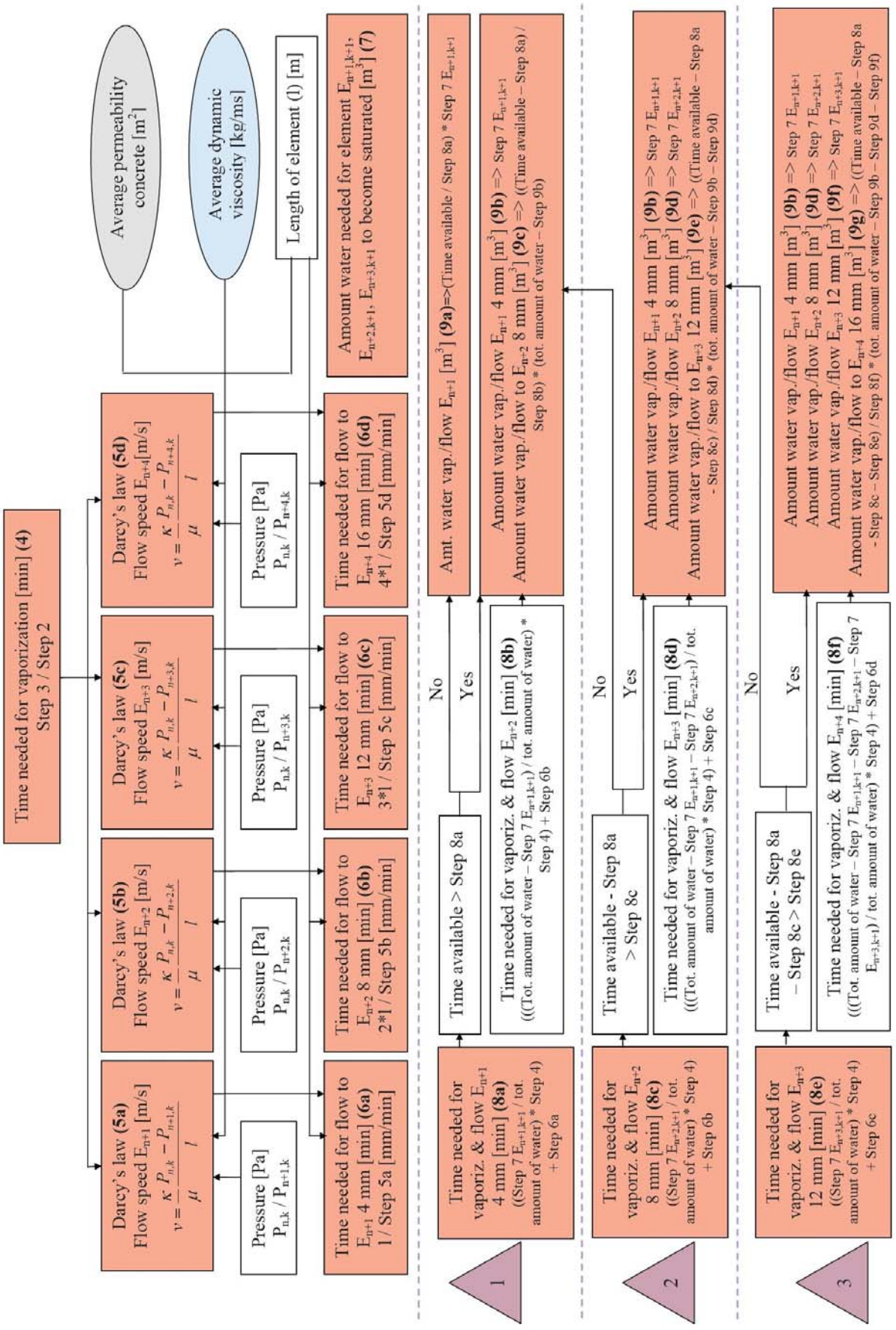

Fig 5.20 Flow chard which further elaborates the third part of the analytical model

Material property		Temp. dependent
Concrete grade	B35 (C28/35)	
Thickness	400 mm	
Width	1000 mm	
Height	1000 mm	
Number of elements	100	
Stability criterion $a_c * \frac{\Delta t}{(\Delta x)^2} \leq 1/2$	$\Delta t = 0{,}36\,\text{min}$, $\Delta x = 4mm$	
Density of water	1000 kg/m^3	No
Density of concrete	2400 kg/m^3	No
Specific heat of concrete [kJ/kg K] [50]	c_c = 0,8+0,001*(T-20) (*)	Yes
Latent heat of vaporization [kJ/kg] [X]	(*)	Yes
Dynamic viscosity [kg/ms] [50]	$\mu = 1{,}0*10^{-5}+3{,}4*10^{-8}*(T-38{,}72)$ (*)	Yes
Permeability of concrete [m^2] [50]	$\kappa = 7{,}0*10^{-17}*10^{(0{,}0046*T)}$ (*)	Yes
Porosity of concrete [%] [50]	n = (0,142+0,0001*(T-20))*100 (*)	Yes
Initial temperature	20 ^{o}C	
Initial degree of saturation	63 %	

Table 5.4 material properties used in the analytical model

5.5.7. Numerical example for the calculation of the transport of water vapour

In the previous paragraphs the theory and the numerical simulation for the evaporation of water, the transport of water vapour and the development of a saturated layer was elaborated. To further clarify the numerical simulation an example is depicted in figure 5.21 which describes the transport of water vapour into the interior of the concrete. Furthermore the build up of a saturated layer is also depicted. The figure consists out of 6 rows with in between 3 tables. The rows indicate the elements into the interior of the concrete. The blue colour indicates the amount of water which is present in that element, the degree of saturation. Every element is indicated by the circle at the front of the element. These circles have the same colours as used in the explanation of the general idea behind the model, in figure 5.17. The green circles indicate the elements which are evaporating and the red circles the elements in which the water accumulates, which are the destination elements. The white arrows indicate the flow of water vapour, from the evaporating elements to the destination elements. The tables in between the rows indicate the amount of water vapour which flows to the corresponding element.

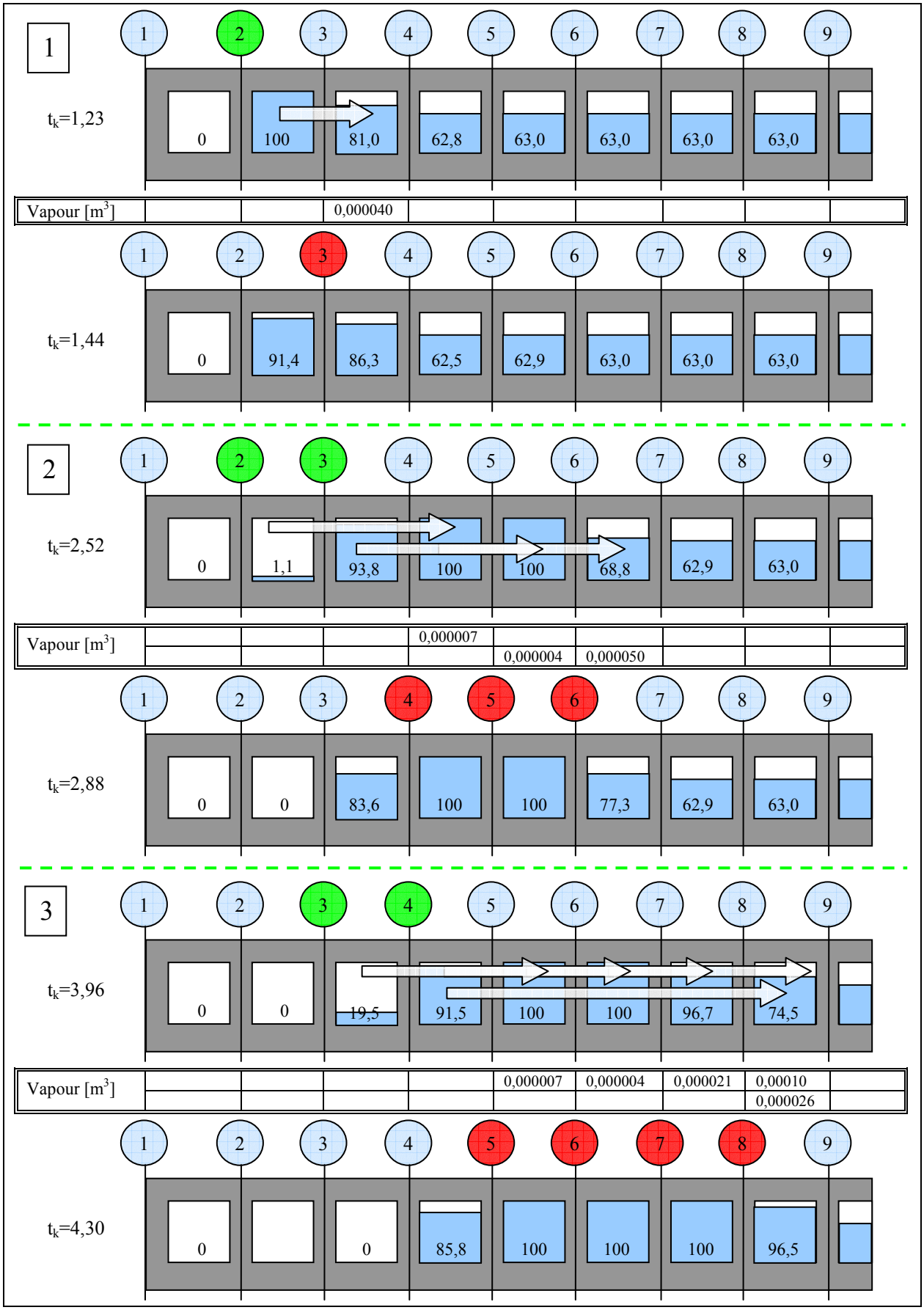

Fig 5.21 numerical example of the evaporation of water, the transport of water vapour and the development of a saturated layer

The first time step is from 1,23 minutes until 1,44 minutes. The second element is evaporating and the water vapour flows to the third element. The second time step is from 2,52 minutes until 2,88 minutes and the second and third elements are evaporating. The water vapour flows to respectively the fourth element and the fifth and sixth elements. Also it can be seen that the first two elements are dehydrated and that the fourth and fifth elements are completely saturated. The last time step is from 3,96 minutes until 4,30 minutes. The third and fourth elements are evaporating and the water vapour flows to respectively the fifth, sixth, seventh and eighth elements. This is the last time step before the first saturated layer is formed. This saturated layer can be seen as the fifth, sixth and seventh elements which are completely saturated.

5.5.8. Results and analysis

In figure 5.22 the saturation distribution for the development of the first saturated layer is depicted. After 1 minute the element with the front at 4 mm becomes completely saturated. However at 1,23 minutes the front of this element reaches 100 ^{o}C and therefore the evaporation of this layer starts. In figure 5.22 this can be seen by the drop in the saturation at 4 mm between 1,23 minutes and 2,13 minutes. At this last time step two elements become 100% saturated. The front of this accumulation layer lies at 8 mm and has a thickness of 8 mm. However, at 2,13 minutes also the front of this element reaches a temperature of 100 ^{o}C and the evaporation process starts. At the time step 2,88 minutes the first two elements are completely dehydrated, this means that the drying zone has moved until 8 mm. The front of the accumulation layer has shifted to 12 mm and is still 2 elements or 8 mm thick. This process continues and after 4,30 minutes the first 3 elements or 12 mm is dehydrated. The front of the accumulation layer is at 16 mm and the thickness of the layer is 12 mm. This is the first saturated layer, which will be explained in the next paragraph.

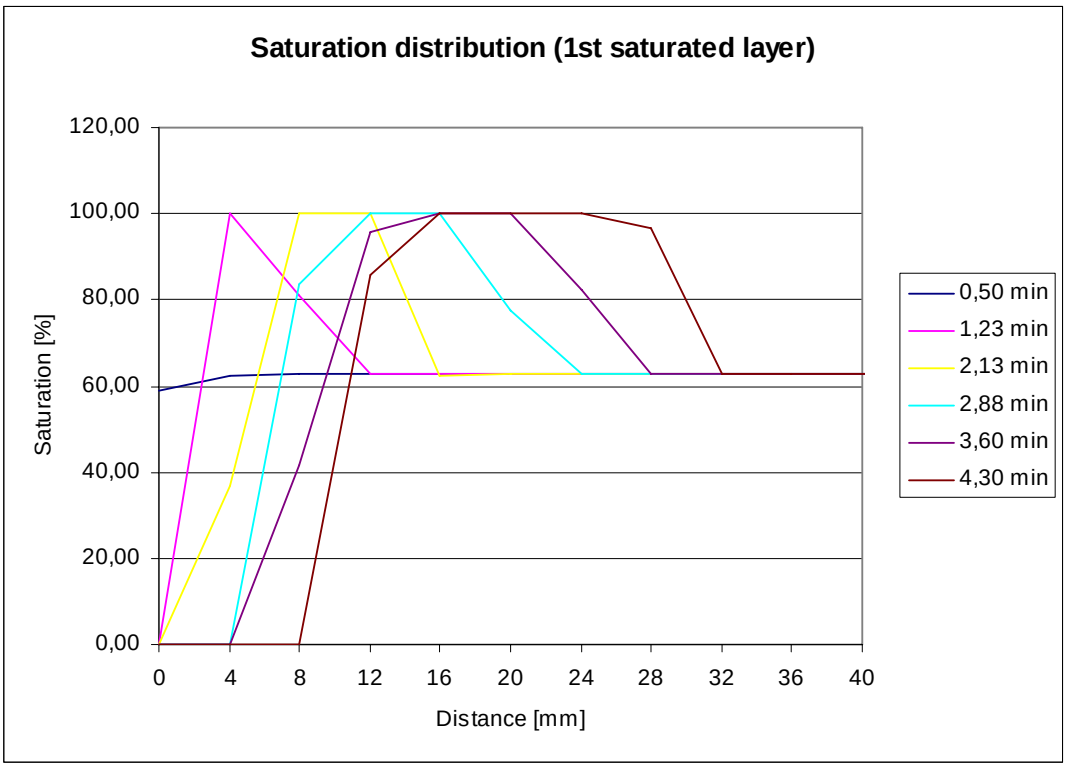

Fig 5.22 Saturation distribution for the development of the first saturated layer

The speed of the evaporation process gradually decreases. This can be observed when looking at the elements at 4mm and 8 mm. The element with the front at 4 mm, which is 100 % saturated, starts to evaporate at 1,23 minutes and is dehydrated at 2,53 minutes. This is an average rate of evaporation of 0,00047 m^3/min. However, the element with the front at 8 mm, which is also 100 % saturated, starts to evaporate at 2,13 minutes and is dehydrated at 4,26 minutes. This is an average rate of evaporation of 0,00029 m^3/min.

In figure 5.23 the saturation distribution for the development of the second saturated layer is depicted. The front of the element behind the saturated layer, at 28 mm, reaches a temperature of 100 ^oC at 8,49 minutes and evaporation of that element starts. With the build up of the first saturated layer the rate of the evaporation process gradually decreases. In the build up for the second saturated layer this process continues and further decreases. In the elements with the front at respectively 28 mm and 32 mm the evaporation process takes increasing more time. The element with the front at 28 mm, which is almost completely saturated (92%), starts evaporating at 8,49 minutes and at 14,54 minutes the element is practically dehydrated (1%). This is an average rate of evaporation of 0,000088 m^3/min. The element with the front at 32 mm, which is not completely saturated (85%), starts to evaporate at 10,27 minutes and at 14,54 minutes the element is still dehydrated (39 %). This means an average rate of evaporation of.0,000063 m^3/min. The first element that reaches a state of complete saturation is the element with the front at 36 mm at 11,88 minutes. At 12,29 minutes the front of this element reaches a temperature of 100 ^oC and the evaporation of this element starts. At 13,32 minutes the next element, the element with the front at 40 mm, becomes completely saturated and at 14,54 minutes the next element, at 44 mm, also becomes completely saturated. This is the first time since the build up of the second saturated layer that there is an accumulation layer of two elements and a thickness of 8 mm. This is the second saturated layer.

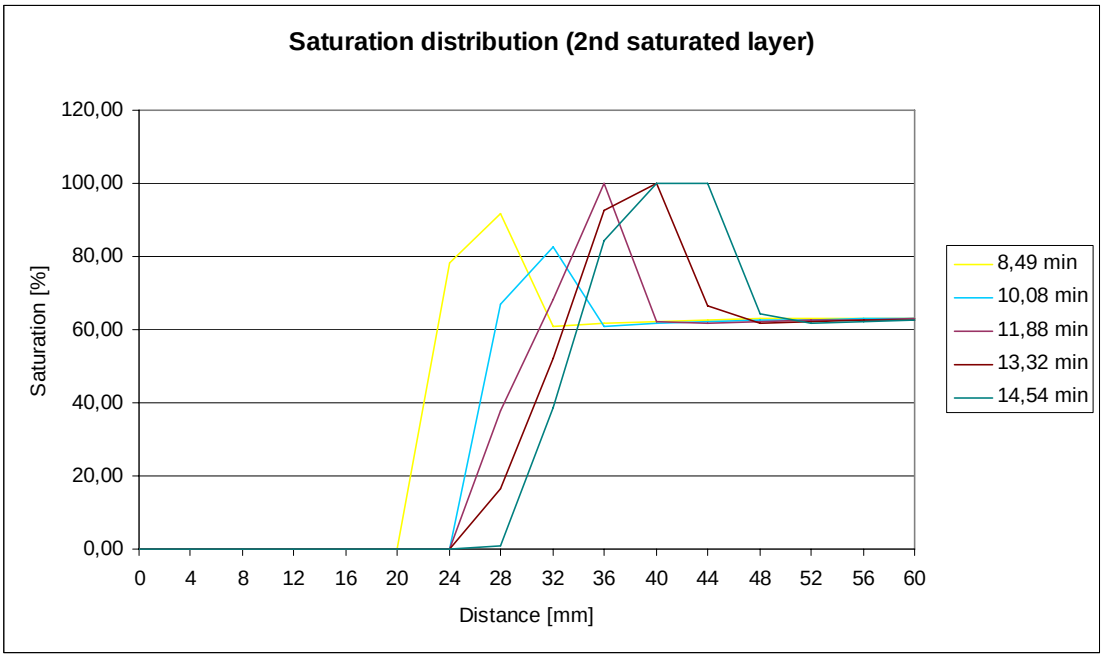

Fig 5.23 Saturation distribution for the development of the second saturated layer

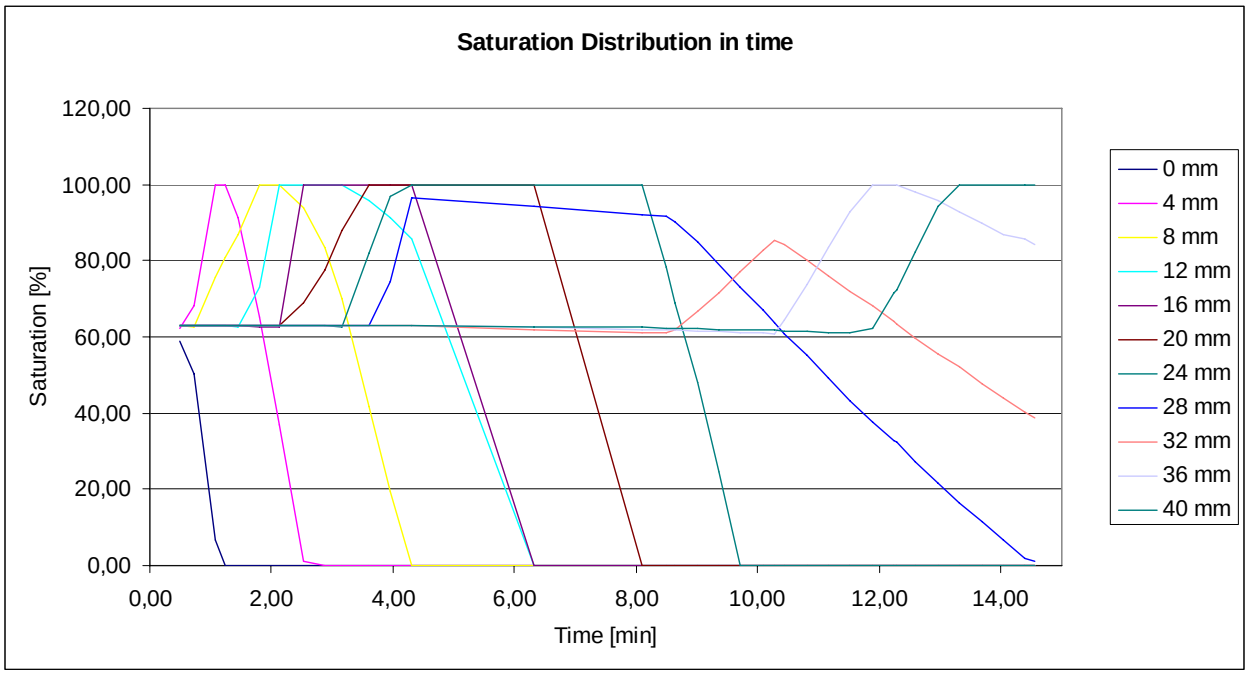

Fig 5.24 Saturation distribution of different points in time

In figure 5.24 the saturation distribution of different points in time is depicted. The points that are depicted are the front of an element. All the points have an initial state of saturation of 63 percent. Then most of the points first increase in saturation until a state of complete saturation and than decrease in saturation until zero. The water vapour flow into the interior of the concrete causes the state of saturation of the points to increase from close to the surface to deeper into the concrete. The decrease in state of saturation of the elements is caused by the evaporation of water from the elements. Furthermore, the gradient of decreasing part of the line of saturation is steeper at the front of the cross section of concrete than deeper into the cross section. The lines of saturation of 4 mm, 8 mm and 12 mm are almost parallel. The lines of saturation of 16 mm, 20 mm and 24 mm are also almost parallel but steeper than the previous lines. These points are however the front of the elements which make up the first saturated layer. The gradient of the lines of saturation of 28 mm, 32 mm and 36 mm are much less steep and are decreasing into the cross section.

The saturation distribution shows that in the early stages of the fire the saturation distribution rapidly progresses through the concrete. This is caused by the rapid heat penetration which causes a large temperature gradient and this leads to a large rate of evaporation and the evaporation of large amounts of water. Furthermore, this temperature gradient also leads to a large pressure differences which causes the rapid movement of water vapour into the interior of the concrete. This process leads to the development of the first saturated layer. However, after 5 minutes the rate at which the heat penetrates the concrete reduces and therefore the temperature gradient gradually decreases. This causes the rate at which the water is evaporated to become smaller and the pressure difference to decrease. This causes the forming of a second saturated layer to take longer and the thickness of this layer to be less then the first layer. The rate at which the heat penetrates the concrete is therefore one of the main factors influencing the process of spalling. In general it can be stated that high heating rates cause a large temperature gradient to be present in the heated layer. This causes high rates of evaporation of water and also a large pressure difference to be present

between the position where the water is evaporated and the interior of the concrete. This pressure gradient causes a high speed at which the water vapour is transported and therefore the saturated layer takes less time to develop and is possibly of greater thickness and therefore the possibility of spalling increases.

The rapid progression of the saturation distribution is also caused by the speed with which the water vapour flows into the interior of the concrete. This is determined from the rate of heat penetration and the permeability of the concrete. The permeability determines the ease with which the water vapour can flow through the concrete. In the early stages of the fire the accumulation of water is still in the beginning of being developed. When the accumulation layer starts to develop, the permeability becomes increasingly important, because the distance the water vapour has to flow increases and the pressure gradient, the driving force behind the flow of water vapour, becomes smaller. Furthermore, when after around 5 minutes the rate of heat penetration reduces and thus the temperature gradient, the importance of the permeability further increases. The pressure difference reduces and the permeability determines more the flow of the water vapour. The permeability of the concrete is therefore one of the main factors influencing the process of spalling. In general it can be stated that low permeability causes the water vapour to flow at lower speed and the saturated layer takes less time to develop and the thickness is reduced and therefore the possibility of spalling increases.

The progression of the saturation profiles is also influenced by the porosity of the concrete, which is a material property. The porosity is the material property which determines the total amount of pores which is present in the concrete. This is than coupled with the initial amount of moisture and the already transport amount of water vapour to determine the total amount of free pores, which is a measure for the free spaces in the concrete which can be filled with water until it forms a saturated layer.
The initial moisture content is the material property which indicates the amount of water which is present in the pores of the concrete. In general it can be stated that when the initial moisture content increases or the porosity decreases, the initial degree of saturation increases. This means than the less pores are empty and therefore the saturated layer is developed in a shorter period of time and therefore the possibility of spalling increases.

In figure 5.25 a general overview of the most important distributions is given: the progress of the 100 ^{o}C front, the progress of the saturation front and the saturation rear and the progress of the drying front. The saturation front and saturation rear indicate the thickness of the saturation layer, which consist out of the elements which are fully saturated, but a saturated layer is not yet formed. The 100 ^{o}C front gradually penetrates the cross section. In the first few minutes the speed of 100 ^{o}C front is higher and with time the speed gradually decreases. The saturation front and the saturation rear penetrate the cross section before the 100 ^{o}C front, but in the first few minutes the speed of both distributions is higher than that of the 100 ^{o}C front. After around 2 minutes the thickness of the saturated layer has become 8 mm. The thickness further increases until it has become 12 mm after 4,30 minutes. This is the first saturated layer and is indicated by the straight line of the saturation front. The front of the saturation does not penetrate further. The thickness of the saturated layer gradually decreases until after almost 10 minutes the layer is completely evaporated.

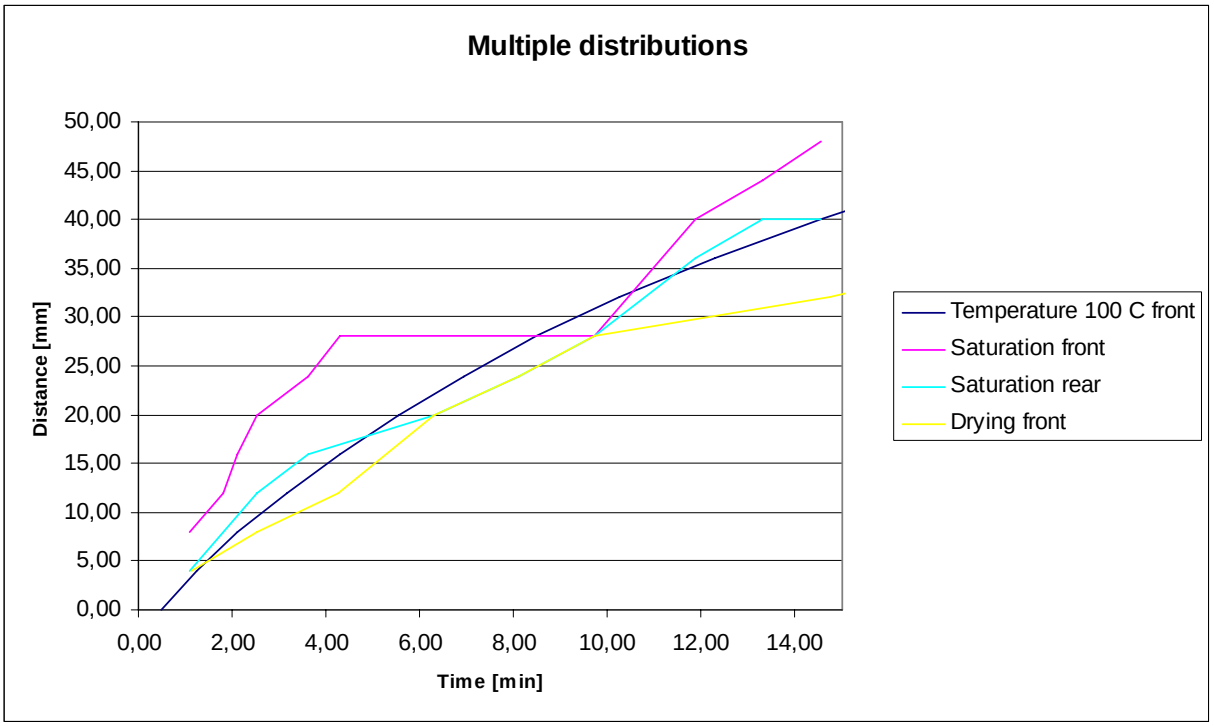

Fig 5.25 Comparison 100 °C front, saturation and drying distribution

Than the saturation front starts to penetrate the cross section again, but the speed at which this happens has decreased. The drying front penetrates the cross section behind the 100 °C front and at the lowest speed. After 4,26 minutes the front of the drying zone is at 12 mm and after 9,74 minutes the front of the drying zone is at 28 mm, which is behind the saturated layer.

5.6. Fourth part: check saturated layer and build up of pore pressure

5.6.1. Theory

In the chapter 4, which deals with the explanation of the process which causes spalling, it was explained that the saturated layer impedes further transport of water vapour into the interior of the concrete. Therefore, the water vapour changes direction and starts to flow, due to a pressure difference, in the direction of the surface of the concrete. However, during this flow the temperature of the water vapour increases rapidly and due to restrained expansion the water vapour flow is hindered. This is the main difference with the previous paragraph, which deals with the water vapour flow into the interior of the concrete and leads to the development of a saturated layer. The flow of water vapour into the cooler interior of the concrete is calculated by Darcy's law. However, this law calculates flow of liquid or gas due to a pressure difference. The effect of the increase in temperature and due to restrained expansion the reduction in flow speed is not covered by this law. In the literature only few basic laws are found which take into account the effects of an increase in temperature and due to the restrained expansion the hindering in flow of the liquid or gas. Further more, the law which can be used in this analytical model must clearly include the most important aspects of this type of water vapour flow and be transparent. Therefore, in this part of the analytical model the flow parameter approach developed by Kodres is chosen, which fulfils the above described requirements [31].

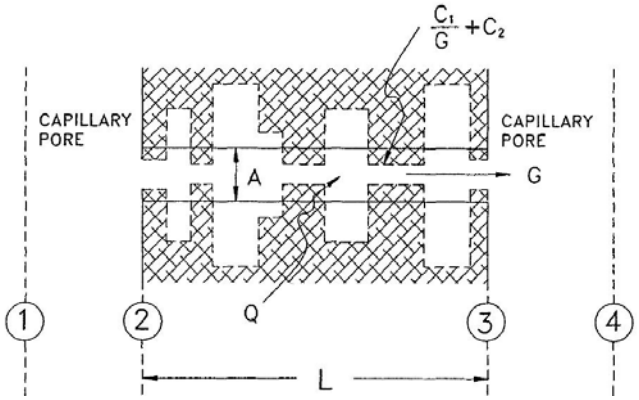

Fig 5.26 basis of the gas flow model developed by Kodres [31]

The flow parameter approach is developed by Kodres and the basis for the derivation of this model is a finite segment of a single passageway through a heated slab of concrete, which is depicted in figure 5.26. Through this passage a gas flows which is caused by a difference in pressure between the two ends of the segment. During the flow the gas is heated. The ends of this segment are each formed by the relatively larger pores of the concrete, although the length of this segment is such that it contains many larger pores and many smaller pores. Thus, the gas velocities at the ends of the segment are negligible compared with the average velocity through the segment.

In the model the following assumptions are made [31]:

1. Energy and mass transport are one-dimensional
2. Steady state exists
3. All gases are ideal
4. The porous structure of the concrete is homogenous

The model is based upon four different equations. The first equation describes the continuity of a segment and is depicted in equation 5.24 [31].

$$\frac{\dot{m}}{A} = \rho * v = G \tag{5.24}$$

With $\dot{m}$ = mass flow rate of gases through the passage [kg/s]
A = effective cross sectional area of the passage [m^2]
ρ = the density of the gases [kg/m^3]
v = the velocity of the gases [m/s]
G = the mass flux of the gas [kg/m^2s]

The second equation conserves the momentum of a one-dimensional steady flow of gases and is depicted in equation 5.25 [31].

$$dP + \rho * v * dv + C_f * \frac{\rho * v^2}{2} dx = 0 \tag{5.25}$$

With P = pressure [Pa]
C_f = coefficient which determines the amount of wall friction [-]

The third equation conserves the energy and is depicted in equation 5.26 [31].

$$dh + d\left(\frac{v^2}{2}\right) = dQ \tag{5.26}$$

With h = specific enthalpy of the gases [J/kg]
Q = heat transfer per unit mass between the gases and the concrete [J/kg]

The fourth equation is the ideal gas law, which was already depicted in equation 5.16

These four equations together form, after some mathematical steps, equation 5.27 which describes the mass flux through the concrete passages [31].

$$G = \frac{\sqrt{R*T_1}*\sqrt{\rho_2^2 - \rho_3^2 - f_1}}{\sqrt{\left(\frac{2*c_p - R}{c_p}\right)*\ln*\left(\frac{\rho_2}{\rho_3}\right) + C_f * L}} \tag{5.27}$$

With f_1 = the function f_1 contains the integrals in equation 5.27. These integrals are evaluated numerically which leads to

$$f_1 = \frac{2*\bar{Q}}{c_p * T_1}*\left(C_4 * \rho_2^2 + C_5 * \rho_3^2\right)$$

$\bar{Q}$ = total amount of heat transferred to the gases as they pass through the concrete [J]
C_4 / C_5 = constants which dependent on the integration scheme. In this case a trapezoidal integration scheme is applied which leads to C_4 = ¼, C_5 = ¾.[-]

The thus far obtained result can be further elaborated until equation 5.28 which relates the flow parameter with the friction coefficient, the difference in pressure and temperature. The unknowns in this equation are the flow parameter and the friction coefficient. Normally the temperature ratio T_1/T_3 is also unknown. However, because the temperature distribution is already calculated in the previous paragraph, use of these results can be made.

$$\psi = \frac{G*\sqrt{R*T_1}}{P_1} = \frac{\sqrt{C_6 - C_7*\left(\frac{P_1}{P_3}\right)^{-2}*\left(\frac{T_1}{T_3}\right)^2}}{\sqrt{\left(\frac{2*c_p - R}{c_p}\right)*\ln*\left[\left(\frac{P_1}{P_3}\right)*\left(\frac{T_1}{T_3}\right)^{-1}\right] + C_f * L}} \tag{5.28}$$

With C_6/C_7 = constants which are determined from the boundary conditions.

$$C_6 = 1 - 2*C_4*\left(\frac{T_{03}}{T_1} - 1\right),\ C_7 = 1 + 2*C_5*\left(\frac{T_{03}}{T_1} - 1\right)$$

c_p = specific heat at constant pressure [J/kgK]
T_{03} = stagnation temperature at location 3 [K]

In the paper which describes the above explained model, the friction coefficient is proposed to be the sum of a viscous and an inertial term [31]. The cross sectional dimensions and the viscosity terms of the Reynolds number N_{Re} are lumped into the coefficient C_1 and C_2. These coefficients are determined experimentally. In equation 5.29 this is depicted [31].

$$C_f = \frac{C_1^{''}}{N_{\mathrm{Re}}} + C_2 = \frac{C_1^{'}}{G} + C_2 \tag{5.29}$$

Furthermore, the flow parameter is to characterize the flow through the total cross section of the concrete rather than through a single passage. To account for this difference a constant C_3 is added to equation 5.28 [31]. This constant can be seen as the total porosity which is available for the water vapour to flow through.

$$G_{tot} = G * \left(\frac{A}{A_{tot}} \right) * \text{number of passages}$$

$$C_3 = \left(\frac{A}{A_{tot}} \right) * \text{number of passages}$$

With A = effective cross section of a single passage [m^2]
A_{tot} = total cross section of the concrete [m^2]

Finally, the desired equation is obtained and is depicted in equation 5.30 [31].

$$\psi = \frac{G_{tot} * \sqrt{R * T_1}}{P_1} = \frac{C_3 * \sqrt{C_6 - C_7 * \left(\frac{P_1}{P_3} \right)^{-2} * \left(\frac{T_1}{T_3} \right)^{2}}}{\sqrt{\left(\frac{2 * c_p - R}{c_p} \right) * \ln * \left[\left(\frac{P_1}{P_3} \right) * \left(\frac{T_1}{T_3} \right)^{-1} \right] + \left(\frac{C_1}{G_{tot}} + C_2 \right) * L}} \tag{5.30}$$

With ψ = flow parameter
G_{tot} = total mass flux of the gas [kg/m^2s]
T_1 / T_3 = temperature at respectively the front of the saturated layer and the surface of the concrete [K]
P_1 / P_3 = pressure at respectively the front of the saturated layer and the surface of the concrete [Pa]
C_3 = constant which describes the porosity of the cross section of concrete [-]
C_6 / C_7 = constants which are determined from the boundary conditions [-]
c_p = specific heat at constant pressure [J/kgK]
R = universal gas constant = 8,3145 J/mol K
C_1 / C_2 = constants which are determined experimentally and describe the amount of friction [-]
L = length of the passage between two large capillary pores and through which the gas flows [m]

The above depicted equation can be used to calculate the total mass flux (G_{tot}) when the pressure- and temperature difference and the constants are known. Most of the constants are known, however the constants C_6 and C_7 are still unknown. In the calculation of these constants the stagnation temperature T_{03} is present. The stagnation temperature is the temperature at which the pressure difference is insufficient to overcome the hinder the flow of the gas experiences due to the restrained expansion. This temperature is normally experimentally obtained. However, this temperature can also be approximated by using the theory on Rayleigh flow [52,53,VIII].

The Rayleigh flow is a model for the flow of heated gases through a pipe, from the upstream to the downstream location, under influence of a pressure difference. This theory is used to calculate the stagnation temperature T_{03}. In the equation set 5.31 the used equations are depicted. First the isentropic index γ is determined. From this the downstream Mach number is obtained. These both result are used to calculate the downstream stagnation temperature T_0. This result can be used to calculate the desired stagnation temperature at location 3, T_{03}.

Isentropic index $\Rightarrow \gamma = \frac{c_p}{c_v}, c_p - c_v = R$ [-]

Downstream mach number $\Rightarrow Ma = \frac{1}{\sqrt{\gamma}}$ [-]

Downstream stagnation temperature T_0 $\Rightarrow T_0 = T_1 * \left(1 + \frac{\gamma - 1}{2} * Ma^2\right)$ [K] (5.31)

Stagnation temperature at location 3 T_{03} $\Rightarrow T_{03} = -\left[-1 + \left(\frac{1 - \frac{1}{\gamma}}{1 + \frac{\gamma}{\gamma}}\right)^2\right] * T_0$ [K]

With c_p = specific heat of water vapour at constant pressure [J/kgK]
c_v = specific heat of water vapour at constant volume [J/kgK]

The flow of water vapour onto the surface of the concrete is calculated with equation 5.30. The build up of pore pressure, at the front of the saturated layer, is estimated by using the saturated vapour pressure. The saturated vapour pressure is present in the pores of the concrete and leads to a pore pressure which results in tensile stress in the concrete which lead to cracks and can eventually lead to spalling. The pore pressures can be converted to tensile stresses by using the theory of the hollow spherical model [26].

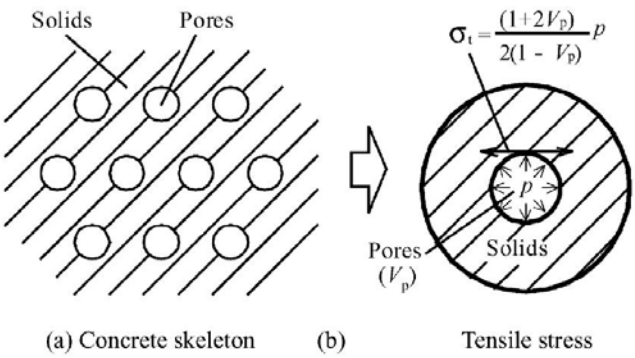

With σ_t = tensile stress [MPa]
V_p = pore volume [m^3]
p = pore pressure [MPa]

Fig 5.27 hollow spherical model for determination of the tensile stresses [26]

This theory uses the uniform pore pressure to calculate the elongation of the edge of the pore and the tensile stresses this causes. The tensile stresses are calculated with the formula depicted in figure 5.27 and act tangential to the edge of the pore resulting in radial cracks.

5.6.2. Saturated layer and build up of pore pressure: general idea

In the previous part of the analytical model the development of a saturated layer was calculated. The general idea in this part of the analytical model is first to check whether a saturated layer has developed and secondly the one dimensional numerical calculation of the evaporation of water from the saturated layer, the flow of water vapour onto the surface of the concrete and the build up of pore pressure at the front of the saturated layer. These four aspects are depicted in figure 5.28. The check is indicated by the purple triangle and the three processes are depicted with the respectively the green and white circle. The red circle indicates the surface of the concrete.

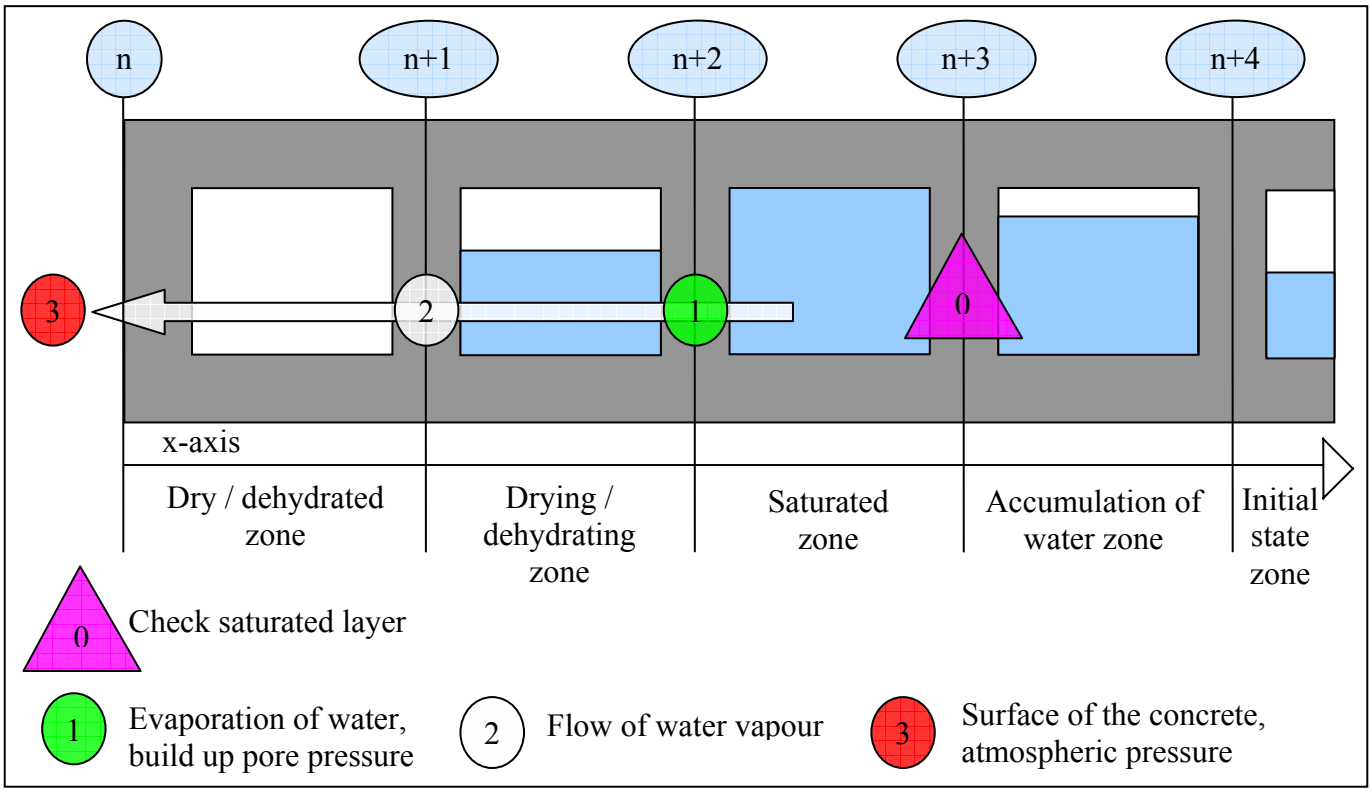

Fig. 5.28 general idea for the calculation of the build up of pore pressure

The build up of pore pressure can only start when the saturated layer has developed. This is the case when three criteria are met. The first criterion is that the zone must be in a fully saturated state. When the temperature on the front of this zone reaches a temperature of 100 ^{o}C, the second criterion, the water is evaporated into water vapour. In case the saturated zone is large enough, it impedes further water vapour flow into the interior of the concrete. This is simulated by the third criterion, which states that the speed at which the water vapour flows into the interior of the concrete is smaller than the speed at which the 100 ^{o}C front penetrates the concrete. In case the speed of the 100 ^{o}C front is higher, the condition for the water vapour to condensate back to water is never met.

When all three criteria are met, a saturated layer is formed which is large enough to impede further transport of water vapour into the interior of the cross section. The saturated layer impedes further water vapour transport and therefore the water vapour flows towards the surface of the concrete. In the direction of the surface of the concrete the temperature rapidly increases which causes the temperature of the water vapour to increase. Due to restrained expansion of the water vapour the flow of water vapour is hindered. The amount of water that is evaporated into water vapour, at the front of the saturated layer, can not be fully transported away from this saturated layer. This leads to the build up of a pore pressure at the front of the saturated layer. This process continues until the pressure difference is sufficient to 'push' enough water vapour through the concrete onto the surface of the concrete to ease the build up of pore pressure.

In figure 5.29 the general idea for this part of the analytical model is transferred to the basis of a model. The three main processes from figure 5.28 are again indicated as main parts and subdivided into intermediate steps which are given a number to indicate the correct order. Also the input needed in this part of the analytical model is indicated in the top right corner. The input for this part of the analytical model is the same as for the previous part of the analytical model, the temperature distribution calculation. This means that, for the calculation of the build up of pore pressure, also the same number and division of elements is used as for the calculation of the temperature distribution.

The first part is the evaporation of water. The first intermediate steps of this part of the analytical model are the same as for the previous part of the analytical model (step 1, 2, 3 and 4). However, after step 4 this part of the analytical model changes. First the discharge of vaporization from the saturated layer and the amount of water that is vaporized from the saturated layer is calculated (step 5 and 6).

The second part deals with the flow of water vapour out of the concrete. This is calculated with the flow parameter equation by Kodres [31] (step 8). The temperature difference, between the front of the saturated layer and the surface of the concrete, is obtained from the temperature distribution calculation. The pressure difference is obtained form the saturated vapour pressure at the front of the saturated layer and the atmospheric pressure at surface of the concrete. The saturated vapour pressure is used in this part of the analytical model to predict the pore pressure at the location of evaporation. The actual pore pressure is determined by a mixture of water and water vapour.

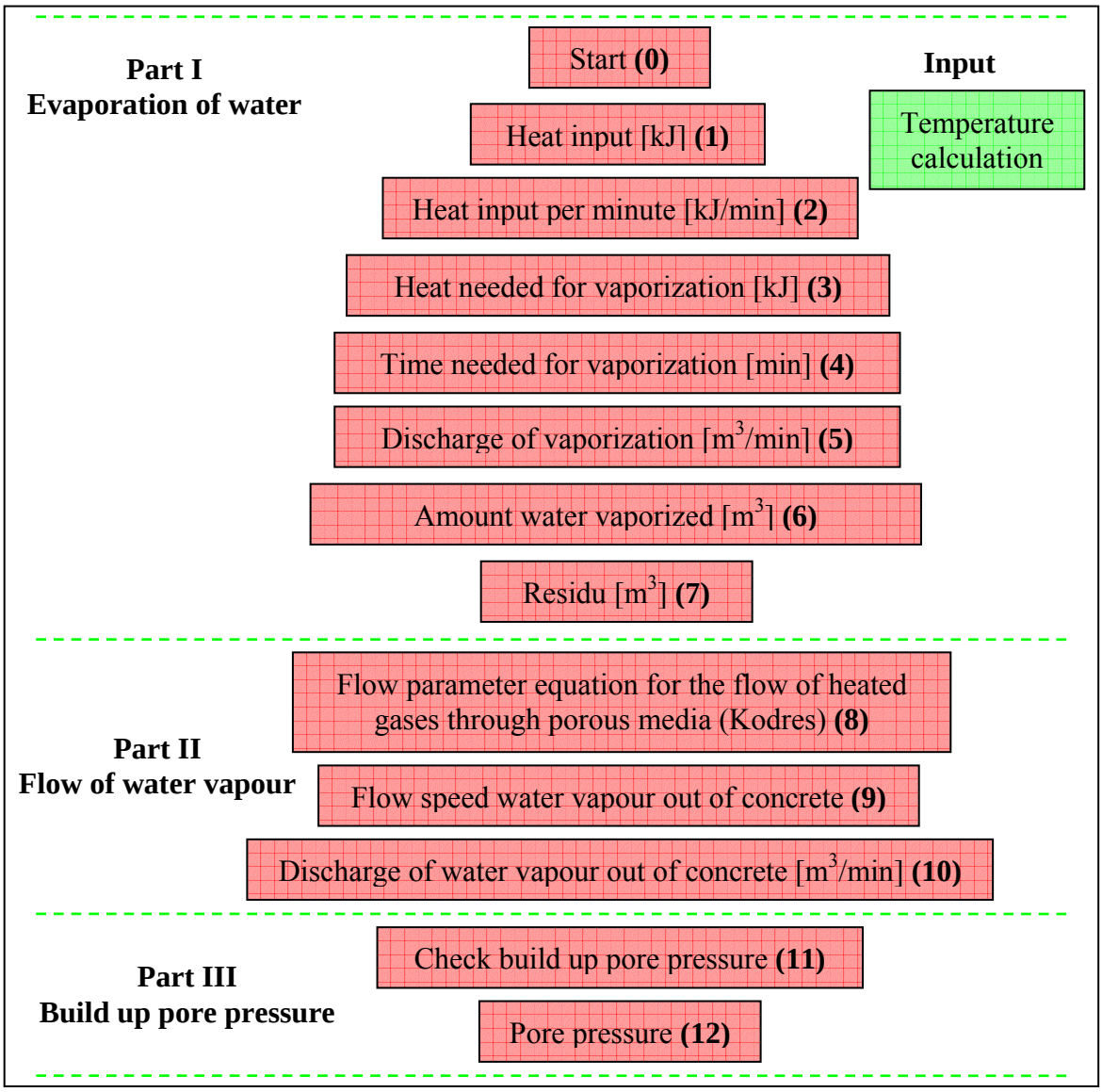

Fig 5.29 basic parts and intermediate steps part II

However, due to the confinement of the pores it is assumed that the saturated vapour pressure curve can be used to estimate the pore pressure. Furthermore, the constants C_1 and C_2 are obtained form experimental data into the behaviour of water vapour movement through heated concrete. The constant C_3 is estimated by taking the average porosity of the cross section of concrete along the flow path and then multiplying this by a reduction factor. The reduction factor accounts for the fact that some of the passages are to narrow to be used for the transport of water vapour. This correctness of this reduction factor is checked by comparing the results of the analytical model to results of experiments into pore pressure development. The constants C_6 and C_7 are calculated using the stagnation temperature obtained by the theory on Rayleigh flow. Finally, the length is taken as the length of the flow path. This means from the front of the saturated layer onto the surface of the concrete. This is the distance the water vapour is transported over. From the flow parameter the flow speed can be obtained by making use of equation 5.24, which relates the mass flux to the flow speed of the water vapour (step 9). This is then used to calculate the discharge from water vapour out of the concrete by making use of the constant C_3 (step 10). The constant C_3 can be used because the cross section has unite dimensions.

Finally, the third part determines the build up of pore pressure. First the check is made if the pore pressure builds up. This is obtained by comparing the discharge of vaporization and the discharge of water vapour out of the concrete. In case the discharge of vaporization is larger, than the pore pressure builds up (step 11). The pore pressure at that time step is than the saturated vapour pressure at the front of the saturated layer (step 12). This process continues until the discharge of vaporization is equal to the discharge of water vapour out of the concrete.

5.6.3. Assumptions

The assumptions made in this part of the analytical model are stated below. However, some of the assumptions made for the previous part of the analytical model are the same for this part. For completeness these assumptions are indicated by (*):

1. The evaporation of water from the pores of the concrete starts at a temperature of 100 ^{o}C. Before this temperature is reached the water in the pores of the concrete remains in these pores and thus not undergo a phase change (*).
2. The saturated layer consists out of that part of the concrete which is in a fully saturated state. All the pores of the concrete are filled with water.
3. The speed of the water vapour flow into the concrete is smaller than the speed of the 100 ^{o}C front.
4. The results from the temperature calculation are used as input in this part of the model. The total amount of heat the fire generates and penetrates the concrete is used for the evaporation of the evaporable water in the pores of the concrete (*).
5. The water vapour is considered an ideal gas. This means that the water vapour behaves according to the ideal gas law. This means that the saturated vapour pressure curve and the specific enthalpy of evaporation can be used. Furthermore, water is assumed to be incompressible (*).
6. During evaporation of water at elevated temperatures, the pressure inside the pores increases. It is assumed that, due to the confinement of the pores, the pressure can be characterized with the saturated vapour pressure(*).
7. The evaporable water which is generated during the decomposition process of the concrete is not taken into account. The evaporable water used in this calculation is the evaporable water which is present in the pores of the saturated layer.
8. For the calculation of the water vapour mass flux the theory by Kodres is assumed.
9. When the saturated layer is formed and impeded further water vapour flow into the cross section, the water vapour is assumed to flow in the direction of the surface of the concrete.
10. The pore structure of the concrete is assumed to homogenous (*).
11. It is assumed that the contribution of the air, inside the pores of the concrete to the pressure development, can be neglected (*).
12. The build up of pore pressure stops when there is more water vapour flowing onto the surface of the concrete as there is water evaporated from the saturated layer. This is assumption, because the discharge of evaporated water only slightly increases in time, but the discharge of transported water vapour onto the surface of the concrete increases rapidly in time. This means that when both discharges are the same, actually there is still a backlog of water vapour. However, the discharge of water vapour out of the concrete increases almost exponentially and therefore the mistake is limited.

13. The influence of reinforcement on the pore pressure build up is not taken into account.

5.6.4. Numerical solution

The above mentioned description is the general idea and this is transformed into a flow chard which gives a schematic representation and a complete overview in detail of the process of the evaporation of water, the transport of water vapour and the build up of a pore pressure in every time step for every element. On this flow yard, which is depicted in figure 5.30, the same colour and shape indication are used as in the previous flow chard 5.19.

The general idea and the most important parameters which are depicted in figure 5.30 were already elaborated in the paragraph which deals with the description of the general idea. Therefore, only the numerical implementation is elaborated here.

However, the numerical implementation needs further elaboration. The numerical implementation of the elements is the same as for the previous part of the analytical model. The numerical implementation of the equation by Kodres is further explained. This equation can numerical be solved by using Maple [tm], because on both sides of the equation the mass flux is present. Furthermore, in the derivation of this equation the length 'L' was used to indicate the length between to large capillary pores. However, this is difficult to implement in the numerical solution of this analytical model, because the cross section is divided into constant elements which have a length which is much larger than the distance between two capillary pores. To still use this equation, the length is set equal to the length the water vapour is transported over. This is the distance between the front of the saturated layer and the surface of the concrete. The numerical solution of the build up of pore pressure is further done by using Microsoft Office Excel[tm].

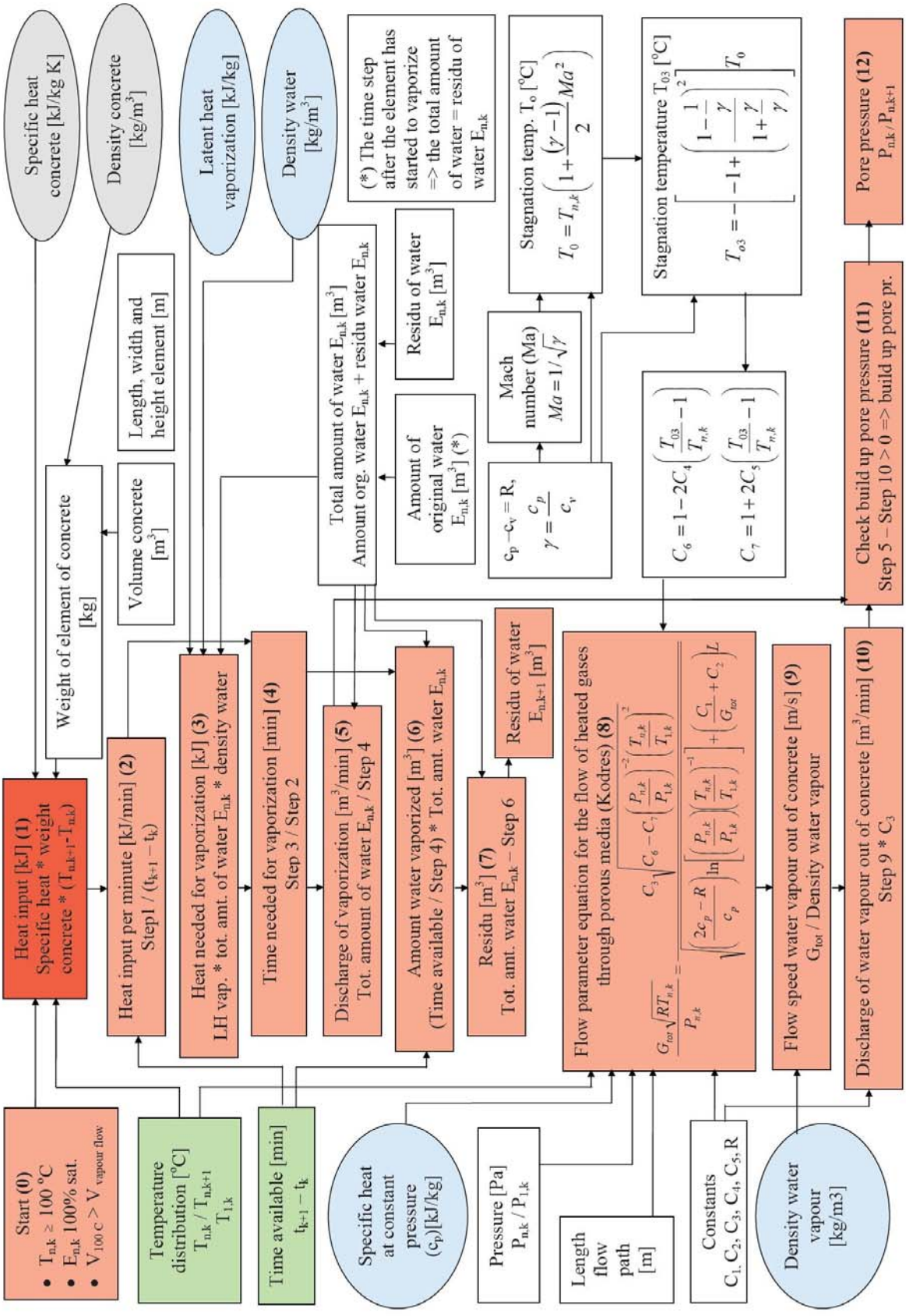

Fig 5.30 Flow chard which describes the fourth part of the analytical model

5.6.5. Material properties used in the analytical model

The grade of the concrete used in the numerical simulation is B35 (C28/35).

Material property		**Temp. dependent**
Concrete grade	B35 (C28/35)	
Thickness	400 mm	
Width	1000 mm	
Height	1000 mm	
Number of elements	100	
Stability criterion $a_c * \frac{\Delta t}{(\Delta x)^2} \leq 1/2$	$\Delta t = 0{,}36\,\text{min}$, $\Delta x = 4mm$	
Density of water	1000 kg/m^3	No
Density of concrete	2400 kg/m^3	No
Specific heat of concrete [kJ/kg K] [50]	c_c = 0,8*0,001*(T-20) (*)	Yes
Latent heat of vaporization [kJ/kg] [X]	(*)	Yes
Specific heat at constant pressure [kJ/kg] [50]	(*)	Yes
Density of water vapour [kg/m^3] [X]	(*)	Yes
Porosity of concrete [%] [50]	n = (0,142+0,0001*(T-20))*100 (*)	Yes
C_1 / C_2	0,345*10^{10} / 0,25*10^{10}	No
C_3 = 0,25 * n_{avg}	n_{avg} = average porosity across the flow path which is reduced	Yes
Tensile strength concrete [MPa] [6]	(*)	Yes
Modulus of elasticity [N/mm^2] [6]	(*)	Yes

Table 5.5 material properties used in the analytical model

The material properties of this type of concrete, which are used in the analytical model, are depicted in table 5.5. In the last column of this table the indication is given which of the material properties that are used are temperature dependent. The material properties indicated by (*) are graphically depicted in the Appendix B.

5.6.6. Results and analysis

In table 5.6 the results for the check whether a saturated layer has formed are depicted. The depicted times and the corresponding points indicate the process of the development of a saturated layer according to the analytical model. At each of times the front of a saturated element reached a temperature of 100 ^{o}C. The first two criteria, which are the temperature on the front of an element is 100 ^{o}C and the element is fully saturated, are then met. The third criterion is the check whether the speed of the 100 ^{o}C front is higher then the speed of the water vapour flow into the interior of the concrete. This criterion is indicated in the sixth column of table 5.6.

The table indicates that two saturated layers have been formed. The front of the first saturated layer is at 16 mm and is formed after 4,30 minutes. The front of the second layer is at 40 mm and is formed after 14,54 minutes.

Check build up of pore pressure						
Time [min]	**Distance [mm]**	**Thickness of layer [mm]**	**Speed 100 °C front [mm/min]**	**Speed of vapour flow [mm/min]**	**3rd criterion**	**Start build up pore pressure**
1,23	4	4	4,47	11,24	-6,76	no
2,13	8	8	3,92	4,69	-0,78	no
3,15	12	8	3,47	3,99	-0,52	no
4,30	16	12	3,18	2,47	0,71	*yes*
12,29	36	4	1,77	1,96	-0,18	no
14,54	40	8	1,60	1,43	0,17	*yes*

Table 5.6 Check for saturated layer and the start for the pore pressure to build up

The first saturated layer has a thickness of 12 mm, 3 elements. The second saturated layer has a thickness of 8 mm, 2 elements.

The flow parameter equation by Kodres is used in the calculation of the flow speed of the water vapour across the flow path, from the front of the saturated layer onto the surface of the concrete. This equation is used, but important is to know how this equation behaves when the parameters are changed. The most important parameters are the temperature ratio, the pressure ratio and the length of the flow path. In figure 5.31 the behaviour of the flow parameter equation is depicted. The first set of lines represents the behaviour during the build up of the pore pressure at the front of the first saturated layer. The temperature ratio (T_3/T_1) decreases from 8,19 at the beginning of the pore pressure build up (4,30 minutes) to 4,62 at the end of the pore pressure build up (6,30 minutes). However, the pressure ratio (P_1/P_3) increases rapidly from 1,39 at 4,30 minutes to 22, 36 at 6,30 minutes. The flow speed of the water vapour starts at $1{,}55*10^{-6}$ m/s at 4,30 minutes and the first minute lacks behind the pore pressure ratio. After around 1 minute the water vapour flow speed rapidly increase to $1{,}99*10^{-4}$ m/s at 6,30 minutes.

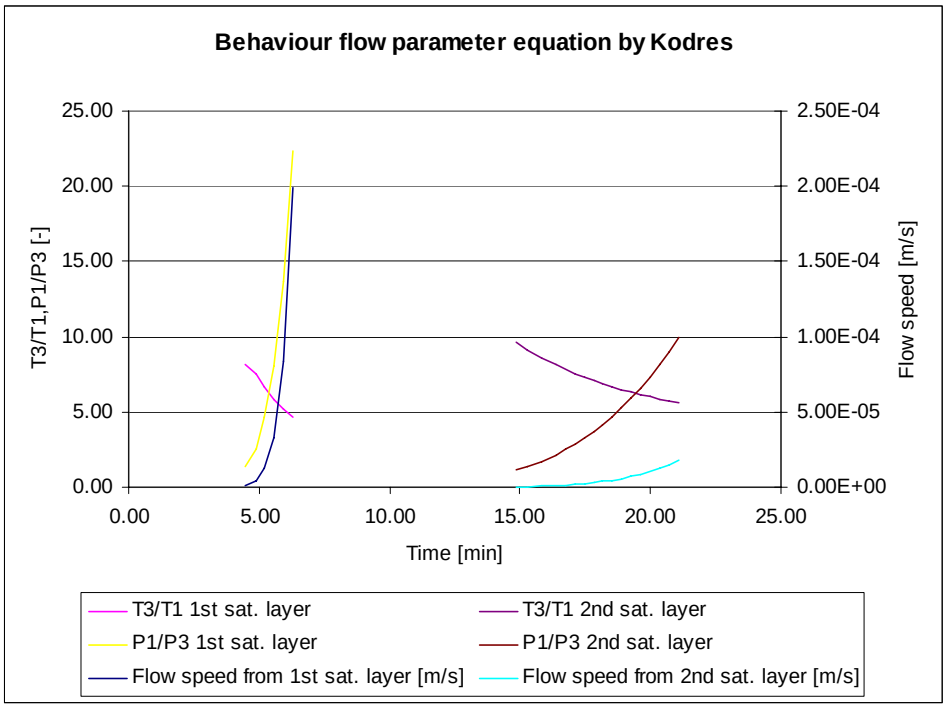

Fig 5.31 Behaviour of the flow parameter equation by Kodres

This behaviour is caused by the temperature ratio and the pore pressure ratio. The temperature ratio and the low pressure ratio at the beginning of the build up of pore pressure are sufficient to reduce the flow speed of the water vapour. However, as the temperature ratio gradually decreases and the pore pressure ratio rapidly increases, the flow speed of the water vapour also rapidly increase although the flow speed of the water vapour lacks behind the rapid increase of the pore pressure ratio and only starts to increase rapidly after around 1 minute. This means that the temperature ratio at the beginning of the build up of pore pressure is sufficient to reduce the flow speed, but after around 1 minute the pore pressure ratio becomes increasingly sufficient the 'push' the water vapour through the concrete and onto the surface of the concrete.

The second set of lines represents the build up of pore pressure at the front of the second saturated layer. The temperature ratio decreases from 9,65 at the beginning of the pore pressure build up (14,54 minutes) to 5,59 at the end of the pore pressure build up (21,06 minutes). The pressure ratio increases from 1,13 at 14,54 minutes to 9,92 at 21,06 minutes. This increase is less rapid than for the first saturated layer. The flow speed of the water vapour increase from $4{,}82*10^{-7}$ m/s at 14,54 minutes to $1{,}80*10^{-5}$ m/s at 21,06 minutes. The speed of the water vapour flow from the second saturated layer is lower and increases less rapidly as the speed of the water vapour flow from the first saturated layer. This is caused by the lower pressure ratio which also increases less rapidly. Furthermore, the length of the flow path is in case of water vapour flow from the second saturated layer also longer, which means that the flow of water vapour is hindered over a longer length.

In figure 5.32 the discharge of vaporization of water and the discharge of water vapour out of the concrete from the first saturated layer are depicted by the first set of lines. These lines represent the check whether the pore pressure builds up, which is step 11 in the flow chard of figure 5.30. The discharge of vaporization increases from $1{,}95*10^{-4}$ m^3/min to $3{,}32*10^{-4}$ m^3/min at respectively 4,30 minutes and 6,30 minutes. The discharge of water vapour out of the concrete increases rapidly from $4{,}42*10^{-6}$ m^3/min to $6{,}13*10^{-4}$ m^3/min and follows the same trend as the speed of the water vapour in figure 5.31. The lines of the discharges intersect at 6,02 minutes. The second set of lines describes the same discharges for the second saturated layer. The discharge of vaporization is almost constant around $5{,}0*10^{-5}$ m^3/min. The discharge of water vapour out of the concrete increases from $9{,}27*10^{-7}$ m^3/min to $5{,}33*10^{-5}$ m^3/min at respectively 14,54 minutes and 21,06 minutes. The lines of the discharges intersect at 21,01 minutes.

The lines for the discharge of water vapour out of the concrete follow the same trend as for the flow speed of the water vapour depicted in figure 5.31. This is due to the fact that the flow speed of the water vapour determines the discharge of water out of the concrete. Furthermore, also important is the difference between the discharges of the second saturated layer compared to the first saturated layer. The discharge of vaporization of the second saturated layer is much smaller than the one of the first saturated layer, because the rate at which the heat penetrates the concrete gradually reduces and thus the temperature gradient also reduces. This causes the amount of water which can be evaporated to reduce. Furthermore, the discharge of water vapour out of the concrete of the second saturated layer is also much smaller then the one of the first saturated layer, because the lower pressure ratio and the longer flow path reduce the flow speed of the water vapour.

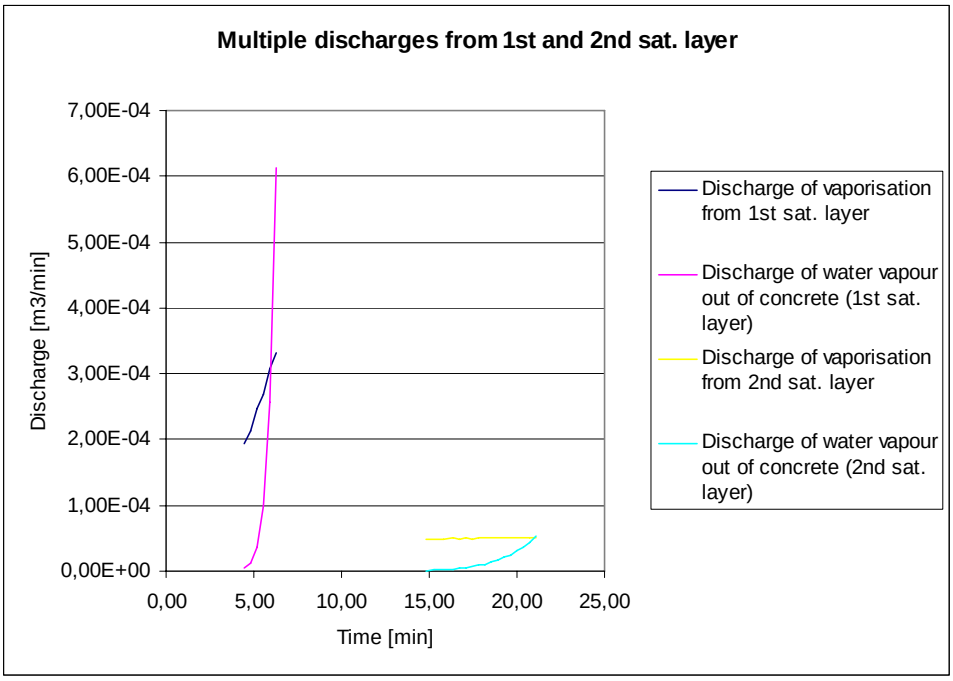

Fig 5.32 Discharge of vaporization an discharge of water vapour out of concrete from 1st and 2nd saturated layer

The most important result of the analytical model is the pore pressure distribution, which is depicted in figure 5.33. In this figure the build up of pressure in the pores of the concrete at the front of the saturated layer is depicted. The pore pressure of the first saturated layer develops rapidly from 4,30 minutes onto a maximum pore pressure of 1,58 MPa at 6,02 minutes. The end of the build up of pore pressure is at the same time the two discharges from figure 5.32 are equal. This means that the first pore pressure develops in 1,72 minutes.

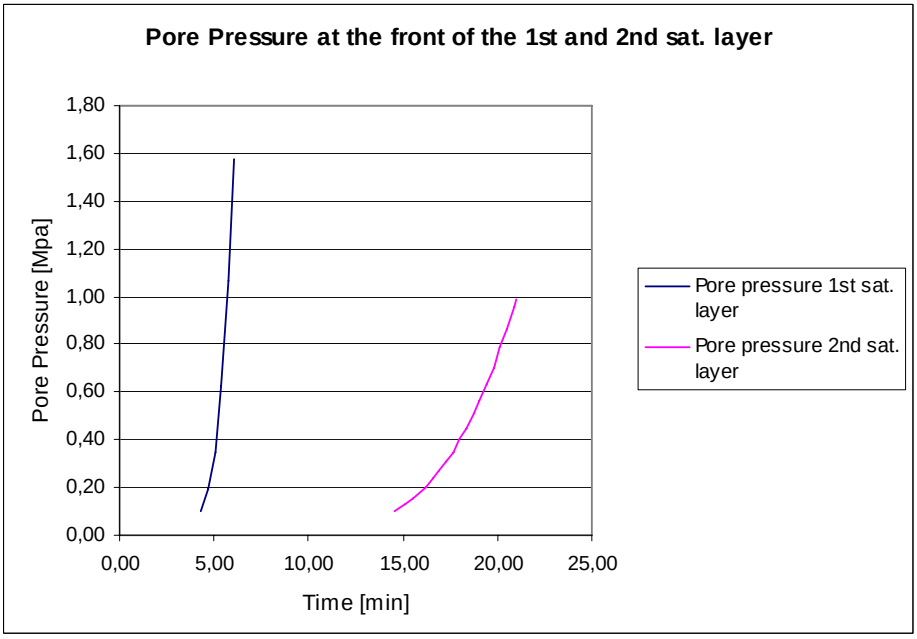

Fig 5.33 Pore pressure distribution at the front of the 1st and 2nd saturated layer

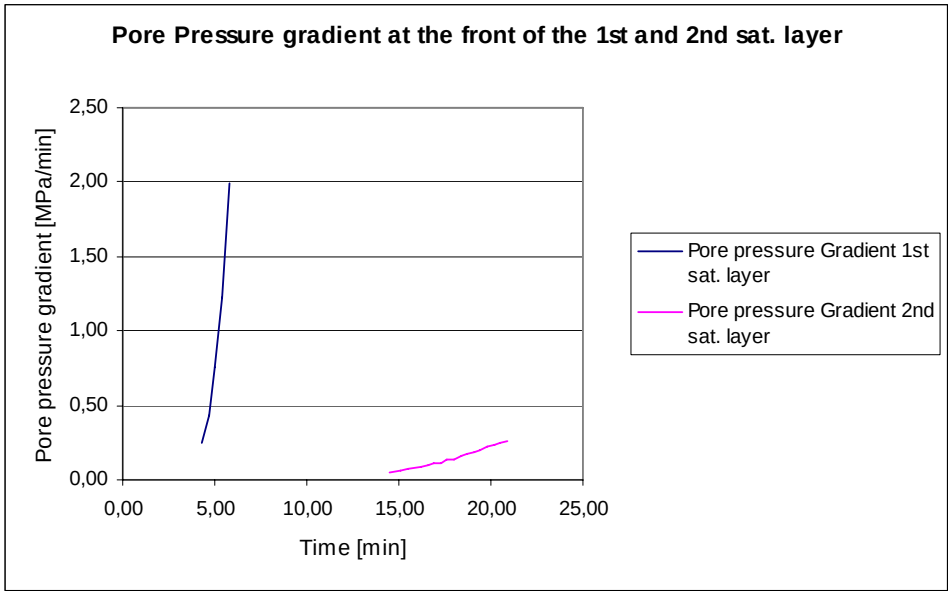

Fig 5.34 Pore pressure gradient at the front of the 1st and 2nd saturated layer

The pore pressure of the second saturated layer develops from 14,54 minutes onto a maximum of 0,99 MPa at 21,01 minutes. This means that the second pore pressure develops in 6,46 minutes. Furthermore, in figure 5.34 the gradient of the pore pressure distribution is depicted. The gradient of the pore pressure of the first saturated layer increases from 0,24 MPa/min onto 2,00 MPa/min. The gradient of the pore pressure at the second saturated layer increases from 0,05 MPa/min onto 0,16 MPa/min.

The figures 5.33 and 5.34 indicate that there is a difference in the behaviour of the pore pressure which develops at the front of the first saturated layer and the pore pressure which develops at the front of the second saturated layer. The pore pressure at the front of the first saturated layer develops rapidly and after a short period of time the peak pore pressure is reached. This behaviour is different form the pore pressure which develops on the front of the second saturated layer. This pore pressure develops less rapid and takes longer to reach a lower pore pressure peak. This difference is influenced by the heat penetration, because the first pore pressure develops after around 5 minutes in which the rate of heat penetration is still high. This high rate of heat penetration causes the development of high temperatures on the front of this saturated layer and therefore also high pore pressures develop. Furthermore, the high rate of heat penetration also causes a high temperature gradient which leads to an increase in the rate of evaporation as well as the temperature in the heated layer, in front of the saturated layer. The high pore pressures on the front of the saturated layer tends to ease the build up of pore pressure by, after around 1 minute, causing the rapid discharge of a large amount of water vapour flowing onto the surface of the concrete. However, the high temperature on the front of the saturated layer and in the heated layer tends to stimulate the build up of pore pressure by a high rate of evaporation from the saturated layer and the hindered flow of the water vapour onto the surface of the concrete. After 1 minute the pressure ratio has become sufficient to overcome the large rate of evaporation and the temperature increase end long the flow path and the flow speed of the water vapour and thus the discharge of water vapour out of the concrete rapidly increases.

In general it can be stated that a high rate of heating leads to evaporation of large amounts of water from the saturated layer. The rapidly increasing pressure difference becomes sufficient after only a short period of time to 'push' enough water vapour onto the surface of the concrete to ease the build up of pore pressure. However, the rapidly increasing pore pressure also causes the possibility of spalling to increase.

The difference with the second saturated layer is that this layer develops after around 15 minutes and therefore the rate of heat penetration is much lower. This means that the temperature and the pore pressure at the front of this saturated layer are lower, which leads to a lower pressure difference. This means that the mean driving force behind the flow of water vapour and the thus the factor which eases the build up of pore pressure, reduces. Furthermore, the difference between the first and the second pore pressure build up is also the length of the flow path, which is longer in case of the pore pressure build up at the front of the second saturated layer. This increased length of the flow path means that the water vapour has to flow over a longer length and thus is more hindered during its flow. In addition the temperature gradient reduces, which causes a lower rate of evaporation. This has a beneficial reducing effect on the build up of pore pressure, because the discharge of vaporization from the saturated layer reduces. However, the relative slow increase of the flow speed of water vapour and thus the discharge of water vapour out of the concrete has more influence than the lower rate of evaporation and therefore the build up of pore pressure takes a longer period of time to develop.

The flow of water vapour onto the surface of the concrete is influence by three factors. The first is the rate of heat penetration and the second the length of the flow path. Both these aspects are already elaborated. The third is the permeability of the concrete. This parameter also influenced the flow of water vapour into the interior of the concrete. The permeability is included by the constant C_3, which is the reduced porosity of the cross section of concrete. This means the amount of passages which are available for the water vapour to flow through.

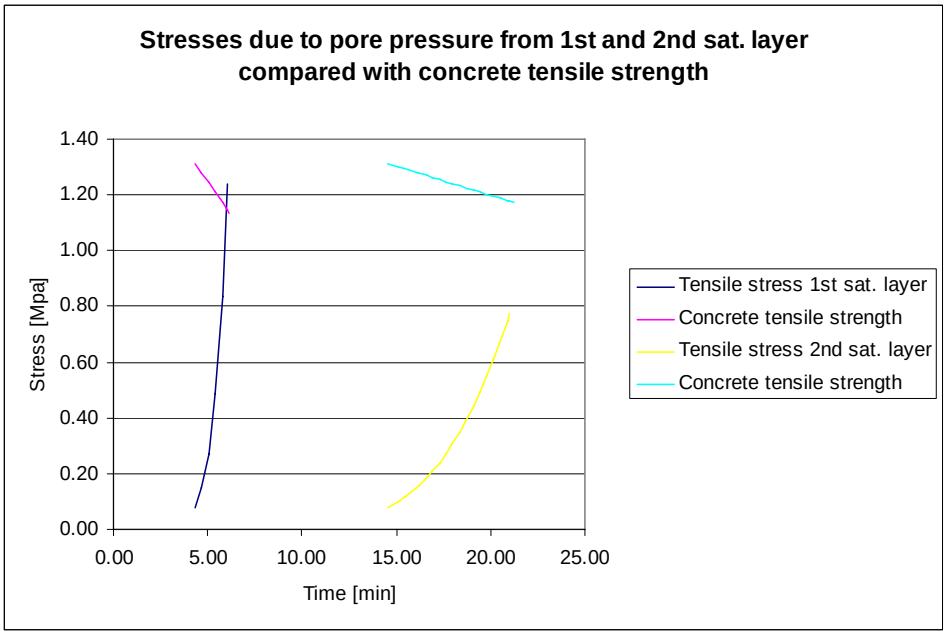

Fig 5.35 Stresses due to pore pressure form 1st and 2nd sat. layer compared with concrete tensile stress

This factor has a large influence on the outcome of the equation of Kodres and thus the peak pore pressure.

In case this constant increases, the permeability increases which means that the flow of water vapour is less hindered due to restrained expansion and thus the period of time needed for the flow of water vapour to become large enough and to ease the build up of pore pressure becomes shorter. This means that the possibility of spalling decreases. Furthermore, the permeability becomes increasing more important when the length of the flow path increases. In case of a short flow path, the pressure difference takes a shorter period of time to develop sufficiently to 'push' the water vapour through the concrete and therefore the permeability is of less importance. When the length of the flow path increases, the water vapour has to flown over a longer distance and is therefore more dependent on the permeability of this flow path. The temperature of the water vapour increase and therefore the restrained expansion of the water vapour cause the flow of water vapour to be hindered. In case the permeability is high enough, which means that the amount of passages is high and the amount of larger passages also increases, the water vapour has more space to expand and therefore the effect of restrained expansion will need more time to develop and the flow of water vapour is less hindered.

In figure 5.35 the tensile stresses are depicted which are caused by the pore pressure build up. These tensile stresses act tangential to the edge of the pores and are compared with the tensile strength of the concrete at elevated temperatures. The tensile stress, which develops during the first saturated layer, increase rapidly from 4,30 minutes until it reaches a maximum tensile stress of 1,24 MPa at 6,02 minutes. The tensile strength of the concrete at the front of the first saturated layer decreases in time, because the temperature on this front increases from a temperature of 100 ^{o}C to 200 ^{o}C. The tensile stresses and the tensile strength can be compared with each other and this is done in the first set of lines in the graph. Just before the maximum tensile stress is reached, the tensile stress becomes larger than the tensile strength. The tensile stress, which develops during the second saturated layer, increase gradually from 14,54 minutes onto a maximum tensile stress of 0,78 MPa at 21,01 minutes. These tensile stresses are not high enough to reach the tensile strength of the concrete.

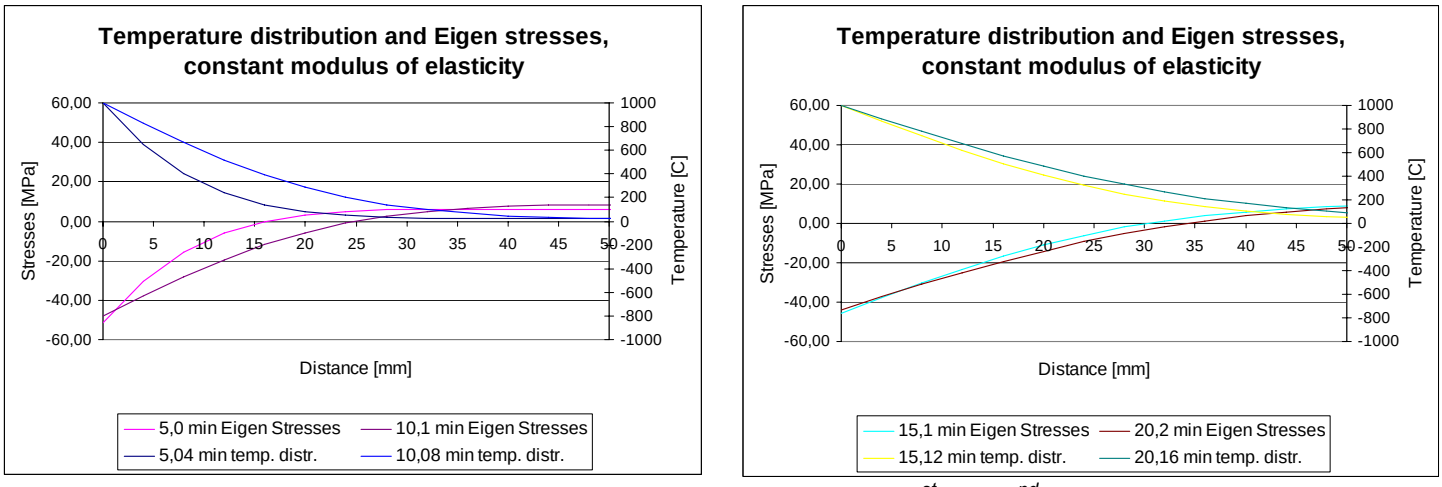

Fig 5.36 Eigen stresses in time at the front of the 1st and 2nd sat. layer

The cross section is also loaded with the Eigen stresses due to the temperature gradient across the cross section. In figure 5.36 the development of the Eigen stresses and the temperature distribution in part of the cross section of the concrete in time are depicted. The left part of the figure shows the temperature and Eigen stress distribution at respectively 5 and 10 minutes. In this time the Eigen stresses at the front of the first saturated layer increase from -0,18 MPa to -11,89 MPa while the temperature increases rapidly from 138,6 ^{o}C to 390,1 ^{o}C. This means that at the front of the first saturated layer a compression stress is present. As was already elaborated in the paragraph of the Eigen stresses, the elevated temperature cause the modulus of elasticity and these stresses to be smaller than calculated. However, the compressive stress will be present. The right part of the figure shows the temperature and Eigen stress distribution at respectively 15 and 20 minutes. At the front of the second saturated layer the Eigen stresses increase from 5,95 MPa to 3,78 MPa while the temperature increases from 107,4 ^{o}C to 168,7 ^{o}C. These tensile stresses are developed at the front of the second saturated layer. In this part of the cross section the temperatures are lower and therefore the modulus of elasticity is less reduced. This means that the tensile stresses are present and only slightly reduced.

On the front of the first saturated layer the pore pressure causes tensile stresses which just exceed the tensile strength of the concrete. The tensile stresses act in every direction tangential to the pore edge. Furthermore also Eigen stresses develop on this front which are compressive stresses. These Eigen stresses act perpendicular to the depth direction of the cross section. For the determination of spalling the yield criterion of Mohr-Coulomb can be used, which is depicted in figure 5.37 [47]. In this yield criterion the stresses in two direction perpendicular to each other are depicted and the yield criterion describes which combination of these stresses can be allowed in the cross section of concrete to ensure that the concrete does not yield, which means behaves according to the theory of plasticity. The positive direction of the axis is a tensile stress.

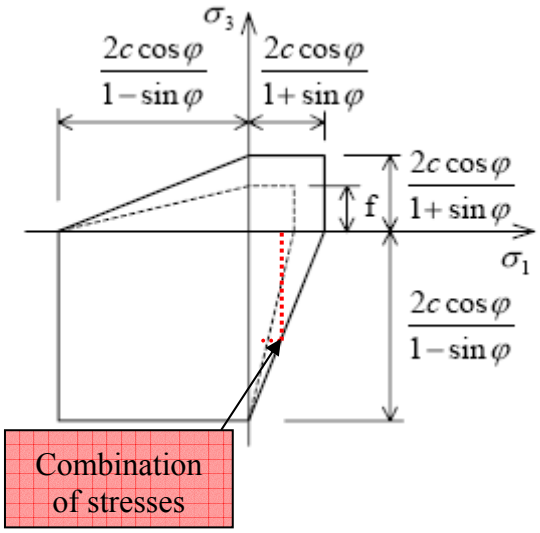

Fig 5.37 Mohr Coulomb yield criterion frequently used for unreinforced concrete [47]

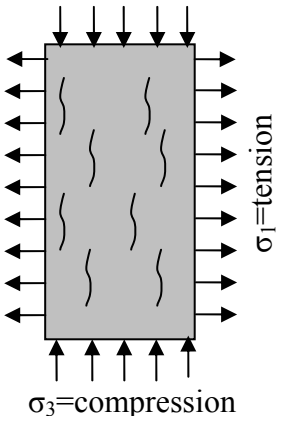

Fig 5.38 Compressive stresses σ_1 cause vertical cracks which weaken the concrete and reduce the tensile stress σ_2 of the concrete

The compressive Eigen stresses cause compressive σ_3 stresses and due to the large compressive stresses on the surface of the cross section cause vertical cracks in the cross section, which is depicted in figure 5.38. These cracks weaken the cross section and therefore reduce the horizontal tensile strength of the concrete, which can be seen in figure 5.37.

Furthermore, also the poisson ratio is a factor which influences the stress behaviour in two directions. The Eigen stresses causes besides compressive stresses in the vertical direction, also tensile stresses in the horizontal direction, which also further reduce the tensile strength of the concrete. Therefore, it can be concluded that the tensile strength of the concrete is further reduced by the compressive Eigen stresses and that the tensile stress resulting from the pore pressure development exceed the limit tensile strength of the concrete and therefore cracks start to develop in radial direction from the edge of the pores. These cracks further weaken the structure of the concrete and in case the concrete is weakened enough spalling of the layer in front of the saturated layer occurs. Beneficial is the effect that this concrete layer is being restrained by friction forces.

In general it can be stated that when the tensile strength of the concrete is increased, the developed pore pressures lead to less cracks and the possibility of spalling decreases.

6. Numerical model

6.1. General outline and goal of the presented model

In this chapter a numerical model is presented which describes the effects of exposure of the concrete to a fire. As was already mentioned in the previous chapters, the heat of the fire will penetrate the concrete. This causes the strength and stiffness of the concrete to decrease. Furthermore, due to evaporation of water from the pores of the concrete the process which leads to the development and occurrence of spalling arises. The numerical model is developed in the general purpose finite element program called ABAQUS and in conjunction with ABAQUS Benelux BV.

The main goal of this chapter is to derive a numerical model which is relatively simple and therefore the main theories and factors influencing the process can be identified and examined. From this it can be concluded which information is already present and in which fields further information needs to be gathered. Furthermore the numerical model needs to give a good impression in the behaviour of concrete during exposure to a fire. Especially the water vapour transport, build up of a saturated layer and the development of the pore pressure should be modelled. Finally, the obtained results from the numerical model can be compared to the results of the analytical model and to experimental data to validate if the model behaves correctly.

6.2. The different parts of the numerical model

The numerical model is divided into two main parts. The first part deals with the determination of the temperature distribution throughout the cross section. The second part is the most important part of the numerical model and deals with the process which leads to spalling. The numerical model predicts the development and distribution of pore pressures throughout the cross section and the transport of water (vapour) into the interior of the concrete where gradually a fully saturated layer is developed. Furthermore, the pore pressures induce tensile stresses in the concrete which, in case of exceeding the limit tensile stress, indicate that spalling occurs. The numerical model then generates the needed information about the thickness of the spalled of layer. The geometry of both parts of the numerical model are adapted to exclude the spalled of layer and the model is restarted and continues until the development of pore pressures and the resulting tensile stresses exceed for the second time the limit tensile stress of the concrete. By adapting the geometry of the model and restarting and continuing the calculation, the progressing nature of spalling is taken into account.

6.3. First part: Heat transfer model

6.3.1. Theory

The first part of the numerical model predicts the temperature distribution over the cross section of concrete. The temperature distribution over the cross section of concrete is calculated by using an uncoupled heat transfer analysis in ABAQUS/Standard. This model describes the heat conduction of a solid body under influence of temperature dependent material properties. The heat transfer analysis is uncoupled, which means that the thermal and mechanical problems are also uncoupled and therefore the strain or displacements of the body do not influence the

temperature of the body. This means that the temperature is the only degree of freedom in this analysis [1].

The heat transfer analysis is based on solving the basic energy balance of equation 6.1 [1]. In this equation the term on the left hand side is the internal energy of the body. The term on the right hand side represents the external energy or the loading of the body. Furthermore, also a constitutive relationship is present, which couples the specific heat to the change of internal energy per temperature, which is depicted in equation 6.2 [1]. Finally, heat conduction is assumed to be governed by the Fourier law of equation 6.3 [1].

$$\int_V \rho \dot{U}\, dV = \int_S q dS + \int_V r dV \tag{6.1}$$

$$c(\theta) = \frac{dU}{d\theta} \tag{6.2}$$

$$f = -k \frac{\partial \theta}{\partial x} \tag{6.3}$$

in which:

V = volume of the solid material [m^3]
S = surface area of the body [m^2]
ρ = density of the material [kg/m^3]

$\dot{U}$ = the material time rate of the internal energy [J/s]
q = heat flux per unit area of the body and flowing into the body [J/m^2s]
r = heat supplied externally into the body per unit volume [J/m^3]
c = specific heat of the solid material [J/kgC]
θ = temperature of the solid material [K]
k = conductivity of the solid material [J/smC]
f = heat flux [J/s]
x = indicator for the position [m]

To obtain a numerical solution a variational statement of equations 6.1 and 6.3 is obtained by making use of the standard Galerkin approach, which is depicted in equation 6.4 [1].

$$\int_V \rho \dot{U}\, \delta\theta dV + \int_V \frac{\partial \delta\theta}{\partial x} k \frac{\partial \theta}{\partial x} dV = \int_V \delta\theta r dV + \int_{S_q} \delta\theta q dS \tag{6.4}$$

in which

δθ = arbitrary variational field satisfying the boundary conditions

The body is approximated with finite elements which use shape functions to determine the temperature distribution over the element together with the nodal temperatures, which is depicted in equation 6.5. The Galerkin approach assumes that the variational field is interpolated by the same functions and therefore equation 6.6 also holds.

$$\theta = N^N(x)\theta^N \tag{6.5}$$

$$\delta\theta = N^N(x)\delta\theta^N \tag{6.6}$$

in which θ^N = nodal temperature [C]
N^N = shape function of first and second order polynomials

The equations 6.5 and 6.6 are substituted in the variational statement of equation 6.4 and equation 6.7 is obtained [1]. In this equation the term 'δθN' can be left out. The obtained equation is the continuous time description of the geometric approximation.

$$\int_V N^N \rho \dot{U}\, dV + \int_V \frac{\partial N^N}{\partial x} k \frac{\partial \theta}{\partial x} dV = \int_V N^N r dV + \int_{S_q} N^N q dS \tag{6.7}$$

To solve this equation numerically, ABAQUS/Standard uses a backward difference algorithm to approximate the internal energy. In equation 6.8 the backward difference method is depicted. A backward difference method is chosen, because of its simplicity. Furthermore, the backward difference method is unconditional stable, which means that there are no limitations to the time step which can be used. The backward difference method is substituted into equation 6.7 and equation 6.9 is obtained.

$$\dot{U}_{t+\Delta t} = (U_{t+\Delta t} - U_t)/(1/\Delta t) \tag{6.8}$$

$$\frac{1}{\Delta t}\int_V N^N \rho (U_{t+\Delta t} - U_t)\, dV + \int_V \frac{\partial N^N}{\partial x} k \frac{\partial \theta}{\partial x} dV - \int_V N^N r dV - \int_{S_q} N^N q dS = 0 \tag{6.9}$$

This equation is nonlinear and is solved by using a modified Newton method. The Newton method can be explained symbolically with the aid of equation 6.10 [1].

$$F^N(u^M) = 0 \tag{6.10}$$

in which F^N = force component to the N^{th} variable in the problem
u^M = value of the M^{th} variable in the problem

The problem is to solve u^M throughout the history of interest. The Newton method assumes that after an iteration 'i', an approximation u_i^M for the exact solution is obtained [1]. The difference between the exact solution and the approximate solution is c_{i+1}^M, which means that equation 6.10 becomes equation 6.11. The left hand side of this equation can be expanded by using a Taylor series to approximate the solution u_i^M.

$$\begin{aligned} &F^N(u_i^M + c_{i+1}^M) = 0 \\ &F^N(u_i^M) + \frac{\partial F^N}{\partial u^P}(u_i^M)c_{i+1}^P + \frac{\partial^2 F^N}{\partial u^P \partial u^Q}(u_i^M)c_{i+1}^P c_{i+1}^Q + ... = 0 \end{aligned} \tag{6.11}$$

In the Taylor expansion only the first two terms are used, because in case u_i^M is a close approximation for the exact solution, the contribution of the c_{i+1}^M can be

neglected. Equation 6.11 than reduces to a linear system of equations, which is depicted in equation 6.12.

$$K_i^{NP} c_{i+1}^{P} = -F_i^{N} \tag{6.12}$$

in which $K_i^{NP} = \frac{\partial F^N}{\partial u^P}(u_i^M)$ => Stiffness matrix or Jacobian matrix

$F_i^N = F^N(u_i^M)$

The next approximation to the solution then becomes equation 6.13 and the iteration continues until the c_{i+1}^M are sufficiently small.

$$u_{i+1}^M = u_i^M + c_{i+1}^M \tag{6.13}$$

In case of the heat transfer analysis the modified Newton method is used, which means that the Jacobian matrix is not recalculated in each iteration to save calculation time.

The obtained system of equations is solved numerically by using full Gauss integration schemes. This means that the stiffness matrix is integrated exactly by using 4 integration points per element and evaluating the stiffness matrix at each of these integration points after which the results are added and the total, at the integration points evaluated, stiffness matrix is obtained. The shape functions of the elements used in the heat transfer analysis are linear and in equation 6.9 the shape function and the derivatives of these shape functions are present. These linear terms give a quadratic variation when they are squared. To integrate a quadratic function in two dimensions, two points are required in each direction. The evaluated stiffness matrix is then used to determine the nodal degrees of freedom and the problem is solved. Furthermore, the time step size is determined by using the ability of ABAQUS to automatically select a suitable time step.

6.3.2. Numerical implementation

The heat transfer model in ABAQUS is based on a small strip of concrete subjected to a temperature curve which is prescribed at the surface of the concrete. The heat transfer analysis then determines the temperature distribution through the cross section of the concrete. The heat transfer model is based upon five main components, the geometry, the material properties, the mesh, the boundary conditions and the steps in the analysis. These components are further elaborated and depicted in figure 6.1.

Geometry

The strip of concrete is model as a solid homogenous part of concrete in two dimensions.

Material properties

The theory behind the heat transfer analysis shows that only three material properties of the concrete are needed: the conductivity, the density and the specific heat.

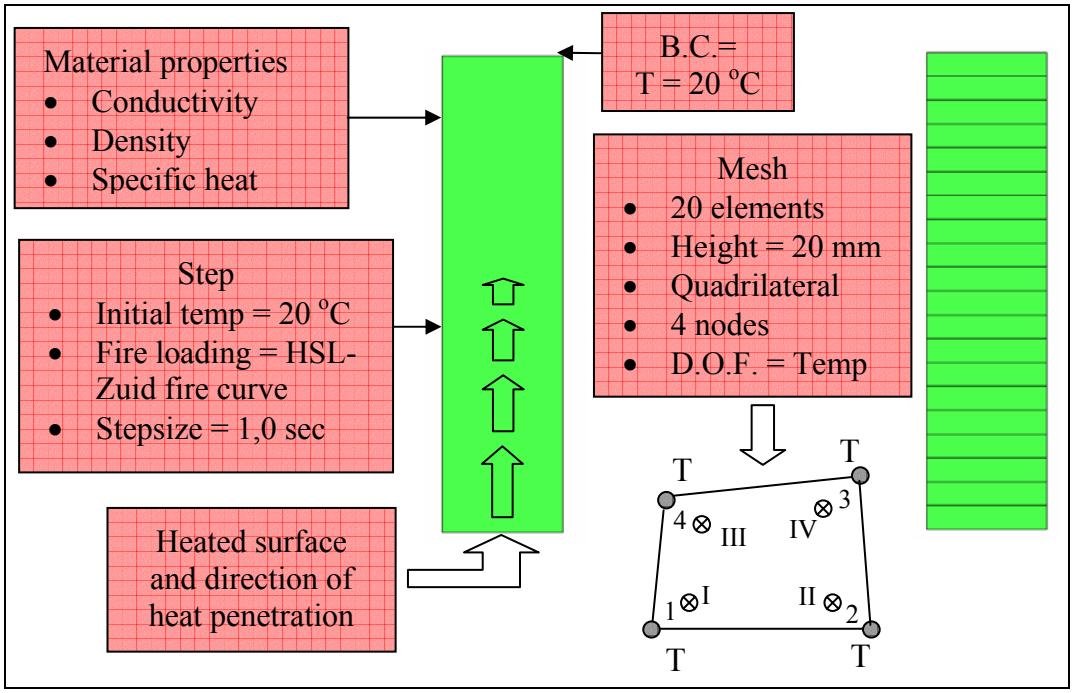

Fig 6.1 Overview of heat transfer model

Mesh

The mesh of the heat transfer model is kept relatively simple, because the temperature is prescribed with a fire curve over the entire heated surface of the cross section of concrete. This generates a relative simple one dimensional temperature distribution over the cross section of concrete with for instances no edge effects. The mesh consists out of, in depth direction, 20 elements with a height of 20 mm per element. The elements are quadrilateral heat transfer elements with 4 nodes and per node the temperature as the single degree of freedom [2]. The shape functions are linear across the element [2].

Boundary conditions

The heat transfer model has two boundary conditions. The first boundary condition is the prescribed temperature, through a fire curve, over the entire heated surface of the cross section of concrete. One of the possibilities in ABAQUS is to use a film coefficient to prescribe the temperature on a surface [2]. By choosing the film coefficient very high, the temperature is directly prescribed on this surface. Furthermore, the fire curve, which is used for the surface temperature, is an amplitude function which raises the temperature in 300 seconds (5 minutes) from a temperature of 20 °C to 1000 °C. This is in accordance with the HSL-Zuid fire curve (appendix A). The second boundary condition is the temperature on the opposite side of the heated surface of the cross section of concrete. This temperature is kept constant at 20 °C throughout the analysis [2].

Steps

The heat transfer model consists out of two steps. The first step is the initial step. This step describes the initial conditions of the cross section of concrete [2]. Due to the fact that this analysis is a heat transfer analysis with only the temperature as a degree of freedom, only the temperature is prescribed as an initial condition. Throughout the entire strip of concrete the initial temperature is 20 °C. The second step is the step in

which the fire and thus the temperature loading of the surface of the concrete starts [2]. In this step the details of the calculation are given. The most important are the initial, minimal and maximal time step size. The initial and maximal time step sizes are chosen to be 1,0 second. This ensures enough information is present to be used in the Pore fluid/Stress model.

6.3.3. Assumptions

In this part of the numerical model the following assumptions are made:

1. The evaporation of water will consume heat and therefore slow down the rate at which the temperature penetrates the cross section. This effect is neglected in the heat transfer model.
2. The material properties of the concrete are kept constant throughout the calculation. ABAQUS offers the ability to make the material properties temperature dependent. However, to adequately compare the analytical model with the numerical model, the material properties should be chosen the same as much as possible.
3. The boundary condition on the heated surface is prescribed by the temperature of the HSL-Zuid fire curve. (appendix A) This is an assumption, because the surface temperature of the concrete differs from the temperature of the fire curve. This difference occurs because part of the heat of the fire is lost during radiation and convection.
4. The influence of reinforcement on the temperature distribution is not taken into account.

6.3.4. Material properties used in the numerical model

The grade of the concrete used in the numerical simulation is B35 (C28/35). The material properties of this type of concrete, which are used in the numerical model, are depicted in table 6.1. In the last column of this table the indication is given which of the material properties that are used are temperature dependent.

Material property		**Temp. dependent**
Concrete grade	B35 (C28/35)	
Thickness	400 mm	
Width	100 mm	
Number of elements	Height = 20 (20 mm) Width = 1 (100 mm) Ratio = 20	
Thermal conductivity of concrete	2,55 W/mC	No
Density of concrete	2400 kg/m^3	No
Specific heat of concrete	800 J/kgC	No
Time step size	$\Delta t = 1{,}0\,\text{sec}$	
Initial temperature	20 ^{o}C	

Table 6.1 material properties used in the heat transfer model

6.3.5. Results and analysis

In figure 6.2 the temperature distribution throughout the cross section of concrete is depicted. The temperature on the surface of the concrete increases with time and after 5 minutes the temperature reaches 1000 ^{o}C.

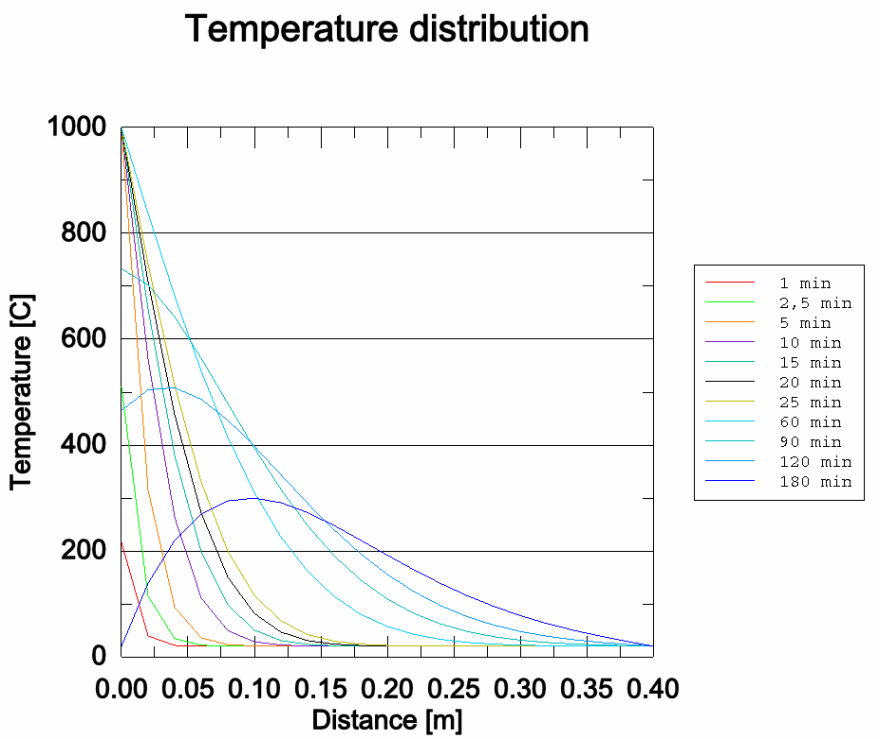

Fig 6.2 temperature distribution throughout the cross section

After 60 minutes the temperature on the surface starts to decreases until around 170 minutes into the fire the temperature becomes 20 ^{o}C again. This is in accordance with the HSL-Zuid fire curve. The heat rapidly penetrates the concrete and after 5 minutes the first 75 mm already experience an increase in temperature from just over 20 ^{o}C until 1000 ^{o}C on the surface of the concrete. This process continues and after 10 and 20 minutes the heated layer has grown to respectively 125 mm and 175 mm. The maximum depth the heated layer reaches after 180 minutes is 400 mm.

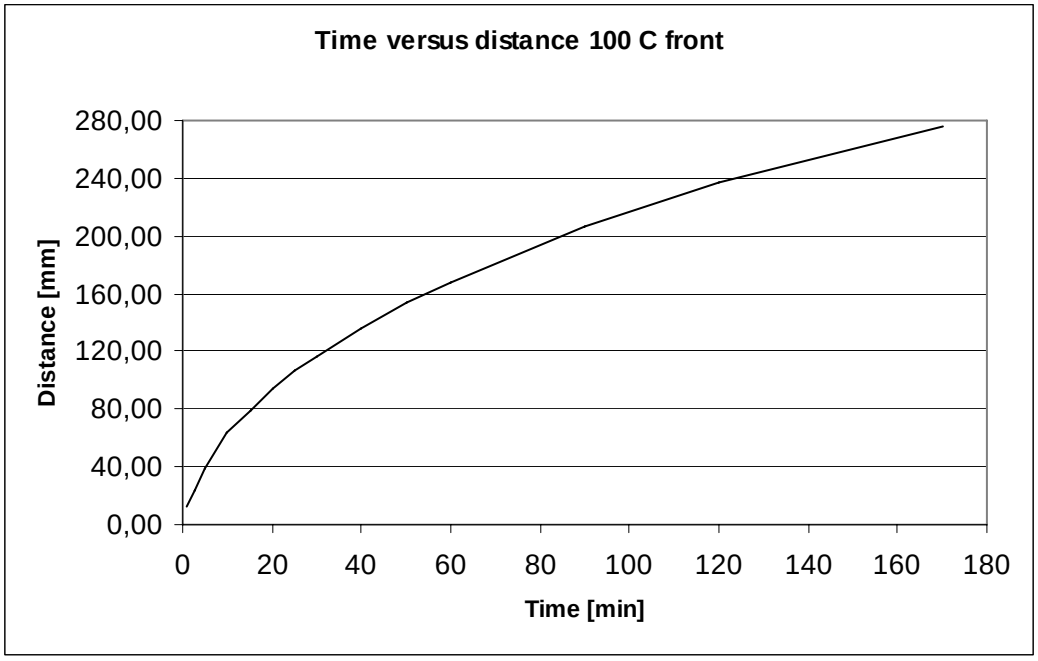

Fig 6.3 development of the time versus distance of the 100 ^{o}C front in the heat transfer model

After 60 minutes the surface temperature decreases, but the temperature within the concrete only gradually follows this decrease. The peak of the temperature distribution therefore shifts, in time, into the cross section of the concrete.

From the temperature distributions the progress of 100 ^{o}C front through the concrete can be obtained, which is depicted in figure 6.3. The 100 ^{o}C front reaches a depth of 40 mm and 80 mm after respectively 5 and 15 minutes. The maximum depth the 100 ^{o}C front reaches is after 180 minutes and is 275 mm.

From figure 6.4 also the speed of the 100 ^{o}C front can be obtained, which is depicted in figure 5.3. In the first 10 minutes the speed at which the 100 ^{o}C front penetrates the cross section decreases from 7,00 mm/min to 3,20 mm/min. After 10 minutes the speed further gradually decreases to around 1,00 mm/min.

The temperature distribution and the speed of the 100 ^{o}C front indicate that in the early stages of the fire the heat rapidly penetrates the concrete and the heated layer rapidly grows. After around 10 minuets the speed at which the heated layer grows gradually reduces over time. The explanation for this is the HSL-Zuid fire curve, which, after 5 minutes, reaches the maximum temperature of 1000 ^{o}C. This temperature then remains constant for 55 minutes. This means that in the first 5 minutes the concrete element is rapidly heated up and after that the amount of heat penetrating the concrete gradually becomes constant. Furthermore, due to the high heating rates almost the entire cross section of concrete experiences an increase in temperature.

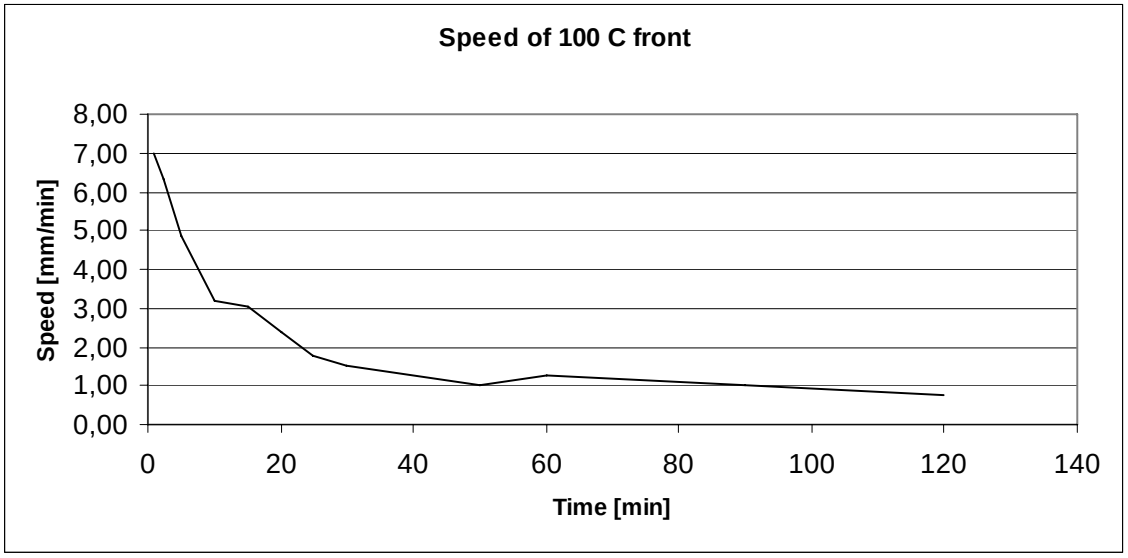

Fig 6.4 speed of the 100 ^{o}C front in the heat transfer model

6.4. Second part: Pore fluid/Stress model

6.4.1. General idea

The general idea behind this part of the numerical model is to model the evaporation of water from the pores of the concrete and the resulting pore pressure development which causes the transport of the formed water vapour through the cross section of concrete which in time causes the and the development of a fully saturated layer.

Furthermore, the pore pressure development leads to stresses which could lead to spalling.

This part of the numerical model is based upon a coupled pore fluid/stress model in ABAQUS/Standard which is normally used for soils with a wetting liquid, for instances groundwater, flowing through the material. This model is therefore based upon a porous medium with a multiphase material [1]. In the medium two fluids are present. The first is the wetting liquid, which is assumed to be relatively incompressible, and the second normally is a gas, which is assumed to be relatively compressible. In case the medium is partly saturated, both fluids are present. When the medium is fully saturated the voids of the material are completely filled with the wetting liquid [1]. Furthermore, the wetting liquid is free to move through the material and the flow is induced by a pressure difference in the wetting liquid. The flow of the wetting liquid is described by Darcy's law [1]. Basically the material volume can be schematized as is depicted in equation 6.14. In case the wetting liquid attaches to the solid particles, this wetting liquid then becomes trapped [1].

$$V_{mat} = V_{grains} + V_{void}$$
$$V_{void} = V_{wet} + V_{gas}, V_{wet} \leq V_{void} \quad (6.14)$$

In which V_{mat} = total elementary volume [m^3]
V_{grains} = total volume of the grains of the solid material [m^3]
V_{void} = total volume of voids in the material [m^3]
V_{wet} = total volume of the wetting liquid in the voids of the material [m^3]
V_{gas} = total volume of the gas in the voids of the material [m^3]

The soil model therefore fulfils two major requirements for a numerical model for the prediction of spalling.

1. The ability of the Pore fluid/Stress model to model a porous medium consisting out of solid material with voids partly or fully saturated with a wetting liquid
2. The ability of the Pore fluid/Stress model to develop pressures in the wetting liquid
3. The ability of the Pore fluid/Stress model to model the flow of the wetting liquid through the material

However, besides the above mentioned abilities which make the Pore fluid/Stress model suitable for the analysis of spalling, this model also has one drawback. The Pore fluid/Stress model is only capable of modelling single phase flow through the material, this means only wetting liquid which general means only water. As was already established in chapter 4 with the theory behind spalling, the process which induces spalling is actually a multi phase flow consisting of water, water vapour and a mixture of water and water vapour. The water is present in the pores of the concrete as is the case in the Pore fluid/Stress model. However, the water is evaporated and the water vapour flows, induced by a pore pressure gradient, onto the surface of the cross section and in time increasingly towards the interior of the concrete. The pore pressure increases due to the evaporation process which causes the water to expand. The Pore fluid/Stress model is not capable of modelling the evaporation of water and

the flow of water vapour. To use this Pore fluid/Stress model as a numerical basis to model spalling means that this drawback needs to be addressed.

In the Pore fluid/Stress model the possibility is present to define the material behaviour of the wetting liquid and the solid material. The main material properties which are used for this are the expansion coefficient of the wetting liquid, the porous bulk modulus and the sorption curve. The expansion coefficient of the wetting liquid determines the expansion of the wetting liquid and is temperature dependent. When the wetting liquid expands, the volume the wetting liquid occupies increases. In case of a partly saturated state of the porous medium exists, the degree of saturation increases to at the most a fully saturated state. When the volume of the wetting liquid wants to expand more than there is space available in the voids of the porous medium, the porous medium not only becomes fully saturated but also the pressure in the wetting liquid increases. This behaviour can thus be used to model the evaporation and subsequent increase in pore pressure.

When the heat of a fire penetrates the cross section, it causes the temperature inside the concrete to increase and a temperature gradient to be present. The evaporation of water, from the pores of the concrete, starts at a temperature of 100 ^{o}C and results in an increase in pore pressure due to the fact that water expands rapidly when evaporated. The general idea is to use the expansion coefficient of the wetting liquid to model this behaviour. When the temperature is below 100 ^{o}C the wetting liquid behaves like water and thus follows the expansion coefficient of water. However, when the temperature increases to 100 ^{o}C and higher the evaporation process starts and thus the wetting liquid has to expand rapidly to simulate the evaporation of water and the development of pore pressures. After some time all the water is evaporated from the pores of the concrete and the evaporation process stops. From the behaviour of the analytical model it was observed that the evaporation of the main part of water from the pores of the concrete starts at a temperature of 100 ^{o}C and continues to a temperature of around 150 ^{o}C. Therefore the assumption is made that at a temperature of 150 ^{o}C all the water is evaporated into water vapour, which means that the expansion coefficient, in the temperature interval of 100-150 ^{o}C, is determined from a mixture of water and water vapour. In case the temperature further increases and wetting liquid is still present in that part of the model, this wetting liquid then behaves like water vapour. This approach ensures that the wetting liquid consist out of three phases, which are water, a mixture of water and water vapour and solely water vapour.

To further complete the behaviour of the wetting liquid is the addition of the porous bulk modulus of the wetting liquid. The bulk modulus is the resistance of a substance to a uniform compression. It is defined as the pressure increase needed to give the substance a relative decrease in volume. The bulk modulus can thus be used to model the compressibility of the wetting liquid. This is important, because in the temperature range of 100 – 150 ^{o}C, when the water is evaporated into water vapour, the wetting liquid simulates this phase change and therefore changes from being relative incompressible (water) to being relative compressible (water vapour). In case the porous bulk modulus is neglected to define, then the behaviour of the wetting liquid would be far to stiff. The wetting liquid would react as incompressible and lead to excessive pore pressures.

Finally, the behaviour of the wetting liquid is also described by the sorption curve of the material, which defines the relationship between the degree of saturation and the pressure in the wetting liquid through sorption curves. There are two sorption curves, the absorption curve (intake of water) and exsorption curve (release of water). In ABAQUS the porous medium becomes partly saturated when the pressure in the wetting liquid becomes negative, while the porous medium is fully saturated when the pressure in the wetting liquid is zero. By defining a suitable sorption curve the pressure in the wetting liquid in the partly saturated state can be defined and thus the difference in wetting liquid pressure which causes the wetting liquid to flow in that part of the cross section which is in a partly saturated state.

The described material behaviour is implemented in the Pore fluid/Stress model and is extended with the permeability, the porosity and the initial degree of saturation. The permeability is required, because the flow of the wetting liquid is based upon Darcy's law. The porosity and initial degree of saturation are needed to define the degree of saturation throughout the cross section.

By adapting the behaviour of the wetting liquid, the previously mentioned drawback is overcome and the Pore fluid/Stress model can be used to predict spalling. The general idea on how to predict spalling is depicted in figure 6.5, which gives a schematic representation of the developed numerical model. The three main parts are indicated by a red rectangle and the output and input for every part of the numerical model is indicated by a green rectangle.

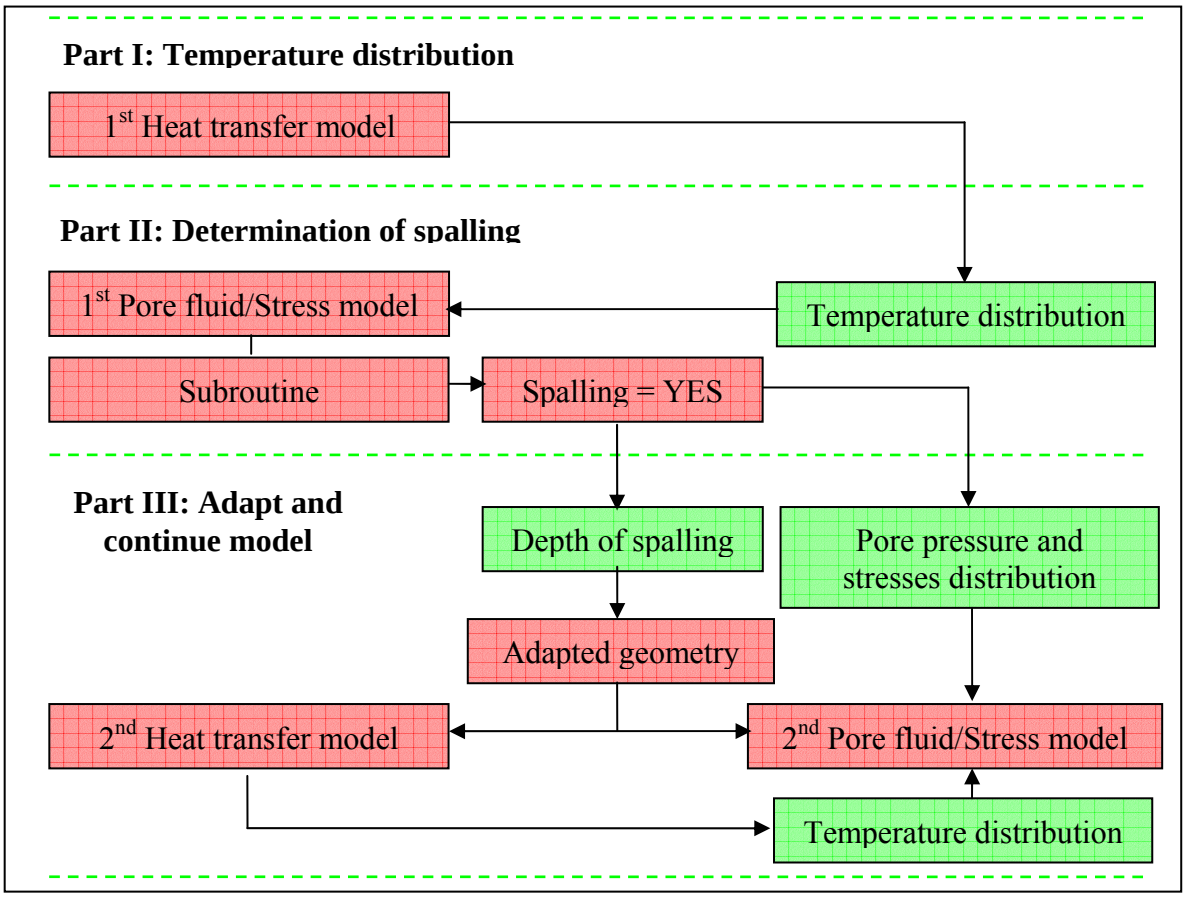

Figure 6.5 schematic representation of the numerical model

The Pore fluid/Stress model (1st Pore fluid/Stress model) determines the flow of the wetting liquid through the concrete, the saturation and pore pressures distribution, the resulting stresses from these pore pressures, the stresses from the temperature distribution, the strains and displacements [1]. These results describe the complete behaviour of the concrete during exposure to a fire. The driving force in this process is the temperature distribution and temperature gradient throughout the cross section. These are determined in the temperature model (1st temperature model) and used as input in the Pore fluid/Stress model. The heat transfer model provides the temperature distribution throughout the cross in a number of time steps and by using a mesh with a number of elements. These results are then mapped onto the mesh of the Pore fluid/Stress model and if necessary interpolated to obtain the temperature at the required position and time. Furthermore, a criterion should be included when spalling occurs. The general idea is to check in the model the resulting stresses and to determine if the limit tensile stress of the concrete is exceeded. The stresses used for this check are the stresses acting perpendicular on a plain parallel to the surface of the concrete, which is depicted in figure 6.6. These stresses lead to cracks parallel to the surface of the concrete and then the pore pressure can spall of the layer in front of this crack.

The check is done automatically at the end of each time step by including a subroutine which checks the critical stresses against the limit tensile stress of the concrete. When the limit tensile stress is exceeded, the subroutine determines the thickness of the layer which is to be spalled of the concrete and stops the calculation. The thickness is determined by searching for the critical stress which exceeds the limit tensile stress and is situated the furthest away from the surface of the concrete. Furthermore, the subroutine also writes to a file the pore pressure and the stress distribution throughout the cross section of concrete at the end of the time step at which spalling is predicted.

The calculation is resumed by adapting the geometry of the heat transfer model (2nd temperature model) to exclude the spalled of layer. The heat transfer model is then used to determine the adapted temperature distribution. The geometry of the Pore fluid/Stress model (2nd Pore fluid/Stress model) is also adapted to exclude the spalled of layer.

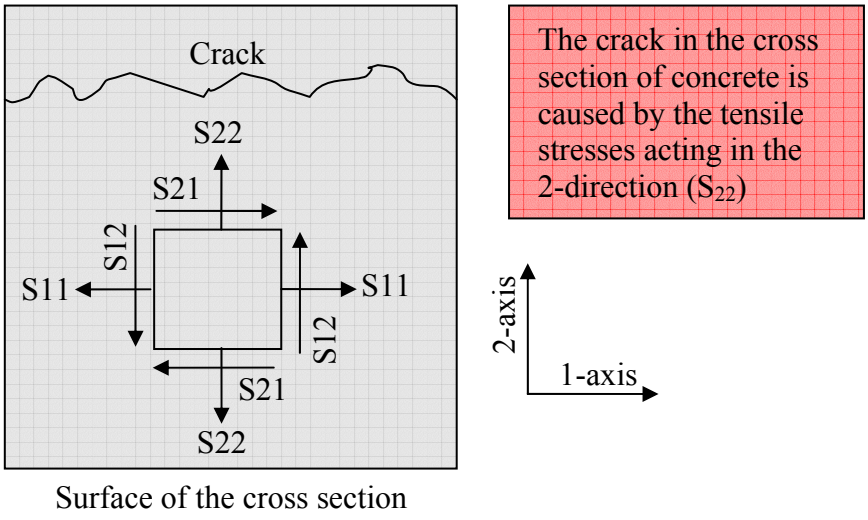

Fig 6.6 Sign convention used in ABAQUS

Furthermore, the pore pressure and stress distribution obtained at the end of the last time step, at which spalling occurred in the 1st Pore fluid/Stress model, are mapped onto the adapted geometry at the first time step of the new calculation. This is done, because the pore pressure, stresses and saturation distribution of the remaining cross section of concrete does not change when a layer is spalled of the surface of concrete. These distributions remain in the cross section and have to be taken into account, because the remaining cross section of concrete is not in a initial state. The calculation then continues until the criterion for spalling again is obtained.

6.4.2. Theory

The behaviour of the porous medium is described by an effective stress principle [1]. The total stress acting at a point, the "effective stress", is assumed to be made up of an average pressure stress in the wetting liquid, called the "wetting liquid pressure", an average pressure stress in the other fluid and a "mechanical stress". In equation 6.15 the effective stress principle is depicted [1].

$$\bar{\sigma}^* = \sigma + (Xu_{wet} + (1 - X)u_a) \tag{6.15}$$

In which
$\bar{\sigma}^*$ = effective stress [Pa]
σ = mechanical stress [Pa]
u_{wet} = wetting liquid pressure [Pa]
u_a = average stress in the other fluid [Pa]
X = factor dependent on the saturation. In case of a fully saturated medium X is 1,0 and is case of a partly saturated medium X is between 0,0 and 1,0. Normally X is chosen equal to the degree of saturation. [-]

The effective stress can be simplified when the assumption is made that the pressure in the non wetting liquid is constant throughout the domain being modelled, does not vary with time and is small enough that it can be neglected. Therefore the effective stress can be simplified to equation 6.16 [1].

$$\bar{\sigma}^* = \sigma + Xu_{wet} \tag{6.16}$$

Besides the effective stress principle also the equilibrium statement of a porous medium is used. Equilibrium is described by using the principle of virtual work for a volume, which is depicted in equation 6.17 [1]. The term on the left hand side is the internal energy of the system and the terms on the right hand side represent the external energy or the loading. The last term on the right hand side represents the weight of the wetting liquid.

$$\int_V \sigma : \delta\varepsilon dV = \int_S t \cdot \delta v dS + \int_V f \cdot \delta v dV + \int_V (sn + n_{trap})\rho_w g \cdot \delta v dV \tag{6.17}$$

In which
δv = virtual velocity field
$\Delta\varepsilon = \partial\delta v / \partial x$, virtual rate of deformation
σ = stress [Pa]
t = surface traction per unit of area [Pa/m^2]
f = body force per unit of volume [Pa/m^3]
$f_w = (sn+n_{trap})\rho_w g$, weight of the wetting liquid [kg]

ρ_w = density of the wetting liquid [kg/m^3]
g = gravitational acceleration constant [m/s^2]
s = V_{wet}/V_{void}, saturation [-]
n = V_{void}/V, porosity of the medium [-]
n_{trap} = V_{trap}/V, volume of trapped wetting liquid per unit of current volume [-]

The obtained equation 6.17 is numerically solved by approximating the equilibrium by using shape functions, which was already demonstrated in the solution procedure for the heat transfer analysis problem. The virtual work equation 6.17 then becomes equation 6.18 [1].

$$\delta v^N \int_V \beta^N : \sigma dV = \delta v^N \left[\int_S N^N \cdot t dS + \int_V N^N \cdot f dV + \int_V (sn + n_{trap}) \rho_w N^N g dV \right] \quad (6.18)$$

In which
$\delta v = N^N \delta v^N$
$\delta \varepsilon = \beta^N \delta v^N$
N^N = shape functions
B^N = derivative of the shape functions

This equation can be further simplified to a more basic form by grouping terms, which is depicted in equation 6.19. This equation describes the discretized equilibrium between the internal and external forces and the degree of freedom present in this equation are the displacements in both directions [1].

$$I^N - P^N = 0 \quad (6.19)$$

In which

$$I^N = \int_V \beta^N : \sigma dV$$

$$P^N = \int_S N^N \cdot t dS + \int_V N^N \cdot f dV + \int_V (sn + n_{trap}) \rho_w N^N g dV$$

In ABAQUS a porous medium is approximated by attaching the mesh to the solid material and allowing the liquid to flow through the solid material and thus through the mesh. Therefore besides an equilibrium equation also a continuity equation for the wetting liquid is necessary [1]. This continuity equation equates the rate of increase in wetting liquid mass stored at a point to the rate of mass of wetting liquid flowing into the point within the time increment. The fundamental basis for this continuity equation is Darcy's law. The excess wetting liquid pressure is the degree of freedom and is the force which drives the flow of wetting liquid through the material [1].

The continuity equation is derived from a volume containing a fixed amount of solid matter. The wetting liquid can flow through this volume when it is driven by a pressure difference in the wetting liquid. The total mass of wetting liquid in the volume is depicted in equation 6.20 [1].

$$\int_V \rho_{wet} \left[V_{wet} + V_{trap} \right] = \int_V \rho_{wet} (n_{wet} + n_{trap}) V \quad (6.20)$$

In which
ρ_{wet} = mass density of the wetting liquid [kg]
n_{wet} = V_{wet}/V, volume ratio of free wetting liquid [-]

The left- and right hand side of equation 6.20 are differentiated with respect to the time to obtain the time rate change of mass of the wetting liquid in the volume, which is depicted in equation 4.21. Besides this equation also a description of the rate of mass of wetting liquid flowing into the volume per unit of time is needed, which is depicted in equation 4.22 [1].

$$\frac{d}{dt}\left(\int_V \rho_{wet}\left[V_{wet}+V_{trap}\right]\right)=\int_V \frac{1}{J}\frac{d}{dt}\left(J\rho_{wet}(n_{wet}+n_{trap})\right)V \tag{6.21}$$

$$-\int_S \rho_{wet} n_{wet}\,\bar{n}\cdot v_{wet}\,dS \tag{6.22}$$

In which J = Jacobian matrix

$\bar{n}$ = outward normal to the surface (S)

v_{wet} = average velocity of the wetting liquid relative to the solid phase [m/s]

Both equations, 6.21 and 6.22, are equated to obtain the liquid mass continuity equation 6.23.

$$\int_V \frac{1}{J}\frac{d}{dt}\left(J\rho_{wet}(n_{wet}+n_{trap})\right)V=-\int_S \rho_{wet} n_{wet}\,\bar{n}\cdot v_{wet}\,dS \tag{6.23}$$

By making use of the divergence theorem and after some further elaborations the weak form is obtained. This relationship is the continuity equation and is depicted in equation 6.24 [1].

$$\int_V \delta u_{wet}\frac{1}{J}\frac{d}{dt}\left(J\rho_{wet}(n_{wet}+n_{trap})\right)dV+\int_V \delta u_{wet}\frac{\partial}{\partial x}\cdot(\rho_{wet} n_{wet} v_{wet})dV=0 \tag{6.24}$$

In which δu_{wet} = arbitrary variational field that satisfies the boundary conditions

This continuity equation is integrated approximately in time by the backward Euler formula, which can be written in a general form as in equation 6.25 [1].

$$a_{n+1}=a_n+\Delta t\,\dot{a}_{n+1} \tag{6.25}$$

In which a_{n+1} = variable to be solved at position 'n+1'

a_n = variable at position 'n'

The discretized equilibrium equations of 6.19 and the continuity equation 6.24 define the state of the porous medium. Both equations are solved as a coupled system by using the Newton Method and full Gauss integration schemes after which the nodal degree of freedoms are solved. In the previous paragraph the solution procedure was already elaborated.

The mechanical behaviour of the porous medium consists of the response of the wetting liquid and the solid material to the local pressure and of the response of the

overall material to the effective stress. To obtain these responses a constitutive law is necessary for the wetting liquid as well as the solid matter, which are the grains [1].
The constitutive behaviour of the wetting liquid is based on the assumption depicted in equation 6.26[1]. The right hand side of the equation consist out of a part contributed by the pressure in the wetting liquid and a part caused by the temperature change.

$$\frac{\rho_{wet}}{\rho^{o}_{wet}} \approx 1 + \frac{u_{wet}}{K_{wet}} - \varepsilon^{th}_{wet} \tag{6.26}$$

In which
ρ_{wet} = density of the wetting liquid [kg/m^3]
ρ^{o}_{wet} = density of the reference configuration of the wetting liquid [kg/m^3]
K_{wet} = bulk modulus of the wetting liquid [Pa]
$\varepsilon^{th}_{wet} = 3\alpha_{wet}(\theta - \theta^{o}_{wet}) - 3\alpha_{wet}\big|_{\theta^I}(\theta^I - \theta^{I}_{wet})$, volumetric strain of the wetting liquid caused by a temperature change [-]
α_{wet} = thermal expansion coefficient of the wetting liquid [1/C]
θ = temperature [C]
θ^I = initial temperature [C]
θ^{o}_{wet} = reference temperature for thermal expansion [C]

Furthermore the constitutive behaviour of the grains is assumed to be based on equation 6.27 [1]. The right hand side of this equation consist out of a contribution of the pressure in the wetting liquid and a contribution by the temperature change.

$$\frac{\rho_{grains}}{\rho^{o}_{grains}} \approx 1 + \frac{1}{K_{grains}}\left(su_{wet} + \frac{\bar{p}}{1 - n - n_{trap}} \right) - \varepsilon^{th}_{grains} \tag{6.27}$$

In which
K_{grains} = bulk modulus of the solid material [Pa]
$\varepsilon^{th}_{grains} = 3\alpha_{grains}(\theta - \theta^{o}_{grains}) - 3\alpha_{grains}\big|_{\theta^I}(\theta^I - \theta^{I}_{grains})$, volumetric strain of the grains caused by a temperature change [-]
α_{grains} = thermal expansion coefficient of the grains [1/C]
θ^{o}_{grains} = reference temperature for thermal expansion [C]

The "effective strain" of the total material consists out of the strain on the grains and a strain due to entrapped wetting liquid. The 'effective strain" is assumed to modify the "effective stress" and is depicted in equation 6.28[1].

$$\bar{\varepsilon} = \varepsilon + \left(\frac{1}{3}\left(\frac{su_{wet}}{K_{grains}} - \varepsilon^{th}_{grains} \right) - \frac{1}{3}\ln\left(1 + Jn_{trap} - n^{o}_{trap}\right) \right) \tag{6.28}$$

The flow of the wetting liquid is described by the continuity equation and also a constitutive law. The basic behaviour of the wetting liquid is based upon Darcy's law [1]. Darcy's law was already mentioned in chapter 5, but in ABAQUS an adapted version is used. In equation 6.29 the adapted Darcy's law is depicted with the left hand side of this equation representing the volumetric flow rate of the wetting liquid through a unit area. The gravitational acceleration constant is assumed to be constant.

$$snv_{wet} = -k \cdot \frac{\partial \varphi}{\partial x} \tag{6.29}$$

In which k = permeability of the medium [m/s]

$\varphi = z + \frac{u_{wet}}{g_I \rho_{wet}}$, piezometric head

$$\frac{\partial \varphi}{\partial x} = \frac{1}{g_I \rho_{wet}} \left(\frac{\partial u_{wet}}{\partial x} - \rho_{wet} g \right)$$

$$g = -g_I \frac{\partial z}{\partial x}$$

z = elevation above a datum plane [m]
g_I = magnitude of the gravitational acceleration [m/s]
g = gravitational acceleration [m/s]

Furthermore, also the material properties of the wetting liquid need further elaboration. In the description of the general idea behind the Pore fluid/Stress model the important material properties of the wetting liquid were already mentioned. However, the determination of these properties is described in more detail in this paragraph. The first important material property of the wetting liquid, is the expansion coefficient. The behaviour of the wetting liquid is subdivided into three phases. In the first phase the expansion coefficient is equal to the expansion coefficient of water. In table 6.2 these expansion coefficients are depicted.

Temperature [^{o}C]	**Expansion coefficient [1/C]**
20	0,000207
100	0,000752

Table 6.2 expansion coefficient of the wetting liquid in the temperature range of 20 – 100 °C

In the third phase, the wetting liquid behaves like water vapour which means like a gas. The general idea is to calculate, by using the ideal gas law, the expansion of a unit amount of water when this unit amount of water is being heated up from a temperature of 20 ^{o}C to a temperature of 150 ^{o}C and higher. This then can be used to determine the expansion coefficient. In figure 6.7 the calculation of the expansion coefficient is depicted. This calculation can be repeated for increasing temperatures to obtain the expansion coefficient for the wetting liquid in the temperature range of 150 ^{o}C – 500 ^{o}C, which is depicted in table 6.3. The expansion coefficient decreases with increasing temperature, due to the large strain definition used in ABAQUS.

The second phase of the wetting liquid behaves like a mixture of water and water vapour. This mixture of water and water vapour changes at every temperature and determines the development of the pore pressure. To obtain a first estimate of this part of the expansion coefficient curve, the curve is fitted between the end of the first phase and the beginning of the third phase. In table 6.4 the expansion coefficient for the wetting liquid in the temperature range of 100 – 150 ^{o}C is depicted.

Initial temperature = 20 ^{O}C
Initial amount of water = 1,0 m^3 (unit cube of water)

molecular mass of water =>	18,02 g/mol
density of water of 20 ^{o}C =>	998,3 kg/m^3
weight of the water =>	998,3 kg/m^3
number of mol =>	55399,56 mol

At a temperature of 150 ^{o}C, the initial amount of water expands under the assumption that the pressure remains constant at the atmospheric pressure:

$$V_{150} = \frac{nRT}{P} = \frac{55399{,}56.8{,}3145.(150+273{,}15)}{101325} = 1923{,}62m^3$$

The cube of water expands in all three directions. The lengths of the cube expand from 1,0 m to $L_{150} = \sqrt[3]{V_{150}} = \sqrt[3]{1923{,}62} = 12{,}44m$

The large strain definition in ABAQUS => $\varepsilon^{th} = \ln\frac{L_\theta}{L_o} = \ln L_\theta = \frac{1}{3}\ln V_\theta = \alpha\Delta T$ [1]

in which L_θ = length of side of the unit cube at temperature θ
L_o = initial length of the side of the unit cube = 1,0 m
α = expansion coefficient

$$\alpha = \frac{\frac{1}{3}\ln V_{150}}{\Delta T} = \frac{\frac{1}{3}\ln 1923.62}{150-20} = 0{,}019\,39\ 1/C$$

Fig 6.7 calculation of the expansion coefficient of the wetting liquid at 150 °C

Temperature [^{o}C]	Volume [m^3]	Expansion coefficient [1/C]
150	1923.624	0.019390
160	1969.084	0.018060
180	2060.003	0.015897
200	2150.922	0.014210
220	2241.841	0.012858
240	2332.761	0.011750
260	2423.68	0.010824
280	2514.599	0.010038
300	2605.518	0.009364
320	2696.438	0.008777
340	2787.357	0.008263
360	2878.276	0.007809
380	2969.195	0.007404
400	3060.115	0.007041
500	3514.711	0.005670

Table 6.3 expansion coefficient of the wetting liquid in the temperature range of 150 – 500 °C

Temperature [^{o}C]	Expansion coefficient [1/C]
101	0.00100
102	0.00200
104	0.00400
106	0.00500
108	0.00800
110	0.00900
120	0.01200
130	0.01500
140	0.01800

Table 6.4 expansion coefficient of the wetting liquid in the temperature range of 100 – 150 °C

The obtained expansion coefficient of the wetting liquid in the temperature range of 20 ^{o}C – 500 ^{o}C is depicted in figure 6.8.

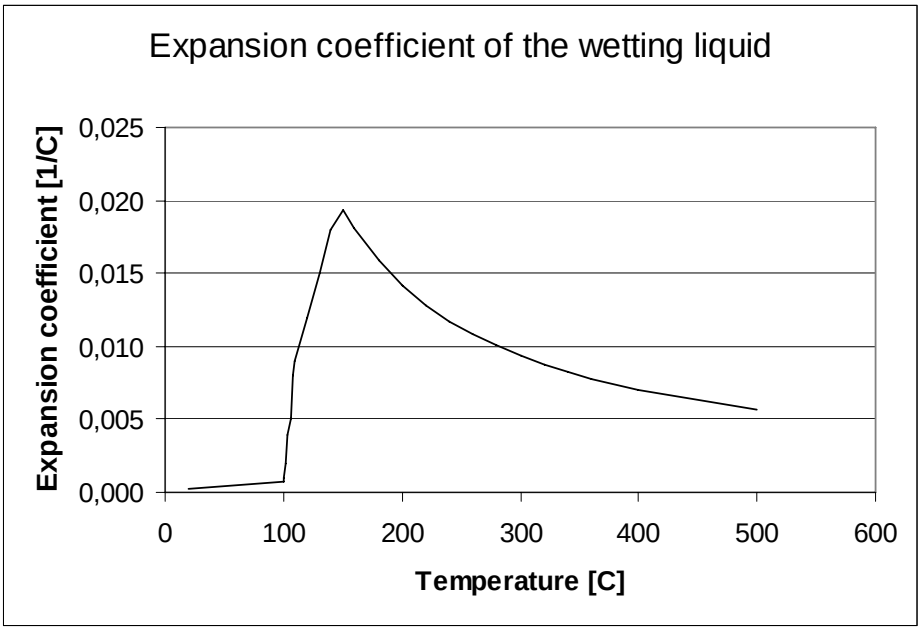

Fig 6.8 expansion coefficient of the wetting liquid in the temperature range of 20 °C – 500 °C

The second important material property of the wetting liquid, is the porous bulk modulus of the material, which is divided into two contributions, the first being the wetting liquid and the second the solid material. The general idea behind the calculation of the bulk modulus of the wetting liquid is that when the temperature of the material becomes 100 ^{o}C or higher, the wetting liquid rapidly expands. However, the solid material only gradually expands and not nearly as much as the wetting liquid. This means that the expansion of the wetting liquid is restrained by the solid material. This causes a pressure to be present in the wetting liquid. From this pressure, which is calculated using the ideal gas law and the strain in the wetting liquid, the bulk modulus can be calculated. However, to ensure that the behaviour of the wetting liquid is compressible when the evaporation process starts, the temperature at which the wetting liquid changes its behaviour is estimated at a temperature of 110 ^{o}C. In figure 6.9 the calculation of the bulk modulus of the wetting liquid is depicted.

Initial temperature = 20 ^{O}C
Initial amount of water = 1,0 m^3 (unit cube of water)

molecular mass of water =>	18,02 g/mol
density of water of 20 ^{o}C =>	998,3 kg/m^3
weight of the water =>	998,3 kg/m^3
number of mol =>	55399,56 mol

At a temperature of 100 ^{o}C, the initial amount of water expands. The solid material expands only slightly and therefore restrains the expansion of the wetting liquid and thus causing a pressure in the wetting liquid. The pressure in the wetting liquid at a temperature of 110 ^{o}C =>

$$P_{110} = \frac{nRT}{(1+\alpha_c \Delta T)} = \frac{55399{,}56.8{,}3145.(110+273{,}15)}{(1+1*10^{-5}*(110-20))} = 176{,}3MPa$$

The bulk modulus is defined as => $P = K_{wet}\varepsilon_{th}$

in which K_{wet} = bulk modulus of the wetting liquid

$$K_{wet} = \frac{P_\theta}{\varepsilon^{th}} => K_{110} = \frac{P_{110}}{\alpha^{th}_{110}\Delta T} = \frac{176{,}3*10^6}{0{,}02764(110-20)} = 7{,}087*10^7\,Pa$$

Fig 6.9 calculation of bulk modulus of the wetting liquid

In the temperature range of 20 ^{o}C – 100 ^{o}C the bulk modulus of the wetting liquid is equal to the bulk modulus of water. This calculation can be repeated for increasing temperatures, which is depicted in table 6.5.

Temperature [^{o}C]	**Pressure in the wetting liquid [Pa]**	**Bulk modulus of the wetting liquid [Pa]**
20		2.20E+09
100		2.20E+09
110	1.760E+08	7.076E+07
120	1.805E+08	7.233E+07
130	1.851E+08	7.390E+07
140	1.896E+08	7.546E+07
150	1.942E+08	7.702E+07
160	1.987E+08	7.858E+07
180	2.077E+08	8.167E+07
200	2.168E+08	8.474E+07
220	2.258E+08	8.780E+07
240	2.348E+08	9.084E+07
260	2.438E+08	9.386E+07
280	2.528E+08	9.686E+07
300	2.618E+08	9.985E+07
500	3.510E+08	8.332E+07

Table 6.5 bulk modulus of the wetting liquid in the temperature range of 20 °C – 500 °C

The second contribution to the bulk modulus of the material is by the grains. The bulk modulus of the grains is calculated by using equation 6.30.

$$K_{grains,\theta} = \frac{E_{c,\theta}}{3(1-2\upsilon)} => K_{grains,20} = \frac{3*10^{10}}{3(1-2.0{,}15)} = 1{,}43*10^{10} \qquad (6.30)$$

in which $K_{grains,\theta}$ = bulk modulus of the grains at a temperature [Pa]
υ = poisson ratio of the grains

The obtained bulk modulus of the wetting liquid and the grains is depicted in figure 6.10.

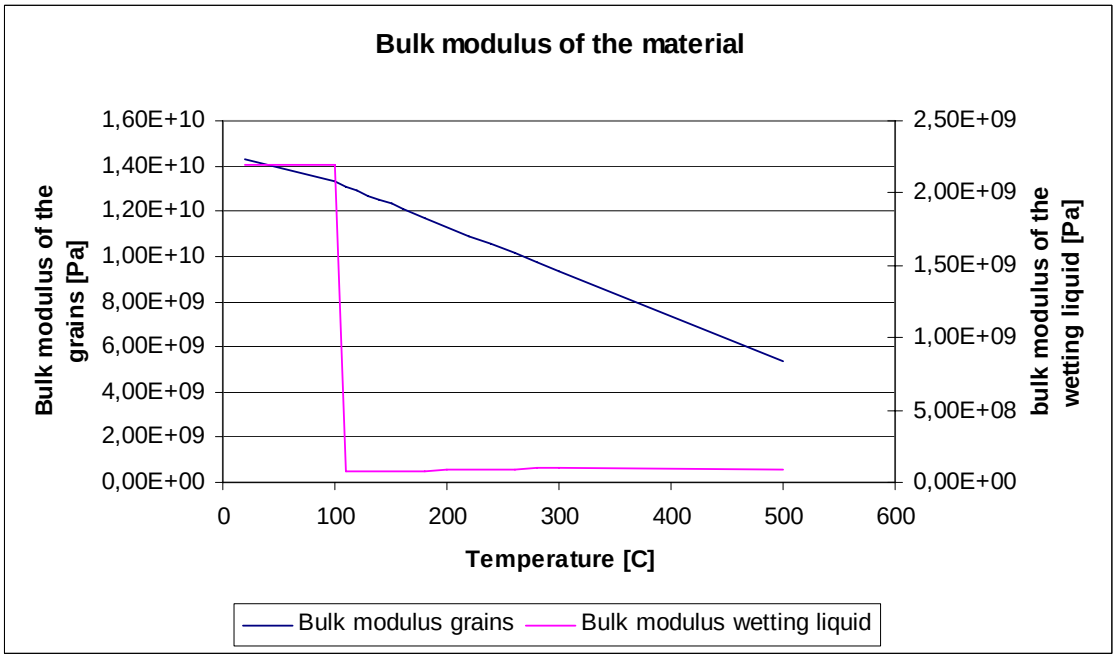

Fig 6.10 expansion coefficient of the wetting liquid and grains

6.4.3. Numerical implementation until spalling occurs

The Pore fluid/Stress model in ABAQUS is based on the same small strip of concrete which is used in the heat transfer model. The heat transfer analysis determines the temperature distribution through the cross section of concrete and these obtained results are used as input in the Pore fluid/Stress model. This model then determines the development of the pressure in the wetting liquid, the flow of the wetting liquid through the cross section of concrete, the saturation distribution and the resulting stresses. In the Pore fluid/Stress model also a FORTRAN based subroutine is implemented, which determines if the criteria are met that spalling occurs. The Pore fluid/Stress model is based upon six main components, which are the geometry, the material properties, the mesh, the boundary conditions, the steps in the analysis and the subroutines. These components are further elaborated and depicted in figure 6.12.

Geometry

The strip of concrete used in the Pore fluid/Stress model has the same geometry as the strip used in the heat transfer model. This means that the part is a solid and homogeneous part of concrete in two dimensions.

Material properties

The theory behind the Pore fluid/Stress model shows that the important material properties needed are the density, modulus of elasticity, expansion coefficient of the concrete, permeability, pore fluid expansion coefficient, porous bulk modulus, sorption curve and specific heat.

Mesh

The important aspect of the mesh is to ensure that the mesh is dense enough to ensure convergence of the solution, but coarse enough to save calculation time. Therefore the mesh of the Pore fluid/Stress model is biased, which means that the region close to the surface has a dense mesh, which becomes less dense into the cross section. The mesh consists out of, in depth direction, 400 elements with a height that increases per element in depth direction. The first element after the heated surface has a height of 0,25 mm and the element on the side opposite of the heated surface has a height of 2,55 mm. The mesh used is depicted in figure 6.11 and in the next paragraph it will be shown that the chosen mesh meets these requirements. The elements are quadrilateral, plane strain, Pore fluid/Stress elements with 4 nodes and per node the three degrees of freedom, which are the displacement in 1-direction, the displacement in 2-direction and the pore pressure [2]. The shape function for the displacement and the pore pressure are bilinear across the element [2].

Boundary conditions

The pore pressure model is a coupled pore pressure and stress model, which means that the pore pressure and the displacement u_1 and u_2 are a degree of freedom [2]. Therefore the boundary conditions can be described in each of these degrees of freedom. The first boundary condition is the pore pressure, which is being prescribed at the heated surface as being -4000 Pa. This value ensures that the pore pressure at the surface of the concrete remains constant and relative zero throughout the fire. Furthermore, this value also ensures that, when ABAQUS uses the sorption curve, the correct initial saturation is used at the edge of the element. The side opposite of the heated surface also is assigned the same boundary condition.

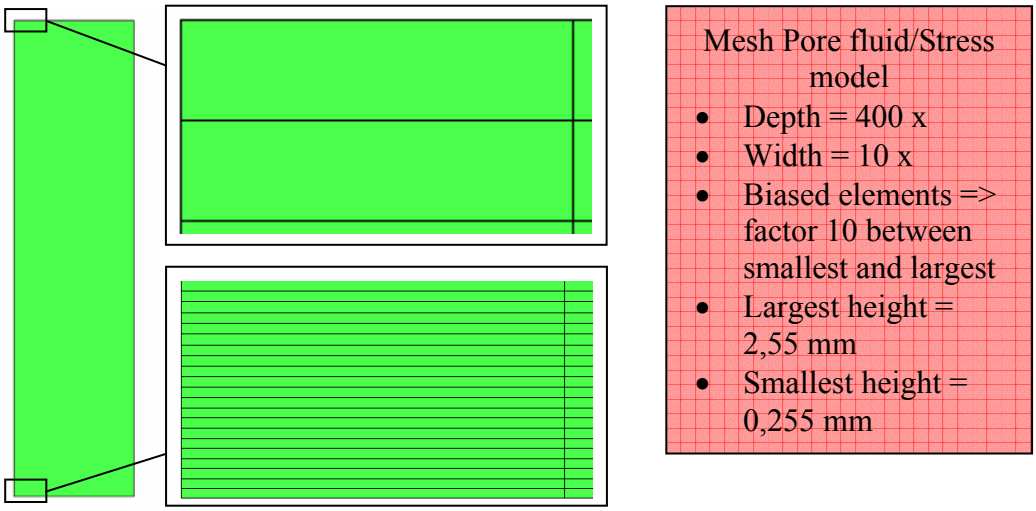

Fig 6.11 mesh used in the Pore fluid/Stress model

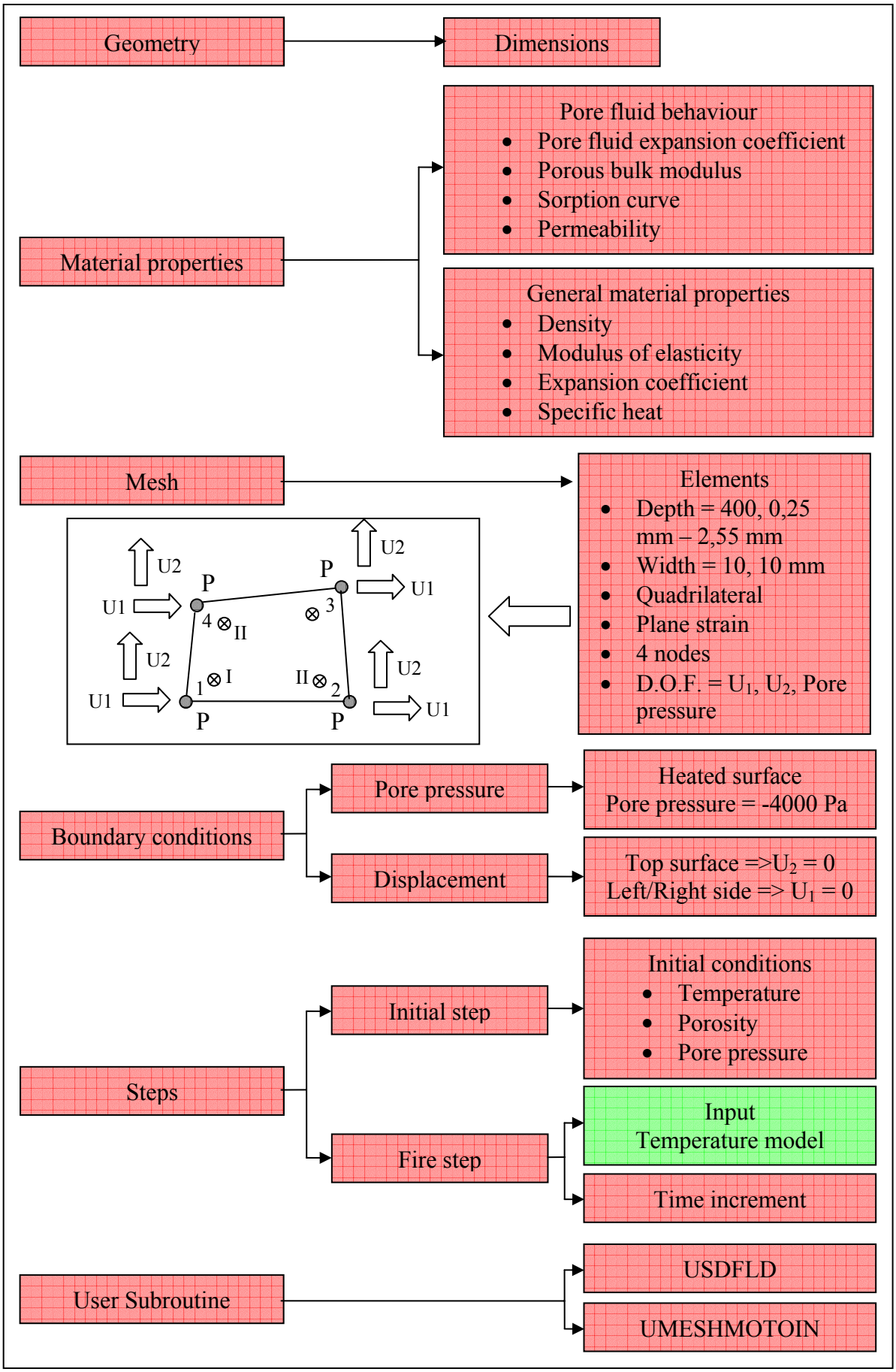

Fig 6.12 Basic parts of the Pore fluid/Stress model

The remaining boundary conditions are the restriction of displacement of the strip of concrete. To ensure this, the left and right edges of the part are restrained in movement in the u_1 direction and the top of the part is restrained in movement in the u_2 direction. The front or heated surface of the part is not restrained to ensure that this edge can expand due to the temperature increase.

Steps

The Pore fluid/Stress analysis consists out of two steps. The first step is the initial step. This step describes the initial conditions of the cross section of concrete [2]. The first initial condition is the pore pressure, which is prescribed throughout the entire cross section to be -4000 Pa. This value ensures that the pore pressure in the cross section is relative zero and that, when ABAQUS uses the sorption curve, the concrete initial saturation of 63% is used in cross section. The second initial condition is the porosity of the concrete, which is indicated in ABAQUS by the ratio and is set to 0,142. The third initial condition is the temperature throughout the cross section, which is prescribed to be 20 ^{o}C. The second step is the step in which the fire loading of the cross section of concrete takes place [2]. The results obtained from the temperature model are used as input. This means that ABAQUS uses the temperature distribution throughout the cross section of concrete as the starting point for the calculation in each time increment. In case the chosen time increment or position is not calculated by the temperature model, linear interpolation is used to determine the temperature distribution. Furthermore, the increment size is chosen to be 1,0 second in this calculation.

User subroutine

The finite element program ABAQUS has the possibility to include a FORTRAN based subroutine [3]. This subroutine consists out of predefined variables and commands which can be called to be used in the subroutine. These variables can either be variables to be defined by the user or variables which are passed in to the subroutine already containing information, such as coordinates [3]. In the numerical model the subroutine used contains four parts. The first and second part is used to determine whether spalling occurs in the model. The third and fourth part is used to restart the calculation after spalling has occurred and are explained in the next paragraph. The complete used subroutine is depicted in appendix D.

The first part of the subroutine is called USDFLD. This subroutine is used to store information from the model, into common blocks. This information then can be used in other subroutines. In the USDFLD the information is called at each integration point in each element by the command GETVRM [3]. For the determination if spalling occurs in the model, the stresses at each integration point in each element have to be saved. The important stress is s_{22}, which acts perpendicular on a plane parallel to the surface of the concrete. In figure 6.13 the important part of the USDFLD is depicted.

The second part of the subroutine is called UMESHMOTOIN [3]. This subroutine is used to implement user defined ALE adaptive meshing [2]. ALE adaptive meshing is a tool that makes it possible to maintain a high quality mesh throughout the analysis, even when large deformations or loss of material occurs [2]. This is accomplished by allowing the mesh to move independently from the material. The user subroutine UMESHMOTOIN is used to define the ALE adaptive meshing [2].

```
C GET STRESSES FROM PREVIOUS INCREMENT
      IF (SPALLING .NE. 1.0D0) THEN
        CALL GETVRM('S',ARRAY,JARRAY,FLGRAY,JRCD,JMAC,JMTYP,
     1      MATLAYO,LACCFLA)
        Sstress(1,NOEL,NPT) = coord(1)
        Sstress(2,NOEL,NPT) = coord(2)
        Sstress(3,NOEL,NPT) = ARRAY(1)
        Sstress(4,NOEL,NPT) = ARRAY(2)
        Sstress(5,NOEL,NPT) = ARRAY(2)
```

in which SPALLING = parameter which is checked if spalling is present
Sstress(x,NOEL,NPT) = matrix of information stored by USDFLD at each integration point of each element. This matrix has 5 columns (x): coordinate in 1-direction, coordinate in 2-direction, s_{11}, s_{22}, s_{22}
NOEL = element number
NPT = integration point number

Fig 6.13 part of the USDFLD subroutine which calls and stores the stresses at each integration point in each element

The general idea behind UMESHMOTOIN is that ABAQUS calls this routine in every increment for every node on the surface and starts to check the s_{22} stress behind this surface node. The stresses used for this check are taken from the stresses stored by the USDFLD subroutine. These stresses are called by implementing a loop over all the stored points. However, the USDFLD calls and stores these stresses at the integration points where as UMESHMOTOIN is implemented on the nodes. To cope with this difference between integration points and nodes, a search routine is implemented. This search routine is called for every node on the surface of the cross section and determines the horizontal distance (the 1-direction) between each integration point and this node. If this distance is smaller than half of the elementsize, then this integration point is used to determine the S_{22} stress behind the surface node. This criterion is used to ensure that only the integration points, which are situated in the 1-direction close to the surface node, are used to estimate the s_{22} stresses behind this surface node. In figure 6.14 this part of the search routine is depicted. The integration points which fulfil the previous criterion are checked if they exceed the limit tensile stress of the concrete. In case that occurs, the coordinates of the integration point in the vertical direction (2-direction) together with the vertical coordinate of the surface node are used to determine the depth.

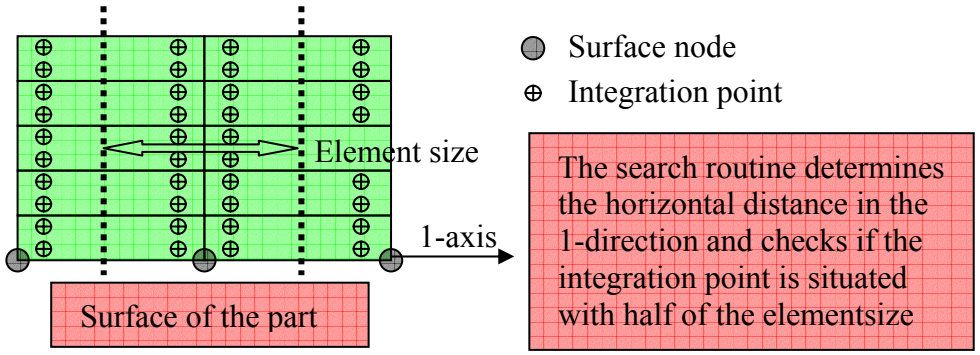

Fig 5.14 part of the search routine which determines if which stored integration point can be used as estimate for the stress behind the surface node

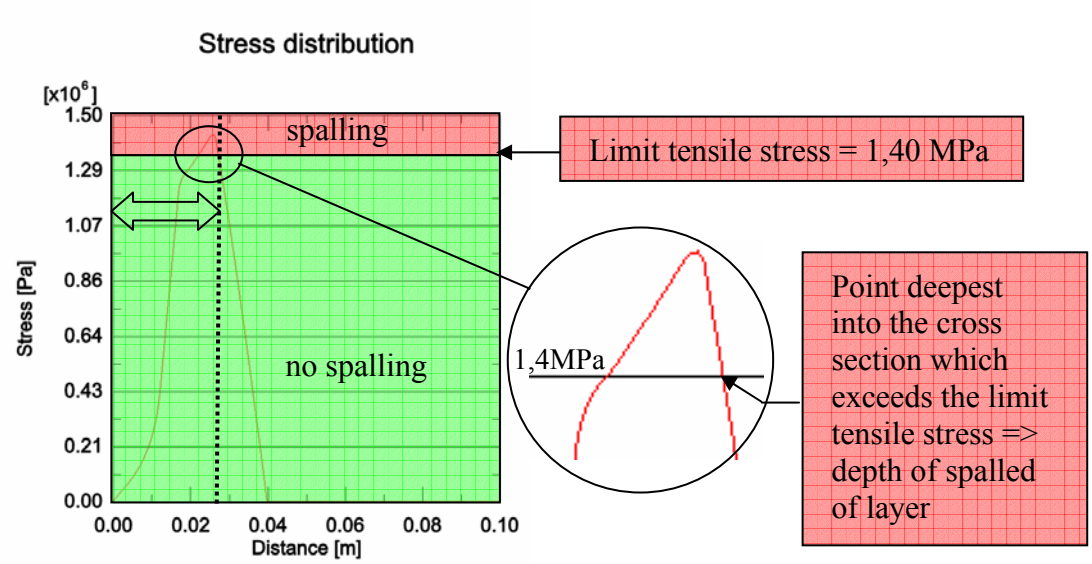

Fig 6.15 part of the search routine which determines the depth of the spalled of layer

The loop searches through all the integration points and obtains the deepest integration point which exceeds the limit tensile stress and the depth of this point is equal to the depth of the spalled if layer. This is used to include the total part of the cross section which exceeds the limit tensile stress. In figure 6.15 the part of the search routine which determines the depth of the spalled of layer is depicted. In figure 6.17 the part of the UMESHMOTOIN subroutine is depicted which searches for the integration points to be used and checks which of these integration points exceeds the limit tensile stress and is situated the deepest into the cross section.

```
C stresses to file for start up of next spatstep

      IF ((SPALLING .EQ. 1.0D0).AND.(ptIsDone.LT.1.0e15)) THEN
         Sstress(1, NOEL, NPT) = 1.0e16
         WRITE (7,*) 'OK, spalling is going on for node: ',
     1   TIME(2)

         open(unit=96,file='C:\Temp\PressureI.out',
     1   status='unknown',form='formatted')

C GET PORE PRESSURE FROM PREVIOUS INCREMENT
         CALL GETVRM('POR',ARRAY,JARRAY,FLGRAY,JRCD,JMAC,JMTYP,
     1   MATLAYO,LACCFLA)
         Pressure(1,NOEL,NPT) = coord(1)
         Pressure(2,NOEL,NPT) = coord(2)
         Pressure(3,NOEL,NPT) = ARRAY(1)
C        WRITE (7,*) 'Pressure = ', Pressure(1,NOEL,NPT),
C     1  Pressure(2,NOEL,NPT), Pressure(3,NOEL,NPT), NOEL

C WRITE PORE PRESSURE TO FILE
      WRITE(96,'(4e14.5)') SPALLING, coord(1),coord(2), pressure
```

PressureI.out consist out of 4 columns: Spalling parameter, coordinate in 1-direction, coordinate in 2-direction, pressure

Fig 6.16 Part of USDFLD which writes the pore pressure distribution to the file PressureI.out

```
      YCOORD = -1.0d7
      SPAT=0
      DO IPOS1=1,NELEMENTS
         DO IPOS2=1,IPOINTS
            XCOORD=Sstress(1,IPOS1,IPOS2)
            DIST=SQRT((XCOORD-ARRAY(1))**2.0d0)
C            WRITE(7,*) 'Afstand: ',IPOS1,IPOS2,XCOORD,DIST
              IF (DIST.LT.(elsize/2.0d0)) THEN
                 IF (Sstress(5,IPOS1,IPOS2).GT.Lstress) THEN
                    SPAT=1
                    IF (Sstress(2,IPOS1,IPOS2).GT.YCOORD) THEN
                       YCOORD=Sstress(2,IPOS1,IPOS2)
                       DEPTH = (YCOORD-ARRAY(2))
                       WRITE(7,*) 'SPATTEN: ',NODE,
     1                 Sstress(5,IPOS1,IPOS2),TIME(2),DEPTH
                    END IF
                 END IF
              END IF
         END DO
      END DO
```

in which XCOORD = coordinate in the 1-direction of the looped point
YCOORD = coordinate in the 2-direction of the looped point
ARRAY(1) = coordinate in the 1-direction of the surfacenode
ARRAY(2) = coordinate in the 2-direction of the surfacenode
NELEMENTS = number of elements in the model
IPOINTS = number of integration points in the model
Sstress(x,IPOS1,IPOS2) = stored matrix of information in USDFLD which is looped over by IPOS1 and IPOS2
elsize = length of the used elements in 1-direction
DIST = determination of the distance between integration point and surface node in the 1-direction
Lstress = limit tensile stress of the concrete
SPAT = parameter to indicate whether spalling is present in the model (0 = no spalling present, 1 = spalling is present)
NODE = node number
DEPTH = determination of the depth of the spalled of layer
SPATTEN = matrix of information stored by UMESHMOTOIN consisting of 4 columns: node number, s_{22}, total time, depth of the spalled of layer

Figure 6.17 part of UMESHMOTOIN which determines if spalling is present, the position and the depth of the spalled of layer

The results are written to the message file of the model, which can be seen by the write command followed by "SPATTEN". The matrix "SPATTEN" includes the number of the node, the stress S_{22}, the time and the depth of the spalled of layer.

In case spalling is indicated by UMESHMOTOIN, the subroutine furthermore stores the pore pressure and stress distribution throughout the cross section of concrete at the time increment at which spalling takes place. This is done by USDFLD and includes the GETVRM call for these distributions and the opening and write command of the pore pressure and the stress distribution to respectively PressureI.out and StressI.out. These distributions have to be written to a separate file, because the adapted model

cannot read from the message file of the previous model. Finally the calculation is stopped by UMESHMOTOIN by the command 'CALL XIT'. In figure 6.16 the part of USDFLD which writes the pore pressure distribution to the file PressureI.out is depicted.

6.4.4. Numerical implementation to resume the calculation

To resume the calculation, the geometry of both the heat transfer model as well as the Pore fluid/Stress model needs to be adapted to exclude the spalled of layer. For the Heat transfer model and the Pore fluid/Stress model the main components which change are indicated and the changes described.

Geometry

The geometry of the part used in the temperature model as well as the Pore fluid stress model is adapted to exclude the spalled of layer. The surface of the cross section of concrete is shifted into the interior of the cross section by a distance equal the thickness of the spalled of layer. In figure 6.18 this is depicted.

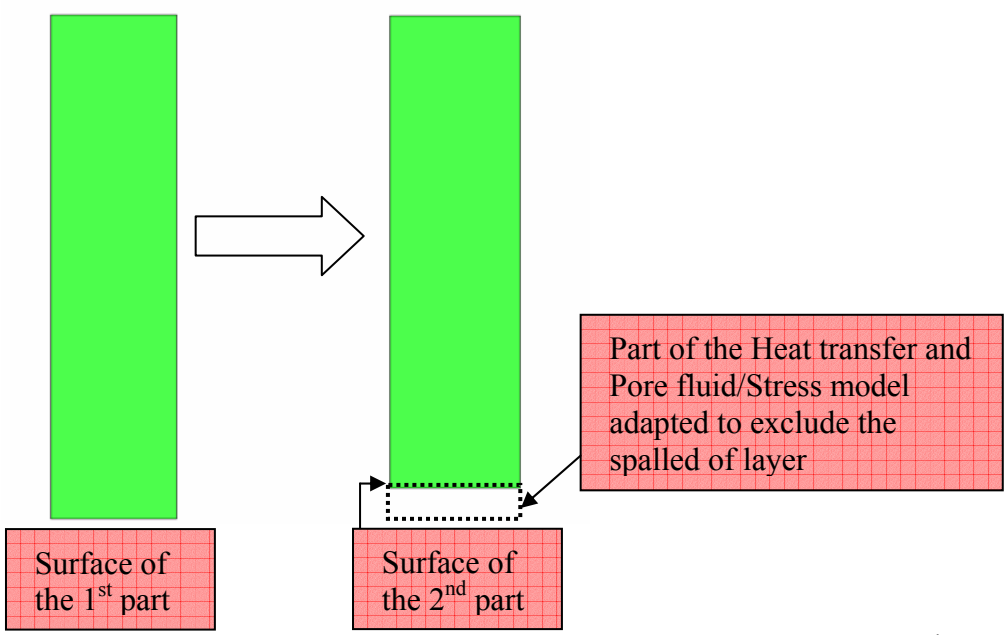

Fig 6.18 adapted part to exclude the spalled of layer and used in the 2nd Heat transfer and Pore fluid/Stress model

At the beginning of the development of the numerical model, the general idea was to use UMESHMOTOIN not only for the check on the stresses and to determine if spalling is present, but also to use the ALE adaptive meshing capabilities. In case spalling is present in the model, the depth of the spalled of layer is used to starts the ALE adaptive meshing technique and to 'wear' this layer from the cross section in a number of short time steps with a total time of around 1 second. After 1 second the layer is completely removed from the cross section, which means that the surface is shifted into the cross section. However, the ALE adaptive meshing caused the pressure in the wetting liquid to rapidly increase, which is most likely caused by the wetting liquid in this layer. The movement of the mesh causes the wetting liquid to also move into the cross section and due to the already present amount of wetting liquid, the pressure in the wetting liquid rapidly increases. To solve this problem

would take some time and therefore the decision was made to remove the spalled of layer manually from the part.

Mesh

The part of the Heat transfer model is meshed with a new mesh, with the same number of elements as the mesh of the first Heat transfer model. The part of the Pore fluid/Stress model is meshed in a biased way and with elements with the same dimensions. This is done to save in elements and calculation time.

Boundary conditions

In the Pore fluid/Stress model the boundary condition on the surface of the cross section of concrete is changes to a pore pressure of 0 Pa. This is done to be able to restart the calculation. The difference in pore pressure is negligible. Furthermore, the pore pressure distribution which is stored at the end of the first Pore fluid/Stress model determines the saturation.

Steps

The initial step of the Heat transfer model is adapted to include the temperature distribution which is already present in the remaining part of the cross section of concrete. The results from the first Heat transfer model at the time at which spalling takes place are used as the initial conditions for the second Heat transfer model. In the fire step, the amplitude function of the fire curve is adapted to exclude the time which is already used to obtain the first time spalling. The initial step of the Pore fluid/Stress model is adapted to include the temperature distribution which is already present in the remaining part of the cross section of concrete. The results from the second Heat transfer model are used, because these already include this temperature distribution. Furthermore, also the pore pressure, saturation and stress distributions throughout the cross section of concrete have to be included as initial conditions for the Pore fluid/Stress model. The saturation distribution is implicitly included by the pore pressure distribution and the sorption curve. The pore pressure and stress distributions throughout the cross section of concrete are included by two subroutines and the stored output file, at the end of the previous Pore fluid/Stress model, containing this information (PressureI.out, StressI.out).

User subroutine

In the Pore fluid/Stress model two additional subroutines are included to map the pore pressure and stress distributions, which are respectively the UPOREP and SIGINI. Both subroutines are identical, with the only difference being the pore pressure or the stresses which are being mapped. The subroutine UPOREP is further elaborated here. The pore pressures are stored by USDFLD, at the end of the first Pore fluid/Stress model, in an output file PressureI.out. The subroutine UPOREP has to map these pore pressures onto the new mesh of the second Pore fluid/Stress model. However, again USDFLD calls and stores the information at each integration point and UPOREP calls each pore pressure at the node. Furthermore, the nodes of the first Pore fluid/Stress model not necessarily and most like do not coincide with the node of the second Pore fluid/Stress model. Thus a search routine has to be implemented which searches through the stored pore pressures and calculates the pore pressure at the desired node. The general idea is to implement a weightfactor which includes the cross distance between each stored integration point and the node. A criterion of 0,5 * elementsize ensures that only the integration points near the node and thus with in the search zone

are used to determine the pore pressure at the node. Furthermore, this criterion also limits the number of integration points used. However, the sum of all these weightfactors should be equal to 1, thus ensuring that the estimated pore pressure is not overestimated. In case an integration point coincides with a node, the pore pressure at the integration point should be used. The search routine can mathematically be described as is depicted in figure 6.19.

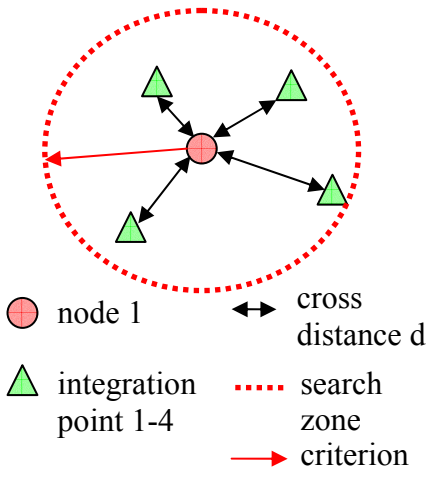

$$u_{wet,i} = \sum_{j=1}^{j=n} \left(w_j * u_{wet;j} \right),$$

$$w_j = \frac{c_j}{\sum_{i=1}^{i=n} c_i}, c_j = \sum_{i=1}^{i=n} d_i - d_j$$

example:

$$\sum d_i = d_1 + d_2 + d_3 + d_4$$

$$\sum c_j = \left(\sum d_i - d_1 \right) + \left(\sum d_i - d_2 \right) \ldots$$

$$u_{wet} = \frac{\sum d_i - d_1}{\sum c_i} * u_{wet,1} + \frac{\sum d_i - d_2}{\sum c_i} * u_{wet,2} \ldots$$

Fig 6.19 basic idea on the mapping of the pore pressure and the stress distribution is respectively UPOREP and SIGINI

6.4.5. Assumptions

In this part of the numerical model the following assumptions are made:

1. The evaporation, the flow of water vapour and the development of the pore pressure is simulated using a coupled Pore fluid/stress model. It is assumed that this model can form a general basis to model the process which leads to spalling.
2. The coupled Pore fluid/stress model simulates the flow of the wetting fluid through the material. However, this model only simulates the flow of wetting liquid in a single phase. To include in the model the evaporation of water from the pores of the concrete and the flow of water vapour due to a difference in pore pressure, the behaviour of the wetting liquid is adapted by defining the expansion coefficient and bulk modulus of the wetting liquid. Until the temperature of the concrete reaches 100 ^{o}C, the wetting liquid behaves like water. In the temperature interval of 100 ^{o}C-150 ^{o}C the wetting liquid behaves like a mixture of water and water vapour. With further increasing temperatures the wetting liquid behaves like water vapour. Furthermore, the sorption curve is added. It is assumed that the present material model is sufficient to implicitly model the evaporation of water and the flow of water vapour.
3. The behaviour of the material is linear elastic, which means that the solid material, the grains, behave according to Hooke's law ($\sigma = E * \varepsilon$). Furthermore, non linear effects such of cracking of concrete, creep and relaxation are neglected and no incorporated in this model.
4. The elements used in the mesh of the Pore fluid/Stress model are plane strain elements. This means that it is assumed that the normal strain in the outer plane direction is zero ($\varepsilon_{33} = 0$). It is then likely that the stress in the out-of-

plane direction is not equal to zero. This is reasonable for problems which are relatively thick in the third direction, such as a concrete wall.

5. The results from the Heat transfer model are used as input in this part of the model. The results of the Heat transfer model do not include the stagnation of the temperature penetration by the evaporation of water from the pores of the concrete.
6. The water vapour is considered an ideal gas. This means that the water vapour behaves according to the ideal gas law. This means that the expansion coefficient and the bulk modulus can be determined by using the ideal gas law.
7. The evaporable water which is generated during the decomposition process of the concrete is not taken into account. The water used in this calculation is the evaporable water which is present in the pores of the concrete under normal conditions.
8. For the calculation of the flow of water vapour Darcy's law is assumed. This means that the flow is assumed to be viscous and slow and the flow is therefore characterized as laminar.
9. The pore structure of the concrete is assumed to homogenous.
10. The influence of reinforcement on the water vapour transport is not taken into account.

6.4.6. Material properties used in the numerical model

The grade of the concrete used in the numerical simulation is B35 (C28/35).

Material property		**Temp. dependent**
Concrete grade	B35 (C28/35)	
Thickness	400 mm	
Width	100 mm	
Number of elements in depth direction	Height: 400 0,25 mm – 2,55 mm	
Number of elements in width direction	Width: 10, 10 mm	
Density	2400 kg/m^3	NO
Modulus of Elasticity	3*10^{10} N/m^2 at 20 ^{o}C (*)	YES
Expansion coefficient of the solid material (orthotropic)	1*10^{-5} 1/C	NO
Permeability	8,49*10^{-10} m/s at 20 ^{o}C (*)	YES
Porosity	0,142 at 20 ^{o}C (*)	YES
Pore fluid expansion coefficient [1/C]	Figure 5.7	YES
Porous bulk modulus [Pa]	Figure 5.9	YES
Sorption curve	(*)	N.A.
Specific heat	800 J/kgK	NO
Initial temperature	20 ^{o}C	
Initial ratio (porosity)	0,142	
Initial pore pressure	4000 Pa => initial degree of saturation = 63 %	

Table 6.6 material properties used in the Pore fluid/Stress model

The material properties of this type of concrete, which are used in the numerical model, are depicted in table 6.6. In the last column of this table the indication is given which of the material properties that are used are temperature dependent. The material properties indicated by (*) are graphically depicted in the Appendix C.

The permeability of the concrete used in the Pore fluid/Stress model is different from the permeability used in the analytical model. First of all is the dimension of the permeability different. In the analytical model the permeability has dimension [m^2] and in the Pore fluid/Stress model the dimension is [m/s]. However, according to the theory manual of ABAQUS the permeability are related through equation 6.31 [2].

$$K_{darcy} = \frac{\upsilon}{g} k_{ABAQUS} \tag{6.31}$$

in which K_{darcy} = permeability coefficient used in Darcy's law [m^2]
υ = kinematic viscosity of the wetting liquid [m^2/s]
g = gravitational acceleration constant [m/s^2]
k_{ABAQUS} = permeability coefficient used in ABAQUS [m/s]

For the permeability of the concrete at a temperature of 20 ^oC, the permeability to be used in ABAQUS can be obtained by using equation 6.31 resulting in equation 6.32.

$$K_{darcy;20} = \frac{\upsilon_{20}}{g} k_{ABAQUS;20} \Rightarrow 8{,}65 * 10^{-17} = \frac{1 * 10^{-6}}{9{,}81} k_{ABAQUS;20} \tag{6.32}$$
$$\Rightarrow k_{ABAQUS;20} = 8{,}49 * 10^{-10}\, m/s$$

The permeability at a temperature of 20 ^oC is used together with figure 4.22 to obtain the permeability distribution for increasing temperatures. However, in this temperature range the wetting liquid expands rapidly and the permeability of the concrete is insufficient to allow enough wetting liquid to flow towards the surface of the cross section to reduce the pore pressure build up. The Pore fluid/Stress model therefore develops large pore pressures close to the heated surface of the concrete and therefore spalling occurred frequently with a depth of a few millimetres. This process is spalling, but no explosive spalling. The problem in the Pore fluid/Stress model is that the model is only capable of one phase flow. This means that the evaporation of water into water vapour is not possible in the Pore fluid/Stress model. Furthermore, the phase change of water into water vapour caused the water to expand resulting in the pore pressure the increase. The pore pressure development is modelled in the Pore fluid/Stress model by the expansion coefficient of the wetting liquid. However, in the most important temperature range of 100 – 150 ^oC the expansion coefficient of the wetting liquid is fit between the expansion at a temperature of 100 ^oC and 150 ^oC, which means that the expansion coefficient of the wetting liquid is an assumption. The permeability and the pore pressure development, which means the expansion coefficient of the wetting liquid and the porous bulk modulus, are the major factors influencing the flow of the wetting liquid. The expansion coefficient of the wetting liquid, in this temperature range, is dependent on the exact amount of water and water vapour present in the model and this should be used to determine the exact expansion coefficient of the wetting liquid. However, this is not possible, because the Pore fluid/Stress model only has one phase flow and therefore the exact mixture of water and water vapour can not be determined. A number of expansion curves were tried,

but a progressing pore pressure peak was not obtained. Therefore, more attention was paid to the permeability of the concrete. The permeability was varied to obtain a progressing pore pressure peak. However, to obtain this pore pressure peak the permeability is increased in the temperature range of 100 -150 ^{o}C. This increase in permeability is not found in figure 4.22. However, the permeability of fig 4.22 is determined by subjecting a concrete specimen to a difference in water pressure and then determining the flow of water, in time, through the specimen at a constant water pressure gradient. The permeability obtained is therefore a permeability measurement for the complete concrete cross section. In the Pore fluid/Stress model the process of the flow of water vapour is through a small part of the cross section and is largely influenced by the degree of saturation and the liquid which is flowing. The permeability of the concrete decreases also when the degree of saturation increases, because it becomes more difficult for the water vapour to flow through the concrete. Furthermore, water vapour is capable of flowing through smaller pores and interconnection spaces then water and therefore is the permeability also dependent on the liquid flowing through the concrete.

Furthermore, the first 20 – 30 mm of the cross section of concrete is not the same concrete quality as the rest of the cross section. This part of the cross section is close to the formwork and therefore has less aggregate and the cement paste is less developed. This leads to a more porous concrete pore structure which means that the permeability is higher. Therefore, the elevated permeability in the surface layer of the concrete is possible.

Finally, the above mentioned process indicates that the Pore fluid/Stress model is mostly determined by the expansion coefficient of the wetting liquid and the permeability. Therefore, a strong recommendation is made to include in a numerical model the evaporation of water and the resulting pore pressure development, because the analytical model demonstrates that by including theses effects the simplified permeability function can be used to obtain reliable results. Furthermore, more research has to be done into the permeability and the influence of the degree of saturation, the temperature and the liquid flowing through the concrete. Furthermore, the concrete cover should be further examined if the permeability is higher in this part of the cross section.

6.4.7. Results and analysis

Before the results and the analysis are given of the Pore fluid/Stress model, first the convergence of the developed numerical model should be checked. Convergence is an important issue when developing a new numerical model, especially when this model simulates a process which occurs in the first 50 mm or less of the model. Therefore it is important that the number of elements in the depth direction or sufficient to obtain a converged numerical solution. This means that the numerical solution does not change or only negligible when the number of elements in the depth direction are increased. However, to minimize the calculation time as much as possible, the number of elements in the depth direction of the cross section should be chosen as low as possible. In figure 6.20 the results of the convergence test are depicted. On the horizontal axis the different used meshes in depth direction of the cross section are depicted. The mesh is described by the total number of elements used and the height of smallest respectively the largest element in this mesh.

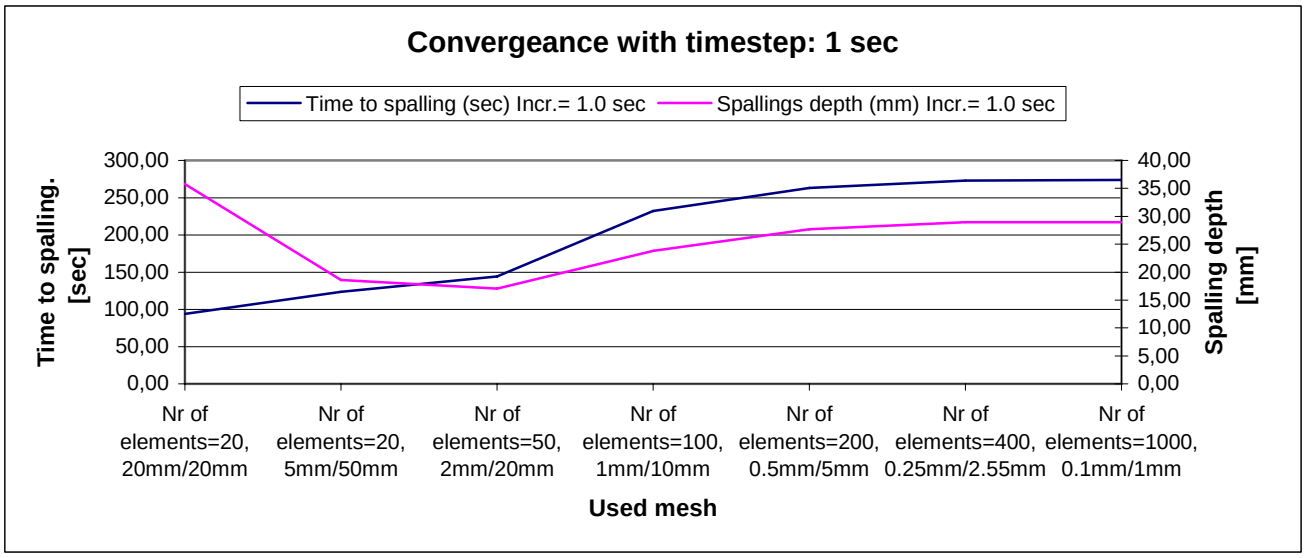

Fig 6.20 results convergence test for the number of elements in depth direction

The smallest element is situated at the heated surface and the largest element on the opposite side of the heated surface. The results are obtained for a time step size of 1 second and a fire curve which increases the temperature of the surface of the cross section in 5 minutes from a temperature of 20 ^{o}C to 500 ^{o}C. The graph indicates that the coarsest mesh, the mesh with 20 elements all with the same size in depth direction, estimate the time of spalling around 94 seconds and a depth of 36 mm. When this mesh is refined to a mesh with also 20 elements, but with smaller elements at the surface of the cross section, the Pore fluid/Stress model estimates the time of spalling around 124 seconds and a depth of 19 mm. This is an extra time of 30 seconds or 32 percent and more important reduction in depth of 17 mm or 47 percent. This illustrates the importance for the Pore fluid/Stress model to test the convergence. When the mesh is further refined, the time of spalling and the depth gradually convergence to respectively 273 seconds and 29 mm. The convergence test also indicated that the difference between the meshes with respectively 400 and 1000 elements is negligible. Furthermore, the mesh with 200 elements estimates the time of spalling after 263 seconds and the depth 28 mm, which is more or less the same as the converged results.

Furthermore, also the chosen time step size is important, because this determines the number of steps needed to reach the time at which spalling occurs. In figure 6.21 the results from the convergence test are depicted. In this graph the time to spalling is compared to the calculation time required to obtain these estimates. The time step size used in this convergence test are 0,1 sec and 1,0 sec. When the estimates for the time to spalling for the time step size of respectively 0,1 sec and 1,0 sec are compared for each mesh, it can be seen that the difference in the obtained estimates is relative small. Furthermore, by decreasing the time step size to 0,1 sec, the amount of steps needed to obtain a result roughly increases by a factor 10. This can be clearly seen by the difference in calculation time for the different meshes, especially for the meshes with the largest amount of elements.

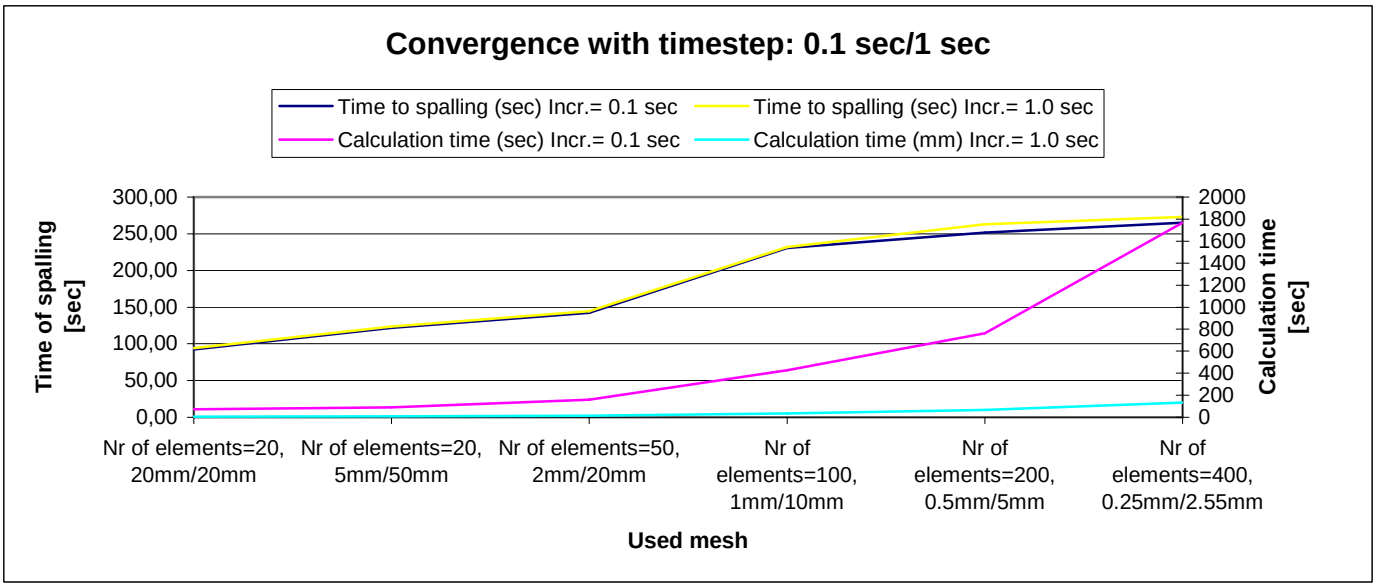

Fig 6.21 results convergence test for the time step size

Therefore it can be stated that by using the time step size of 1,0 seconds and a mesh in depth direction of 400 elements, the obtained results have converged and the calculation time as well as the number of elements used are reduced to a minimum.

In the remaining part of this paragraph, the results of the Pore fluid/Stress model are presented and analysed. In table 6.7 the result with respect to time when spalling occurred and the depth of the spalled of layer are depicted.

Pore fluid/Stress model number	**Time of spalling [sec]**	**Cumulative time [min]**	**Depth of spalling [mm]**	**Cumulative depth [mm]**
1	166	166	26,08	26,08
2	128	294	24,36	50,44
3	120	414	23,43	73,87

Table 6.7 results from Pore fluid/Stress model

The table indicates that the first time spalling occurred was after 166 seconds of fire exposure. The depth of the spalled of layer is 26 mm.
The 2nd and 3rd Pore fluid/Stress model have both the same heating rate as the 1st Pore fluid/Stress model, which means that the heating rate is a constant 196 °C/min in all three models. This first build up of pore pressure towards spalling and the behaviour of the Pore fluid/Stress model are further elaborated.

In the first 25 seconds of the exposure to a fire, the heat gradually penetrates the cross section. This causes the wetting liquid to gradually expand due to the low expansion coefficient. The cross section is still in a partially saturated state and therefore the wetting liquid has the possibility to expand, which causes the degree of saturation to increase. In figure 6.22 the pore pressure distribution is depicted and in the first 25 seconds the pore pressure is between 0,0 MPa and -0,004 MPa, which is due to the definition of the sorption curve.

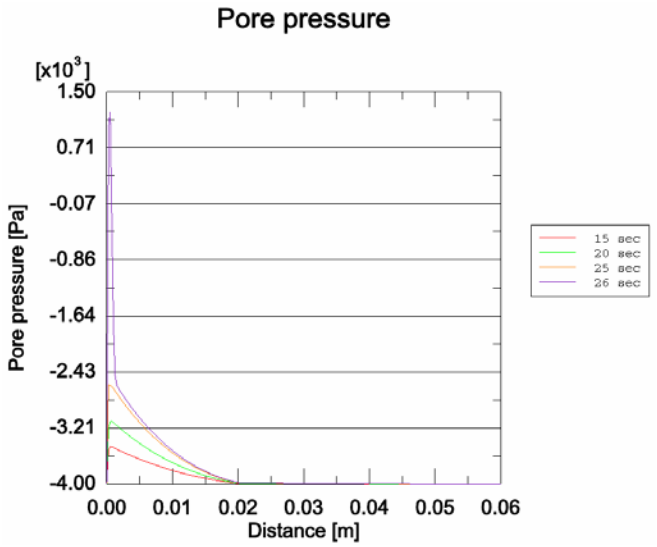

Fig 6.22 Pore pressure distribution in the cross section of concrete (0 – 60 mm)

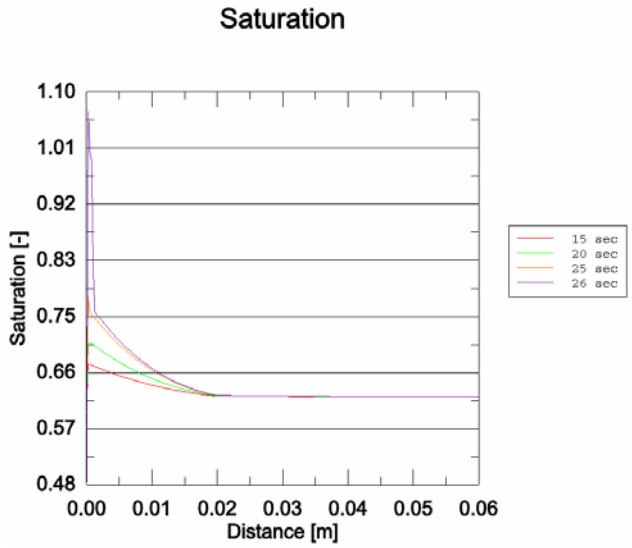

Fig 6.23 Saturation distribution in the cross section of concrete (0 – 60 mm)

The sorption curve is defined to enable a partially saturated state to be present in the model and indicates the relationship between the degree of saturation and the pore pressure. Furthermore, the temperature gradient over the cross section causes a pore pressure gradient to be present, which induces the flow of wetting liquid. The pore pressure gradient is larger towards the surface of the concrete due to the boundary condition on that surface stating that the pore pressure is constant in time and -4000 Pa. This causes the wetting liquid to mostly flow onto the surface of the concrete with a maximum flow speed of $7{,}5*10^{-7}$ m/s, which is relative low. The pore pressure gradient towards the interior of the cross section is lower, which result in a lower flow speed of around $5{,}0*10^{-9}$ m/s. The expansion of the wetting liquid and the flow of the wetting liquid cause a partially saturated zone to develop in which the degree of saturation decreases towards the interior of the cross section. The saturation distribution is depicted in figure 6.23. After 25 seconds, the surface and the first few millimetres of the cross section reach a temperature of 100 ^{o}C. The expansion coefficient of the wetting liquid increases rapidly and therefore the wetting liquid rapidly expands simulating the evaporation of water from the pores of the concrete. Furthermore, the bulk modulus is reduced, simulating the compressibility of the wetting liquid. The expanding wetting liquid causes the first few millimetres of the cross section to obtain a saturated state. Furthermore, also the pore pressure increases rapidly.

The difference in pore pressure gradient towards the surface and towards the interior of the cross section is less than before, causing the wetting liquid to flow respectively onto the surface and into the interior with a maximum flow speed of respectively $2{,}05*10^{-5}$ m/s and $2{,}13*10^{-6}$ m/s. The cross section is, by this time, subdivided into three different zones. The first zone develops from the surface into the cross section and is in a saturated state. In this zone the pore pressure peak and the maximum pore pressure are present, which result in larger flow speeds of the wetting liquid. The saturated zone is followed by a partially saturated zone, which has lower pore pressures and therefore also lower flow speeds. The remaining part of the cross section is the zone of the concrete which is still unaffected by the fire and the initial degree of saturation is present.

The most important zone of the cross section is the saturated zone. In this zone the temperature is equal to or greater than 100 ^{o}C and therefore the wetting liquid simulates the evaporation of water and the pore pressure increases. In case these pore pressures develop high enough, spalling occurs in this zone. Therefore, the behaviour of the Pore fluid/Stress model is further elaborated by using a number of graphs which are depicted in this paragraph. In figure 6.24 the temperature distribution from the surface of the concrete onto 100 mm into the cross section of concrete is depicted. The most important aspect of the temperature distribution is the progress of the 100 ^{o}C front, which reaches a depth of 3 mm, 13 mm and 24 mm at respectively 30 seconds, 60 seconds and 150 seconds. In figure 6.25 the pore pressure distribution across the same 100 mm of concrete is depicted. The pore pressure peak develops in time, in which the maximum value of the peak pore pressure increases and progresses further into the cross section of concrete. In figure 6.26 the pore fluid effective velocity is depicted, which means the speed of the wetting liquid in the direction perpendicular to the heated surface. On the vertical axis the negative flow speed means that the wetting liquid is flowing in the direction of the heated surface of the cross section of concrete and a positive flow speed means that the wetting liquid is flowing into the interior of the concrete. Furthermore, in figure 6.27 the saturation distribution is depicted in which the initial degree of saturation is 63%, which can be seen by the degree of saturation deeper into the cross section.

After 30 seconds of exposure to the fire, the saturated zone has a depth of 4 mm. The maximum pore pressure, at this time, has a value of 0,21 MPa is situated at 3 mm into the cross section and the main width of the pore pressure peak is 4 mm. The maximum pore pressure is situated at the same position as the 100 ^{o}C front. In the partially saturated zone the pore pressures are between 0,0 MPa and -0.004 MPa. Furthermore, the pore fluid effective velocity indicates that the position of the maximum pore pressure also is the point at which the flow of the wetting liquid changes direction.

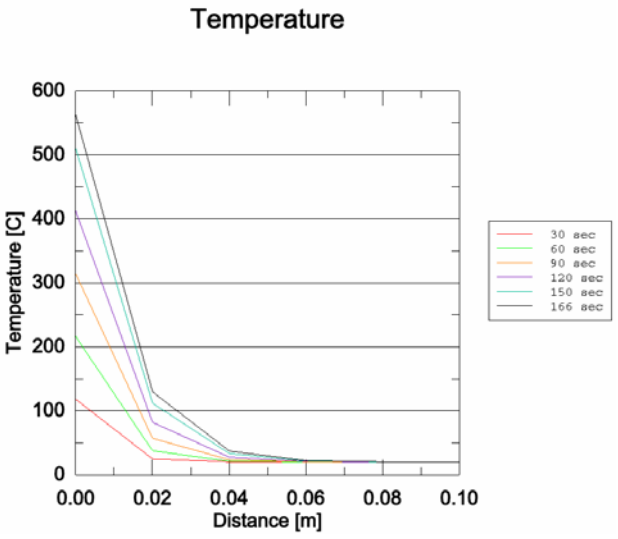

Fig 6.24 Temperature distribution in the cross section of concrete (0 – 100 mm)

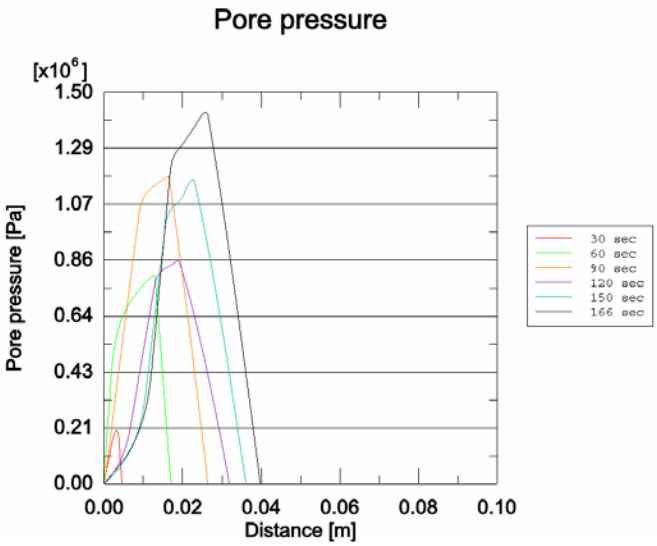

Fig 6.25 Pore pressure distribution in the cross section of concrete (0 – 100 mm)

In front of the maximum pore pressure the wetting liquid flows onto the surface of the concrete with a maximum flow speed of $0{,}32*10^{-3}$ m/s, which is caused by a pore pressure gradient in the direction of the surface of the cross section and the permeability increasing in the same direction. This causes the flow speed of the wetting liquid to increase towards the surface of the cross section. Behind the maximum pore pressure, the wetting liquid flows into the interior of the concrete with a maximum flow speed of $0{,}02*10^{-3}$ m/s, which is caused by a pore pressure gradient in this direction and a constant permeability. The values for the flow speed of the wetting liquid indicate that most of the wetting liquid flows onto the surface of the concrete. The difference in the position of the maximum pore pressure and the depth of the saturated zone indicates the zone in which the wetting liquid is flowing with relative high flow speeds into the interior of the concrete, which is after 30 seconds only 1 mm. In the partially saturated zone, width a depth of 16 mm, the low pore pressures causes a relative low flow speed of the wetting liquid.

In time the 100 ^{o}C front further progresses into the cross section and the process continues. After 60 and 150 seconds the saturated zone has reached a depth of respectively 18 mm and 36 mm. However, the maximum pore pressure is, at these times, situated at respectively 13 mm and 24 mm and has a value of respectively 0,8 MPa and 1,16 MPa. The main width of the pore pressure peak is, at these times, respectively 18 mm and 36 mm. This means that the saturate zone progresses faster through the cross section then the pore pressure peak. The maximum pore pressure is after 166 seconds obtained and has a value of 1,42 MPa and is situated at 26 mm into the cross section. The saturation distribution has progressed 40 mm into the cross section and a fully saturated zone or “moisture clog” is obtained. Furthermore, the pore fluid effective velocity indicates that the zone in which the wetting liquid is flowing into the cross section increase, but the flow speed at which this happens decreases. After 60 and 150 seconds the width of the zone at which the wetting liquid is flowing into the concrete is respectively 5 mm and 12 mm. The maximum flow speed into the interior of the concrete is respectively $0{,}017*10^{-3}$ m/s and $0{,}0086*10^{-3}$ m/s.

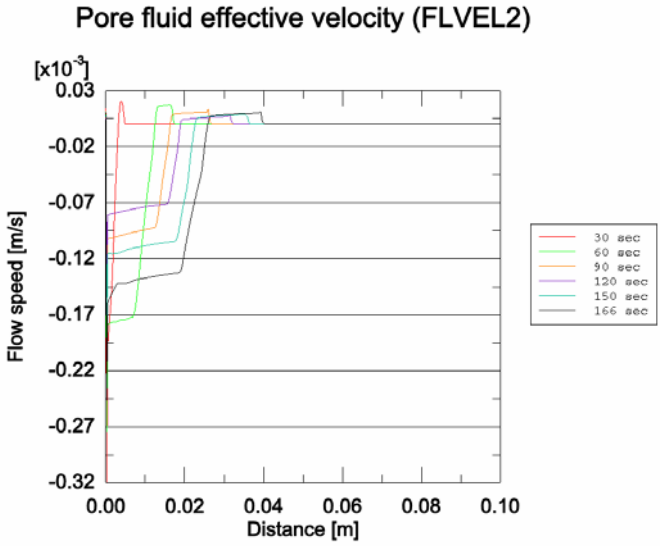

Fig 6.26 Pore fluid effective velocity distribution in the cross section of concrete (0 – 100 mm)

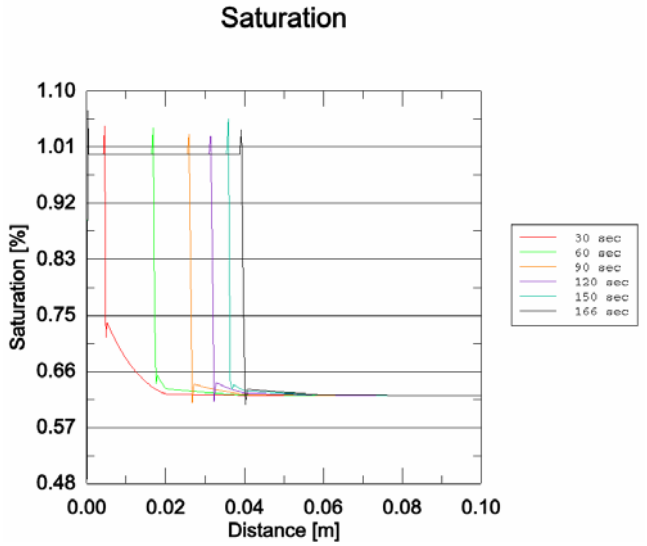

Fig 6.27 Saturation distribution in the cross section of concrete (0 – 100 mm)

The pore pressure distribution indicates this by the pore pressure gradient towards the interior of the concrete reducing in time. In the time interval from 120 to 166 seconds the flow speed of wetting liquid slightly increases from $0{,}0082*10^{-3}$ m/s to $0{,}012*10^{-3}$ m/s due to the increasing pore pressure gradient. However, the pore pressure gradient in this time interval is still lower than the pore pressure gradient at 60 seconds. In this zone the permeability of the material is not of importance, due to the temperature being lower than 100 ^{o}C and therefore the permeability is not reduced yet. In the zone in which the wetting liquid is flowing onto the surface of the cross section, the pore pressure gradient as well as, due to the temperature being higher than 100 ^{o}C, the permeability of the material are important. The flow speed of the wetting liquid onto the surface can be subdivided into three sub zones. The first zone is located from the surface into the interior of the cross section. In this sub zone the maximum flow speed of the wetting liquid is located at the surface and decrease from $0{,}28*10^{-3}$ m/s after 60 seconds to $0{,}12*10^{-3}$ m/s after 120 seconds and than increases again to $0{,}25*10^{-3}$ m/s at 166 seconds.. This behaviour is caused by the pore pressure gradient reducing in time in this sub zone and thus causing the flow speed to reduce. However, after 150 seconds the flow speed of the wetting liquid increases again due to the increasing permeability. Furthermore, the flow speed of the wetting liquid reduces in the depth direction of this sub zone, which is caused by the decreasing temperature which causes the permeability to decrease. In the second sub zone there is a more or less constant flow speed of the wetting liquid, between $0.18*10^{-3}$ m/s after 60 seconds and $0.08*10^{-3}$ m/s after 120 seconds, indicated by the plateau at each time. This plateau is situated in the part of the cross section where the temperature is between 200 ^{o}C-150 ^{o}C and therefore this plateau shifts in time into the cross section. In this region the permeability increases which is done to ensure that the pore pressure peak can fully develop and start to progress into the cross section. Furthermore, the difference in flow speed of the wetting liquid is mostly determined by the pore pressure gradient slightly changing in time. Finally, in the third sub zone the flow speed of the wetting liquid decreases further to the point where the wetting liquid flows towards the interior of the concrete. This behaviour is induced by the decreasing temperature and thus the decreasing permeability. The pore pressure gradient first reduces over time and then increases slightly again. These flow speeds and the width over which the wetting liquid is flowing onto the surface indicate that most of the wetting liquid flows onto the surface of the concrete. Furthermore, the partially saturated zone has a depth of around 22 mm after 60 seconds and 22 mm after 150 seconds, which means that the width of the partially saturated zone increases from 30 seconds towards 60 seconds. However, the degree of saturation decreases rapidly in these partially saturated zones compared to the partially saturated zone after 30 seconds. In these partially saturated zones the pore pressure is between 0,0 MPa and -0.004 MPa and the flow speed of the wetting liquid is relative low. Finally, in the pore pressure distribution there is a sudden drop in maximum pore pressure at 120 seconds. This is caused by an increase in the amount of wetting liquid which flows towards the interior of the cross section compared to 90 seconds. At 90 seconds the flow speed of the wetting is higher than at 120 seconds, however the zone in which the wetting liquid is flowing into the cross section increases and thus causing a larger amount of wetting liquid to flow in this direction. After 150 seconds the flow speed of wetting liquid only slightly increases and the zone in which this flow speed is present increases, but the pore pressure peak further develops and the maximum pore pressure increases.

The described results indicate that the 100 °C front penetrates the cross section and progress through the cross section. At this front the rapidly increasing expansion coefficient causes the wetting liquid to also expand rapidly and a fully saturated zone is developed. Furthermore, in this zone the pore pressure increases also rapidly and causes the flow of wetting liquid. The pore pressure gradient determines the direction of the flow of the wetting liquid. The position and the value of the maximum pore pressure is obtained from respectively the position of the 100 °C front and the amount of wetting liquid which flows into the cross section and onto the surface. In time the depth of the saturated zone progresses faster through the cross section than the pore pressure peak. The maximum pore pressure lags behind the front of the saturated zone. This means that in front of the maximum pore pressure the thickness of the saturated zone increases. The pore pressure peak becomes, in time, increasingly insufficient to level off enough wetting liquid to reduce the build up of the pore pressure peak and the maximum pore pressure. Therefore the maximum pore pressure and the width of the pore pressure peak increases over time. The zone in which wetting liquid is flowing into the interior of the cross section increases, but due to the reducing pore pressure gradient the flow speed of the wetting liquid decreases. The pore pressure gradient reduces, because the part of the saturated zone in front of the maximum pore pressure grows faster in time than the maximum pore pressure. Furthermore, the pore pressure peak progresses into the cross section and therefore the pore pressure gradient towards the surface of the concrete reduces, resulting in a lower flow speed of the wetting liquid in this direction. The saturated layer stays connected to the surface of the cross section, because the flow of the wetting liquid onto the surface keeps that zone in a saturated state. In front of the saturated zone, a partially saturated zone is present. This zone progress in time through the cross section and increases in depth in the first 60 seconds and than becomes constant. However, the degree of saturation in this zone decreases in time indicating that the flow of wetting liquid in into this zone decreases in time, which is caused by the pore pressure peak becoming increasingly insufficient to level off the wetting liquid. Furthermore, in the partially saturated zone the pore pressures are low as well as the flow speed of the wetting liquid.

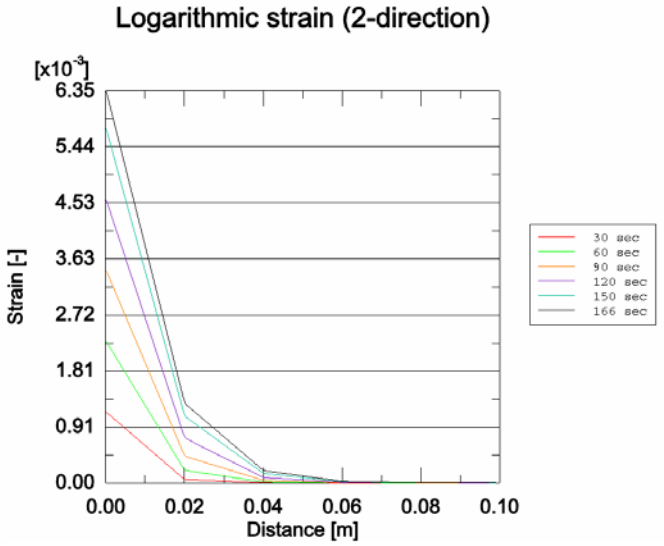

Fig 6.28 Logarithmic strain distribution in the cross section of concrete (0 – 100 mm)

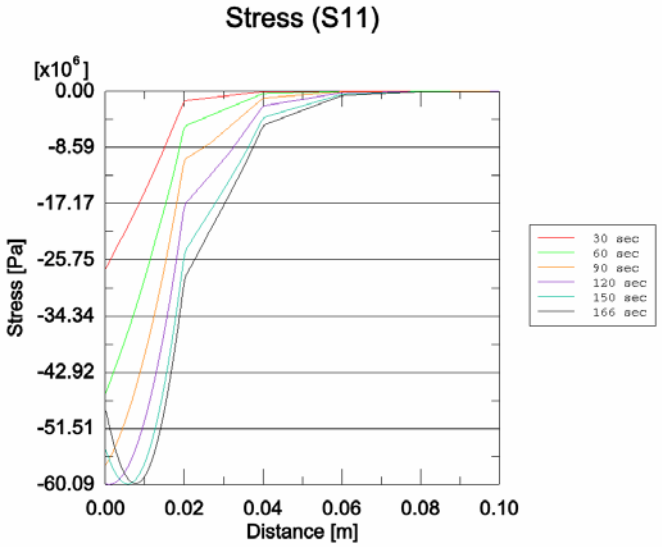

Fig 6.29 Stress (S11) distribution in the cross section of concrete (0 – 100 mm)

The temperature distribution over the cross section also induces strains and stresses which are depicted in respectively figure 6.28 and 6.29. These strains act perpendicular to the heated surface and are a result of the temperature distribution throughout the cross section. The shape of the lines of the strains is similar to the lines of the temperature distribution depicted in figure 5.23. After 60 seconds and 150 seconds of fire the maximum strain is situated on the heated surface and is respectively $2{,}27*10^{-3}$ and $5{,}7*10^{-3}$. The strain rapidly decreases into the cross section of concrete and in time progresses into the cross section. Furthermore, in figure 6.29 the stresses acting parallel to the heated surface are depicted. These stresses are, the in chapter 5 explained, Eigen stresses due to the temperature distribution. After 60 seconds of fire exposure the compressive stress on the surface of the concrete has build up to 47 MPa. This stress rapidly decreases into the cross section of concrete and 20 mm into the cross section only a compressive stress of 4,5 MPa remains. The compressive stress on the surface further develops and after 150 seconds reaches a value of 55 MPa. However, the maximum compressive stress shifts into the cross section and is situated at 6 mm and has a value of 60 MPa. Furthermore, the stress also progress further into the cross section and at 20 mm a compressive stress is present of 24,7 MPa. The shifting of the maximum compressive stress into the cross section of concrete is caused by the temperature dependency of the modulus of elasticity. The temperature decreases from the surface into the cross section of concrete and therefore the modulus of elasticity increases in this direction, causing the build up of stress on the surface of the cross section to reduce and the maximum compressive stress to shift into the cross section. However, the presented stresses are based on linear elasticity theory. The large compressive stresses on the surface and the first 20 mm of the cross section exceed the limit compressive stress of the concrete and will cause cracking of the concrete and redistribution of stresses, which is nonlinear elastic behaviour and is not included in the Pore fluid/Stress model.

The stresses acting perpendicular to the heated surface are depicted in figure 6.30, which are a result from the pore pressures.

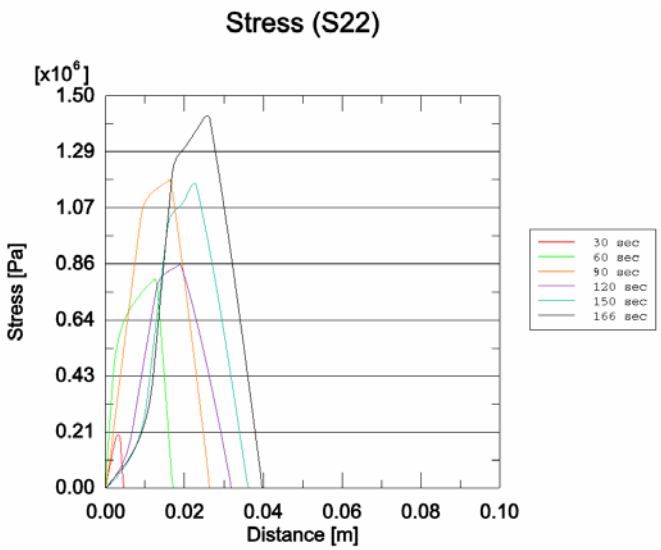

Fig 6.30 Stress (S22) distribution in the cross section of concrete (0 – 100 mm)

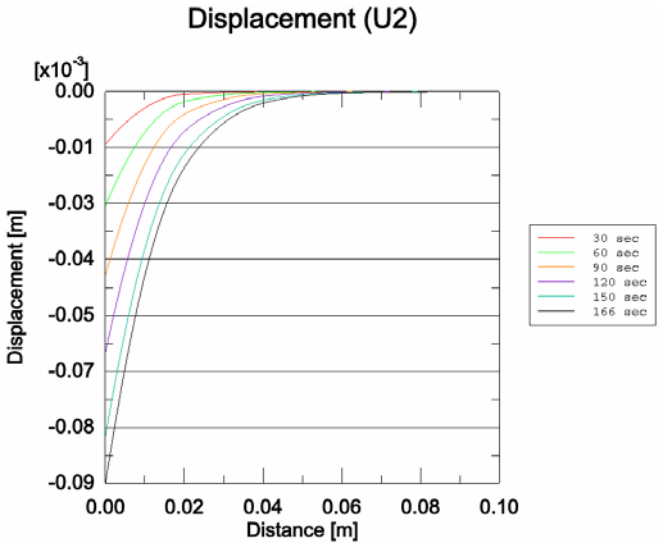

Fig 6.31 Displacement distribution in the cross section of concrete (0 – 100 mm)

In general it can be stated that these stresses largely follow the same shape, position and value as the pore pressure distribution, because the equilibrium equation determines that the pore pressure is equal to this tensile stress. The stress peak develops in time, in which the maximum value of the peak stress increases and progresses further into the cross section of concrete. After 60 seconds and 150 seconds the maximum tensile stress is respectively 0,8 MPa at 13 mm and 1,16 MPa at 24 mm. The maximum tensile stress is 1,43 MPa at a depth of 26 mm after 166 seconds of fire exposure and exceeds the limit tensile stress of the concrete and therefore forced the Pore fluid/Stress model to interrupt the calculation and indicate that spalling is present in the model.

Finally, in figure 6.31 the displacement of the cross section is depicted. These displacements act perpendicular to the heated surface and are a result of the temperature. The temperature distribution causes the cross section to expand and due to the fixation of the left and right side and the side opposite of the heated surface, the cross section only expands perpendicular to this surface. The maximum displacement is therefore situated on the heated surface and decreases into the cross section of concrete. After 60 seconds and 150 seconds the maximum displacement is respectively $0{,}03*10^{-3}$ m and $0{,}08*10^{-3}$ m.

After the Pore fluid stress model has interrupted the calculation, an estimate for the depth of the spalled of layer is given. The first spalled of a layer has a depth of 26 mm. The cross section of the concrete is reduced from the surface into the cross section with this depth and first the Heat transfer model and the second Pore fluid/Stress model are started. In the remaining part of this paragraph the result are given from the seconds Pore fluid/Stress model.

The second Pore fluid/Stress model has the same behaviour as the first Pore fluid/Stress model, because the material model is not adapted. Therefore, in the graphs which are depicted here only the main results are described. In figure 6.32 the pore pressure distribution is depicted. After 166 seconds of fire exposure the 1st layer spalled of the concrete surface. The 2nd Pore fluid/Stress model is restarted at the same time, but with a reduced cross section and with the pore pressure distribution from the end of the 1st Pore fluid/Stress model 'mapped' onto the remaining cross section. The maximum pore pressure after 166 seconds is 1,3 MPa and is situated at 26 mm into the cross section. The graph further indicates the reduced cross section by the first 26 mm not having any values. Due to the prescribed boundary condition of the pore pressure at the surface of the cross section, the front of the pore pressure distribution after 176 seconds (10 seconds after the start of the 2nd Pore fluid/Stress model) is 0,0 MPa. The process which developed during the 1st Pore fluid/Stress model also develops in the 2nd Pore fluid/Stress model.

The pore pressure peak progresses through the cross section and the main width and maximum pore pressure increases in time, which is similar to the behaviour of the 1st Pore fluid/Stress model. The main width of the pore pressure peak increases from 44 mm after 176 seconds to 64 mm after 226 seconds (60 seconds after the start of the 2nd Pore fluid/Stress model). After 176 and 226 seconds the maximum pore pressure is respectively 0,36 MPa at a depth of 33 mm and 1,03 MPa at 42 mm. The maximum pore pressure is obtained after 294 seconds and has a value of 1,40 MPa and is situated at a depth of 50 mm into the cross section.

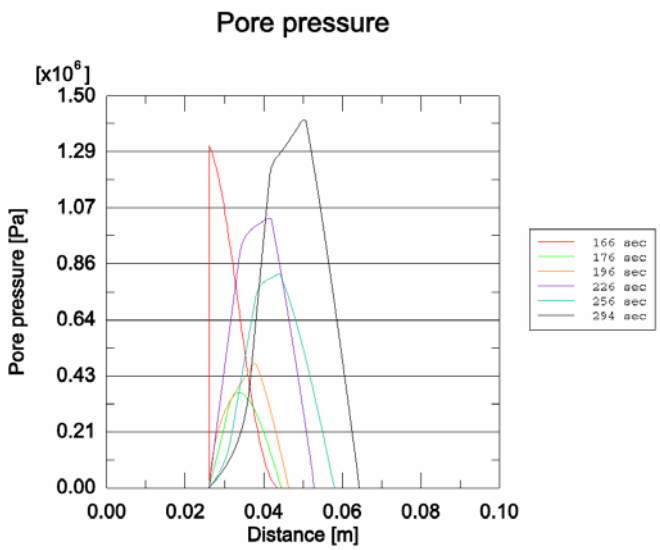

Fig 6.32 Pore pressure distribution in the cross section of concrete (0 – 100 mm) after 1st spalling

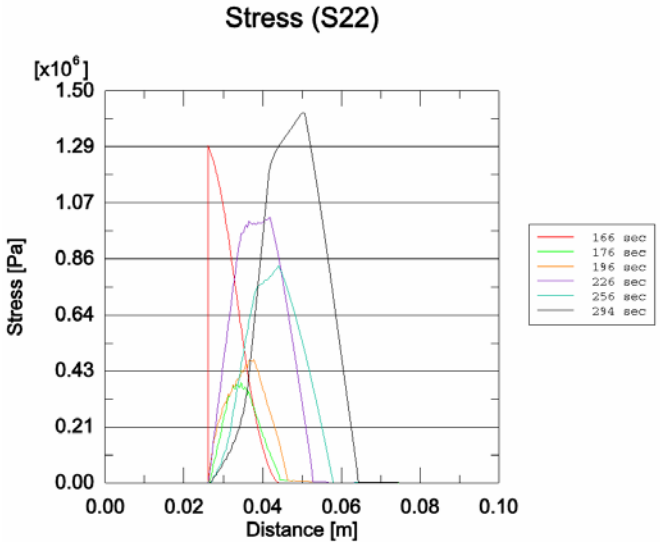

Fig 6.33 Stress (S22)distribution in the cross section of concrete (0 – 100 mm) after 1st spalling

The pore pressure distribution causes stresses in the cross section, which act perpendicular to the surface of the cross section and are depicted in figure 6.33. In general it can be stated that these stresses largely follow the same shape, position and value as the pore pressure distribution. At the beginning of the 2nd Pore fluid/Stress model not only the pore pressure distribution from the 1st Pore fluid/Stress model is mapped onto the remaining cross section, also the stress distribution is 'mapped'. In figure 6.33 this can be seen by the stress peak present in the cross section at 166 seconds. The maximum value of this tensile stress is 1,3 MPa. In time the pore pressure distribution develops and progresses through the concrete. The stress distribution follows the same trend and after 176 and 226 seconds the maximum tensile stress is respectively 0,38 MPa at 33 mm and 1,01 MPa at 42 mm. The maximum tensile stress obtained is 1,41 MPa and is situated 50 mm into the cross section after 294 seconds. The Pore fluid/Stress model again interrupts the calculation and indicates that spalling is present in the model.

In figure 6.34 the pore fluid effective velocity is depicted. At the beginning of the 2nd Pore fluid/Stress model the flow speed of the wetting liquid is zero. Only the pore pressure and stress distribution from the end of the 1st Pore fluid/Stress model are mapped. The next time step after the mapping of the pore pressure distribution, the 2nd Pore fluid/Stress model predicts the flow of wetting liquid. After 176 seconds the pore pressure gradient causes the flow of wetting liquid onto the surface of the cross section with a maximum flow speed of $0{,}32*10^{-3}$ m/s. The pore pressure gradient into the cross section causes the flow of wetting liquid with a flow speed of $0{,}0047*10^{-3}$ m/s over a width of 11 mm. After 226 seconds the wetting liquid flows onto the surface of the cross section with a maximum flow speed of $0{,}10*10^{-3}$ m/s. The flow of wetting liquid into the cross section occurs over a width of 11 mm and with a maximum flow speed of $0{,}012*10^{-3}$ m/s. The flow speed of the wetting liquid into the cross section increases in time and the region in which the wetting liquid is flowing into the cross section also increases in time. This is similar to the behaviour of the 1st Pore fluid/Stress model in the time interval of 90 – 166 seconds. The flow speed of the wetting liquid onto the surface of the cross section decreases over time.

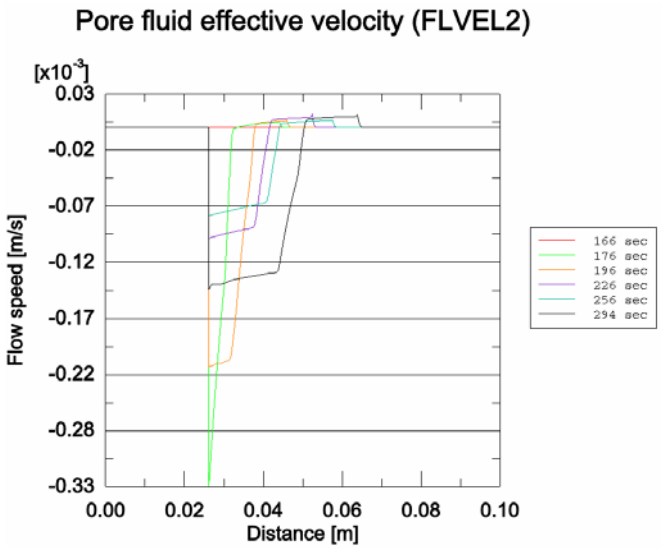

Fig 6.34 Pore fluid effective velocity distribution in the cross section of concrete (0 – 100 mm) after 1st spalling

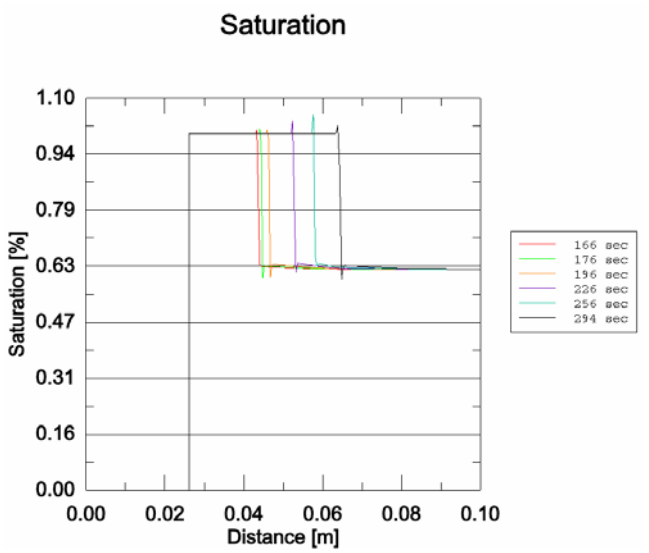

Fig 6.35 Saturation distribution in the cross section of concrete (0 – 100 mm) after 1st spalling

Only after 294 seconds the flow speed onto the surface increases again due to the increasing permeability. This behaviour is similar to the behaviour of the 1st Pore fluid/Stress model.

Finally the saturation distribution is depicted in figure 6.35. At the beginning of the 2nd Pore fluid/Stress model, the pore pressure distribution is mapped, which through the sorption curve also defines the degree of saturation throughout the cross section. After 166 seconds the saturated zone has reached a depth of 43 mm and followed by a partially saturated zone of 17 mm. The saturation distribution progresses through the concrete and after 226 the saturated zone has reached a depth of 53 mm with a partially saturated zone of 17 mm. The maximum depth the saturated zone reaches is 64 mm. The front of the saturated zone progress through the cross section and, as was already observed with the 1st Pore fluid/Stress model, the saturated zone progresses faster through the cross section than the pore pressure peak.

Finally, a comparison is made between the most important result of the 1st and the 2nd Pore fluid/Stress model to indicate the difference the process undergoes when a layer has spalled of the surface of the cross section. In table 6.8 an overview is given of the main result of both Pore fluid/Stress models. In the columns of the 2nd model a few numbers are given between brackets. These number represent a relative depth when the actual depth is reduced with the spalled of first layer of 26 mm. This is done to compare the progress of both models with each other.

In the 1st Pore fluid/Stress model the front of the saturated zone has reached a depth of 18 mm after 60 seconds. The maximum pore pressure is then 0,8 MPa and is situated at a depth of 13 mm. In the 2nd Pore fluid/Stress model the front of the saturated zone has reached a relative depth of 38 mm after 60 seconds and the maximum pore pressure is 1,03 MPa and is situated at a relative depth of 16 mm. These values indicate that the process in the 2nd Pore fluid/Stress model is more developed after 60 seconds of calculation.

	1st model 60 sec	**1st model 90sec**	**2nd model 226 sec**	**1st model 166 sec**	**2nd model 294 sec**
Spalling present in Pore fluid/Stress model	NO	NO	NO	YES	YES
Time after start of 1st resp.2nd model [sec]	60	90	60	166	128
Maximum pore pressure [Pa]	0,80	1,18	1,03	1,42	1,40
Depth spalled of layer [mm]	n.a.	n.a.	n.a.	26	24
Location max. pore pressure [mm]	13	16	42 (16)	26	50 (24)
Location front of saturated zone [mm]	18	26	53 (27)	40	64 (38)

Table 6.8 Comparison between the main result of the 1st and the 2nd Pore fluid/Stress model

This is caused by the pore pressure and stress distribution being mapped on the remaining cross section at the beginning of the 2nd Pore fluid/Stress model. The cross section is therefore no longer in an initial state, which means there is already a pore pressure, saturation and stress distribution present. The state of the cross section of the 2nd Pore fluid/Stress model after 60 seconds can be compared to the state of the cross section of the 1st Pore fluid/Stress model after 90 seconds. This difference of 30 seconds is also present when the time of spalling of both model are compared with each other. The 1st Pore fluid/Stress model predicts spalling after 166 seconds, while the 2nd Pore fluid/Stress model predicts spalling after 294 seconds or 128 seconds when the first 166 seconds are subtracted. This is a difference of 38 seconds. The maximum pore pressure in both model is around 1,40 MPa and the front of the saturated zone is in both models around 40 mm into the cross section. Furthermore, both models predict spalling of around 25 mm. This means that the state of the cross section when spalling occurs comparable is and therefore the depth of the spalled of layer also comparable is.

7. Comparison and validation of the analytical and the numerical model

7.1. General

In the development of a new model for spalling and for that matter any new model in general, whether an analytical or a numerical model, it is always important to compare and validate the developed model. Usually this means comparison of the developed model with existing models and to validate if the developed model behaves according to the general theories applying to this model. Furthermore, the results obtained should always be checked against experimental results, because the applied theories in the model are also based on assumptions and other theories which may not be general applicable in the current situation or are not applicable at all. Therefore in this chapter a comparison is made between the analytical model and the numerical model to judge whether the results, obtained in both models, are comparable and in case of differences to indicate the origin of these differences. Furthermore, the results of both models are compared with experimental results to validate if the results obtained are plausible.

7.2. Comparison

The analytical and the numerical model presented in the previous chapters both deal with the phenomenon of spalling in concrete. One of the main goals of both models is to estimate the saturation distribution over the cross section in time, the development of a fully saturated layer and the build up of pore pressure and stresses which, in case of exceeding the limit tensile stress of the concrete, causes spalling. Furthermore, the depth of the spalled of layer is also to be estimated. To enable the possibility of comparing the results from the analytical model and the numerical model, the geometry and fire curve on the surface of the cross section of both models are equal. Furthermore, the material properties used in the analytical model and the numerical model are kept the same as much as possible. However, due to the differences between the applied theories and the used models, some of the material properties are not the same or are even not present in the other model. The main difference in material properties between the analytical model and the numerical model is the use of the pore fluid expansion coefficient, the porous bulk modulus and the sorption curve in the numerical model. In the analytical model these material properties are not present. However, the pore fluid expansion coefficient and the porous bulk modulus are based upon the ideal gas law and this same law is used in the analytical model. Furthermore, the permeability and the modulus of elasticity are different in both models. The permeability in the analytical model is kept relative simple with a straight line dependent on the temperature. In the numerical model this restricted the pore pressure peak from developing and progressing into the cross section. Therefore, the permeability behaviour of the concrete was adapted to more fit the actual permeability with the exception of the temperature range of 100 ^{o}C – 200 ^{o}C, which was already explained in the previous chapter. The modulus of Elasticity is kept constant in the analytical model for simplicity. In the numerical model the modulus of Elasticity is temperature dependent.

	Analytical model	Numerical model I	Numerical model II
Heating rate at the surface of the cross section [^{o}C/min]	196	196	96
1st Spalling present in the model	YES	YES	YES
Time of spalling [min]	6,02	2,77	4,55
Thickness of spalled of layer [mm]	16	26	29
Max. pore pressure [MPa]	1,58	1,42	1,43
Position of maximum pore pressure [mm]	16	26	29
Temperature at the position of the maximum pore pressure [^{o}C]	200	100	100
Front of saturated layer [mm]	28	40	45
Thickness of saturated layer [mm]	12	40	45
End of saturated layer [mm]	16	0	0
2nd Spalling present in the model	NO	YES	YES
Time of spalling or max. pore pressure [min]	21,00	4,90	7,90
Depth of spalled of layer [mm]	n.a.	24	27
Max. pore pressure [MPa]	1,00	1,40	1.37
Position of maximum pore pressure [mm]	40	24	27
Front of saturated layer [mm]	48	38	43
Thickness of saturated layer [mm]	8	38	43
End of saturated layer [mm]	40	0	0
3rd Spalling present in the model	NO	YES	NO
Time of spalling [min]	n.a.	6,90	n.a.
Thickness of spalled of layer [mm]	n.a.	23	n.a.

Table 7.1 Main results of the analytical and the numerical model

In table 7.1 the most important results of both models are depicted.
In this table two numerical models are present. The first numerical model has the HSL-Zuid fire curve, which means heating up of the surface of the cross section in 5 minutes from a temperature of 20 ^{o}C to 1000 ^{o}C, which is the same as for the analytical model. The second numerical model has a different fire curve, which heats up the surface of the cross section in 5 minutes from a temperature of 20 ^{o}C to 500 ^{o}C. This fire curve is referred to as the adapted fire curve.

The first main difference between the analytical model and the numerical model is the behaviour of the water and water vapour in the analytical model compared to the wetting liquid in the numerical model and the resulting saturation distribution. In the analytical model the water from the pores of the concrete is evaporated at flows into the interior of the cross section. There, when the conditions are met, the water vapour condensates back to water. This ensures that the cross section obtains a saturation distribution which from the surface to the interior of the cross section has a dry zone, drying zone and an accumulation / saturated zone. In time the saturated zone gradually develops and progress through the cross section until the thickness is sufficient to impede further water vapour transport and then, if the pore pressure develops high enough, spalling occurs. The fully saturated zone then has a thickness of 12 mm and is situated a depth of 16 mm. The numerical model has only the

capability of flow of the wetting liquid, which is one phase flow. The wetting liquid flowing into the cross section of the concrete causes the front of the saturated zone to progresses into the cross section, while the wetting liquid flowing onto the surface of the cross section causes the back of the saturated zone to stays at the surface of the cross section. In the first and second numerical model the saturated zone develops from the surface into the cross section and reaches a depth, when spalling occurs, of 40 mm respectively 45 mm. Furthermore, in the analytical model the water is explicitly evaporated from the pores of the concrete and due to the phase change the water expands causing the pore pressure to increase. The pore pressure gradient causes the formed water vapour to flow into the cross section. In the numerical model the evaporation of water is taken into account implicitly by the expansion coefficient of the wetting liquid and the porous bulk modulus, which means that the in the Pore fluid/Stress model the water is not physically evaporated. The expansion coefficient increases the pore pressure and the pore pressure gradient causes the flow of wetting liquid. Finally, in the analytical model the flow of water vapour is strictly prescribed. For the build up of a saturated layer the water vapour flows into the cross section and for the build up of pore pressure on the front of the formed saturated layer the water vapour flows onto the surface of the concrete. In the numerical model the wetting liquid can flow into the cross section as well as onto the surface of the cross section.

The second main difference between the results of the analytical model and the numerical model is the fact that in the analytical model only one occurrence of spalling is present after 6,02 min. In the first numerical model spalling is present after 2,77 and 4,90 min, while the second numerical model predicts spalling after 4,55 and 7,90 min. In both numerical models spalling is repeated. This difference is caused by the temperature input in both models is different. In figure 7.1 the progress of the 100 ^{o}C front through the cross section of concrete, in case of the analytical model and numerical model, is depicted. In this figure it can be observed that the 100 ^{o}C front of the first numerical model, progresses faster through the cross section than in case of the analytical model, even though both models are subjected to the same HSL-Zuid fire curve. After 5 minutes of fire exposure the 100 ^{o}C front has progressed in case of the first numerical model respectively the analytical model 39 mm en 20 mm into the cross section. Furthermore, in figure 7.2 the speed at which the 100 ^{o}C front progresses through the cross section in the different models is also depicted. In case of the first numerical model the speed of the 100 ^{o}C front is around 6 mm/min, whereas the speed of the 100 ^{o}C front in case of the analytical model is around 4,00 mm/min. The result of this difference in the progress of the process which causes spalling, is that spalling occurs at in the first numerical model after 2,77 min, while in the analytical model after 6,02 min. In both figures also the progress and speed of the 100 ^{o}C front in case of the second numerical model is depicted. The progress of the 100 ^{o}C front after 5 minutes of fire exposure is around 32 mm into the cross section and the speed at which this happens is 6,14mm/min (which is mostly due to the high speed in the fist minute of fire exposure). The progress of the 100 ^{o}C front in the second numerical model is slower than the one used in the first numerical model and closer to the progress of the 100 ^{o}C front used in the analytical model. Therefore the second numerical model develops at a slower speed than the first numerical model which causes spalling to occur in the second numerical model after 4,55 min, which is around the same time as spalling occurred in the analytical model.

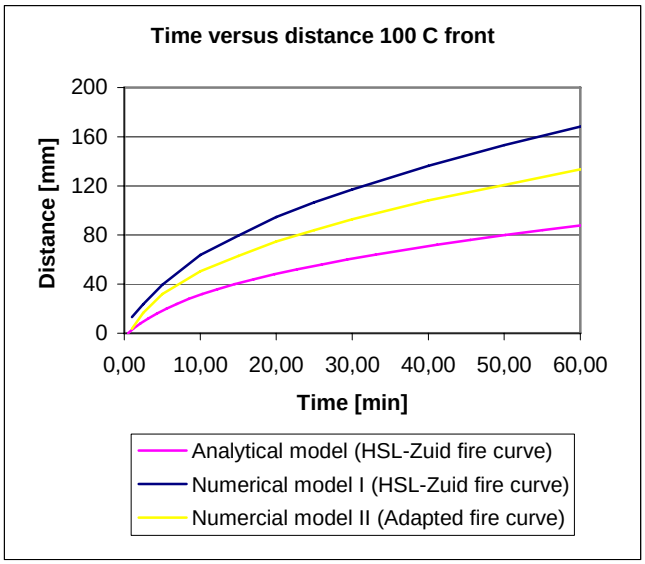

Fig 7.1 Progress of the 100 °C front of the analytical and the numerical model

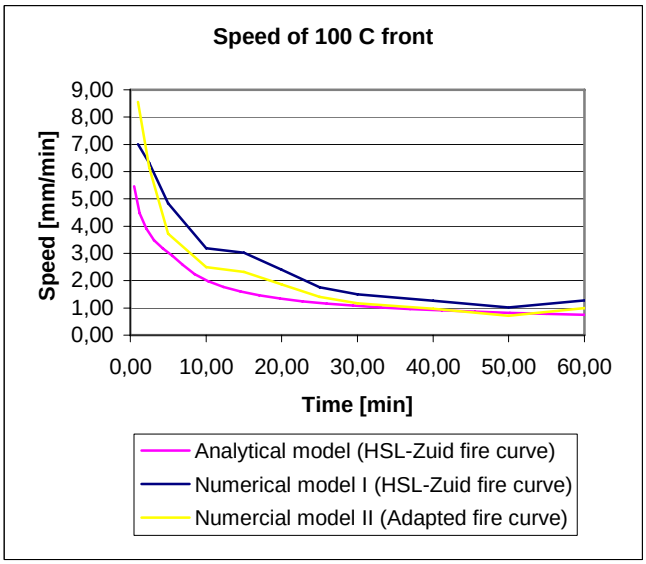

Fig 7.2 Speed of the 100 °C front of the analytical and the numerical model

Finally, in the analytical model spalling only occurs once, because the progress of the 100 °C front reduces over time and therefore the pore pressure does not develop high enough to cause spalling. The higher speed of the progress 100 °C front in the numerical model ensures that the spalling occurs at least twice.

The third main difference between the results of the analytical model and the numerical model is the depth of the spalled of layer. In case of the analytical model the spalled of layer has thickness of 16 mm, while in the first and second numerical model the thickness of the spalled of layer is respectively 26 mm and 29 mm. This difference in thickness is partly due to the difference in the progress of the 100 °C front used in both models and partly due the difference in the made assumptions, the theories and the material properties used in both models. Especially in the numerical model the behaviour of the wetting liquid largely determines the behaviour of the model and thus the thickness of the spalled of layer. In the analytical model the saturated zone progress through the cross section and resulting in a fully saturated layer and on the front of this layer, when the temperature reaches 100 °C, the evaporation process of from water from this layer starts and thus the build up of pore pressure. The maximum pore pressure is at a temperature of 200 °C. In the numerical model the position of the maximum pore pressure coincides with the 100 °C front, which means that the 100 °C front progress through the cross section resulting in a progressing pore pressure peak with an in time increasing maximum pore pressure. This means that the maximum pore pressure is at a temperature of 100 °C. The difference in the development of the pore pressure and the difference in the progress of the heat into the cross section, causes the difference in thickness of the spalled of layer.

Besides these differences, the analytical and the numerical model also have an important general similarity. Both models predict a saturation distribution with a saturated zone which progress through the cross section and a pore pressure peak which gradually develops over time. The maximum pore pressure which occurs in both models is comparable, because the slightly higher maximum pore pressure of the analytical model is causes by the different relationship between stress and pore

pressure used in this model. Furthermore, taken into the account the influence of the difference in the heat penetration used in both models, the analytical model and the second numerical model predict spalling to occur after around the same time of fire exposure. Furthermore, both these models predict a depth of the spalled of layer which is of the same order. This especially holds when considered the number of assumptions made and the simplification used in the analytical model and numerical model.

7.3. Validation

The validation of the analytical and numerical model is done on two bases. First the used theory and the analyzed behaviour of both models are compared with the theory about the general behaviour of concrete during exposure to a fire and especially the process which causes spalling. The second important validation of the analytical and numerical model is based on the comparison of the obtained results and the analysed behaviour with the results and behaviour obtained from experiments.

7.3.1. Theoretical validation

The theoretical validation is done by comparing the behaviour and results from the analytical and numerical model with the, in chapter 4, described general behaviour of concrete exposed to a fire. For the analytical and the numerical model this comparison indicates that these models incorporate the penetration of heat into the cross section, which is in agreement of the general theory. However, both models neglect the influence the evaporation of water from the pores of the concrete have on the temperature distribution. Furthermore, the general theory states that water is evaporated from the pores of the concrete. The phase change of water to water vapour causes the water to expand and a pore pressure to develop, which induces the flow of water vapour. At the beginning of fire exposure, the water vapour will mostly flow towards the surface of the cross section, however in time the heat penetrates further into the cross section and the water vapour increasingly flows towards the interior of the cross section. The analytical model incorporates the evaporation of water and the resulting development of pore pressures and the resulting flow of water vapour. However, the water vapour flows only into the cross section. In the numerical model the evaporation of water is not present and the pore pressure development is caused by the expansion coefficient and the bulk modulus. The resulting flow of wetting liquid is onto the surface of the cross section and into the cross section. The general theory furthermore states that a saturated zone is developed which progress through the cross section until a fully saturated layer is formed. On the front of this layer the evaporation process causes the build up of pore pressures, which can result in spalling if the build up of pore pressure is insufficiently reduced by the flow of water vapour towards the surface of the cross section. The analytical model develops a fully saturated layer, which is present in the cross section and on the front of this layer the pore pressure builds up and causes spalling. In the numerical model a saturated zone develops and is situated at the surface of the cross section and progresses into the cross section. This zone is not a typical fully saturated zone as described in the general theory. The position and the value of the maximum pore pressure is obtained from respectively the position of the 100 ^{o}C front and the amount of wetting liquid which flows into the cross section and onto the surface. In case the pore pressure develops high enough, spalling occurs.

7.3.2. Experimental validation

The second important base is the validation of the analytical and numerical model by comparing the obtained results and the analyzed behaviour with results and behaviour obtained from experiments. In the literature a large amount of information can be found which deals with the behaviour of concrete during exposure to a heat source. The most available information however deals with audio and visual observations during testing of a concrete specimen. These observations can be as crude as the indication of the time when a sound was observed which indicated the occurrence of spalling to the complete video recording of the spalling process and the measurement of the spalled concrete layers. These observations can therefore be used to determine if the obtained time when spalling occurs and the depth of the spalled of layer are correct. However, information about the transport of water vapour, the saturation distribution and the build up of pore pressures are much more difficult to find. Only in a few experiments was the specimen fitted with measurement instruments for the pore pressure development. Furthermore, experiments which obtain information about the transport of water vapour and the saturation distribution are even harder to find.

The experimental information, which is depicted in table 7.2, indicates that especially in the audio and visual observations, there is a large difference in obtained information. This is usually due to the chosen method of heating of the concrete. In case of a radiant heater the rate of heating is much lower than compared to an oven where the concrete is exposed to a gas flame. In case of an oven with a gas flame the first sounds of spalling, usually surface spalling, are heard after 2-2,5 minutes into the fire. After 5-7 minutes the first explosive spalling is heard and this process continues at regular intervals. The thickness of the spalled of layer is around 20-30 mm. After 10 minutes the intervals between the sounds of explosive spalling starts to increase and the intensity of the ‘bang’ decreases. After 30 minutes into the fire the process stops. In case of a radiant heater the first sounds of explosive spalling are usually heard after around 20-25 minutes and continue until 50 minutes. Furthermore, the temperature at which spalling occurs is most of the time indicated with the surface temperature and is in the range of 250-420 ^{o}C for an oven which is a temperature of 200-325 ^{o}C at the position of the build up of pore pressure. In case of a radiant heater the temperature is in the range of 400-600 ^{o}C. In addition, the limited amount of experimental information that deals with the build up of pore pressures and especially the position and value indicate that in case of normal strength concrete and a rapid heating up of the cross section, the pore pressure at a depth of 20 mm into the cross section of the concrete is around 1,3-1,6 MPa. Furthermore, the maximum peak is around 30 mm to 40 mm into the cross section of the concrete and is in the range of 1,8-3,0 MPa.

These general observations can be compared to the obtained results from the analytical and the numerical model. In the analytical and numerical model a rapid heating of the cross section of the concrete takes place. In the analytical model spalling takes place after 6,02 min and the thickness of the spalled of layer is 16 mm. The pore pressure at that position has reached 1,58 MPa and the temperature is 200 ^{o}C. This behaviour fits perfectly on the general observations mentioned above. The second pore pressure development is after 14,54 min at a depth of 40 mm. The maximum pore pressure is obtained after 21,00 min and is 1,00 MPa and the temperature is 180 ^{o}C.

TYPE	OBSERVATION	GENERAL REMARKS
Explosive spalling [28]	Time of occurrence: 7-30 min, loud bang	Spalling of a violent nature with serious influence
Surface spalling [28]	Time of occurrence: 7-30 min, Cracking sound	Spalling of a violent nature which can be serious influence
Spalling [28]	Surface temperature: 250-420 ^{o}C	Depends on heating rate and concrete properties
Explosive spalling [46]	Time of occurrence: 26 min, temperature in furnace: 480 ^{o}C	Normal weight concrete, water/cement ratio:0,5, high rate of heating, no applied load, curing at 65 % RH
Cracking [46]	Sever cracking at the surface	Normal weight concrete, water/cement ratio 0,25, high rate of heating, 10% percent loading, moist curing at 85%-100% RH
Cracking [46]	Cracking only on the bottom surface of the beam	Normal weight concrete, water/cement ratio:0,5, low rate of heating, no applied load, moist curing at 85%-100% RH
Explosive spalling [46,38]	Time of occurrence: 27-50 min, furnace temperature: 400-600 ^{o}C	At higher temperatures the spalling is more violent
Explosive spalling [46]	Beams with curing at RH > 65 % are more susceptible to explosive spalling	
Explosive spalling [46]	Beams with a high rate of heating are more susceptible to explosive spalling	
Spalling [36,27]	The temperature at which spalling occurs, at 25 mm deep, is in the range of 200-325 ^{o}C	
Explosive spalling [38]	The temperature at which spalling occurs is the range of 400-600 ^{o}C	High and normal strength concrete (with silica fume)
Explosive spalling [48]	First sounds of spalling noticed after 2-2,5 minutes.	Normal strength concrete and a heating curve which follows the RWS-curve
Explosive spalling [48]	Explosive spalling occurs, during rapid heating, in the first 10 minutes of the fire. The sounds of explosive spalling are heard in short intervals. After 10 minutes the intervals between the sounds increases and the intensity of the sound decreases. After 30 minutes no sounds are heard and the process of spalling has stopped.	Normal strength concrete and a heating curve which follows the RWS-curve.
Explosive spalling [48]	Spalling depths of as much as 20 mm are reported.	Normal strength concrete and a heating curve which follows the RWS-curve

Pore pressure build up [48]	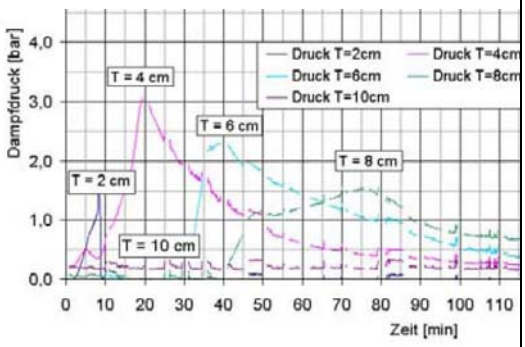	Pore pressure is measured at different points in the cross section of the concrete. At a depth of 20 mm the pore pressure is 1,5 MPa. The maximum pore pressure is measured at 40 mm and is 3,0 MPa. The concrete is of normal strength and the heating curve follows the RWS-curve
Pore pressure build up [36]	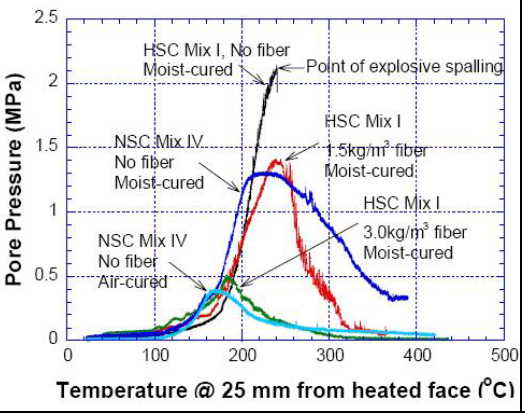	Pore pressure is measured at a depth of 25 mm into the cross section of the concrete. In case of Normal strength concrete the pore pressure develops to 1,3 MPa. Heating rate was 5 °C/min
Pore pressure build up [36]	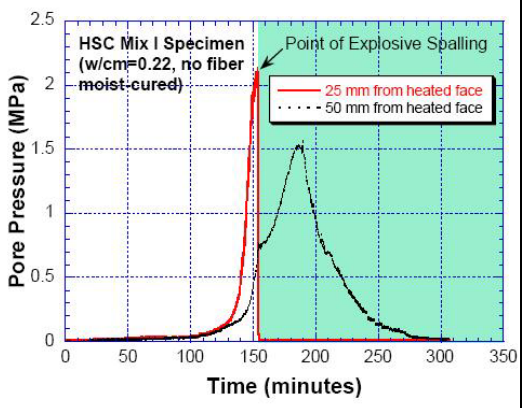	Pore pressure is measured at a depth of 25 mm into the cross section of the concrete. In case of High strength concrete the pore pressure developed to 2,1 MPa and explosive spalling happened. The thickness of the spalled layer was around 25 mm. Pore pressure continued to build up at 50 mm. Heating rate was 5 °C/min
Pore pressure build up [27]	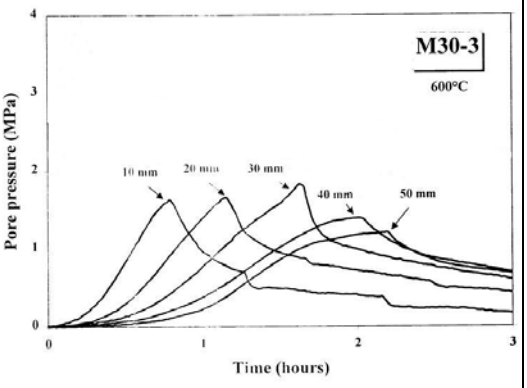	Pore pressure is measured at different depths into the cross section of the concrete. The pore pressure slightly increases from 10 mm to 20 mm. The pore pressure is around 1,6 MPa. The maximum pore pressure is measured at 30 mm and is 1,8 MPa. The concrete used is of normal strength and a radiant heater is used a heat source.

Table 7.2 Experimental information about concrete during fire from numerous sources

Again the results fit onto the general observation, except the interval between both peak pore pressures is rather large and the peak pore pressure is lower as expected. Both of these aspects are influenced by the heating rate, which reduces in time. This influences the development of the build up of the second pore pressure. In most of the test conducted the heating rate is constant and therefore the intervals between the first and the second pore pressure build up is smaller and the second peak pore pressure has the same value or is even higher than the first peak pore pressure.

In the first numerical model spalling takes place after 2,77 min and the thickness of the spalled of layer is 26 mm. The pore pressure at that position has reached 1,42 MPa and the temperature is 100 ^{o}C. Furthermore, spalling takes place for the second time after 4,90 min and the thickness of the spalled of layer is then 24 mm. The maximum pore pressure and temperature are comparable to the first time. This behaviour fits on the general observations mentioned above, however the times when spalling occurs indicate that the process is to fast, but this is due to the high heating rate of the cross section. Furthermore, the temperature is relative low, but this is due to the assumptions and theories used in the model. In the second numerical model spalling takes place after 4,55 min and the thickness of the spalled of layer is 29 mm. The pore pressure at that position has reached 1,43 MPa and the temperature is 100 ^{o}C. Furthermore, spalling takes place for the second time after 7,90 min and the thickness of the spalled of layer is then 27 mm. The maximum pore pressure and temperature are comparable to the first time. This behaviour fits on the general observations mentioned above. The relative low temperature is due to the assumptions and theories used in the model.

8. Case study: HSL-Zuid 'Groene Hart' tunnel

8.1. General

In this chapter a case study is presented in which the developed numerical model is implemented in simulating a fire in the "Groene Hart" tunnel in the HSL-Zuid. The HSL-Zuid is a new high speed railway connection in the East of the Netherlands between Amsterdam, Schiphol, Rotterdam and Paris (figure 8.1). The railway line is designed for a maximum speed of 300 km/h and connects to the high speed railway infrastructure in Belgium and France. The project incorporates the construction of a bored tunnel underneath the "Groene Hart" to preserve a natural and ecological area [IX].

The bored tunnel is made with a concrete segmental lining and has a length of 7160 meters. The tunnel is situated around 30 meters below N.A.P [IX]. The tunnel has an outer diameter of 14,50 meters and a concrete lining with a thickness of 600 mm. The bored tunnel is made up out of rings with a length of 2 meters and consisting out of 9 lining elements and 1 closure element [IX]. The tunnel consists out of two railway lines, one in each direction, which are separated by a concrete wall with a thickness of 450 mm. In this separation wall every 150 meters an emergency door is situated which can be used is case of an emergency like a fire, to pass into the next part of the tube. In figure 8.2 a general overview is depicted of the inside of the bored tunnel. In this figure the concrete lining is still visible, because after construction of the tunnel the lining is covered with fire resistant cladding. When a fire occurs inside the tunnel, the concrete lining is exposed to the heat of the fire. The fire is simulated using the already mentioned HSL-Zuid fire curve. The fire resistant cladding is used to ensure that the concrete lining is not damaged and that failure of the lining does not occur throughout the complete duration of the HSL-Zuid fire curve. Furthermore, the fire resistant cladding itself is not allowed to suffer damage for at least the first 30 minutes of the fire. In figure 8.3 a cross section of the tunnel is depicted.

Fig 8.1 location of the HSL-Zuid in the Netherlands [IX]

Fig 8.2 inside of the "Groene Hart" tunnel with the lining still visible [IX]

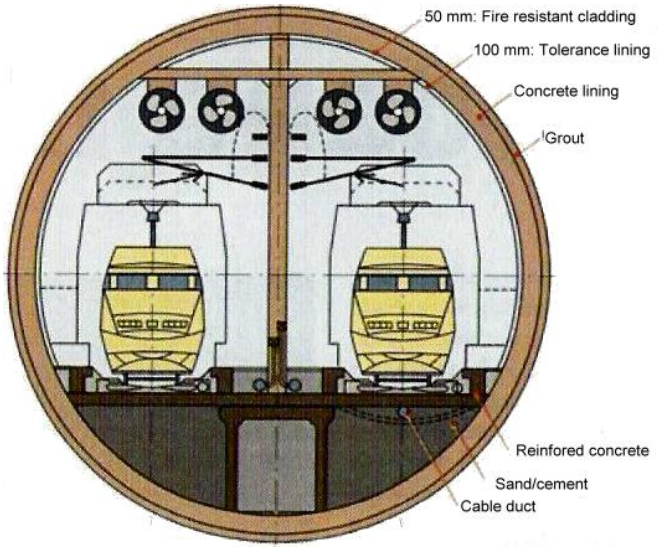

Fig 8.3 cross section of the "Groene Hart" tunnel [51]

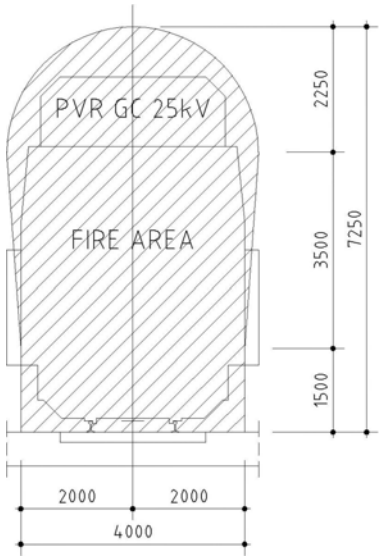

Fig 8.4 Profile of free space with added fire curve

The general idea of this case study is to simulate a fire on the right side of the bored tunnel. The developed numerical model is than used to estimate the temperature distribution throughout the tunnel and the occurrence of spalling.

8.2. The Heat transfer model

In figure 8.5 a general overview is given of the Heat transfer model used for the "Groene Hart" tunnel.

Basis of the Heat transfer model

The Heat transfer model consists out of two parts. The first part is the tunnel itself, which is modelled as a homogeneous concrete ring. The material properties of the concrete used in the Heat transfer model of chapter 6 are used to describe the material behaviour of the concrete ring. The second part is the fire. The fire is modelled using the profile of free space of a train and added to this profile a fire box, which is depicted in figure 8.4. The profile of free space of a train is used in the design of a structure to obtain the available space for the train needed to base through the structure. The fire box is added to this profile to simulate a fire in the train in which a carriage is completely on fire. The top side of the fire box has a circle like shape. This can be explained by a small fire, like a match, which radiates heat in a circle like shape in which every point with the same distance to the heat source has an equal temperature. Around 1,5 meters above the tracks, the fire box widens, which is due to flames of the fire coming out of the windows of the carriage. The complete outer edge of the fire box has an equal temperature, which results in prescribing the HSL-Zuid fire curve to the complete fire box.

Determination of the temperature distribution

The initial temperature of the lining is 20 ^{o}C and increases due to the fire. The increase in the surface temperature of the lining is calculated by using the ability of ABAQUS to model surface-to-surface contact. This means that the space between the fire box and the surface of the lining is assumed to be air, which transmits the heat from the fire on to the surface of the lining by radiation and thermal conductance.

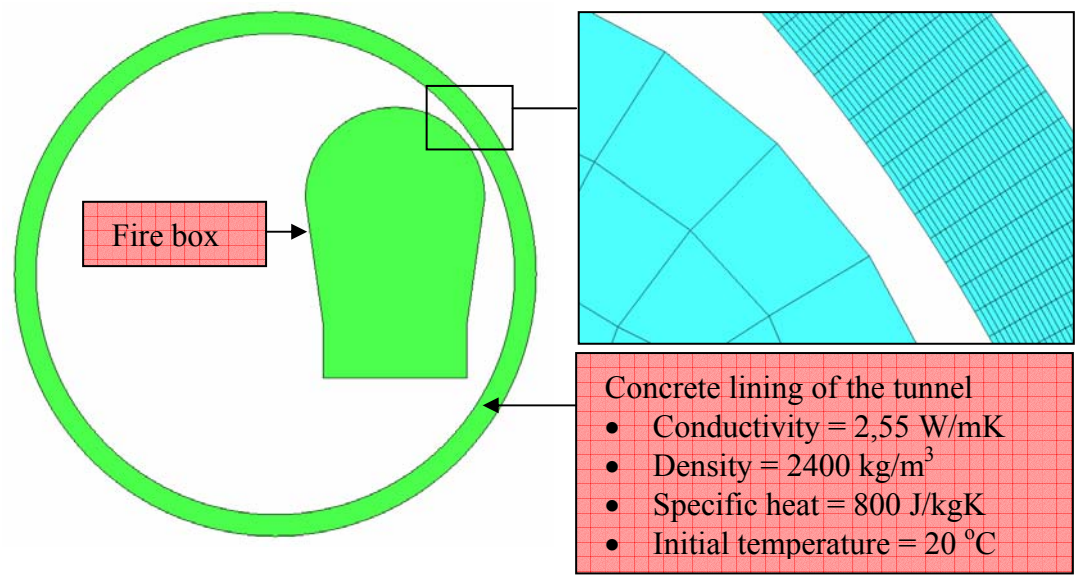

Fig 8.5 general overview of the Heat transfer model of the "Groene Hart" tunnel

The thermal conductance of air is 0,026 W/mK and the radiation is determined by an emmissivity factor of 0,8. With the increasing surface temperature, the heat transfer model then determines the penetration of the heat into the lining by using the conductivity, density and specific heat of the concrete.

Mesh

The mesh used in the Heat transfer model is a radial mesh with 30 elements with a height of 20 mm in depth direction of the lining. The elements have a width of around 100 mm. The elements are quadrilateral heat transfer elements with 4 nodes and per node the temperature as the single degree of freedom. The shape functions are linear across the element. The mesh for the fire box consists out of relative large elements, because the temperature is uniformly prescribed on this area.

8.3. The Pore fluid/Stress model

Basis of the Pore fluid/Stress model

In designing a tunnel there are two main directions, which are the longitudinal direction and the ring direction. In study and primary design phases it is mostly satisfactory to analyse the structural behaviour of the tunnel by making use of a two dimensional model, such as the continuum model and the bedded beam model which represent the ring direction of the tunnel. These ring models, which are depicted in figure 8.6 [16], determine the interaction between the soil and the lining of the tunnel, because the soil around the tunnel determines the loading on the tunnel and at the same time also works as support condition for the lining [4,5,15]. This interaction causes resulting normal forces and moments in the lining of the tunnel. The springs support at the crown of the tunnel is neglected in the bedded beam model, because this part of the ground will settle in time and it is therefore assumed that no stiffness and only loading maybe contributed to this ground column. However, this only applies to shallow tunnels for which it holds that H<4*R [17,14,15].

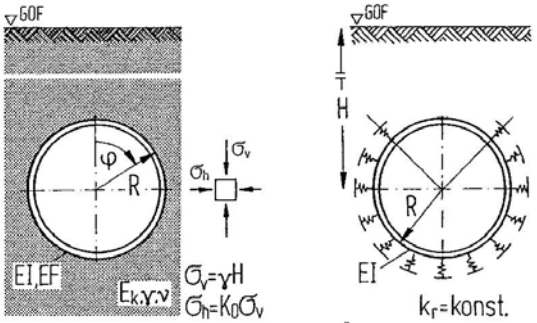

Fig 8.6 two dimensional tunnel models: continuum model (left), bedded beam model (right) [16]

The general idea behind the Pore fluid/Stress model is to model the tunnel as an elastic supported ring, which means that the support of the lining of the tunnel is based upon springs supporting the lining. These springs are positioned in radial direction of the lining and represent the elastic support of the lining. Furthermore, the soil loading, the developed material model and the results from the Heat transfer model are implemented to obtain the Pore fluid/Stress model. However, the rapidly expanding wetting liquid and the size of the problem causes convergence problems. Therefore, the Pore fluid/Stress model is subdivided into two separate models. The first model is a spring supported ring which determines the stresses due to the soil loading and the interaction with the soil. In this model the results from the Heat transfer model, the temperature dependence of the material properties and the expansion of the lining are also incorporated. The second model determines the stresses caused by the pore pressure. This model is not loaded or supported by the soil. The support of the lining of the tunnel is implemented by restraining the movement of the tunnel at the top in the 1-direction and the bottom in both the 1 and 2-direction. The stresses of the different models are then combined to obtain the resulting stresses. This procedure can be done, because the model is based upon linear elasticity theory and therefore the calculated stresses can be superimposed to obtain the resulting stresses. In figure 8.7 an overview is depicted of the tunnel model.

The soil loading model

This model is a spring supported ring which determines the stresses from the soil loading and the springs. Furthermore the material properties are temperature dependent and the results from the Heat transfer model are incorporated to include the effect the heating of the lining has on the stress distribution in the lining.

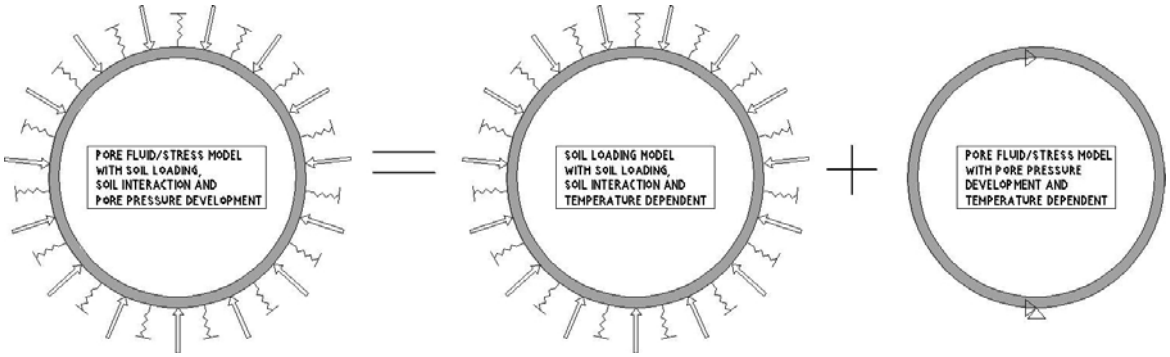

Fig 8.7 overview of the tunnel model of the "Groene Hart" tunnel

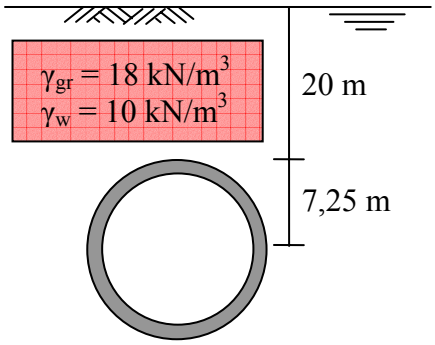

Fig 8.8 ground profile and depth situation "Groene Hart" tunnel

The loading of the soil on the tunnel is determined by the depth of the tunnel and by specific type of ground in which the tunnel is situated, which is depicted in figure 8.8. The soil loading consist out of a vertical and horizontal soil stress, which are rewritten to and radial and a tangential component. The radial stress on the lining can be written as equation 8.1. The soil loading can be implemented in ABAQUS by defining an analytical field with equation 8.1.

$$\sigma_{rad} = \sigma_v \cos^2(\varphi) + \sigma_h \sin^2(\varphi) \tag{8.1}$$

in which σ_v = vertical soil stress, according to fig 8.7 => $\sigma_v=\sigma_v'+\sigma_w$
$\sigma_v=(\gamma_{gr}-\gamma_w)*H+\gamma_w*H=(18-10)*27,25+10*27,25=490,5$ kN/m^2
σ_h = horizontal soil stress, according to fig 8.7 => $\sigma_h=K_o*\sigma_v'+\sigma_w$
$\sigma_h=K_o*[(\gamma_{gr}-\gamma_w)*H]+\gamma_w*H=0,46*[(18-10)*27,25]+10*27,25=381,5$ kN/m^2

The springs of the lining are implemented using equation 8.2.

$$k_r = \frac{E_{soil}}{R} = \frac{75000}{7,25} = 10344 kN/m \tag{8.2}$$

in which k_r = spring constant [kN/m]
E_{soil} = Modulus of Elasticity of the soil [kN/m^2]
R = outer radius of the tunnel [m]

The mesh used in the soil loading model is a radial mesh with 20 elements with a height of 30 mm in depth direction of the lining. The elements have a width of around 43 mm. The elements are quadrilateral plane strain elements with 4 nodes and per node the displacement in the 1 and 2-direction as the degree of freedom. The shape functions are bilinear across the element.

The pore fluid/Stress model

This model is a simply supported ring which determines the stresses from the pore pressure development and the heat penetration. The results from the Heat transfer model are incorporated to be used as the input in the determination of the pore pressure development. The developed behaviour of the wetting liquid and the other material properties are implemented to describe the behaviour of the lining. The initial saturation of the lining is again 62 % by defining the initial pore pressure to be -4000 Pa. The interior surface of the lining is kept at a constant -4000 Pa. The Pore

fluid/Stress model then determines the pore pressure development and the resulting stresses.

The difference with the developed numerical model described in the previous chapter is the subroutine. In the developed subroutine a rectangular coordinate system is used, but for a tunnel it is more convenient to use a cylindrical coordinate system which is depicted in figure 8.9. For the subroutine this implies that in USDFLD the stresses of the integration point have to be stored at a radius at an angle.

Therefore, the subroutine is adapted to determine the radius and the angle for every integration point. The integration points are stored for all the zones, however for zone III zone IV the angle is chosen $1*10^5$, which in UMESHMOTOIN ensures that these values are not used. This saves calculation time, because the fire is only present in the zone I and zone II of the tunnel. Furthermore, the definition of the angle φ ensures that the integration point has a positive radial angle for zone I and a negative angle for zone II.

In UMESHMOTOIN the rectangular coordinate system is also changed into a cylindrical coordinate system. The absolute difference in angle between the integration point and the surface node multiplied with the inner radius of the tunnel and is used to determine the distance in the 2-direction, which is tangential to the surface of the lining. This distance is then used to determine which integration points are used to estimate the stress distribution in 1-direction, which is the radial direction and thus perpendicular to the surface of the lining. The S_{11} stress of these integration points are then checked whether the limit tensile stress is exceeded. Furthermore, the integration point with the largest radius which just exceeds the limit tensile stress is searched for. This then determines the depth of the spalled of layer. However, besides the stresses resulting from the pore pressure development, there are also stresses from the Soil loading model and therefore a resulting stress from both models should be used in determining if spalling occurs. In the next paragraph it will be explained that the S_{11} stresses are largely influenced by the pore pressure development and only slightly influenced by the Soil loading model and therefore the S_{11} stresses caused by the pore pressure development can be used.

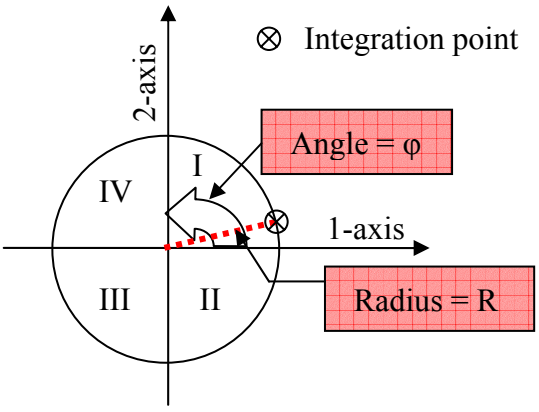

$$R = \sqrt{coord(1)^2 + coord(2)^2}$$
$$\varphi = a\tan\left(coord(2)/coord(1)\right)$$

The definition of φ ensures that the angle determines if the integration point is situated in the I or the II zone

Fig 8.9 determination of the radius and angle of the integration point

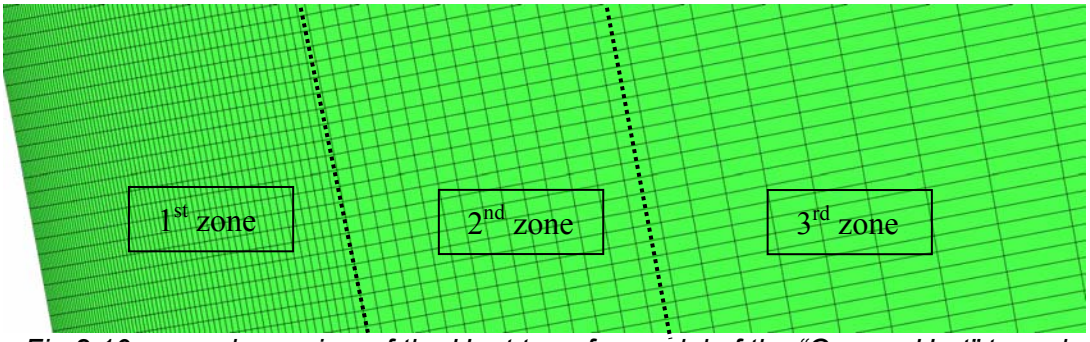

Fig 8.10 general overview of the Heat transfer model of the "Groene Hart" tunnel

The mesh used in the Pore fluid/Stress model is important, because the previous chapter has shown the effects the chosen mesh has on the convergence and the calculation time. The mesh consists out of two parts. The first part is the region which is exposed to the heat of the fire and the second part is the region which is not exposed to the fire. The first part is subdivided in depth direction in three zones, which is depicted in figure 8.10. The first zone, which is situated close to the surface, has a depth of 100 mm and is meshed with a very fine mesh to ensure convergence. The elements are in depth direction biased with the first elements having a height of 0,5 mm and the last elements having a height of 2,8 mm. The width of the elements is 5 mm. The second zone is a transition zone in which the height of the elements increases to 9,2 mm over a distance of 100 mm.

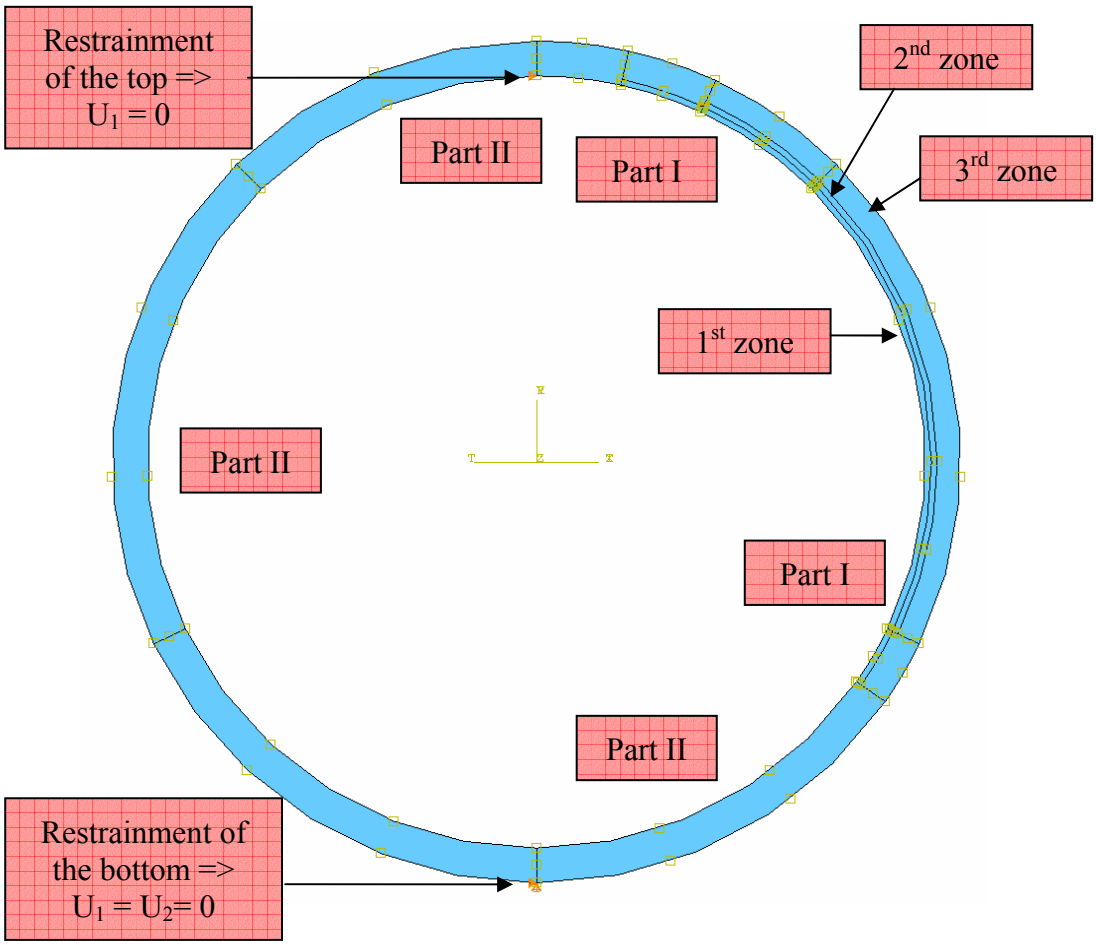

Fig 8.11 general overview of the Pore fluid/Stress model of the "Groene Hart" tunnel

The last zone is the remaining 400 mm of the cross section and the elements increase to a height of 52 mm. The mesh is a radial mesh, which means that the width of the elements gradually increase in depth direction to 5,4 mm. The second part of the mesh is meshed uniformly with elements with a height and width of 60 mm. Furthermore, between both parts a transition zone is present, which gradually transforms the mesh from the very dense mesh on the surface of the first part to the coarse mesh of the second part. The above described mesh consists out of 217.848 elements. To reduce the number of calculation, the elements of the second part are reduced integration Pore fluid/Stress elements, whereas the elements of the first part are the more accurate full integration Pore fluid/Stress elements.

In figure 8.11 a general overview is depicted of the Pore fluid/Stress model. The restrained movement of the top and bottom of the tunnel are depicted by oranges triangles, which represents applied hinges. The parts used in the mesh are also indicated.

8.4. Results and analysis

Before the results during fire exposure are depicted and analysed, first the results from the Soil loading model after 1 second of fire exposure are depicted in figure 8.14 and 8.15. These figures represent the stresses resulting from the soil loading and the interaction with the springs when the temperature is still 20 ^{o}C. The soil loading model is based upon springs supporting the lining. The main loading bearing direction of the ring are the stresses acting in tangential direction of the lining, which are the S_{22} stresses. These stresses can be compared to the analytical obtained stress distribution of the continuum model or the bedded beam model by Duddeck. However, the advantage of the continuum model is that the ring is fully supported and therefore the stress distribution is more comparable with the Soil loading model. The stresses in the continuum model can be obtained from figure 8.12 and 8.13 and equation 8.3.

$$N_{top/bottom} = \gamma H \frac{1+K_o}{2} R\left[\frac{1}{1+0{,}75\beta} - \frac{1-K_0}{1+K_0}.\frac{1+0{,}064\alpha}{1+0{,}085\alpha}\right]$$

$$N_{side,middle} = \gamma H \frac{1+K_o}{2} R\left[\frac{1}{1+0{,}75\beta} + \frac{1-K_0}{1+K_0}.\frac{1+0{,}064\alpha}{1+0{,}085\alpha}\right] \qquad (8.3)$$

$$M_{top'/bottom/side,middle} = \gamma H \frac{1-K_0}{2} R^2 \frac{1}{2+0{,}18\alpha}$$

in which $\alpha = \frac{E_{soil} R^3}{EI}$, $\beta = \frac{E_{soil} R^3}{EF}$

Equation 8.2 can be used to determine the stress distribution throughout the lining and compare these stresses with the S_{22} stress distribution of the Pore fluid/Stress model.

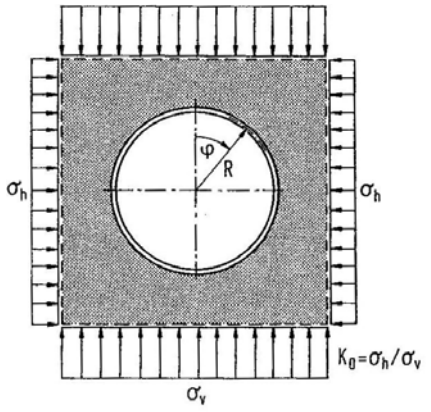

Fig 8.12 basis of the continuum model [16]

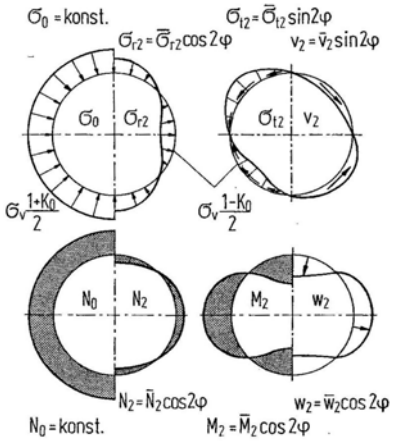

Fig 8.13 determination of the internal forces [16]

$$N_{top/bottom} = 1772kN/m \Rightarrow \sigma_{top/bottom} = \frac{1772*10^3}{600*1000} = -2{,}95MPa$$

$$N_{side,middle} = 3305kN/m \Rightarrow \sigma_{side,middle} = \frac{3305*10^3}{600*1000} = -5{,}50MPa$$

$$M_{top'/bottom/side,middle} = 603kNm/m \Rightarrow \sigma_{top/bottom/side,middle} = \frac{603*10^6}{1/6*1000*600^2} = 10{,}06MPa$$

$$\varphi_{top,inside} = -2{,}95 + 10{,}06 = 7{,}11MPa$$

$$\varphi_{top,outside} = -2{,}95 - 10{,}06 = -13{,}01MPa$$

$$\varphi_{side,middle,inside} = -5{,}50 - 10{,}06 = -15{,}56MPa$$

$$\varphi_{side,middle,outside} = -5{,}50 + 10{,}06 = 4{,}56MPa$$

When the resulting stresses from the continuum model are compared to the S_{22} stress distribution of the Soil loading model, it can be observed that the behaviour of the Soil loading model is not exactly the same as the continuum model. This is due to the springs in the Soil loading model behaving to stiff and therefore causing the ring of the tunnel to be less subjected to bending moments. However, for a first model to be used to indicate how the developed numerical model can be implemented the Soil loading model behaves well enough.

The Heat transfer model determines the build up of the temperature throughout the lining of the tunnel and a general overview of the results are depicted in figure 8.16. The main picture depicts the progress of the heating of the lining after 60 minutes of exposure to the HSL-Zuid fire curve and indicates that only a part of the lining experiences in increase in temperature. This is the part of the lining which is the situated the nearest to the fire and therefore experiences the largest increase in temperature. In the figure 8.17 the temperature distribution is depicted of the cross section indicated in the smaller picture of figure 8.16. The temperature on the surface of the lining increases rapidly in time and after 5 minutes and 30 minutes of fire exposure the temperature is respectively 300 ^oC and 900 ^oC.

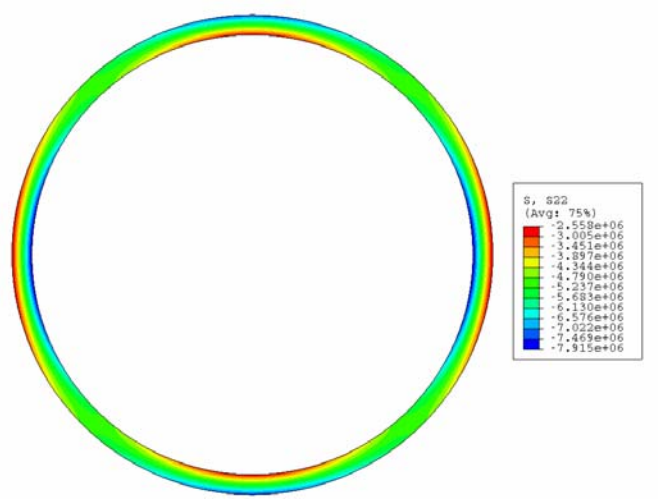

Fig 8.14 Tangential stress distribution (S_{22}) throughout the tunnel

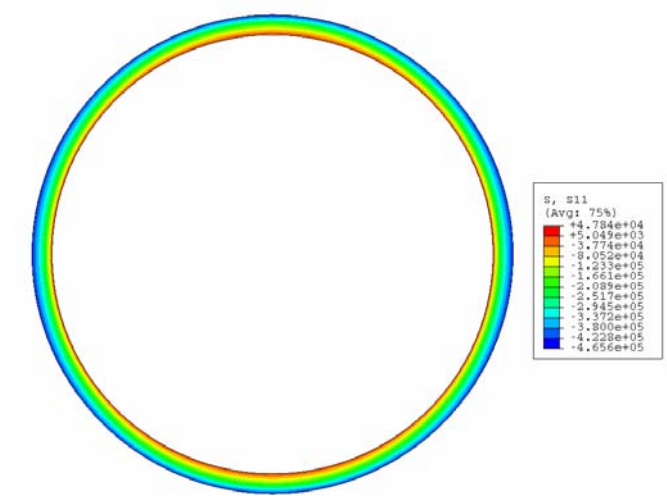

Fig 8.15 Radial stress distribution (S_{11}) throughout the tunnel

Furthermore, the temperature distribution also indicates that after 5 minutes of fire exposure already 40 mm of the cross section experience an increase in temperature. This process continues and after 30 minutes and 60 minutes the heated layer has progresses to a depth of respectively 180 mm and 280 mm. The temperature distribution indicates that in time the speed at which the heated layer progresses into the cross section decreases, which is due to the fire box obtaining a constant temperature of 1000 ^{o}C after 5 minutes. The Pore fluid/Stress model determines the pore pressure and saturation distribution throughout the cross section and the resulting stresses.

In figure 8.18 the temperature distribution at the cross section of node 8445 of the Pore fluid/Stress model is depicted.

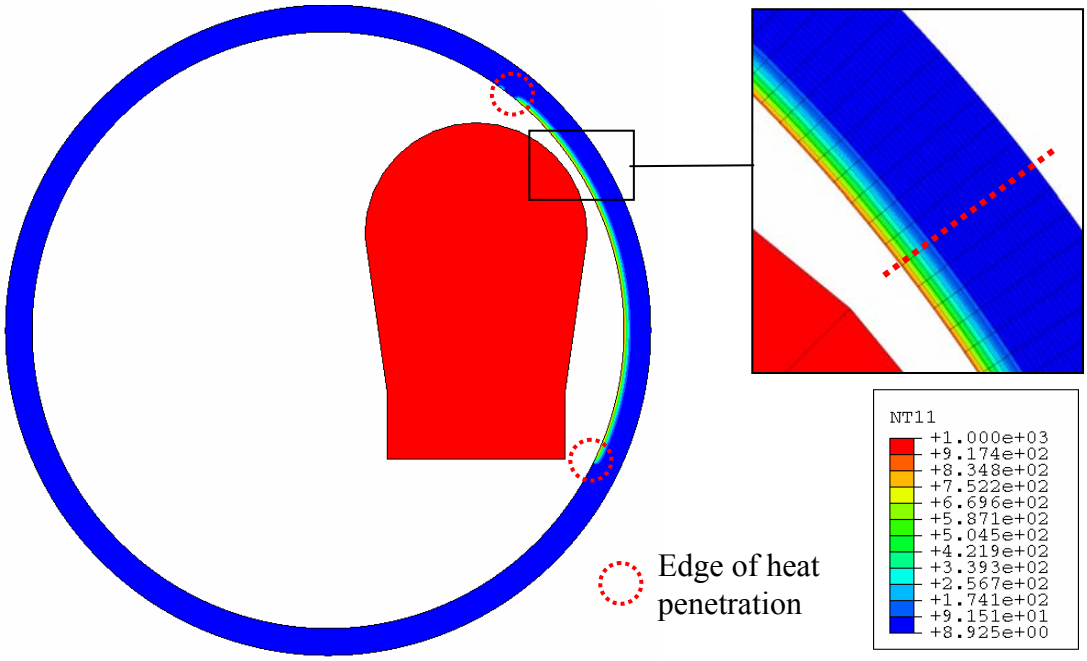

Fig 8.16 general overview of the results from the heat transfer model of the "Groene Hart" tunnel after 60 minutes of exposure to the HSL-Zuid fire curve

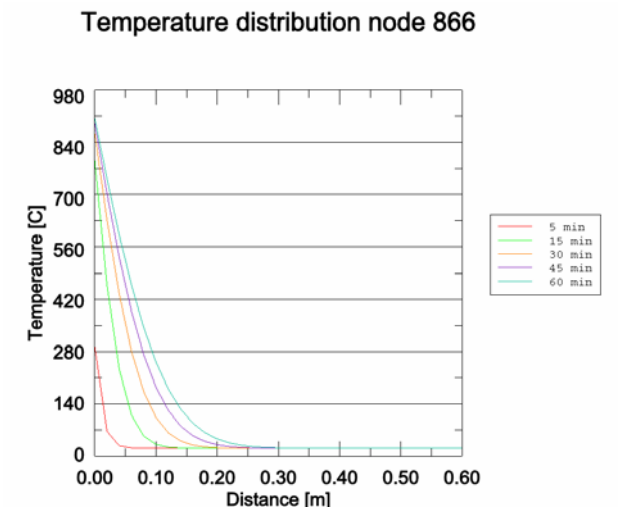

Fig 8.17 temperature distribution in the "Groene Hart" tunnel at node 866 (Heat transfer model)

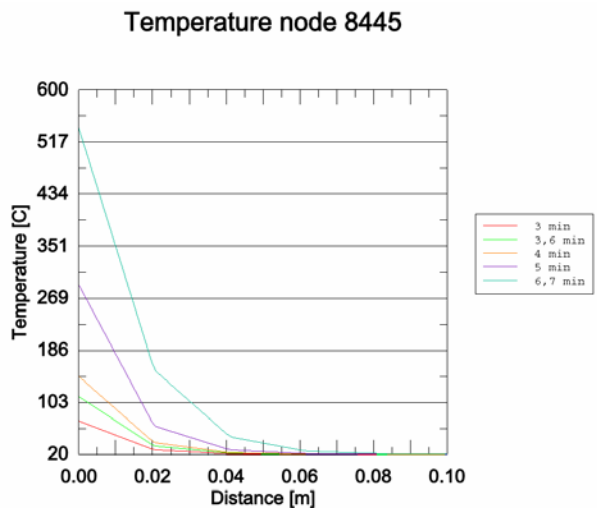

Fig 8.18 temperature distribution in the "Groene Hart" tunnel at node 8445 (Pore fluid/Stress model)

This cross section is situated at the same position as the cross section of node 866 of the Heat transfer model. Furthermore, in this cross section is the heat penetration the largest, which is due to the close proximity to the fire.

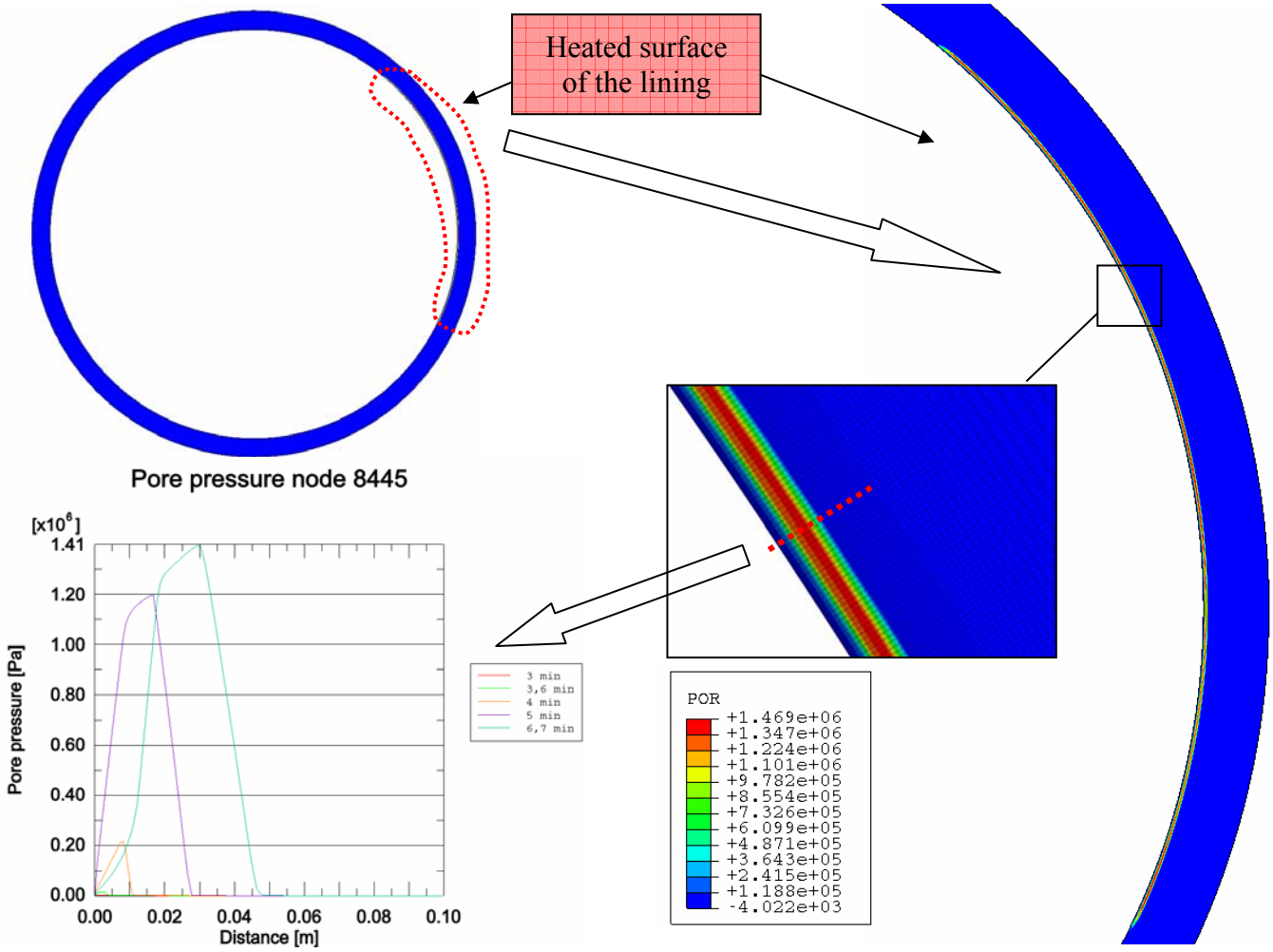

Fig 8.19 general overview of the results from the Pore fluid/Stress model in the "Groene Hart" tunnel

After 3,5 minutes the temperature on the surface of the lining already reaches a temperature of 100 °C, which means that the process starts. In figure 8.19 a general overview is depicted of the results of the Pore fluid/Stress model. The pore pressure distribution, at node 8445, indicates that after 3,6 minutes of fire exposure the pore pressure peak starts to build up. In time the temperature on the surface of the lining increases to a temperature of 290 °C after 5 minutes. The 100 °C front has then progressed to around 16 mm into the cross section. The pore pressure peak also progresses through the cross section and has reached a maximum pore pressure of 1,2 MPa at a depth of 16 mm. The maximum pore pressure reached is 1,41 MPa at a depth of 30 mm after 6,7 minutes.

The saturation distribution of node 8445 of the Pore fluid/Stress model is depicted in figure 8.20. The saturation distribution progress into the cross section and after 5 and 6,7 minutes has reached a depth of respectively 26 mm and 45 mm. When this progress is compared to the pore pressure peak, it is again observed that the saturation distribution progresses faster through the cross section than the pore pressure peak, which means that the pore pressure becomes increasingly insufficient to level off the wetting liquid and therefore the maximum pore pressure increases.

In chapter 6 it was already established that the pore pressure distribution is in equilibrium with the stresses acting in the direction perpendicular to the heated surface of the cross section. Furthermore, these stresses are equal in shape and value of the pore pressure distribution. This means that in this case the pore pressure distribution is in equilibrium with the S_{11} stresses and that the resulting S_{11} stresses are equal to the pore pressure distribution. Therefore the pore pressure development of figure 8.15 can also be seen as the S_{11} stress distribution resulting from these pore pressures. However, besides the S_{11} stresses resulting from the pore pressure development, also stresses act in this direction resulting from the soil loading, the springs and the heat penetration of the lining. These stresses are obtain from the Soil loading model and are depicted in figure 8.21. The S_{11} stress distribution is taken at node 1721 of the Soil loading, which is the same position as node 8445 of the Pore fluid/Stress model.

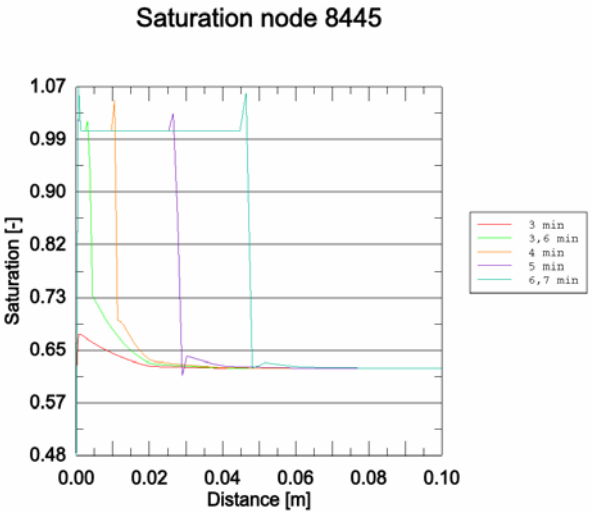

Fig 8.20 Saturation distribution at node 8445 (Pore fluid/Stress model)

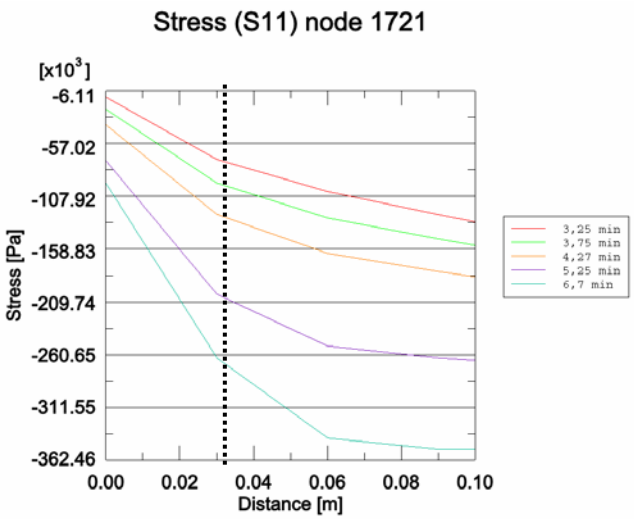

Fig 8.21 Radial stress (S_{11})at node 1721 (soil loading model)

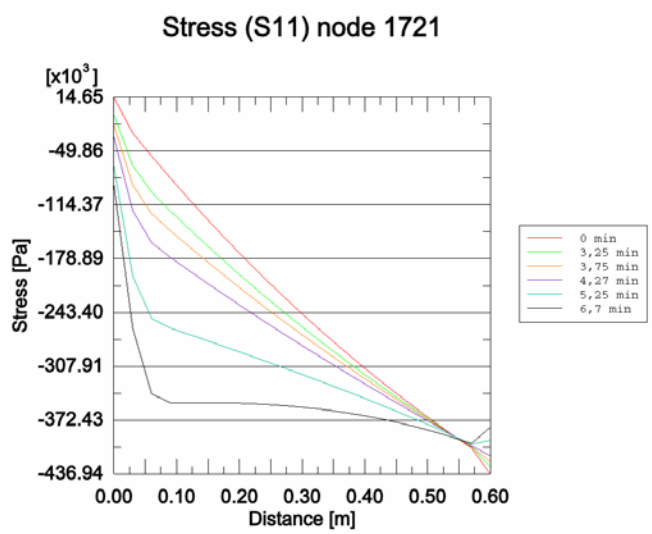

Fig 8.22 Radial stress (S_{11}) at node 1721 (Soil loading model)

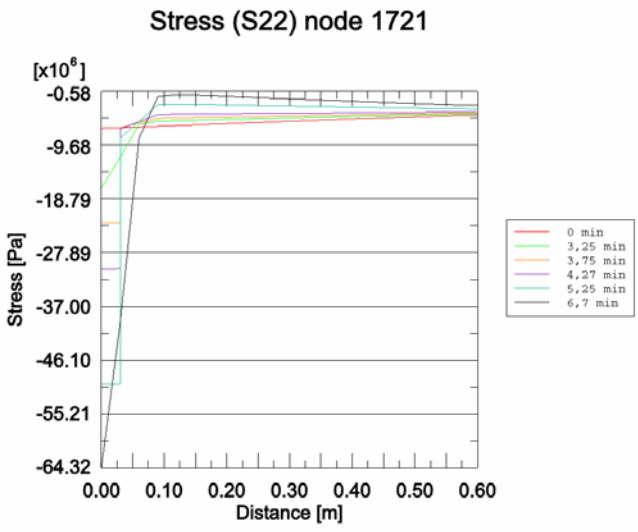

Fig 8.23 Tangential stress (S_{22}) at node 1721 (Soil loading model)

This S_{11} stress distribution is based upon secondary stresses resulting from the soil loading, the interaction of the springs and the ring and the heat penetration. After 3,25 minutes the main compressive stress on the surface of the cross section is 0,0061 MPa. The compressive stresses increase into the cross section and is 0,13 MPa at a depth of 100 mm. In time theses stresses increase and after 6,7 minutes the compressive stress on the surface is 0,095 MPa and at a depth of 100 mm the compressive stress is 0,35 MPa. Furthermore, in figure 8.22 the S_{11} stress distribution for the complete cross section at node 1721 is depicted. The S_{11} stress distribution indicates that throughout the cross section, in this direction, compressive stresses are present which are at the most 0,5 MPa.

In figure 8.23 the S_{22} stress distribution is depicted. These stresses are the main load bearing direction of the ring for the soil loading and the interaction between the springs and the ring. Furthermore, the in chapter 5 explained Eigen stresses due to the temperature distribution influence this stress distribution. At the beginning of the fire exposure, the S_{22} stress at the surface of the cross section is a compressive stress of 6,32 MPa. In time the compressive stress on the surface of the cross section increases to 64,32 MPa, which is due to the Eigen stresses. Furthermore, at the beginning of the fire exposure the cross section is in compression with a average compressive stress of 5,20 MPa. However after 6,7 minutes of fire exposure the centre of the cross section has a compressive stress of 1,28 MPa, which is due to the tensile Eigen stress in the middle of the cross section.

The S_{11} stress distribution of the Pore fluid/Stress model and the Soil loading model can be superimposed to obtain the resulting S_{11} stress distribution over the cross section. The maximum S_{11} stress resulting from the pore pressure development is a tensile stress of 1,41 MPa at a depth of 30 mm. The S_{11} stress at this location resulting from the soil loading and the heat penetration is a compressive stress of 0,26 MPa. This means that the resulting stress is a tensile stress of 1,15 MPa. When both S_{11} stress distributions are compared it can be observed that the S_{11} stresses resulting from the pore pressure development can be become larger than 0,4 MPa, while the S_{11} stresses from the soil loading and the heat penetration are, in this time interval, always

lower than 0,4 MPa. This means that the S_{11} stresses of the Soil loading model can slightly reduce the tensile stresses from the Pore fluid/Stress model.

Furthermore, the general idea is to check if spalling occurs by comparing the resulting S_{11} stress distribution with the limit tensile stress of the concrete. This is a good first order approximation for a small block of concrete. However, for a structure as a tunnel, the total stress distribution should be taken into account. This can be done by obtaining the pore pressure distribution at the end of each increment of the Pore fluid/Stress model and prescribing this distribution as a boundary condition on the Soil loading model which then determines the resulting stress equilibrium. The S_{11} stress distribution is mostly influenced by the stresses resulting from the pore pressure development. However, the S_{22} stress distribution is besides the Eigen stresses resulting from the temperature distribution largely influenced by the soil loading. This means that the biaxial strength of the concrete has to be taken into account by using the Mohr Coulomb yield criterion, which is depicted in figure 5.37. The tensile stresses in the S_{11} stress direction are checked against the reduced tensile strength of the concrete. The tensile strength of the concrete is reduced by the increased temperature, but also by the compressive stress which acts in the S_{22} stress direction. This compressive stress caused cracks in tangential direction which further weaken the radial tensile strength.

In a next phase of the design of the tunnel, the Soil loading model can be improved by using a continuum model and modelling the segments the tunnel. Furthermore, the check whether spalling occurs can be completed by using fracture mechanics to analyze the behaviour of the concrete. The Mohr Coulomb yield criterion is not based on fracture mechanics, but on the stresses in the concrete exceeding a limit stress state by a combination of the tensile and compressive stresses [27].

The criterion of spalling for the lining of the tunnel is based upon the subroutine exiting the calculation if anywhere in the model the limit tensile stress is exceeded.

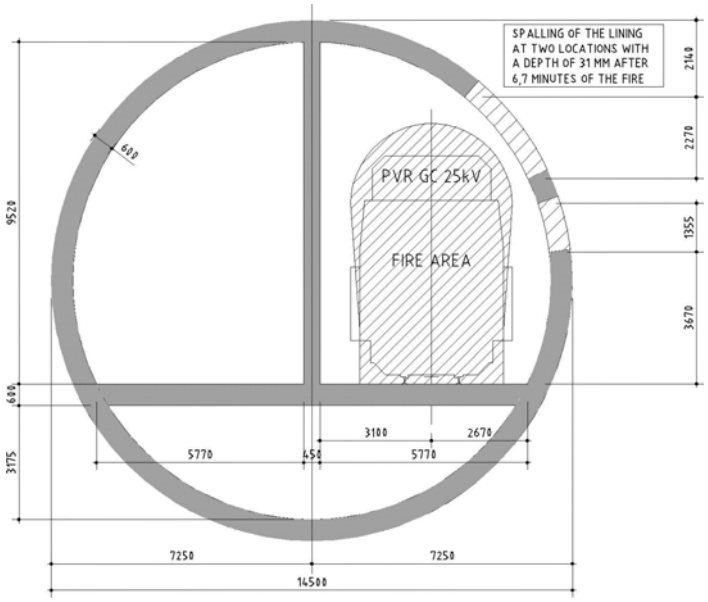

Fig 8.24 damage to the lining estimated by the Pore fluid/Stress model

Fig 8.25 damage to the lining of the Channel tunnel after the fire in November 18, 1996 [8]

At the edge of the heat penetration, which is depicted in figure 8.16, there are peak tensile stresses which are due to the wetting liquid flowing in all directions. These stresses determine the exit of the Pore fluid/Stress model. Therefore, the criterion for spalling is extended to incorporate every part of the lining where the S_{11} stress is between 1,2 MPa and 1,4 MPa. This means that the cross section of node 8445 fulfils this criterion. The presented behaviour of the lining of the tunnel during exposure to the fire predicts spalling at two locations with a depth of 30 mm after 6,7 minutes of fire exposure. In figure 8.24 a general overview is depicted of the "Groene Hart" tunnel with the position of the fire area and the damage due to spalling of the lining. When the predicted damage zones are compared with figure 8.25, which is a photo taken inside the Channel tunnel at the location where the carriages were burning, it can be observed that the position of the damage zones is comparable. The difference is magnitude of the damage and the fact that in figure 8.25 the spalling damage is present over the entire height of the tunnel, is because this photo was taken after the fire and not after 6,7 minutes. The Pore fluid/Stress model therefore gives a good indication of where the process of spalling starts.

8.5. Remarks

From the presented case study a few remarks can be made:

- The proposed procedure to determining spalling in the tunnel is the following:
    1. Obtain a Soil loading model, which is based upon springs supporting the ring and the soil loading acting as radial forces. Alternatively a complete continuum model could be used. These models then determine the structural behaviour of the tunnel, including resulting stresses and displacements
    2. Obtain a Heat transfer model, which is based upon a simple ring and a modelled fire using for instance a fire box. This ring is not supported or loaded by the soil, because the temperature is the only degree of freedom in the uncoupled heat transfer model
    3. Obtain a Pore fluid/Stress model in which the results from the Heat transfer model is used to develop the pore pressure distribution. This model then determines the pore pressure distribution throughout the tunnel.
    4. Include in the Soil loading model the results from the Heat transfer model to determine the stresses in the lining due to the soil loading, the interaction with the soil and the heat penetration. Furthermore, the pore pressure distribution obtained in the Pore fluid/Stress model can be mapped onto the cross section of the Soil loading model. This pore pressure distribution causes stresses which are then included in determining equilibrium in the lining.
    5. The subroutine needs to be adapted to check the biaxial stress state and compare this with Mohr Coulomb yield criterion and by taking into account the temperature dependence of the tensile strength of the concrete.

- The calculation times of the presented numerical model where very long. Most of the model tested had a calculation time of at least 40 hours. The amount of calculation time can be reduced by a "smarter" programmed subroutine.

- The restarting of the calculation after spalling has occurred proved to be difficult, which is due to the removal of the estimated spalled of layer. This layer was part of the lining and therefore carried part of the soil loading. By removing part of the lining and restarting the calculation with a mapped pore pressure and stress distribution caused sever convergence problems. These convergence problems could be solved by using the UMESHMOTOIN technique, which ensures that the layer is removed in small parts and therefore the change in cross section is less abrupt. However, this means that the previous mentioned pore pressure increase should be addressed first. A second solution is restraining the velocity of the new surface, which ensures that the new surface of the lining does not undergo large displacements due to a sudden increase in stress. After 1 second the new surface can be gradually released by ABAQUS which cause the stresses to redistribute and the calculation can be continued.

9. Conclusions and recommendations

In this chapter the main conclusions and recommendations are given based upon the contents of the presented master thesis. The general direction and contends of this master thesis is aimed at fulfilling the main goals which are stated in chapter 3. The conclusions are subdivided into two categories. The first category deals with the general conclusions about spalling such as the relevance of spalling, the main theory about the process which causes spalling and the main factors influencing the process. The second category deals with the results of the analytical and numerical model and the conclusions that can be drawn from the development of these models. The recommendations are based upon both categories.

9.1. Conclusions

9.1.1. General conclusions

- In recent years there have been a number of serious fires in tunnels throughout Europe which caused injured people and even human casualties. Furthermore, there was damage to the tunnel which in some cases jeopardized the structural integrity of the tunnel. Finally, there was always economical damage. This indicates why fire in tunnels can have a serious impact on human life and therefore more research is needed into the behaviour of concrete structures during exposure to a fire.

- After 5 – 7 minutes of normal concrete being exposed to a high heating rate, a layer with a thickness of 20 – 30 mm is spalled of the surface of the cross section. This process is called explosive spalling and is the most dangerous type of spalling. Explosive spalling is a local phenomenon which when it continues causes the cross section and therefore the load bearing capacity to reduce and could result in global consequences such as failure of a structural member and ultimately failure of a structure.

- The main theory of the process which causes spalling of concrete is the penetration of the heat from the fire into the cross section of concrete and the subsequent evaporation of water from the pores of the concrete. Due to the phase change the development of water vapour coincides with an increase in pore pressure, which induces the flow of water vapour. In time the water vapour increasingly flows into the cross section and condensates into water which causes the gradual development of a fully saturated layer called a moisture clog. This layer impedes further water vapour transport and on the front of this layer the pore pressure can build up and could lead to spalling of the layer in front of the fully saturated layer.

- The main factor of the material which influences the occurrence of spalling is the permeability of the concrete. When the permeability of the concrete decreases, the pore structure is badly interconnected and therefore the possibility of spalling increases.

- The main factor of the fire which influences the occurrence of spalling is the heating rate of the concrete. The heating rate determines the progress of the evaporation front and the development of the pore pressures. The possibility of

spalling increases when the heating rate of the concrete increases. Furthermore, by increasing the heating rate, the process which leads to spalling occurs at a higher speed and therefore the process develops faster. This leads to explosive spalling to occur more frequently, but the depth of the spalled of layer decreases.

- The factor of the fire which contributes to the occurrence of spalling is the number of sides of the construction which are exposed to the fire. A construction which is exposed to a fire at two or more sides is heated up with a greater speed and therefore the possibility of spalling increases.

- The factors of the material which contribute to the occurrence of spalling are the porosity, the initial degree of saturation and the tensile strength of the concrete.
  - When the porosity decreases and/or the initial degree of saturation increases, the amount of empty space which the water vapour can fill reduces and therefore the possibility of spalling increases.
  - The tensile strength of the concrete determines the capability of the concrete to withstand the development of pore pressures and therefore when the tensile strength of the concrete reduces, the possibility of spalling increases.

- The factors of the construction which contribute to the occurrence of spalling are the loading of construction and reinforcement.
  - Compressive stresses, especially on the heated surface, tend to close the cracks which are formed by the degradation process of the concrete and therefore the permeability is locally reduced increasing the possibility of spalling. Furthermore, compressive Eigen stresses cause cracks parallel to the heated surface which reduce the tensile strength in the direction perpendicular to heated surface.
  - Tensile stresses in the cross section decrease the capability of the concrete to withstand tensile stresses due to pore pressure build up and therefore the possibility of spalling increases.
  - Concrete with dense reinforcement in a construction tends to impede further water vapour transport and exhibit locals tensile stress peaks which increases the possibility of spalling.

9.1.2. Conclusions about the analytical and numerical model

- The analytical model estimates spalling for the first time after 6 minutes and the depth of the spalled of layer is 16 mm. The pore pressure on the front of the fully saturated layer was 1,58 MPa and the temperature 200 ^{o}C. The pore pressure on the front of the second fully saturated layer started to develop after 14,5 minutes and at a depth of 40 mm. However, the pore pressure developed very slow and not high enough to cause spalling.

- The numerical model, with the adapted fire curve, estimates spalling for the first time after 4,5 minutes and the depth of the spalled of layer is 29 mm. After 7,9 minutes, the model estimates spalling for the second time with a depth of the spalled of layer of 27 mm.

- The behaviour and the results from the analytical model indicate that an analytical model for spalling can be based upon the following parts:

- The evaporation of water from the pores of the concrete can be modelled using an energy equation between the heat input from the fire and the heat usage for the evaporation.
- The flow of water vapour into the cross section can be modelled using Darcy's law due to the fact that the influence of the temperature can be neglected.
- The flow of water vapour onto the surface of the cross section can be modelled by using Kodres flow parameter equation, because this equation is based upon a the flow of a gas induced by a pressure difference and during the flow exposed to a increasing temperature.
- The pore pressure build up on the front of the saturated layer can be modelled by using the saturated vapour pressure in case of normal strength concrete.
- For the development of a saturated layer, the flow of water vapour is assumed to be into the cross section of concrete. This assumption has the largest influence on the results of the analytical model. By taking into account also, especially in the first minute of fire exposure, the flow of water vapour onto the surface the saturated layer will take more time to develop. However, the difference in time when the first saturated layer will be developed is around 1 or 2 minutes.

➢ The developed analytical model is relative simple and therefore insight is obtained into the main theories and factors influencing the process which causes spalling.

➢ The behaviour and the results from the numerical model indicate that an numerical model for spalling can be based upon the following parts:
  - The process which causes spalling can be modelled using the Pore fluid/Stress model in ABAQUS, because this model is based upon a porous medium through which the wetting liquid, induced by a pressure difference, can flow.
  - The evaporation of water from the pores of the concrete and the subsequent increase in pore pressure can be modelled by incorporating the expansion coefficient of the wetting liquid and the porous bulk modulus and thus adapting the behaviour of the wetting liquid to simulate, with increasing temperature, the presence of water and water vapour in the model.
  - The Pore fluid/Stress model is capable of taking into account the stress distribution in the cross section due to the loading. Furthermore, after spalling has occurred the calculation can be restarted and continued.
  - The assumption of the expanding wetting liquid to incorporate the evaporation of water and the subsequent increase in pore pressure combined with the adapted permeability is the largest assumption in the numerical model. The expansion coefficient of the wetting liquid is estimated in the temperature range of 100 – 150 ^{o}C, which is the most important temperature range. The actual values of the expansion coefficient in this temperature range should be obtained from the mixture of water and water vapour. However, this is not possible in the Pore fluid/Stress model due to the one phase flow. To obtain a progressing pore pressure peak, the permeability is adapted. The behaviour of the Pore

fluid/Stress model then confirms with the general theory of spalling and the analytical model.

- The case study of the "Groene Hart" tunnel indicates that a Soil loading model, which incorporates the soil loading and the interaction of the lining with the ground, can be used to obtain the structural behaviour. This Soil loading model can then be adapted to incorporate the heat penetration and the pore pressure distribution, which is obtained from the Pore fluid/Stress model, to determine if spalling occurs. The obtained stress distribution should be compared to the yield criterion developed by Mohr Coulomb and by also taking into account the temperature dependence of the tensile strength of the concrete. The developed model then becomes applicable for the practise to use.

9.2. Recommendations

- During the development of the analytical and the numerical model information about the permeability and the porosity and their relationship at increasing temperatures and especially temperatures in excess of 500 ^{o}C was difficult to obtain. Furthermore, the influence of the degree of saturation on the permeability and the type of liquid flowing though the concrete is also of importance, but was difficult to obtain. Therefore more research has to be done into the permeability and porosity.

- Spalling is largely determined by the first 50 mm of the cross section. Therefore further research should be done into the behaviour of this section of concrete especially the possibility of the increase in permeability due to the lesser quality of concrete, the formation of cracks due to Eigen stresses and loading, the presence of stresses and the degradation process of the concrete due to the increasing temperature towards the surface.

- The analytical model should be implemented in a mathematical program to ensure that it can be used for different types of concrete and fire curves. Furthermore, the flow of water vapour should be allowed in both directions by using Darcy's law for flow into the cross section and Kodres law for flow onto the surface of the concrete.

- In the analytical model the pore pressure is estimated by the saturated vapour pressure, which holds for the front of the fully saturated layer. However, mostly the pore pressure is determined by the mixture of water and water vapour. By incorporating this mixture and the resulting pore pressure, the pore pressure distribution in time can be obtained.

- The numerical model should be adapted to incorporate the evaporation of water from the pores of the concrete and the pore pressure should be related to the mixture of water and water vapour. The pore pressure and the temperature gradient should determine the flow of water vapour in every direction.

- The analytical model should be developed to be implemented in a finite element program such as ABAQUS. The analytical model obtains from the finite element program the geometry, the mesh, the boundary conditions and the loading

including the heating of the surface of the cross section. The analytical model uses this to determine, in every increment, the temperature distribution, the evaporation process, the pore pressure development, the flow of water vapour and the saturation distribution. Furthermore, it should indicate if spalling is present in the model. This is coupled to the finite element program, which visualises the results and in case of spalling adapts the mesh.

- A parameter study should be done for the analytical model and the numerical model to check the behaviour for different types of concrete and fire curves.

Appendix A : HSL –Zuid fire curve

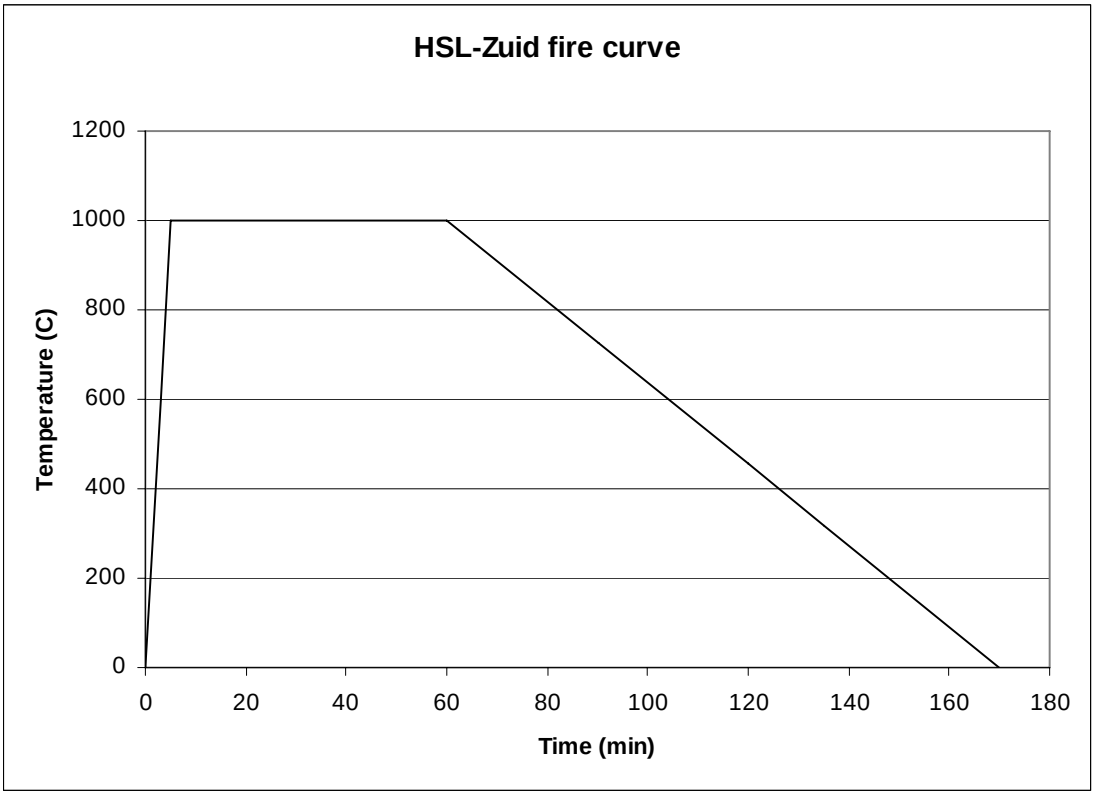

The HSL-Zuid fire curve develops rapidly in the first 5 minuets of the fire. The temperature increases in this time interval from 20 ^{o}C to 1000 ^{o}C. The temperature remains constant for the next 55 minutes, after which the temperature decreases until a temperature of 20 ^{o}C after 180 minutes of fire exposure.

Appendix B : Material properties used in the analytical model

Modulus of Elasticity

The initial modulus of Elasticity used is 30.000 N/mm^2. However, due to relaxation and creep the modulus of Elasticity is reduced by 50 %.

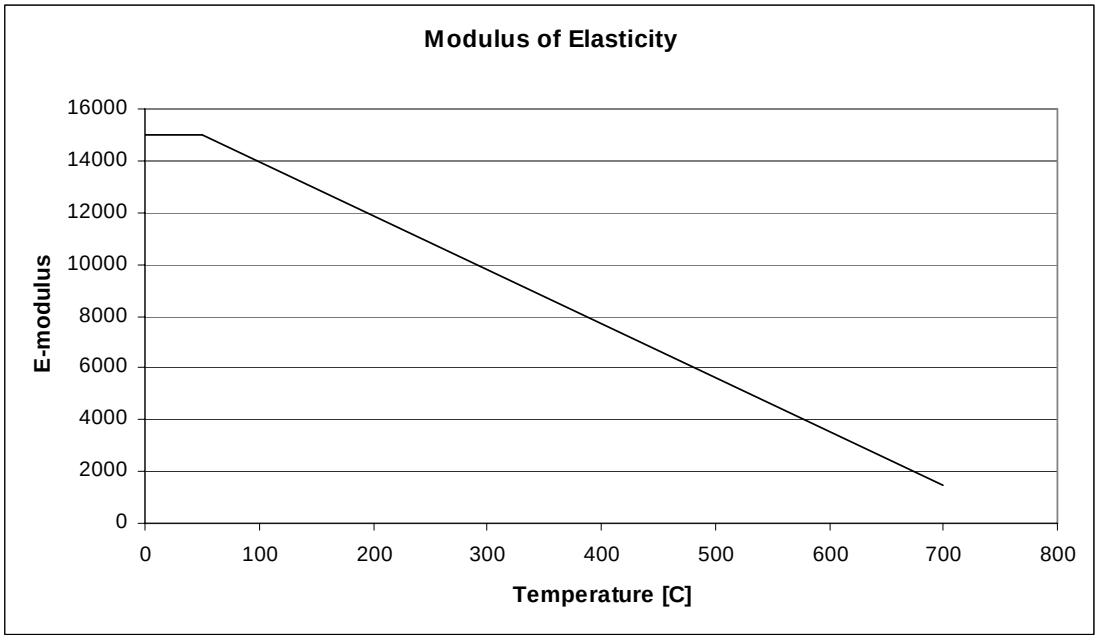

Specific heat of concrete

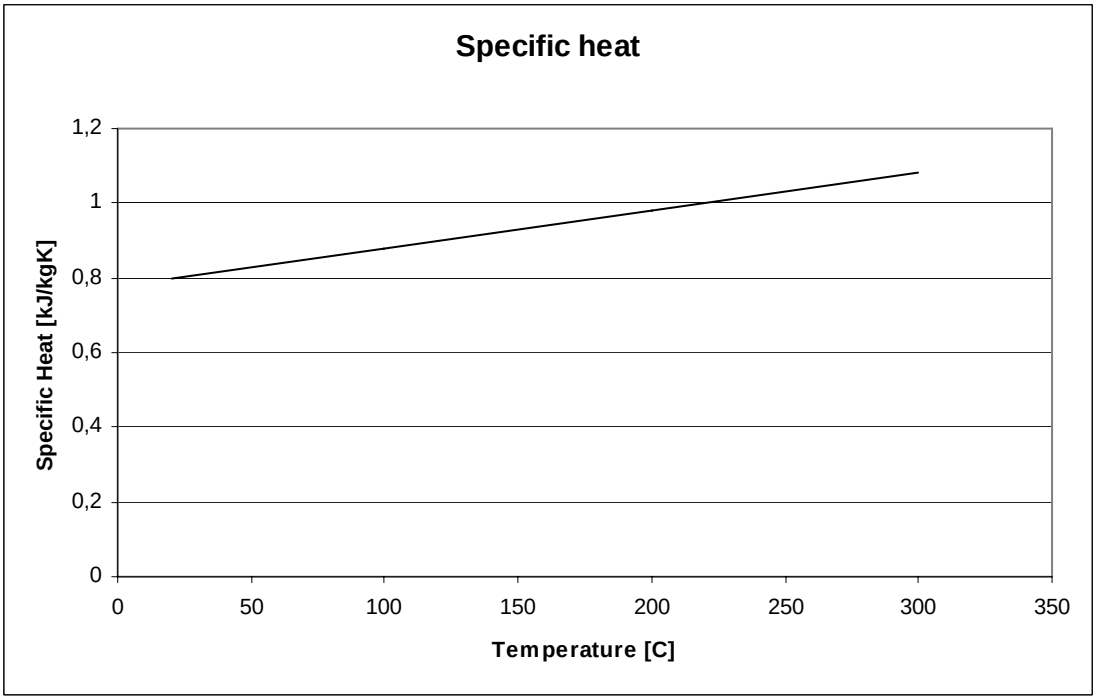

Latent heat of vaporization

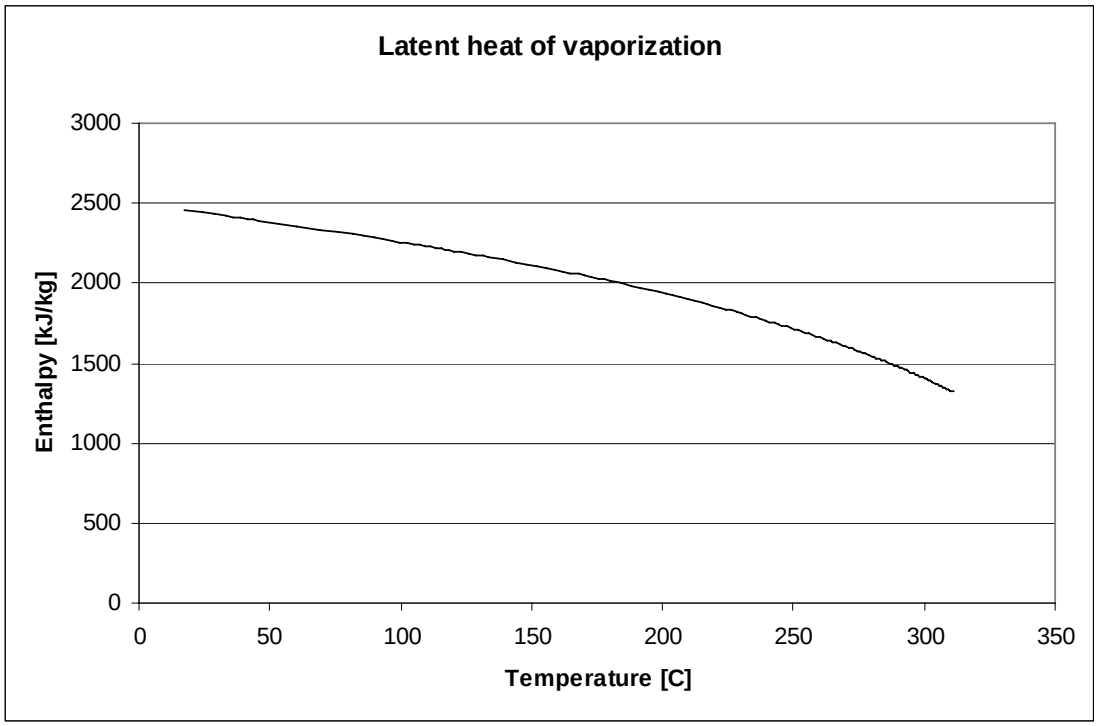

Dynamic viscosity

In the graph the actual dynamic viscosity is depicted and the formula which is used in the analytical model.

Formula => $\mu=1{,}0*10^{-5}+3{,}4*10^{-8}*(T-38{,}72)$

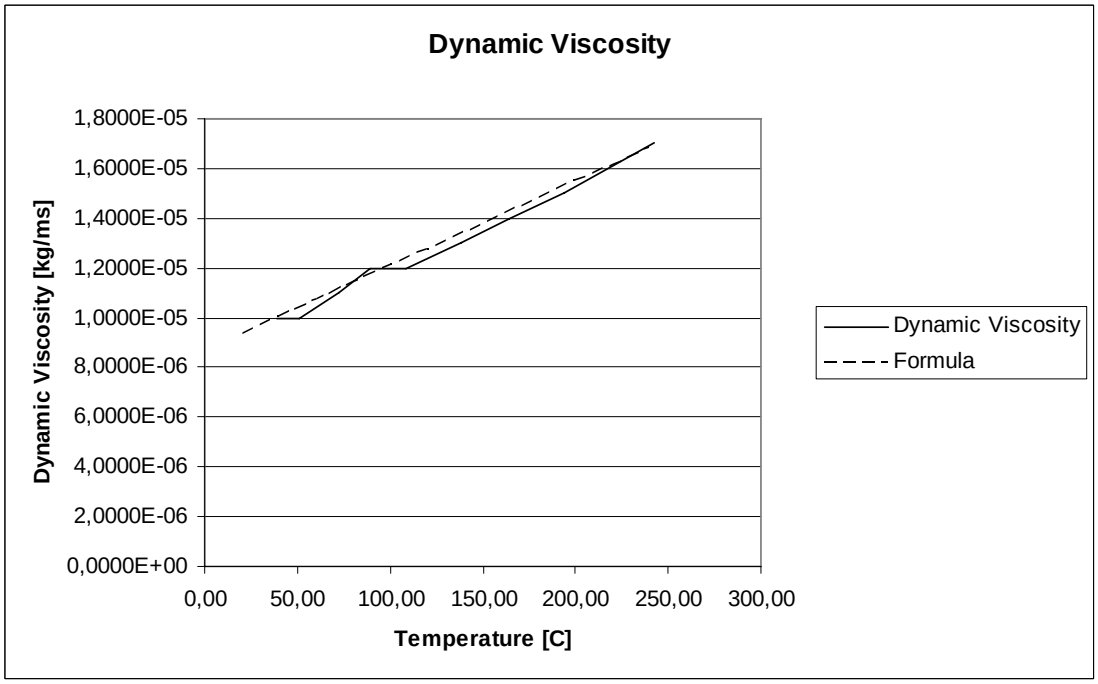

Porosity

This graph is obtained by the following formula =>
n=(0,142+0,0001*(T-20))*100

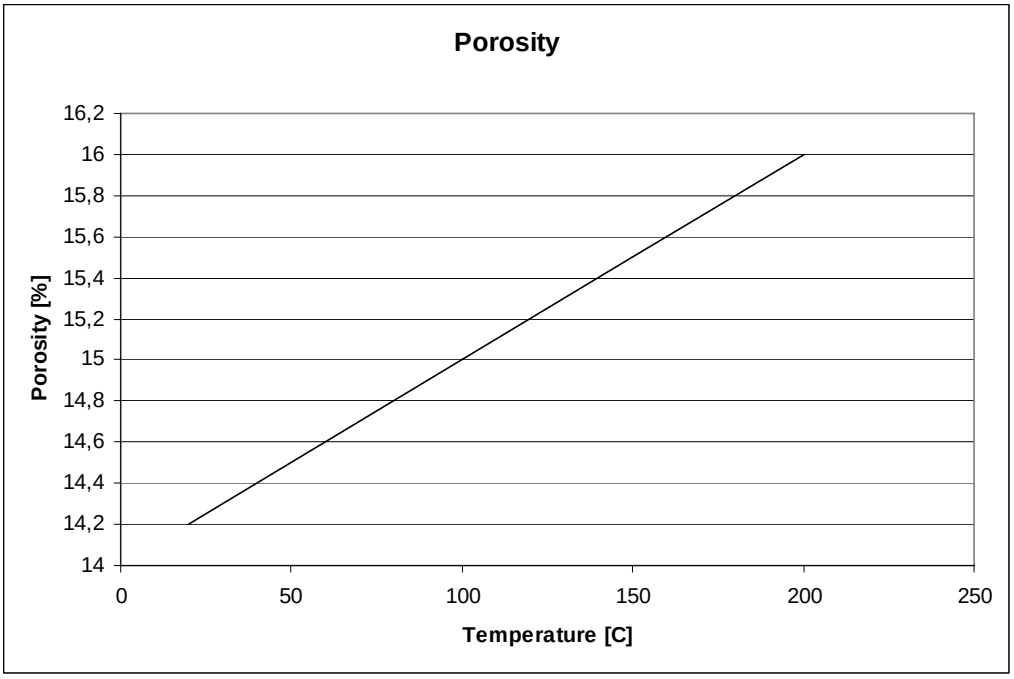

Permeability of concrete

In the graph the permeability is obtained Zeiml [50]. The permeability is corrected to excluding the pore diameters which are not used for the laminar flow of the water vapour. The obtained corrected permeability is approximated by a formula.

Formula => $\kappa=7{,}0*10^{-17}*10^{(0{,}0046*T)}$

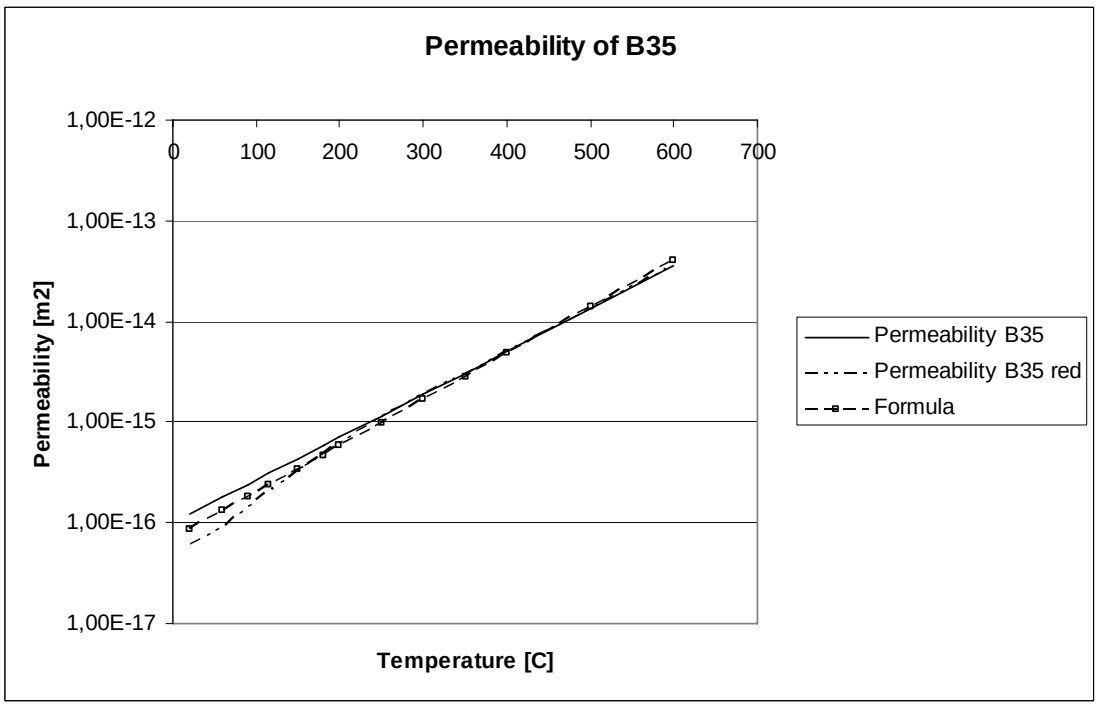

Density of water vapour

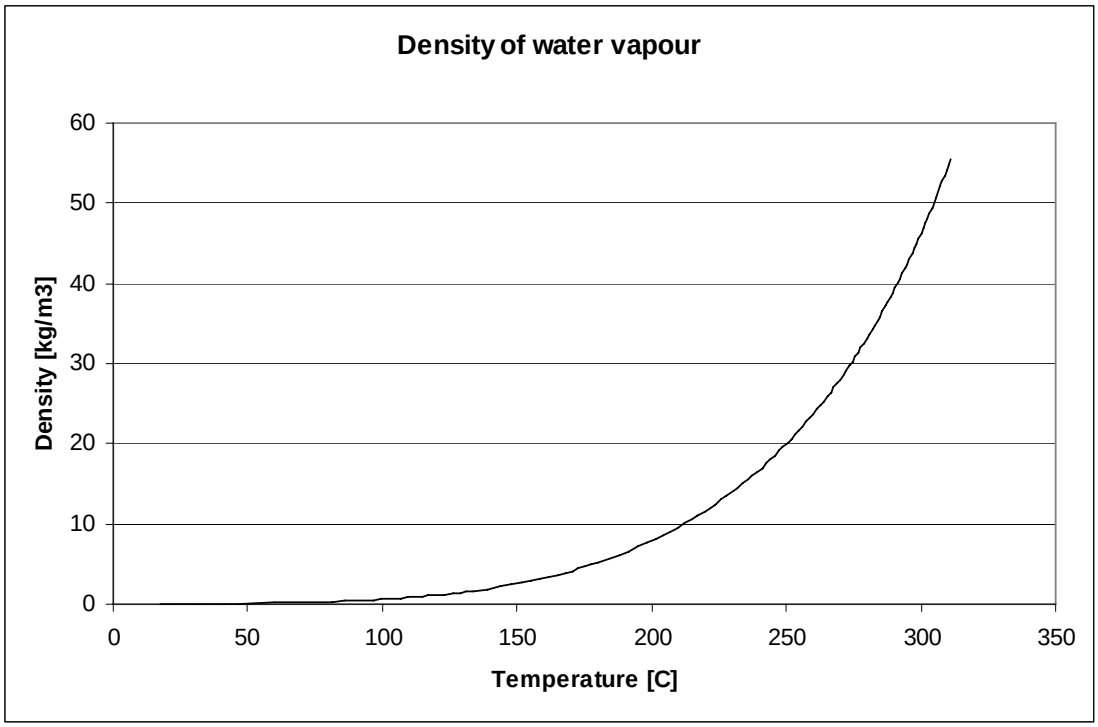

Tensile strength of concrete

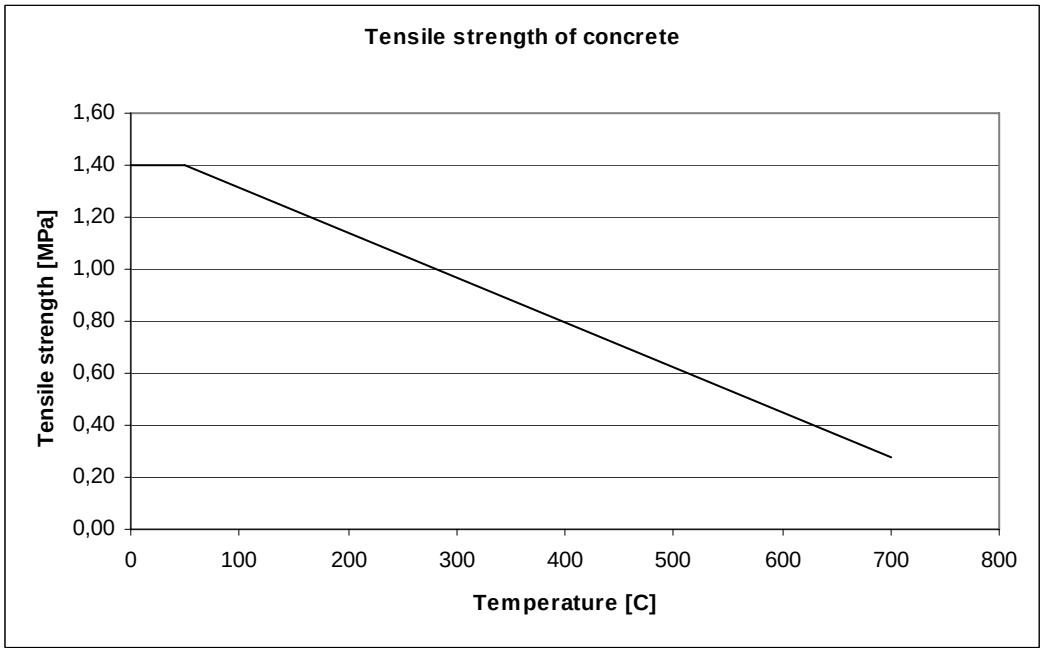

Appendix C : Material properties used in the numerical model

Modulus of Elasticity

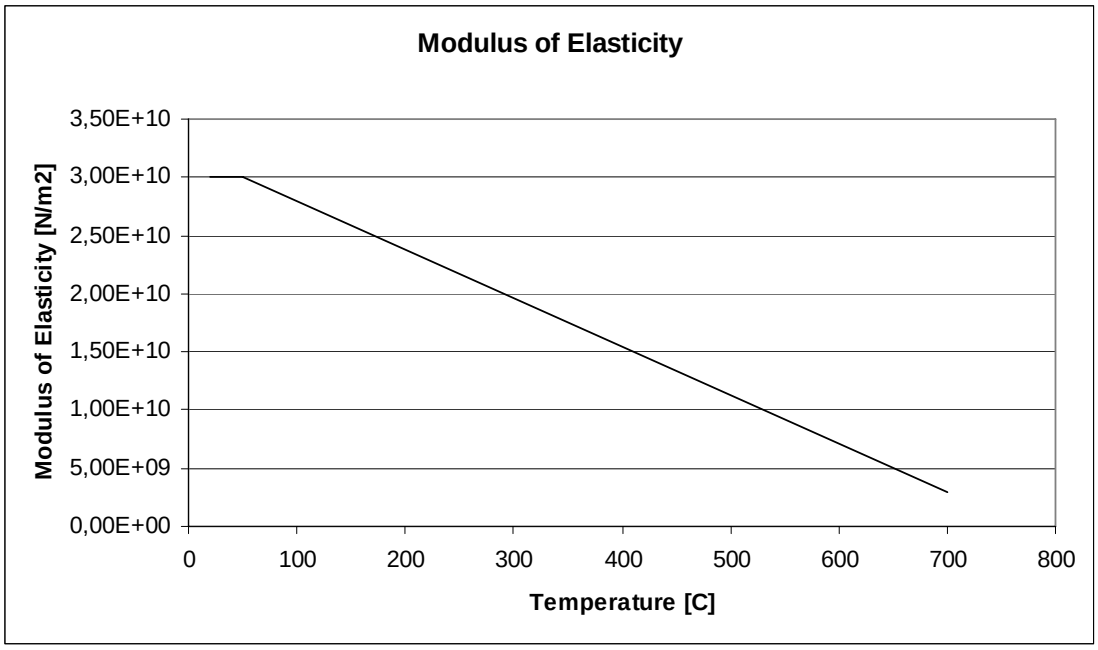

Permeability of concrete

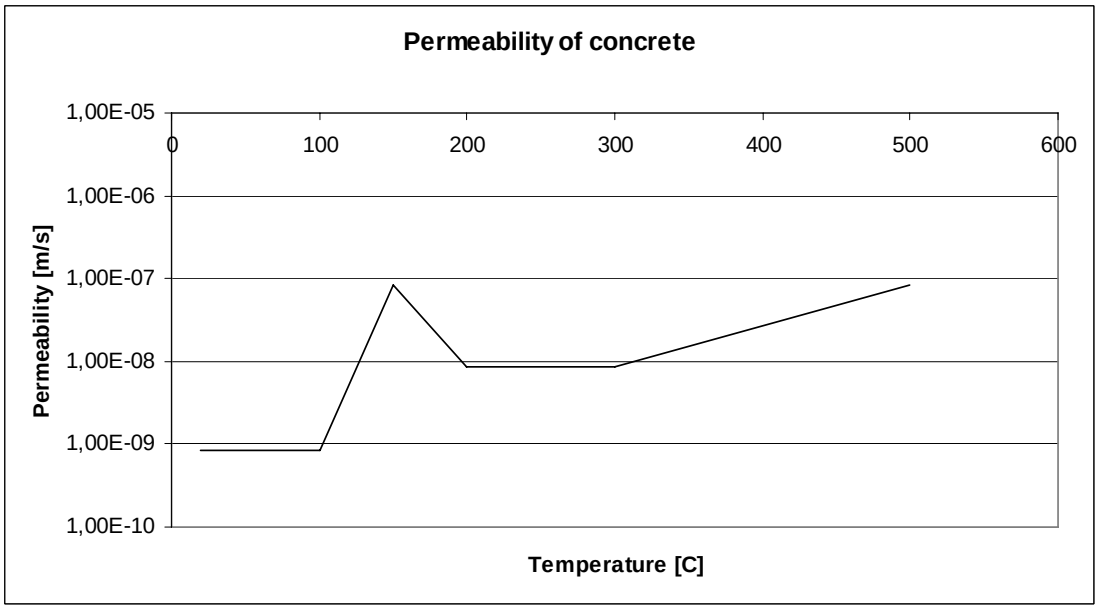

Porosity of concrete

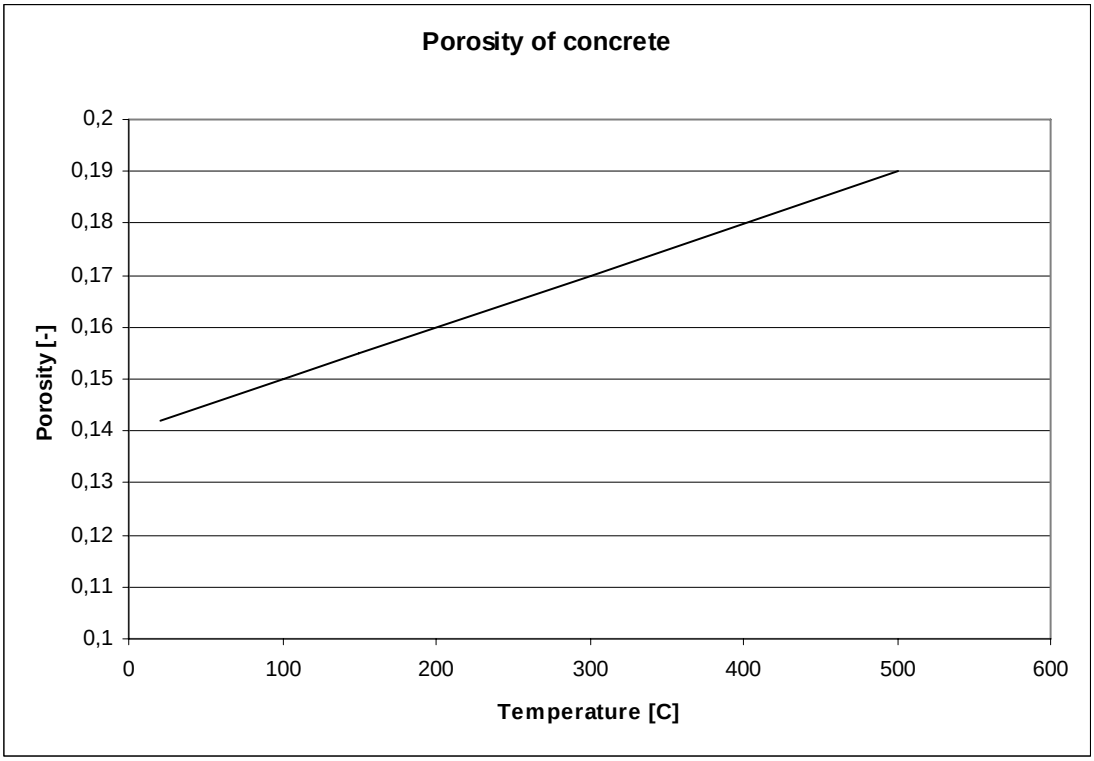

Sorption curve

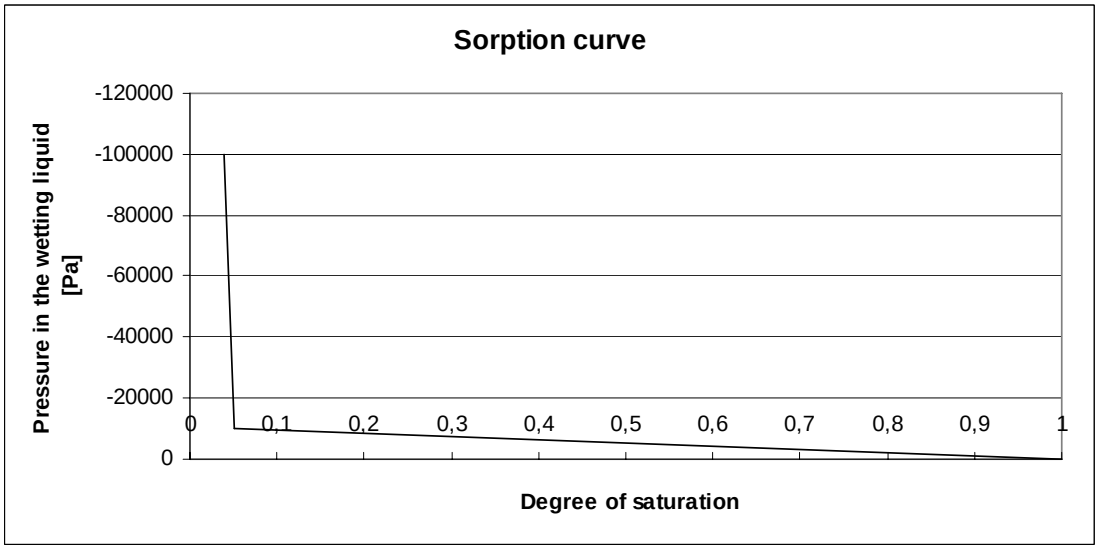

Appendix D : User subroutine used in ABAQUS for the 1D model

```
      SUBROUTINE USDFLD(FIELD,STATEV,PNEWDT,DIRECT,T,CELENT,
     1 TIME,DTIME,CMNAME,ORNAME,NFIELD,NSTATV,NOEL,NPT,LAYER,
     2 KSPT,KSTEP,KINC,NDI,nshr,COORD,JMAC,JMTYP,MATLAYO,LACCFLA)

      INCLUDE 'aba_param.inc'

      PARAMETER (NELEMENTS=4000)
      PARAMETER (IPOINTS=4)
      PARAMETER (NMAXPOINTS=100000)
C
      CHARACTER*80 CMNAME,ORNAME
      CHARACTER*3  FLGRAY(15)
      DIMENSION FIELD(NFIELD),STATEV(NSTATV),DIRECT(3,3),
     1 T(3,3),TIME(2)
      DIMENSION ARRAY(15),JARRAY(15),JMAC(*),JMTYP(*),COORD(*)

C CREATING SPACE FOR STORAGE OF DATA TO BE USED IN UMESHMOTOIN
      COMMON /KSAVESTUFF/ SSTRESS
      DIMENSION SSTRESS(5,NELEMENTS,IPOINTS)

C CREATING SPACE FOR STORAGE OF DATA TO USED IN UPOREP
      COMMON /KSAVESTUFF4/ PRESSURE
      DIMENSION PRESSURE(3,NELEMENTS,IPOINTS)

C CREATING SPACE FOR STORAGE OF DATA TO USED IN SIGINI
      COMMON /KSAVESTUFF5/ STRESS
      DIMENSION STRESS(6,NELEMENTS,IPOINTS)

C CREATING SPACE FOR STORAGE OF WEAR-DATA

      COMMON /KSAVESTUFF2/ WEAR,SPALLING
      DIMENSION WEAR(3,NMAXPOINTS)

C GET STRESSES FROM PREVIOUS INCREMENT
      IF (SPALLING .NE. 1.0D0) THEN
        CALL GETVRM('S',ARRAY,JARRAY,FLGRAY,JRCD,JMAC,JMTYP,
     1      MATLAYO,LACCFLA)
        Sstress(1,NOEL,NPT) = coord(1)
        Sstress(2,NOEL,NPT) = coord(2)
        Sstress(3,NOEL,NPT) = ARRAY(1)
        Sstress(4,NOEL,NPT) = ARRAY(2)
        Sstress(5,NOEL,NPT) = ARRAY(2)
C        WRITE (7,*) 'Sstress = ', SSTRESS(1,NOEL,NPT),
C     1      SSTRESS(2,NOEL,NPT), Sstress(5,NOEL,NPT), NOEL
      ELSE
        ptIsDone = Sstress(1, NOEL, NPT)
      END IF

C Check if spatten is going on, in that case write pore pressure and
C stresses to file for start up of next spatstep

      IF ((SPALLING .EQ. 1.0D0).AND.(ptIsDone.LT.1.0e15)) THEN
         Sstress(1, NOEL, NPT) = 1.0e16
         WRITE (7,*) 'OK, spalling is going on for node: ',
     1   TIME(2)

         open(unit=96,file='C:\Temp\PressureI.out',
     1   status='unknown',form='formatted')
         open(unit=97,file='C:\Temp\StressI.out',status='unknown',
     1   form='formatted')
```

```
C GET PORE PRESSURE FROM PREVIOUS INCREMENT
          CALL GETVRM('POR',ARRAY,JARRAY,FLGRAY,JRCD,JMAC,JMTYP,
     1    MATLAYO,LACCFLA)
          Pressure(1,NOEL,NPT) = coord(1)
          Pressure(2,NOEL,NPT) = coord(2)
          Pressure(3,NOEL,NPT) = ARRAY(1)
C         WRITE (7,*) 'Pressure = ', Pressure(1,NOEL,NPT),
C     1   Pressure(2,NOEL,NPT), Pressure(3,NOEL,NPT), NOEL


C WRITE PORE PRESSURE TO FILE
          WRITE(96,'(4e14.5)') SPALLING, coord(1),coord(2),ARRAY(1)

C GET STRESSES FROM PREVIOUS INCREMENT
          CALL GETVRM('S',ARRAY,JARRAY,FLGRAY,JRCD,JMAC,JMTYP,
     1    MATLAYO,LACCFLA)
          Stress(1,NOEL,NPT) = coord(1)
          Stress(2,NOEL,NPT) = coord(2)
          Stress(3,NOEL,NPT) = ARRAY(1)
          Stress(4,NOEL,NPT) = ARRAY(2)
          Stress(5,NOEL,NPT) = ARRAY(3)
          Stress(6,NOEL,NPT) = ARRAY(4)

C WRITE STRESSES TO FILE
          WRITE(97,'(7e14.5)') SPALLING, coord(1),coord(2),ARRAY(1),
     1    ARRAY(2),ARRAY(3),ARRAY(4)

       END IF

       RETURN
       END



       subroutine umeshmotion(uref,ulocal,node,nndof,
      1 lnodetype,alocal,ndim,time,dtime,pnewdt,kstep,
      2 kinc,kmeshsweep,jmatyp,jgvblock,lsmooth)
C
       include 'aba_param.inc'
C
       CHARACTER*80 PARTNAME
       DIMENSION ARRAY(100000)
       DIMENSION ULOCAL(NDIM)
       DIMENSION JGVBLOCK(*),JMATYP(*)
       DIMENSION ALOCAL(NDIM,*),TIME(2)
       PARAMETER (NELEMMAX=100000)
       PARAMETER (NMAXPOINTS=100000)
       PARAMETER (Lstress=1.4d6)
       PARAMETER (elsize=0.01)
       PARAMETER (IPOINTS=4)
       PARAMETER (NELEMENTS=4000)
       DIMENSION JELEMLIST(NELEMMAX),JELEMTYPE(NELEMMAX)

C CREATING SPACE FOR STORAGE OF WEAR-DATA
       COMMON /KSAVESTUFF2/ WEAR,SPALLING
       DIMENSION WEAR(3,NMAXPOINTS)

C COMMONBLOCK OF STRESSES
       COMMON /KSAVESTUFF/ SSTRESS
       DIMENSION SSTRESS(5,NELEMENTS,IPOINTS)
```

```
C COMMONBLOCK OF COORDINATS
      COMMON /KSAVESTUFF3/ COORDS
      DIMENSION COORDS(3,NMAXPOINTS)

C     NDIM is assumed to be 2 (2-dimensional), so wear normal to the
C     surface is ULOCAL(2)

C     Define common block to be used throughout this routine
      IF (KINC.EQ.1) then
C         CALL GETVRN(NODE,'COORD',ARRAY,JRCD,JGVBLOCK,LTRN)
         WEAR(1,NODE) = NODE
C         WEAR(2,NODE) = COORD(1)
C         WEAR(3,NODE) = COORD(2)
         WEAR(2,NODE) = 1.0d7
         WEAR(3,NODE) = 0.0d0
      END IF

C            WRITE  (7,*)  'WEAR  =  ',  WEAR(1,NODE),  WEAR(2,NODE),
WEAR(3,NODE)

C     Start with check if wear is already present in the model
      IF (TIME(2).GT.WEAR(2,NODE)) THEN
C         WRITE (7,*) 'OK, spalling is going on for node: ',
C     1 WEAR(1,NODE), TIME(2)
C         GOTO 6000
          WRITE (7,*) 'WEAR = ', WEAR(1,NODE), WEAR(2,NODE),
     1    WEAR(3,NODE),SPALLING
C TERMINATE DATA FOR PRESSURE
          open(unit=96,file='C:\Temp\PressureI.out',
     1    status='unknown',form='formatted')
          WRITE(96,'(4e14.5)') -1.0D0, 0.0D0, 0.0D0, 0.0D0
C TERMINATE DATA FOR STRESS
          open(unit=97,file='C:\Temp\StressI.out',status='unknown',
     1   form='formatted')
          WRITE(97,'(7e14.5)') -1.0d0, 0.0d0, 0.0d0, 0.0d0, 0.0d0,
     1    0.0d0, 0.0d0
          CALL XIT
       END IF

C     Check of the stresses behind the node on the surface
      CALL GETVRN(NODE,'COORD',ARRAY,JRCD,JGVBLOCK,LTRN)
      COORDS(1,NODE) = ARRAY(1)
      COORDS(2,NODE) = ARRAY(2)
C      WRITE (7,*) 'COORDS = ', COORDS(1,NODE), COORDS(2,NODE), NODE

      YCOORD = -1.0d7
      SPAT=0
      DO IPOS1=1,NELEMENTS
         DO IPOS2=1,IPOINTS
            XCOORD=Sstress(1,IPOS1,IPOS2)
            DIST=SQRT((XCOORD-ARRAY(1))**2.0d0)
C            WRITE(7,*) 'Afstand: ',IPOS1,IPOS2,XCOORD,DIST
              IF (DIST.LT.(elsize/2.0d0)) THEN
                 IF (Sstress(5,IPOS1,IPOS2).GT.Lstress) THEN
                    SPAT=1
                    IF (Sstress(2,IPOS1,IPOS2).GT.YCOORD) THEN
                       YCOORD=Sstress(2,IPOS1,IPOS2)
                       DEPTH = (YCOORD-ARRAY(2))
                       WRITE(7,*) 'SPATTEN: ',NODE,
     1                 Sstress(5,IPOS1,IPOS2),TIME(2),DEPTH
                    END IF
```

```
                  END IF
                END IF
            END DO
         END DO

         IF (SPAT.EQ.1) THEN
C        Stresses exceed the limit stress
C        The first node that exceeds the limit stress is searched for
          DEPTH = (YCOORD-ARRAY(2))
          WEAR(2,NODE) = TIME(2)
          WEAR(3,NODE) = DEPTH
          SPALLING = 1.0d0
          WRITE (7,*) 'WEAR = ', WEAR(1,NODE), WEAR(2,NODE),
        1 WEAR(3,NODE),SPALLING

C        The wear layer is spalled off in 10 increments
C        with a total time of 0.1 second
C         PNEWDT = 0.01
C /DTIME
          ULOCAL(2) = 0.0d0
C        Stresses to not exceed the limit stress
         ELSE
          ULOCAL(2)=0.0d0
          SPALLING =0.0d0
         END IF
C         GOTO 7000

C        Wear is already present in the model
6000  ULOCAL(2) = 0.0d0

C 7000  WRITE(7,*) 'CHECK: ',NODE, ULOCAL(2), TIME(2)

C        TANGENTIAL MOVEMENT IS ZERO
         ULOCAL(1)=0.0

         RETURN
         END


         subroutine UPOREP(UWO,COORDS,NODE)
C
         include 'aba_param.inc'
C
         PARAMETER (NPOINTS=4)
         PARAMETER (NELEMENTS=4000)
         PARAMETER (NMAXPOINTS=100000)
         PARAMETER (elsize=0.01)
         DIMENSION COORDS(3)
         DIMENSION WS(10000)
         DIMENSION NRP(10000)
C CREATING SPACE FOR STORAGE OF DATA TO USED IN UPOREP
         COMMON /KREADSTUFF/ PRESSURE, IHAVEBEENHERE, NR
         DIMENSION PRESSURE(NMAXPOINTS,3)

C         WRITE(7,*) 'IN UPOREP:',NODE
         IF (IHAVEBEENHERE .EQ. 0) THEN
            IHAVEBEENHERE = 1
            open(unit=95,file='C:\Temp\PressureI.out',
        1   status='old',form='formatted',
        2   action='read')
            nr=0
```

```
         DO
            read(95,*) sindic, xcoord, ycoord,por
            if ( sindic .LE. 0.0D0 ) exit
C            WRITE(7,*) 'DATA:',xcoord, ycoord,por,nr
            nr=nr+1
            Pressure(nr,1)= xcoord
            Pressure(nr,2)= ycoord
            Pressure(nr,3)= por
C            WRITE(7,*) 'Pressure:',Pressure(nr,1),
C     1      Pressure(nr,2),Pressure(nr,3)
         END DO
      END IF

C Calculate the distance between the integration point and the node
C This used as a weighing function to determine the pore pressure
C at the node
      DO I=1,NR
C            WRITE(7,*) 'Pressure:',Pressure(i,1),
C     1      Pressure(i,2),Pressure(i,3)
      END DO
      Factortot=0.0d0
      UWO=0.0d0
      NUMWS = 0
      DO NUM3=1,nr
        xcoord=Pressure(NUM3,1)
        ycoord=Pressure(NUM3,2)
        XDIST=(xcoord-COORDS(1))
        YDIST=(ycoord-COORDS(2))
        W=SQRT((XDIST**2.0d0)+(YDIST**2.0d0))
C         WRITE(7,'(1I4,5E10.2)')
C     1          num3, coords(1), coords(2), xcoord, ycoord, w
        IF(W.LT.0.5D0*elsize) THEN
           NUMWS = NUMWS + 1
           WS(NUMWS)  = W
           NRP(NUMWS) = NUM3
C            WRITE(7,*) WS(NUMWS), NRP(NUMWS)
        END IF
      END DO
      WRITE(7,*) NUMWS, 'points found'
      WTOT = 0.0D0
      CTOT = 0.0D0
      DO I = 1, NUMWS
        WTOT = WTOT + WS(I)
C         WRITE(7,*) WTOT, 'total distance'
      END DO
      DO I = 1, NUMWS
        WS(I) = WTOT - WS(I)
        CTOT  = CTOT + WS(I)
      END DO
      UWO = 0.0D0
      DO I = 1, NUMWS
        WS(I) = WS(I)/CTOT
        UWO = UWO + WS(I)*Pressure(NRP(I),3)
      END DO
      WRITE(7,*) 'DONE : ', UWO
      RETURN
      END



.......
```

```
      SUBROUTINE SIGINI(SIGMA,COORDS,NTENS,NCRDS,NOEL,NPT,LAYER,
     1 KSPT,LREBAR,NAMES)
C
      INCLUDE 'ABA_PARAM.INC'
C
      DIMENSION SIGMA(NTENS),COORDS(NCRDS)
      CHARACTER NAMES(2)*80
      PARAMETER (NPOINTS=4)
      PARAMETER (NELEMENTS=4000)
      PARAMETER (NMAXPOINTS=100000)
      PARAMETER (elsize=0.01)
      DIMENSION WS(10000)
      DIMENSION NRP(10000)

C CREATING SPACE FOR STORAGE OF DATA TO USED IN SIGINI
      COMMON /KREADSTUFF2/ STRESS, IHAVEBEENHERE, NR
      DIMENSION STRESS(NMAXPOINTS,6)

C      WRITE(7,*) 'IN sigini:',NODE
      IF (IHAVEBEENHERE .EQ. 0) THEN
         IHAVEBEENHERE = 1
         open(unit=94,file='C:\Temp\StressI.out',
     1   status='old',form='formatted',
     2   action='read')
         nr=0
         DO
            read(94,*) sindic, xcoord, ycoord,stress11,stress22,
     1      stress33,stress12
            if ( sindic .LE. 0.0D0 ) exit
C            WRITE(7,*) 'DATA:',xcoord, ycoord,stress11,stress22,
C     1      stress33,stress12,nr
            nr=nr+1
            Stress(nr,1)= xcoord
            Stress(nr,2)= ycoord
            Stress(nr,3)= stress11
            Stress(nr,4)= stress22
            Stress(nr,5)= stress33
            Stress(nr,6)= stress12
            WRITE(7,*)
'Stress:',Stress(nr,1),Stress(nr,2),Stress(nr,3),
     1      Stress(nr,4),Stress(nr,5),Stress(nr,6)
         END DO
      END IF

C Calculate the distance between the integration point and the node
C This used as a weighing function to determine the stress
C at the node
      DO I=1,NR
C                                  WRITE(7,*)   'Stress:',Stress(i,1),
Stress(i,2),Stress(i,3),
C     1      Stress(i,4), Stress(i,5),Stress(i,6)
      END DO
      Factortot=0.0d0
      UWO=0.0d0
      NUMWS = 0
      DO NUM4=1,nr
        xcoord=Stress(NUM4,1)
        ycoord=Stress(NUM4,2)
        XDIST=(xcoord-COORDS(1))
        YDIST=(ycoord-COORDS(2))
        W=SQRT((XDIST**2.0d0)+(YDIST**2.0d0))
```

```
C        WRITE(7,'(1I4,5E10.2)')
C     1          num4, coords(1), coords(2), xcoord, ycoord, w
        IF(W.LT.0.5D0*elsize) THEN
           NUMWS = NUMWS + 1
           WS(NUMWS)  = W
           NRP(NUMWS) = NUM4
C           WRITE(7,*) WS(NUMWS), NRP(NUMWS)
        END IF
      END DO
      WRITE(7,*) NUMWS, 'points found'
      WTOT = 0.0D0
      CTOT = 0.0D0
      DO I = 1, NUMWS
        WTOT = WTOT + WS(I)
      END DO
      DO I = 1, NUMWS
        WS(I) = WTOT - WS(I)
        CTOT  = CTOT + WS(I)
      END DO
      Sigma(1) = 0.0D0
      Sigma(2) = 0.0D0
      Sigma(3) = 0.0D0
      Sigma(4) = 0.0D0
      DO I = 1, NUMWS
        WS(I) = WS(I)/CTOT
        Sigma(1)= Sigma(1) + WS(I)*Stress(NRP(I),3)
        Sigma(2)= Sigma(2) + WS(I)*Stress(NRP(I),4)
        Sigma(3)= Sigma(3) + WS(I)*Stress(NRP(I),5)
        Sigma(4)= Sigma(4) + WS(I)*Stress(NRP(I),6)
      END DO
      WRITE(7,*) 'DONE : ', Sigma(1),Sigma(2),Sigma(3),Sigma(4)
      RETURN
      END
```

Appendix E : References

[1] **ABAQUS Inc., 2006**
Analysis Theory Manual version 6.6, ABAQUS, Pawtucket, Rhode Island

[2] **ABAQUS Inc., 2006**
Analysis User's Manual version 6.6, ABAQUS, Pawtucket, Rhode Island

[3] **ABAQUS Inc., 2006**
Analysis Subroutine Manual version 6.6, ABAQUS, Pawtucket, Rhode Island

[4] **Blom, C.B.M., 2006**
Concrete linings for shield driven tunnels, lecture notes Delft University of Technology, Delft

[5] **Blom, C.B.M., 2002**
Design Philosophy of concrete linings for tunnels in soft soils, Ph.D. thesis Delft University of Technology, Delft

[6] **Breugel, K. van, Veen, C. van, Walraven, J.C., Braam, C.R., 1998**
Betonconstructies onder temperatuur- en krimpvervormingen, Betonpraktijkreeks 2, 's

[7] **Castellote, M., Alonso, C., Andrade, C., Turrillas, X., Campo, J., 2004**
Composition and micro structural changes of cement pastes upon heating as studied by neutron diffraction, Cement and Concrete Research 34, blz 1633-1644

[8] **Channel Tunnel Safety Authority, 1997**
Inquiry into the fire on heavy goods vehicle shuttle 7539 on 18 November 1996, London

[9] **Chung, J.H., Consolazio, G.R., 2005**
Numerical modeling of transport phenomena in reinforced concrete exposed to elevated temperatures, Cement and Concrete Research 35, blz. 597-608

[10] **Civiel technisch Centrum Uitvoering Research en Regelgeving (CUR), 2004**
Safe and Reliable Tunnels, Innovative European Achievement, Proceedings of the first International Symposium, 4-6 February 2004, Prague

[11] **Civiel technisch Centrum Uitvoering Research en Regelgeving (CUR), 1994**
Rapport 149, Brandwerendheid van betonconstructies, deel 1, Uitgangspunten en gegevens voor een rekenkundige beoordeling, Gouda

[12] **Civiel technisch Centrum Uitvoering Research en Regelgeving (CUR), 1980**
CUR 98b, Spatten van grindbeton en lichtbeton bij brand, Gouda

[13] **Civiel technisch Centrum Uitvoering Research en Regelgeving (CUR), 1994**
CUR 153, Brandwerendheid van betonconstructies, deel 2, Rekenkundige bepaling en vervormingen, Gouda

[14] **Duddeck, H., 1980**
Empfehlungen zur Berechnung von Tunneln im Lockergestein, Die Bautechniek 10, blz. 349-356, Braunschweig

[15] **Duddeck, H., 1972**
Zu den Berechnungsmethoden und zur Sicherheit von Tunnelbauten, Der Bauingenieur 47, blz. 43-52, Braunschweig

[16] **Duddeck, H., Erdmann, J., 1983**
Statik der Tunnel im Lockergestein, Vergleich der Berechnungsmodelle, Bauingenieur 58, blz. 407-414, Braunschweig

[17] **Duddeck, H., Schulze, H.,1964**
Spannungen in schildvorgetriebenen Tunneln, Beton- und Stahlbetonbau, blz. 169-175, Düsseldorf

[18] **Eurocode, 2005**
Eurocode II, Design of concrete structures, Part 1-2, General Rules-Structural fire design

[19] **FIP/CEB, 1981**
Stuvo-rapport nr. 61, Brandwerendheid van betonconstructies

[20] **Fischer, R., 1970**
Über das Verhalten von Zementmörtel und Beton bei höheren Temperaturen, Deutscher Ausschuss für Stahlbeton, heft 214, München

[21] **Frank, K., 2005**
Grundlagen der Warmelehre, lecture notes University of Erlangen

[22] **Gudmundsson, K., 2000**
An approach to determining the water vapour transport properties of builing materials, department of Civil and Architectural Engineering, Hogskolan

[23] **Harmathy, T.Z., 1993**
Concrete Design and Construction Series, Fire Safety Design and Concrete, Ottawa

[24] **Hassen, S., Colina, H., 2006**
Transient thermal creep of concrete in accidental conditions at temperatures up to 400 ^{o}C, Magazine of concrete research 58, blz 201-208

[25] **Heijboer, J., Hoonaard, J., van den, Linde, F.W.J., van de, 2004**
The Westerschelde Tunnel, Approaching Limits, Lisse

[26] **Ichikawa, Y., England, G.L., 2004**
Prediction of moisture migration and pore pressure build-up in concrete at high temperatures, Nuclear Engineering and Design 228, blz. 245-259

[27] **Kalifa, P., Menneteau, F., Quenard, D., 2000**
Spalling and pore pressure in HPC at high temperatures, Cement and Concrete Research 30, blz.1915-1927

[28] **Khoury, G.A., 2000**
Effect of fire on concrete and concrete structures, Progress in Structural Engineering and Materials 2, blz. 429-447

[29] **Khoury, G.A., 2003**
EU tunnel fire safety action, Tunnels and Tunnelling International april

[30] **Khoury, G.A., Grainger, B.N., Sullivan, P.J.E, 1985**
Transient thermal strain of concrete: literature review, conditions within the specimen and behaviour of individual constituents, Magazine of Concrete Research 132, blz. 131-144

[31] **Kodres, C.A., 1994**
Flow parameter approach tomodeling the flow of heated gases through high resistance porous media, Transport in Porous Media 15, blz. 229-249

[32] **Kordina, K., Ehm, H., Postel, R., von, 1975**
Erwärmungsvorgänge an balkenartigen Stahlbetonbauteilen unter Brandbeanspruchung, Deutscher Ausschuss für Stahlbeton, heft 230, Technische Universität Braunschweig, Braunschweig

[33] **Meyer-Ottens, C., 1975**
Zur frage der Abplatzungen an Bauteilen aus Beton bei Brandbeanspruchungen, Deutscher Ausschuss für Stahlbeton, heft 248, Technische Universität Braunschweig, Braunschweig

[34] **Meyer-Ottens, C., 1974**
Abplatzversuche an Prüfkörpern aus Beton, Stahlbeton und Spann beton bei verschiedenen Temperaturbeanspruchungen, Deutscher Ausschuss für Stahlbeton, heft 241, Technische Universität Braunschweig, Braunschweig

[35] **Pel, L., Heijden, G.H.A., van der, Huinink, H.,2006**
Spalling of concrete as studied by NMR, 2nd International Symposium on Advances in Concrete through Science and Engineering, 11-13 September 2006, Quebec city

[36] **Phan, L.T.,**
High strength concrete at high temperatures – An overview

[37] **Poon, C., Azhar, S., Anson, M., Wong, Y., 2001**
Comparison of the strength and durability performance of normal- and high strength pozzolanic concretes at elevated temperatures, Cement and Concrete Research 31, blz. 1291-1300

[38] **Poon, C., Azhar, S., Anson, M., Wong, Y., 2001**
Performance of metakaolin concrete at elevated temperatures, Cement & Concrete Composites 25, blz. 83-89

[39] **Promat, 2002**
Tunnelprospectus Promat

[40] **Qian, C., Wang, H., Sun, W., Guo, Z., Stroeven, P., 2005**
Numerical calculations of vapour pressure in concrete exposed to fire, magazine of Concrete Research 57, blz. 179-184

[41] **Rijkswaterstaat, 1994**
Veiligheidsrichtlijnen deel C, basismaatregelen, Utrecht

[42] **Schneider, U., 1982**
Verhalten von Beton bei hohen Temperaturen, Deutscher Ausschuss für Stahlbeton, heft 337, Technische Universität Braunschweig, Braunschweig

[43] **Schneider, U., Herbst, H.J., 1989**
Permeabilität und Porosität von Beton bei hohen Temperaturen, Deutscher Ausschuss für Stahlbeton, heft 403, Gesamthochschule Kassel, Kassel

[44] **Shamalta, M., Breunesse, A., Peelen, W., Fellinger, J., 2005**
Numerical Modelling and Experimental Assessment of Concrete Spalling in Fire, Hebron Vol. 50 No 4, blz. 303-319, Technische Universiteit Delft, Delft

[45] **Stichting BouwResearch (SBR), 1998**
Ontwerpen en brandveiligheid, Constructie- en materiaalgedrag, Rotterdam

[46] **Sullivan, P.J.E., 2001**
deterioration and spalling of high strength concrete under fire, City University, London

[47] **Vrouwenvelder, A.C.W.M., 2003**
The plastic behaviour and the calculation of beams and frames subjected to bending, lecture notes Delft University of Technology, Delft

[48] **Winterberg, R., Dietze, R., 2004**
Efficient passive fire protection systems for hig
Performance shotcrete, proceedings of the Second International Conference on Engineering Developments in Shotcrete, Cairns

[49] **Wisman, W.H., 1994**
Inleiding Thermodynamica, Delft

[50] **Zeiml, M., Leithner, D., Lackner, R., Manh, H.A., 2006**
How do polypropylene fibers improve the spalling behavior of in-situ concrete, Cement and Concrete Research 36, blz. 929-942

[51] **Multiple speakers, 2007**
Symposium Levensduur en Onderhoud van de "Groene Hart" tunnel, Rijkswaterstaat, Delft Cluster, TNO, Delft
[52] Course notes on Rayleigh Flow, Departement of Mechanical and Chemical Engineering
[53] Lecture notes on gas Dynamic Concepts and Terminology, School of Engineering and Physical Sciences

[54] **CFETIT, 2006**
Cover of master thesis taken from information brochure of CFETIT
Centre de Formation et d'Entraînement aux Techniques d'Intervention en Tunnel, Modane, crédits photos: X. Nuer, O. Chana

[I] http://en.wikipedia.org/wiki/Mean_free_path
[II] http://hyperphysics.phy-astr.gsu.edu/hbase/kinetic/menfre.html
[III] http://hyperphysics.phy-astr.gsu.edu/hbase/kinetic/idegas.html
[IV] http://hyperphysics.phy-astr.gsu.edu/hbase/kinetic/waal.html#c1
[V] http://hyperphysics.phy-astr.gsu.edu/hbase/hframe.html
[VI] http://hyperphysics.phy-astr.gsu.edu/hbase/kinetic/watvap.html#c2
[VII] http://www.natmus.dk/cons/tp/atmcalc/ATMOCLC1.HTM#svp
[VIII] http://en.wikipedia.org/wiki/Adiabatic_index
[IX] http://www.hslzuid.nl/hsl/lijn/Kunstwerken/Boortunnel_Groene_Hart/index.jsp
[X] http://www.engineeringtoolbox.com/saturated-steam-properties-d_101.html